# Studies and integration of Silicon-based light emitting systems

Alfredo A. González Fernández

**U B** Universitat
de Barcelona

Programa de Doctorat en Nanociències

Thesis submitted to obtain the degree of Doctor of Philosophy

# Studies and integration of Silicon-based light emitting systems

Alfredo A. González Fernández

*Supervisors:*
Dr. Carlos DOMÍNGUEZ HORNA
Dr. Mariano ACEVES MIJARES

*Tutor:*
Dr. Blas GARRIDO FERNÁNDEZ

Barcelona, August 2014

Lo doctor no quita lo pendejo

*– Vox populi*

## Acknowledgements

Next, I want to thank my advisers, Dr. Carlos Domínguez and Dr. Mariano Aceves. In particular, I must express my gratitude for the great balance between guidance and liberty provided by Dr. Domínguez, for it is a rare virtue as I have come to understand, and it was essential for me being able to say that I am proud of the work here presented.

This is also a good place to thank J. Juvert. Him and his extraordinary intelligence and generosity permitted each single achievement we have made. Whether such achievements are small or big, is a different discussion (he and his pessimism will always go for 'small'). A special mention is necessary to his resilience (some would say stubbornness) in the defence of an indefensible desktop environment designed having pre-school children in mind.

The support and friendship by the people from the CNM, technicians, colleagues, administration, and friends, must also be acknowledged. In particular, I owe a mention of the great help by Dr. A. Llobera, who always facilitated any material resource to his reach for the development of the experiments. Also, the help by Dr. Gamarra from the Extremadura University deserves my recognition for his invaluable help with the XPS experiments.

Finally, despite I would like to escape from the common places as much as possible, I cannot avoid to mention my infinite gratitude to my family, and in particular, to Carla. For this, no further explanations are needed, I hope. If this is not the case, call me and I can organize a seminar.

# Resumen

Este proyecto aborda el estudio de dispositivos y materiales luminiscentes basados en silicio, con el objetivo final de obtener un Sistema Óptico integrado, transmisor-receptor, fabricado mediante el uso exclusivo de técnicas y materiales compatibles con la tecnología metal-óxido-semiconductor complementaria (CMOS, por sus siglas en inglés). La principal motivación para perseguir los objetivos está basada en las ventajas que el trabajar con la tecnología CMOS y con silicio otorgan, tales como la abundancia del material, el bajo coste de su obtención, el alto conocimiento que se tiene del mismo, y la disponibilidad de infraestructura establecida para el trabajo con dicho elemento, así como posibilidad de integración en circuitos electrónicos de tecnología actual. Desafortunadamente, a pesar de todas estas ventajas, las características de banda indirecta del Si hacen que éste sea un material inviable para aplicaciones fotónicas, dada su ineficiencia para la emisión de luz. Sin embargo, hace ya más de dos décadas que se conoce que esta barrera puede ser superada al aprovechar fenómenos cuánticos que ocurren cuando se trabaja con estructuras de silicio de dimensiones nanométricas. Esto, teóricamente abre la puerta para poder utilizar el Si como material para fabricar emisores de luz. En particular, para la incorporación de estos dispositivos en la fabricación circuitos integrados estándar, con la posibilidad de aprovechar todos los beneficios que esto conlleva.

Para el presente trabajo, se fabricó y estudió un material basado en silicio que contiene nano-estructuras conocido como Dóxido de Silicio Enriquecido con Silicio (SRO por sus siglas en inglés). Este es, en general, una matriz de $SiO_2$ a la que se le agrega un exceso de silicio, que es química y estructuralmente estable una vez concluida su fabricación, y que puede ser obtenido mediante una variedad de técnicas compatibles con la fabricación CMOS estándar. Con el conocimiento adquirido referente a las características y comportamiento del material, se procedió a la fabricación y estudio de dispositivos electrónicos emisores de luz basados en este. Finalmente, tras analizar el comportamiento y respuesta de los dispositivos, así como los parámetros de fabricación y estímulo que influyen en ello, se diseñó y fabricó un sistema óptico integrado por emisor de luz, guía de ondas, y sensor óptico, siempre limitándose al uso de técnicas y materiales compatibles con la tecnología CMOS.

Se fabricaron películas de SRO mediante dos diferentes técnicas: depósito químico en fase vapor con silano y óxido nitroso como precursores, y la implantación de iones de silicio en películas de $SiO_2$ previamente fabricadas. También se estudiaron bi-capas de $SRO–Si_3N_4$. El nitruro se obtuvo mediante depósito químico en fase vapor en todos los casos. Controlando la proporción de los gases precursores, se obtuvo una variedad de películas

con distintos contenidos de silicio, siempre por encima del 33.33 % que se encuentra en el dióxido. En el caso de las películas obtenidas mediante la implantación iónica, distintas dosis de implantación fueron utilizadas para obtener muestras con diferentes excesos de silicio. Con la intención de promover la nucleación del silicio en exceso y así formar nanopartículas, y así aprovechar los fenómenos cuánticos que permiten la recombinación radiativa en ellas, se efectuó un recocido térmico a cada muestra.

Se realizaron estudios de fotoluminiscencia (PL, por sus siglas en inglés) y espectroscopía fotoelectrónica de rayos-X (XPS, por sus siglas en inglés) a las capas activas con el objetivo de entender los mecanismos de emisión de luz que ocurren en ellas, y explorar la relación entre estos y las características estructurales del material. La PL observada fue de espectro ancho, con longitudes de onda entre 625 nm y 950 nm, y con picos de emisión dependientes de los parámetros de fabricación. Se identificó que la fotoluminiscencia es producto de la contribución de al menos dos mecanismos, uno debido a fenómenos de confinamiento cuántico, y otro causado por la presencia de defectos en el material. A través del análisis de la relación entre los resultados de PL y los de XPS, se sugirió y puso a prueba un modelo basado en la aproximación de masa efectiva para explicar los mecanismos de confinamiento cuántico en materiales con determinadas características estructurales. Dicho modelo relaciona la cantidad de enlaces Si–Si en el material, con el volumen de los nano-aglomerados contenidos en él, y la energía de la luz que se emite cuando la recombinación ocurre. En las muestras bi-capa SRO–$Si_3N_4$, se observó una banda de luminiscencia con longitudes de onda entre 400 nm y 600 nm, adicional a la encontrada en muestras con sólo una capa de SRO. El origen de esta luz fue identificado en el material de transición entre el nitruro y el óxido de silicio, y su emisión se pudo relacionar con estados de energía introducidos por defectos. Muestras con un espesor de SRO diez veces mayor que aquel del nitruro, presentaron una clara dominación por parte de la luminiscencia relacionada sólo con el óxido.

Las películas luminiscentes estudiadas fueron replicadas y utilizadas como material activo para fabricar mediante técnicas CMOS estándar los dispositivos electrónicos emisores de luz discretos. Su estructura es planar del tipo metal-óxido-semiconductor, de manera que el estímulo al material se realizó haciendo fuir una corriente de electrones entre el metal (compuerta) y el semiconductor (substrato), tal como en una capacidad MOS. En este caso, el nivel de óxido intermedio fue una película de 30 nm de SRO, o una bi capa de 60 nm de SRO–$Si_3N_4$. Para poder apreciar y estudiar la luminiscencia, la compuerta de los dispositivos de prueba fue fabricada con silicio policristalino altamente dopado, el cual presenta las características de conductividad apropiadas, y es semi-transparente al espectro de emisión del material activo. Se halló que los centros responsables por la electrolumi-

niscencia en los dispositivos electrónicos, son fundamentalmente los mismos que los responsables de la fotoluminiscencia, a pesar de las diferencias en los espectros medidos. También se concluyó que la influencia de la arquitectura sobre el espectro de salida es de importancia significativa. Dicha influencia no sólo se limita a considerar la transmitancia del material de compuerta, sino que los fenómenos ópticos de interferencia en la multi–capa, dominan la modificación que la emisión intrínseca sufre cuando es observada. Se mostró que dispositivos bi-capa entregan mejores resultados en términos de eficiencia, control sobre la luz emitida, distribución de la misma, y estabilidad en el funcionamiento. Se observó que los mecanismos de transporte de carga hallados en los dispositivos están dominados por ruptura del material en el caso de dispositivos de una sola capa, y por Tuneleo Asistido por Trampas en el caso de dispositivos bi-capa.

Una vez estudiados los emisores de luz, los parámetros de fabricación de aquellos con mejores resultados fueron usados para diseñar el Sistema Óptico Integrado (IOS por sus siglas en inglés). Dicho sistema integra el emisor acoplado directamente a una guía de ondas de nitruro de silicio, misma que transmite la luz hasta un fotodiodo fabricado directamente en la oblea de silicio usada como substrato. Como en los casos anteriores, todo el proceso de fabricación y los materiales se acotaron a aquellos compatibles con la tecnología CMOS estándar. Durante esta etapa de diseño, se corroboró mediante simulaciones por computadora, que las características de la luz emitida por los dispositivos que presentaron la máxima eficiencia y fiabilidad, fueran apropiadas para su transmisión a través de la guía de ondas propuesta. También se corroboró teóricamente que las capacidades de detección del fotosensor diseñado, fuera la adecuada para el tipo de luz emitida.

Tras corroborar el funcionamiento teórico del diseño, se llevó a cabo la fabricación del sistema. Se verificó el funcionamiento particular del emisor y del sensor desacoplados, hallándose diferencias en la operación de los dispositivos emisores de luz fabricados previamente, y aquellos integrados en el sistema. Sin embargo, la luminiscencia resultante se encontró dentro de los límites del espectro transmisible por la guía de ondas de acuerdo con las simulaciones. La operación del Sistema Óptico Integrado fue finalmente probada, con la obtención de resultados positivos en su respuesta estímulo–detección, cumpliendo así con el objetivo principal del trabajo, y abriendo la puerta para estudios posteriores que pueden guiar a la optimización del diseño del sistema para aplicaciones particulares.

**Abstract**

This project presents the study of luminescent devices and materials based on silicon for its use in the fabrication of an optical system that integrates light emitter, waveguide, and light sensor in a single chip obtained by the use of standard CMOS techniques and materials. The atomic and structural characteristics of the materials are analysed and related to its luminescent response. Taking into account the results from the active material characterization, the design, fabrication, and characterization of electroluminescent devices based on such materials is presented. Finally, the design, fabrication and characterization of a complete CMOS compatible Integrated Optical System consisting of a transceiver, is discussed and analysed.

The active materials used for light emission were different Silicon Rich Silicon Dioxide (SRO) and SRO-$Si_3N_4$ bi-layers, obtained by a variety of CMOS compatible techniques and fabrication parameters. Two contributing mechanisms to photoluminescence in SRO were identified in all cases, respectively linked to the presence of radiative defects, and to Quantum Confinement phenomena. It is proposed and tested a model to describe the latter, based on the effective mass approximation, and the relation between the amount of Si-Si links and the volume of nano-agglomerates present in the material. In bi-layer samples, an additional luminescence band was observed, found to be generated in the transition material between silicon nitride and dioxide, and related to energy states introduced by defects. Samples with SRO thickness ten times higher than that of nitride, presented a clear dominance of the photoluminescence related to the dioxide.

The centres responsible for electroluminescence in the electronic devices were found to be fundamentally the same as those for photoluminescence despite the differences in measured spectra, and it was concluded that the influence of the architecture on the light output is of significant importance. It was shown that bi-layered devices delivered better results in terms of efficiency, light emission control, distribution and stability. The carrier transport mechanisms observed in the devices were dominated by material breakdown in single-layered devices, and Trap-assisted Tunnelling in the bi-layers.

The Optical System integrating the light emitter, a waveguide, and a light detector, was designed and fabricated based on the results from the fabrication and analysis of the stand alone light emitting devices. During the design stage, it was corroborated by computer simulations that the characteristics of the light emitted by the devices that presented the highest efficiency and reliability, were suitable for its transmission trough the proposed waveguide architecture. The detection capabilities of the designed

light sensors were also theoretically corroborated to be appropriated for the detection of the emitted light type.

The proper functioning of the elements conforming the finally fabricated system was probed. Differences were found in the operation of the stand alone light emitting devices and those integrated, but the resulting luminescence was within the boundaries of the transmittable spectrum. The operation of the Integrated Optical System was tested and preliminarily studied, obtaining positive results in its stimulus-detection response, fulfilling the main objective of the work, and opening the door for further studies which can lead to the optimization of the design for particular applications.

# Contents

# List of Notations and Symbols

# List of Figures

# List of Tables

# Chapter 1

# Introduction

## 1.1.  Preface

The studies regarding luminescence in silicon-based (Si-based) materials generally start stating the importance of this element in the industry of microelectronics. It is for a good reason: its syntheses and purification is well known, it is abundant, relatively cheap, and most of the industry is already set-up to work with it. With the increasing demands on miniaturization and processing speeds by the industry of microelectronics, the fall of silicon as the ruler of electronics has been repeatedly predicted as its limits seem to be reached. But such prediction has been wrong and delayed time after time, always finding a new approach to stretch the material capabilities and overcome its deficiencies. This does not mean that the fall of Si will not eventually come, but it illustrates the importance and relevance of studies on it, as its many advantages most of the time outweigh its disadvantages.

One of the latter, and an important one, is its poor capability to emit light due to its indirect band-gap configuration. However, more than two decades ago, this was observed to change at room temperature first in porous silicon[1], and later in many other nano-structured Si materials. Ever since, great efforts on the study, explanation, and control of the phenomenon in order to capitalize it have been deployed, since the attainable possibility of Si emitting light would open the door for the native integration of photonic systems in electronics, as opposite to the current mainstream approach, using III-V semiconductors, significantly more expensive, and not integrable in a monolithic Complementary Metal-Oxide-Semiconductor (CMOS) process.

One material that present this characteristics is the Silicon Rich Silicon dioxide (SRO), which has advantages over the porous silicon, such as its higher chemical stability and ease of fabrication by conventional CMOS processes. Due to its promising characteristics, it has been mater of in-

vestigation for several groups, including the GTQ[1] in the IMB-CNM[2], the respective group and institute in which the present work has been developed.

In this framework, a significant amount of data on silicon rich $SiO_2$ is available from studies performed in the past, and in particular, by our group, though it is often fragmented as the investigations so far can be considered initial in terms of obtaining a reliable light emitting device, let alone an integrated optical system. With this knowledge, which includes results of material obtained by different fabrication techniques and their luminescent response, the present work studies of the material focused on comparing past results, identifying the information that can be expanded and further analysed to better explain the results, and designing new experiments (including fabrication of material, architecture of structures for the relevant studies, and characterization), always with the main objective of attaining a reliable electroluminescent device that could be used for a functional integrated optical system.

The studies to the previously existing fabrications were published in a peer reviewed article[2], which was an important part of the development of this thesis, and is included in the appendixes. However, the information here exposed is mostly from new designs and fabrications of materials, structures, and devices, obtained specifically for the development of two studies: the one you are reading, which approaches the obtaining of an integrated optical transceiver trough the understanding of the basic mechanisms taking place in the active material, and a recently published one, more focused on the optical effects taking place in a particular light-emitting device configuration[3].

In the present work, the intrinsic luminescence of the SRO is experimentally studied and analysed, giving significant importance to the structural and atomic characteristics, with the objective of finding a clear link between them and the luminescence response. Such information is used to develop an electroluminescent device, that is also studied in its electrical and electro-optical characteristics, which are compared to those of the active material. A particular objective was to detach the behaviour of the SRO from the fabrication technique, treating the samples obtained by several techniques as the same material, just with different structural characteristics, which is the case indeed. With this information, it is dressed the ultimate goal: developing a functional Integrated Optical System consisting of a transmitter–receiver (or transceiver), which integrates the light emitters with the best characteristics, a waveguide, and a light sensor. The design, fabrication, and characterization of a system obtained by all com-

---

[1]Grupo de Transductores Químicos. http://gtq.imb-cnm.csic.es

[2]Instituto de Microelectrónica de Barcelona-Centro Nacional de Microelectrónica. http://www.imb-cnm.csic.es

patible CMOS technologies, are finally presented and discussed.

## 1.2. Basic theoretical notions

There are some basic notions and terminology necessary to the comprehension of some parts of the present work. In most cases, particular concepts and definitions are included in the sections that need them for their proper understanding, but there are some general notions that is appropriate to know in advance.

In this section a very brief summary of some fundamentals of the main material, its luminescence, and the transport models used often to describe its behaviour, are summarized. The reader familiarized with the SRO may skip this section, and for that who need more deep insight on any of the concepts, useful references are provided at the end of each subsection.

### 1.2.1. Fundamentals on the active material

The silicon rich silicon dioxide or SRO, is basically a silicon dioxide to which silicon atoms have been introduced in a higher proportion, either during, or after its fabrication. Then, it can be generally described as a mixture of $SiO_2$ (stoichiometric Si dioxide), $SiO_x$ whith $0 < x < 2$ (substoichiometric Si oxide), and elemental Si. The stoichiometric dioxide presents an ideal atomic proportion of 33.33 at. % of Si, and 66.66 at. % of O, while the substoichiometric presents higher than 33.33 at. % values for Si, and consequently, lower than 66.66 at. % for O.

The SRO can be fabricated by a variety of CMOS compatible techniques, such as Low Pressure Chemical Vapour Deposition (LPCVD)[4, 5, 6, 7], Plasma Enhanced Chemical Vapour Deposition (PECVD)[8, 9, 10, 11], and the Ionic Implantation of Si in a previously fabricated dioxide matrix (II)[4, 12, 13, 14], among others.

**Structural characteristics of SRO**

The characteristics of the SRO when obtained by Chemical Vapour Deposition techniques (CVD) can be influenced by several conditions, such as the substrate temperature, the reaction chamber pressure, the RF frequency if plasma assisted, *etc.* One of the most used parameters to design a material with specific characteristics is the variation of the flow rate of the precursor gasses, usually Silane and Nitrous Oxide. This translates in the modification of the partial pressure in the deposition chamber when each precursor gas is separately flowing. The ratio of these defines the quantity $R_0$:

$$R_0 = P[N_2O]/P[SiH_4] \qquad (1.1)$$

This is related to the silicon contents, and it is frequently used to define the SRO when obtained by CVD processes[15].

Depending on the fabrication technique and parameters, the material can incorporate other elements, particularly nitrogen when using CVD techniques including nitrous oxide.

After deposition or implantation, the material can be submitted to a variety of thermal treatments, which induce agglomeration of Si and formation of nano-particles. The size and concentration of these depends on the contents of silicon atoms, and the temperature of the annealing[15, 16, 17].

The finished SRO is chemically composed by a mixture of elemental Si agglomerates (or $Si^0$ states), Si atoms in full oxidation states (or $Si^{4+}$), and all the oxidation states in between[15, 18, 19, 20].

There is no universal model to for the electron structure of the material, and it is often considered to adjust either the so called Random Bonding Model (RBM), or the Random Mixture Model (RBM)[21]. The RBM assumes that the SRO is an homogeneous single-phase material with a statistical distribution of the four oxidation states of Si ($Si^{4+}$, $Si^{3+}$, $Si^{2+}$ and $Si^{1+}$); while the RMM model considers the material as a mixture of $SiO_2$ and elemental Si clusters. In these two models, it has been suggested that whether the material adjust to one or the other is dictated by its fabrication conditions([22] in [21]). More recently, the Intermediate Model (IM) has been proposed by Novikov *et al.*[20], which considers the existence of a transition sub-stoichiometric oxide between the $SiO_2$ and elemental Si phases. It has been reported SRO with this characteristics, which are described with the known as core-shell model[23, 24].

Then, as it can be seen, the material can theoretical vary largely on its characteristics, ranging from crystalline Si nanoparticles, embedded in a stoichiometric $SiO_2$ matrix, to an oxide with higher Si concentration that $SiO_2$, but with no agglomerates at all. Between these two extremes, if agglomerates exist, they can be either amorphous, or present different crystalinities, also depending on the thermal treatment and silicon contents[25].

The figure 1.1 presents an example of a part of an SRO film after thermal annealing. It is presented the atomic structure of a Si nano-particle with diameter $d_{nps}$ embedded in the $SiO_2$ matrix. In this case, the particle is in crystalline state, and there is a transition shell formed by $SiO_x$, $0 < x < 2$, between elemental $SiO_2$ and Si surrounding it.

To learn more about the composition of this material and other similar, the works by Barbagiovanni *et al.*[18] and Salh[26] are good references.

**Light emission in Si-based nano-structured materials**

Luminescence is produced by the transition of electrons from a given energy level to a lower one, in which photons are emitted to comply with the conservation of energy. This is known as radiative recombination. If
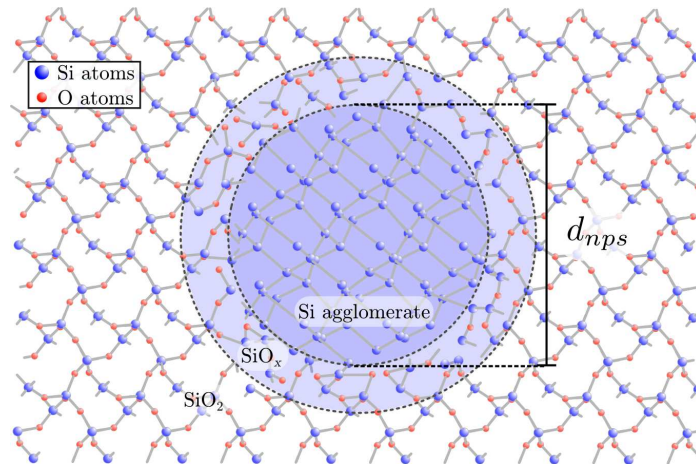
Figure 1.1: Representation of one of the possible SRO atomic configurations in which a Si nano-crystal surrounded by a $SiO_x$ shell is embedded in an $SiO_2$ matrix.

this mechanism of conservation of energy involves exclusively one photon for each electron making a transition, the photon emitted has a wavelength $\lambda = hc/E$, where $h$ is the Planck's constant, $c$ the speed of light, and $E$ the energy difference between the states involved in it.

As already mentioned, the luminescence from nano-structured materials based on silicon has been object of study for more than two decades. From porous silicon, to quantum wells, wires and dots have been proposed and tested as light emitting materials. In the particular case of nano-particles embedded in $SiO_2$, two main phenomena have been pointed as the possible causes of the overcoming of the Silicon indirect band gap limitation, namely Quantum Confinement, and defect-related luminescence; although more and more studies seem to be reaching the consensus of a combination of both phenomena is responsible for the observed luminescence[18, 23, 27, 28, 29].

**Quantum Confinement Luminescence**

Quantum confinement (QC) occurs when a particle is held in a space bounded by high potential barriers, and the dimensions of such space are on the order of the period of the wave function corresponded to the confined particle. This modifies the dispersion relation of the particle, resulting in the presence of energetic states normally not present if the particle is not confined[12, 18, 30].

In the case of interest for this work, namely the confinement of electrons and/or holes in silicon nanoparticles embedded in a dielectric, this can result in states that allow the direct energetic transition of excited electrons,

overcoming the disadvantage of the indirect band gap characteristic of bulk silicon.

The allowable energetic states are related to the dimensions of the system, as well as to the mass of the confined particle. In an effective mass approximation, the band-gap energy for a silicon nano particle with diameter $d_{nps}$ can be roughly expressed as [31, 32]:

$$E = Eg + \frac{C}{d_{nps}^2} \tag{1.2}$$

Where $Eg$ is the band gap energy of silicon in bulk, $d_{nps}$ the diameter of the particle and $C$ is a confinement parameter, which depends on the effective mass of the confined electron, hole, or exciton; and on the relative permittivity of the agglomerate if Coulombic interactions are taken into account[12].

It is noteworthy that the effective masses of the electron, hole, and exciton are different in the agglomerates as compared to those in bulk Si, since they are related to the energy *vs.* quasimomentum structure of the material, which is modified in low dimensions and depending on the crystallinity of the material. The effective mass values on their turn impact on the size of the Bohr radius of the electron, hole, or exciton ($a_e$, $a_h$ and $a_x$, respectively).

The relation between the Bohr radius and $d_{nps}$ defines three distinct categories of QC, namely strong, medium, and weak confinement. Strong confinement is obtained when $d_{nps} < a_e, a_h$, medium when $a_h < d_{nps} < a_e$, and weak when $d_{nps} > a_e, a_h$[30].

Then, the luminescence from nanoparticles can be attributed to QC phenomena if the light emission energy can be described by the equation 1.2, and the value $C$ is consistent to the confinement regime and the effective mass values corresponding to those for the characteristics of the agglomerates.

For a detailed review of Quantum Confinement theory and experiments in Si nanostructures, the reader is referred to the works by Barbagiovanni *et al.*[18] and by Yoffe[30].

**Defect related luminescence**

Despite providing a theoretical explanation for luminescence in a material that does not show it under regular conditions, the results from experimental characterization of luminescence in SRO-like materials often do not match well any model of QC. This is some times attributed to the presence of defects that introduce new allowed energy levels that can lead to radiative recombination[26]. Some studies also suggest these can affect the QC results by modifying the effective mass of the confined particles[18],

but some are known to be optically active by themselves and present in $SiO_2$, and generally found in higher proportions if the material has been submitted to processes such as Ion Implantation, or if there are other elements present in the material, such as nitrogen, or silicon in excess. In the particular case of silicon dioxide containing Si agglomerates, the interface between these two materials is more likely to present a higher concentration of such defects[5, 18]. Despite the mentioned knowledge of them existing in the silica matrix, their nature and properties are still a mater of controversial debates. In general, they can be classified in oxygen deficiency-related and oxygen excess-related[33].

The known oxygen excess-related defects include non-bridging oxygen hole centres (NBOHC), peroxy radicals (POR) and interstitial $O_2$[33]. Their light emission peak energies range from 0.97 eV to 1.95 eV[26]. Regarding the oxygen deficiency-related, the main of the optically active are the so called family of paramagnetic E' centres; and two types of oxygen deficiencies often referred to as ODC(I), or non-bridging oxygen-hole centre (NOV), or E centre; and ODC(II), or E" centre[33]. The variety of ways to refer to the two latter, reflects the existing and long lasting controversy on the defects matter. The photoluminescence peak energies reported for these range between the 1.8 eV and 4.4 eV[26].

The presence of additional emission centres would be rather promising, as would allow for higher range of control on the emitted light by complementing the wavelengths obtainable by QC phenomena. However, the lack of precise knowledge regarding the factors that dictate the type and concentration of defects complicates the design of a material with particular light emission characteristics. In any case, it is difficult to avoid their presence, and should be considered when analysing materials as the here studied if it is desired to have a better idea of the luminescence mechanisms taking place in it.

Very good reviews on optically active luminescent defects present in silicon dioxide network are authored by Skuja[33] and by Salh[26]. It is suggested to the interested reader to refer to them for further information on the matter.

### 1.2.2. Relevant models of carrier transport

The studies of electrical properties of materials containing quantum agglomerates are in early stages as compared to those on optical properties[34]. A in-depth study and modelling of transport mechanisms in these materials is not a simple matter, and some specialist even expect it to yield new basic physics[34]. As an initial approach, materials as the here studied can be modelled in one dimension as a series of potential wells with width $d_{nps}$ like that depicted in the figure 1.2. This is suitable to use known models for tunnelling processes to describe the behaviour of the transport in the

material.
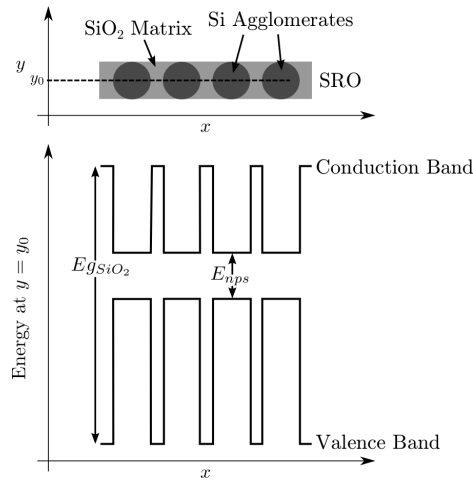


Figure 1.2: Representation of the energetic band structure for SRO along the $\hat{x}$ direction at the point $y = y_0$ as represented in the upper figure.

Given the nature of the material, the current-voltage response is often fitted to models successfully applied to transport in system involving thin dielectric layers (<4 nm-thick), such as Fowler-Nordheim Tunnelling (FN), Poole-Frenkel Emission (PF), and the Trap-assisted Tunnelling (TAT) models[35, 36, 37, 38, 39]. The FN occurs when the applied electric field is high enough as to make the conduction band of the dielectric reach values below that of the metal, causing an effective thickness of the energetic barrier lower than that of the oxide layer, making possible the tunnelling trough it under certain conditions. The mechanism is depicted in the figure 1.3a. The relation between the current density $J$ and the applied electric field $E_f$ is presented in the equation 1.3[40, 41]:

$$J_{FN} = \frac{q^2 m E_f^2}{8\pi h \phi_B m^*} \times \exp\left(-\frac{8\pi\sqrt{2qm^*}\phi_B^{3/2}}{3hE_f}\right) \qquad (1.3)$$

Where, $q$ , $m$ and $m^*$ are respectively the charge, mass, and effective mass of the electron, $h$ is the constant of Planck and $\phi_B$ the potential barrier height.

The other two models are based on the presence of allowed states inside the band gap of the dielectric introduced by defects in the material. The PF considers that the electron can occupy one of these traps, and then gain energy to reach the conduction states; TAT on the other hand consider the electron to tunnel to this state, and then tunnel from this to the semiconductor. The processes are depicted in the figures 1.3b and 1.3c.

8
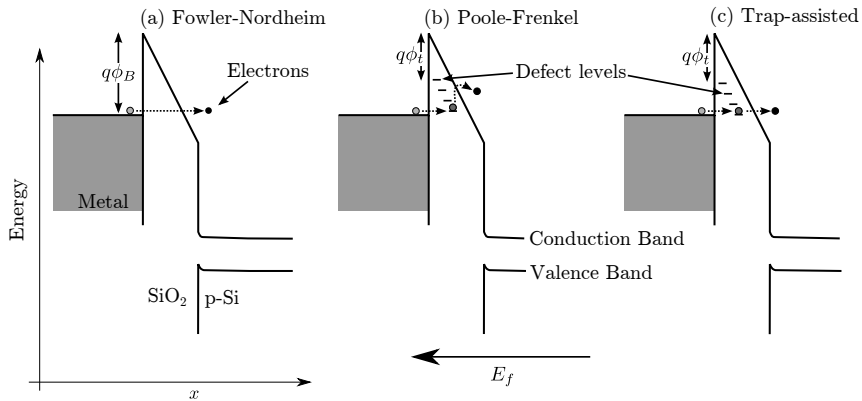
Figure 1.3: Shceme of FN(a), PF(b) and TAT(c) conduction mechanisms in a Metal–SiO$_2$–p-Si system. The dots represent the electrons, grey in initial positions, and darker as they approach to the final states.

The current-field relations for the PF and TAT models are represented in the equations 1.4 and 1.5, respectively[35, 40, 41].

$$J_{PF} \propto E_f \times \exp \left( - \frac{q \left( \phi_t - \sqrt{\frac{qE_f}{\pi \varepsilon_r}} \right)}{kT} \right) \tag{1.4}$$

$$J_{TAT} \propto \exp \left( - \frac{8\pi \sqrt{2qm^*} \phi_t^{3/2}}{3hE_f} \right) \tag{1.5}$$

In these, $k$ is the constant of Boltzmann, $\phi_t$ the energy difference between conduction band and trap level, $\varepsilon_r$ the relative permittivity of the material and $T$ the temperature.

The treatment of the units in these expressions is not trivial, as the used length and energy units are commonly cm and eV in the semiconductors field, whereas the universal constants are usually expressed in SI units. This must be considered when performing numerical fittings, as it is easy to reach misleading results for a careless use of the units of the experimental data and the constants.

A review on electrical transport in ensembles of quantum dots is authored by Balberg[34], and the work by Green *et al.* on ultrathin gate dielectric layers can also provide abundant information on the matter[42].

## 1.3.   Organization of the Thesis

The work is divided in three main chapters following the introductory information, with a final chapter presenting the general conclusions. The

former address, respectively, the nature of the luminescence in the utilized materials, the results from the fabricated light emitting devices, and the development of the integrated optical system concept. All of them begin with a brief experimental section in which the characterization techniques and fabrication methods are explained.

The chapter 2.The Nature of Luminescence in the Active Layers, regards the reasons for light emission in the materials. It is the one that first describes the fabrication processes to obtain the films that will be used thereafter. Then, the results from photo luminescence and X-Ray Photoelectron Spectroscopy studies are discussed and co-related for both for mono-layers of SRO, and for $Si_3N_4$-SRO bi-layers, including a subsection dedicated to studies on bi-layers changing the thickness, necessary to confirm some of the conclusions.

The chapter 3.The Light Emitting Device, deals with the electrical and electro-optical studies to devices obtained using the materials analysed in the previous chapter as basis, both with mono and bi-layers. It begins with a brief description of the subsequent steps followed to obtain the devices; then the electro-optical experiments are addressed, discussing the electro luminescence spectra results, identifying the relation between these, and the photo luminescence previously discussed. The relation between electrical stimuli and optical response is then addressed, including the different manifestations of luminescence for the two types of stack structures, and efficiency results. Finally, transport on the different types of devices is studied and discussed.

The chapter 4.The Integrated Optical System (IOS): Transceiver, begins with the explanation of the concept that describes the transmitter-receiver (transceiver) proposed to test the viability the system. It defines the three basic elements that will be analysed in the design elaborated using the results yielded by the previously presented analyses. The stack structure and materials are then suggested, and a theoretical analysis of the viability of the elements is discussed. The specific characteristics and parameters of the proposed design are then developed and defined. Finally, the last part of this chapter presents the initial studies to the fabricated prototype, beginning with the tests performed to the each element in the assemble, and finalizing with the studies from the stimulus-response characteristics of the whole integrated transceiver system.

The chapter 5.General Conclusion and Perspectives, summarizes the flow of the particular conclusions from each chapter, delineating the path that the thoughts followed to elaborate the proposed design of the integrated system. It finally states the major contributions of the work, and the future actions to take in the development of systems more advanced than this initial exploration one.

At the end of the manuscript, the General Conclusion and Perspectives

section includes the list of published articles, two of which are attached in their full extension, since these are particular relevance for the development of the present work. This section also includes the step-by-step fabrication processes of all the samples and devices studied in the thesis.

# Chapter 2

# The Nature of Luminescence in the Active Layers

If true viability for the use of the proposed materials and devices is to be achieved, complete comprehension of the reasons for luminescence must be attained. If, as expected, the EL and PL are intrinsically related[43], then PL comprehension leads to EL comprehension. The real understanding of the luminescence mechanisms and atomic-energetic structure of the material is the first step in untangling the intricate relation between transport and emission that takes place in the SRO-based devices.

This chapter is intended to link the characteristics of the active material to the different luminescence results obtained from it. To achieve this, the data from structural and atomic studies, and Photoluminescence experiments are analysed, compared, and correlated.

## 2.1. Samples and fabrication

As mentioned before, the SRO can be fabricated by a variety of techniques. For the present study, there was access to PECVD and ionic implantation equipment, which allow the obtaining of the material by more than one technique. This is advantageous because allows a better verification of the conclusions as applicable to the material itself, rather than to one type of SRO, fabricated by an specific technique.

Apart from the studies of single SRO layers, dual layer SRO-$Si_3N_4$ samples were also fabricated and analysed, since it has been reported that the inclusion of a silicon nitride layer in light emitting devices based on the here studied material can improve their behaviour[36, 44], and it is important to know the structural and intrinsic luminescence of the whole dual-layer system in order to further explain the results of an electroluminescent device based on it.

Since there is a significant amount of samples with a variety of characteristics, their labelling is crucial to keep track of the results. In this work, the samples with a particular material will be labelled according to its fabrication method, and its silicon excess $XS_{Si}$ in the middle of the SRO film (not to be mistaken with silicon contents, details on the obtaining of this quantity will be discussed in the section 2.3). One exception to this nomenclature is the dual-layer samples intended to compare the behaviour with different SRO thickness, which are labelled according to the SRO thickness, and not its silicon excess.

This section summarizes the processes and presents the parameters used for each fabrication technique, and defines the labels for the studied samples. More details on the fabrication steps for each technique are included in the appendix C.

### 2.1.1. SRO fabrication

The techniques used to obtain the material were the ionic implantation of thermally grown $SiO_2$ (II-SRO), Plasma Enhanced Chemical Vapour Deposition (PECVD-SRO), and the ionic implantation of SRO deposited by PECVD (PECVD-II-SRO). Unless otherwise stated, all the parameters used for the fabrication were chosen according to the known ranges that have presented good results in the past for the intended purposes (namely PL, conductivity, *etc.*)[2, 7, 8, 45, 46, 47].

**II-SRO**

The fabrication of the II-SRO films started with the thermal growth of 30 nm of $SiO_2$ on p-type silicon wafers with orientation (100) and resistivity between 0.1 $\Omega \times$cm and 1.4 $\Omega \times$cm.
A 30 nm thick $Si_3N_4$ film was deposited by LPCVD at 800℃ using dichlorosilane and ammonia as precursor gasses.
The nitride layer is to serve as a buffer material that helps to achieve a better control of the $Si^+$ ions implantation. This was performed at room temperature in two steps in order to achieve a distribution of silicon as constant as possible according to Stopping and Range of Ions in Matter simulations (SRIM)[48], which was used to determine the implantation energies necessary to have the peak concentration around the middle of the dioxide. The respective energies for first and second implantation were 25 keV and 50 keV. Two films were fabricated by this technique, using final implantation doses (adding the two implantation steps) of $1.2 \times 10^{16}$ cm$^{-2}$, and $3.0 \times 10^{16}$ cm$^{-2}$.
Finally, all the samples were annealed in $N_2$ atmosphere for 240 min at 1100℃ , and the silicon nitride layer was removed by wet etching.
The samples with the two implantation doses obtained are labelled II$_{0.46}$

and $II_{1.30}$ in table 2.1, and the step-by-step fabrication run can be consulted in the appendix C.1.

**PECVD-SRO**

The PECVD-SRO layers were nominally 300 nm-thick and deposited on p-type silicon wafers with orientation (100) and resistivity between 4 $\Omega \times$cm and 40 $\Omega \times$cm.

The precursor gasses were nitrous oxide and silane, which were introduced in the Plasma Chamber at 400℃ .There were obtained samples with two different $R_0$ as defined in equation 1.1: $R_0 = 5.05$ for samples $PECVD_{4.67}$ and $PECVD_{5.67}$, and $R_0 = 10.30$ for sample $PECVD_{2.96}$ (as listed in table 2.1).

Depositions with two different RF power were done: 1.4 W/cm$^2$ for sample $PECVD_{4.67}$, and 0.5 W/cm$^2$ for samples $PECVD_{2.96}$ and $PECVD_{5.67}$.

Finally, all films were annealed in $N_2$ atmosphere for 60 min at 1240℃.

The fabrication run can be consulted in the appendix C.2.

**PECVD-II-SRO**

The fabrication of PECVD-II-SRO films started with the deposition of a nominal 30 nm-thick $SiO_2$ layer by PECVD under the standard procedures to obtain dioxide in a CMOS circuit on p-type silicon substrates with (100) crystalline orientation and resistivity between 0.1 $\Omega \times$cm and 1.4 $\Omega \times$cm.

After this, the $N_4Si_3$ implantation buffer film with thickness of 30 nm was deposited by LPCVD at 800℃ as in the II samples fabrication.

Again like in the II-SRO process, a two-step $Si^+$ ions implantation was performed, the first with an energy of 25 keV, and the second with 50 keV. In this case, three different total doses were used: $2.6 \times 10^{16}$ cm$^{-2}$ for sample PECVD-II$_{1.34}$, $5.3 \times 10^{16}$ cm$^{-2}$ for sample PECVD-II$_{4.56}$, and $7.4 \times 10^{16}$ cm$^{-2}$ for sample PECVD-II$_{4.06}$.

The samples were finally annealed in $N_2$ atmosphere at 1100℃ for 240 min and the nitride buffer was removed by wet etching.

The fabrication run is presented in the appendix C.3.

All the single SRO layers fabricated and reported in this chapter, as well as their refractive index $n$ and thickness as obtained by ellipsometry (laser wavelength of $\lambda = 632.8nm$, incident angle of 70° to the normal of the substrate), are listed in table 2.1. These form the basis for the fabrication and the labelling of the SRO-Si$_3$N$_4$ bi-layer samples.

## 2.1.2. SRO-Si$_3$N$_4$ bi-layers fabrication

Results from studies of two sets of bi-layered samples are presented in this work. One set was mainly designed to obtain information regarding the

Table 2.1: Labels, Ellipsometry results for refractive index $n$ and thickness, and fabrication techniques for the SRO films studied in this section.

| Sample | Refr. index $n$ | Thickness /(nm) | Fabrication Tech. |
|---|---|---|---|
| $SiO_2$ | 1.46* | $38.8 \pm 1.2$ | Thermal $SiO_2$ |
| $II_{0.46}$ | $1.48 \pm 0.01$ | $28.6 \pm 0.3$ | $Si^+$ Ion impl. |
| $II_{1.30}$ | $1.57 \pm 0.01$ | $26.7 \pm 0.6$ | in thermal $SiO_2$ |
| $PECVD_{2.96}$ | $1.52 \pm 0.03$ | $326 \pm 18$ | |
| $PECVD_{4.67}$ | $1.58 \pm 0.02$ | $317 \pm 8$ | PEVCD |
| $PECVD_{5.67}$ | $1.85 \pm 0.04$ | $125 \pm 5$ | |
| $PECVD\text{-}II_{1.34}$ | $1.53 \pm 0.05$ | $25.2 \pm 8.0$ | $Si^+$ Ion impl. |
| $PECVD\text{-}II_{4.06}$ | $1.47 \pm 0.22$ | $19.3 \pm 5.2$ | in PECVD-SRO |
| $PECVD\text{-}II_{4.56}$ | $1.51 \pm 0.13$ | $20.6 \pm 7.0$ | |

*Value reported by the CNM clean room, consistent to the literature[49].

comparison between single-SRO films, and the double layer configuration; whereas the other was thought to verify the influence of different SRO volumes in this configuration.

The first were intended to have the same thickness for each of the layers, namely 30 nm. These were obtained during the same process for the fabrication of samples $II_{0.46}$ and $II_{1.30}$ explained in the previous section 2.1.1. All the steps followed were the same, except for that in which the $Si_3N_4$ buffer obtained by LPCVD was removed. This way, the result is the bi-layer stack-structure of the Si wafer, SRO and $Si_3N_4$, guaranteeing that the SRO films have the same characteristics as their single-layer counterparts, as it was confirmed by the XPS studies that will be addressed later. These samples are labelled Bi-$II_{0.46}$ and Bi-$II_{1.30}$. The fabrication run can be consulted in the appendix C.1.

A sample submitted to the exact same processes, but in which the implantation profile presented its maximum in the Si substrate was also fabricated. Hence, a total dose of $(1.5\times10^{16})$ cm$^{-2}$ was implanted trough the nitride layer with the usual dual-step technique, but no significant Si atoms were expected to be implanted inside the dioxide layer. This was confirmed by the XPS studies as well. Such sample is labeled Bi-$SiO_x$. A "twin" mono-layer sample, identical to Bi-$SiO_x$, but with the nitride wet-etched, was also fabricated to have a mono-layer reference oxide.

In the set of samples intended to verify the influence of the SRO thickness on the system response, the films of this material were II-SRO with thickness of 30 nm and 300 nm (labelled Bi-$SiO_x$-$II_{30nm}$ and Bi-$SiO_x$-$II_{300nm}$, respectively) as well as implanted PECVD-SRO with thickness

of 30 nm and 300 nm (labelled Bi-PECVD-II$_{30nm}$ and Bi-PECVD-II$_{300nm}$, respectively). These were fabricated on their own process run.

The substrates were p-type silicon wafers with orientation (100) and resistivity between 4 $\Omega\times$cm and 40 $\Omega\times$cm in all cases. The matrix oxide for the II-SRO samples was simply thermally grown SiO$_2$, while for the PECVD-SRO matrix, the growth parameters were the same as those of sample PECVD$_{2.96}$ described previously, namely an $R_0$=10.3 and a power density of 0.5 W/cm$^2$, except that the deposition time was ten times longer for the 300 nm-thick sample. As in all Si-implanted samples, a 30 nm-thick LPCVD Si$_3$N$_4$ film was deposited on top of each silicon oxide layer.

For all the samples, the Si$^+$ ions implantations were done in two steps with a total dose of $1.5 \times 10^{16}$ cm$^{-2}$ with an energy tuned to obtain a plateu-like ion concentration with a maximum at a depth of 15 nm within the oxide matrices. Note that for samples with 30 nm-thick SRO this is the middle of the film, but for 300 nm-thick this is rather superficial. All these samples (Bi-SiO$_x$-II$_{30nm}$, Bi-SiO$_x$-II$_{300nm}$, Bi-PECVD-II$_{30nm}$ and Bi-PECVD-II$_{300nm}$)were finally annealed for 60 minutes at 1240℃  in N$_2$ ambient (the PECVD-SRO usual parameters.) The more detailed list of each fabrication step can be found in the appendix C.4.

The list of all the dual SRO-Si$_3$N$_4$ samples with the nominal thickness of each layer, and the fabrication technique for the SRO film, is presented in the table 2.2.

## 2.2.  Experimental details

### 2.2.1.  X-ray Photoelectron Spectroscopy

The characterization technique known as X-Ray Photoelectron Spectroscopy (XPS) relies in the interaction between photons with an energy in the X-ray range (100 eV to 100 keV)[50] with core level electrons in the atoms of the surface analysed. When a photon interacts with an electron with a lower binding energy, the later can be emitted from its orbital. The detection of the number of emitted electrons with a certain energy, allows to determine the amount of a particular bond type it was forming in the surface under study.

The electron binding energies are influenced by its chemical surroundings, making this technique useful for determining chemical states by the observation of the shifts in the peak energies detected. Since the photo-electrons can only be originated in a depth range between 0.5 nm and 5 nm[50], local etching of the surface with an ion-beam sputtering gun is a common technique to obtain depth profiling. This operation is performed under vacuum conditions to avoid local oxidation.

The figure 2.1 shows the schematic of a typical XPS experimental set-

Table 2.2:   Labels, nominal thickness of the layers, and fabrication technique of the SRO in the SRO-Si$_3$N$_4$ Bi-layer samples.

| Sample label | Nominal SRO Thick. /(nm) | Nominal Si$_3$N$_4$ Thick. /(nm) | SRO Fabrication Technique |
|---|---|---|---|
| Bi-SiO$_x$ | | | Si$^+$ |
| Bi-II$_{0.46}$ | 30 | 30 | Ion impl. in |
| Bi-II$_{1.30}$ | | | thermal SiO$_2$ |
| Bi-SiO$_x$-II$_{30nm}$ | 30 | 30 | Si$^+$ Ion impl. |
| Bi-SiO$_x$-II$_{300nm}$ | 300 | | in thermal SiO$_2$ |
| Bi-PECVD-II$_{30nm}$ | 30 | 30 | Si$^+$ Ion impl. in |
| Bi-PECVD-II$_{300nm}$ | 300 | | PECVD SiO$_2$ |

up. In the particular case of this work, XPS is useful to determine not only the contents of silicon, oxygen, and nitrogen in the material, but this is a technique which has the rare ability of delivering information regarding the suboxide states of silicon[51], which may be very useful information for the identification of luminescence and transport mechanisms.

The XPS experiments presented in this work were performed by the *Servicios de Análisis y Caracterización de Sólidos y Superficies, Universidad de Extremadura* (SACSS) using a Thermo Scientific K-Alpha equipment, which uses a monochromatic Al source at an energy $E_{K_\alpha} = 1486.68$ eV. The irradiation was beamed perpendicular to the sample surface with a spot size of 300 $\mu$m. Two types of spectra were obtained for the analysis, namely full spectra and zone spectra. The full spectra comprehended the binding energies between 0 eV and 1350 eV, with a resolution (energy step) of 1.0 eV, and 5 scans to average. The zone spectra were performed in the energy regions corresponding to the orbitals Si2p (95.08 eV to 110.08 eV), O1s (525.08 eV to 545.08 eV) and N1s (392.08 eV to 410.08 eV) in order to obtain more detailed information regarding the contents and chemical states of silicon, oxygen, and nitrogen, respectively. These were obtained using an energy step of 0.1 eV, and 10 scans to average. Depth profiles were also obtained etching the surface of the samples in a vacuum of $1.6 \times 10^{-7}$ mbar using a Ar$^+$ beam sputter gun at an angle of 30° to the surface normal and a raster size of 1.5 mm$^2$. For each sample, a constant etching time was programmed and the XPS spectra were obtained for every etched step. A schematic of the experimental procedure is presented in the figure 2.1.
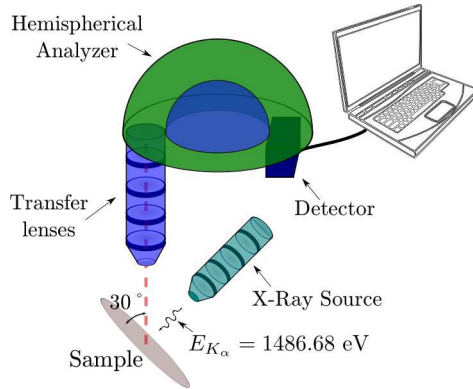
Figure 2.1: Schematic of the XPS Spectra acquisition experimental set-up used for this work.

### 2.2.2. Photoluminescence

Photoluminescence (PL) is a technique that can deliver information on the material in a relatively easy way, since it does not require more processes than its obtaining itself, as opposite to EL which requires the fabrication of a more complex device, apart from a generally more elaborated stimulation-measure set-up. It is based in the transference of energy from photons to electrons in the material. The latter are excited by photons beamed on the sample to energetic states from which then relax again to their base states, conserving on their turn the differential energy among the states by the emission of a photon. The spectral analysis of the emitted light yields information regarding the allowed states in the material, whether introduced by defects, quantum confinement, or other phenomena.

For the present work, PL measurements were performed at room temperature using the arrangement depicted in figure 2.2. The experimental set up can be divided for its description in two optical arranges, one used to stimulate the samples, and other used to detect the PL from them.

The stimulus arrange consisted of an VM-TIM HCL-30UM(I) He+Cd laser with a power of 30 mW at a wavelength $\lambda = 325$ nm incident at an angle of 45° to the normal of the film surface. A Newport 10LF 10-325 laser line filter was used to allow only the pass of the 325 nm wavelength light. In front of this, an UV-VIS double convex lens was used to focus the beam in a sharp spot in the sample.

The detection arrange consisted of an optical fibre with the input placed orthogonal to the sample surface, and the output connected to an Ocean Optics QE6500 spectrometer using a detection range from 400 nm to 1000 nm, and a maximum resolution of 0.14 nm. Before the optical fibre, a Semrock LP02-355RS-25 long-pass filter was used to eliminate all signals
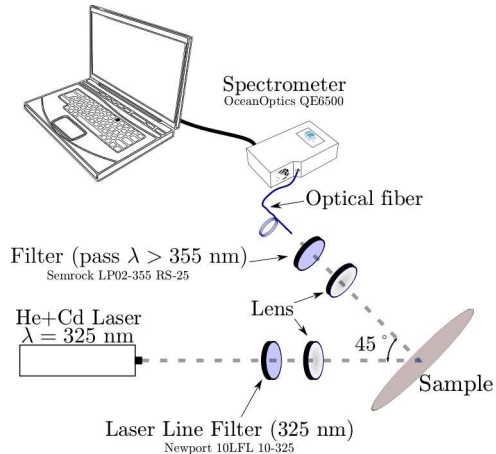
Figure 2.2: Schematic of the experimental set-up used to obtain PL spectra.

with wavelengths below 355 nm, and between the sample and the filter, an UV-VIS double convex lens was used to focus the emission in the input of the optical fibre as much as possible. The adjustment of focal distance was made manually, by the inspection of the highest signal obtained in the spectrometer as the lens position was varied. In all the cases, the dark spectrum was subtracted and same integration time was used in order to make the results comparable with each other intensity-wise. All obtained spectra were corrected according to the responsivity of the spectrometer.

## 2.3. Atomic Composition of SRO

### 2.3.1. Silicon Contents and Silicon Excess ($XS_{Si}$)

When trying to assemble a comprehensive study of the SRO characteristics and their relation to the emission, it is essential to establish a comparison parameter in order to allow the contrast of samples fabricated by various techniques and under different conditions.

It is usual to define the SRO by a value that is well known and controlled during fabrication, such as the precursor gasses partial pressures ratio $R_0$ if it is obtained by chemical vapour deposition[6, 15, 52] or the silicon implantation dose if using II-SRO[6, 19]. However, defining the material by these parameters makes difficult the task of comparing results from samples obtained by different techniques, and usually the possible variation in silicon incorporation due to other parameters, such as annealing temperature, and pressure, is not properly taken into account[53]. Sometimes, this is tried to be solved by the use of the refractive index $n$[54], since it is a quantity possible to measure after the fabrication and can be related to

the silicon contents, but this does not show unique dependency on silicon contents, for parameters such as porosity significantly affect its value[55]. This will be corroborated later, once defined and presented the silicon excess and contents values for all the samples, as it will be observed that, while for a same fabrication technique $n$ matches the trend of increasing as the silicon excess does, there are cases in which samples fabricated by different techniques and presenting similar values of refractive index, present significantly different silicon excess or contents values.

In general, the main objective of varying the fabrication parameters, regardless of the technique, is to change the silicon contents in the material, since this will in turn change its behaviour. Therefore, this seems the logical comparison criterion, provided the means to obtain this value after fabrication are available. There are at least three possibilities of defining silicon contents if the material is SRO: as the plane atomic percent of Si in it ($P_{Si}$ /at. %), as the silicon excess understood as the percent of Si above the 33.33 at. % of an ideal SiO$_2$ (($P_{Si} - 33.33$) /at. %), or as the silicon excess $XS_{Si}$ defined by Barreto $et$ $al.$[53]:

$$XS_{Si} = P_{Si} - \left(\frac{1}{2} \times P_O\right) - \left(\frac{3}{4} \times P_N\right) \tag{2.1}$$

Where $P_O$ and $P_N$ are the atomic percent of oxygen and nitrogen, respectively.

The first two options are basically the same, except for an offset defined by the theoretical contents on Si in an ideal dioxide, which may allow a better visualization of the modification as compared to silicon dioxide. This is straightforward and simple way of defining the material. On the other hand, the $XS_{Si}$ value defines as Silicon Excess all the Si atoms that are not forming either stoichiometric SiO$_2$, or Si$_3$N$_4$. This has the advantage of considering the nitrogen presence, which plays a very important role in the PL characteristics of the material as will be discussed in the section 2.4. Basically, the reasons that justify the use of this parameter to relate it to luminescence is the following: if it is assumed that both stoichiometric SiO$_2$ and Si$_3$N$_4$ do not present PL by themselves, then this should be related only to the rest of the material, namely, the excess of silicon in it. This is a better approximation than only considering the silicon and oxygen contents, but it still may be misleading, since it assumes that all nitrogen atoms form Si$_3$N$_4$, and all oxygen atoms SiO$_2$, but neglects, for instance, the presence of all the sub-oxidation states (Si$^{x+}$, x < 4)[56], which are likely to be present and play a crucial role in the PL of the SRO, as will also be discussed in section 2.4.

As mentioned, the XPS studies are helpful to identify several characteristics of the materials. The figure 2.3 presents examples of these, showing the spectra of the three regions of interest for the silicon excess calculation for thermal SiO$_2$ and SRO fabricated by ion implantation in SiO$_2$,

PECVD, and ion implantation in PECVD-SRO; all with silicon contents between 34.5 at. % and 38.2 at. %. This figure shows how there are evident differences between the materials, both in peak position and areas under the curve. Note for instance, how the sample PECVD-II$_{1.34}$ shows a clear shift towards lower energies in the N1s band, and a greater area under the curve of the spectrum than any of the others, indicating a different configuration of nitrogen atoms in this sample, and in particular, a higher presence of this element as compared to the other samples. On the other hand, the SiO$_2$ sample does not present detectable photoelectrons on the N1s energy range, indicating negligible presence of nitrogen, as expected for a stoichiometric silicon dioxide.

The areas under the curves of all the Si2p, O1s and N1s energy regions of the XPS spectra were studied to calculated the proportion of the elements forming the materials. In all the cases, the spectra of all the available points within an homogeneous zone inside the films were used to calculate an average Si contents and $XS_{Si}$ for each. This homogeneous zone was identified using the depth profiles, and defined as that region in which the silicon contents difference between a point and the subsequent was lower than 2.5 at. %.

A simple Shirley background subtraction[57] was performed to all spectra, and the areas for each element were corrected using the sensitivity factors provided by the characterization laboratory, which on their turn were corroborated to be consistent trough the characterization of an SiO$_2$ pilot with a very controlled fabrication process known to deliver specific results.

Once obtained the corrected areas for silicon, oxygen and nitrogen, their proportion to the total area was calculated, and the $XS_{Si}$ in at. % was obtained using the equation 2.1. The averages with their errors, which arise from the variations within the homogeneous zones, are presented in table 2.3.

The $XS_{Si}$ presents higher errors than silicon contents because its value is not only affected by the variation of the contents of Si, but also of N and O. The samples reported in this manuscript are labelled according to their $XS_{Si}$ because, as mentioned before, while this particular value is not necessarily what defines all the material characteristics, it delivers more information than the only silicon contents in a compact format, as it will be corroborated along the discussions of the results. Here, it can also be confirmed the previously stated fact that $n$ does not follows exclusively the trend of silicon excess or contents; $e.$ $g.$, the samples II$_{1.30}$ and PECVD$_{4.67}$ present similar values for $n$ (1.57 and 1.58, respectively, as indicated in table 2.1), but significantly different values for both silicon contents and $XS_{Si}$.
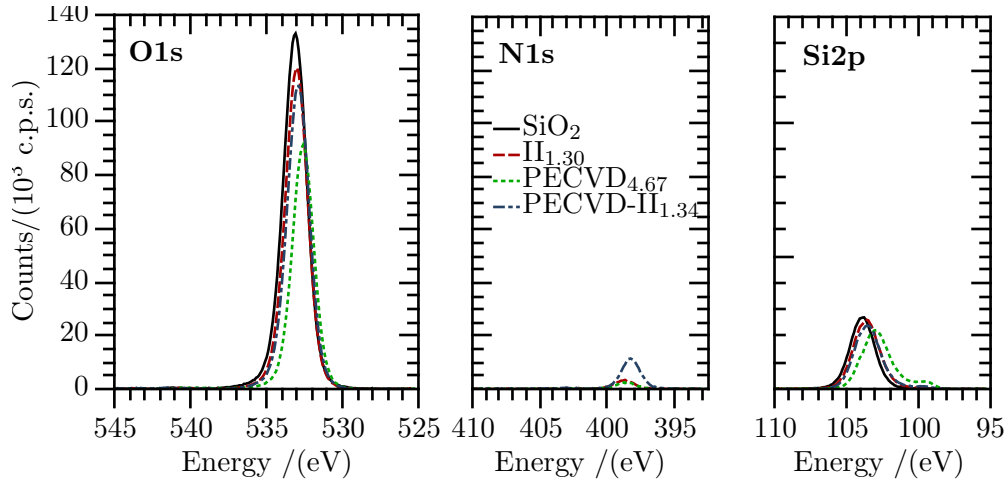
Figure 2.3: XPS Spectra of regions O1s, N1s and Si2p for $SiO_2$ and SRO films fabricated by different techniques.

Table 2.3: Silicon excess and contents, of the studied samples as calculated from XPS spectra. The errors account for the variations within the homogeneous zone of the material ($\sim$5 nm below the surface and above the substrate).

| Sample | $XS_{Si}$ /(at. %) | Element Contents /(at. %) | | |
|---|---|---|---|---|
| | | Si | N | O |
| $SiO_2$ | -0.52 ± 0.09 | 32.99 ± 0.18 | - | 67.01 ± 0.18 |
| $II_{0.46}$ | 0.46 ± 0.02 | 33.78 ± 0.23 | 0.84 ± 0.19 | 65.39 ± 0.21 |
| $II_{1.30}$ | 1.30 ± 0.48 | 34.57 ± 0.09 | 2.25 ± 0.47 | 63.18 ± 0.44 |
| $PECVD_{2.96}$ | 2.96 ± 0.31 | 36.66 ± 0.14 | 8.11 ± 0.33 | 55.24 ± 0.41 |
| $PECVD_{4.67}$ | 4.67 ± 0.32 | 38.12 ± 0.35 | 10.07 ± 0.38 | 51.81 ± 0.76 |
| $PECVD_{5.67}$ | 5.67 ± 0.02 | 38.48 ± 0.30 | 8.23 ± 0.21 | 53.29 ± 0.25 |
| $PECVD-II_{1.34}$ | 1.34 ± 0.28 | 34.53 ± 0.66 | 1.82 ± 0.66 | 63.64 ± 0.89 |
| $PECVD-II_{4.06}$ | 4.06 ± 0.59 | 36.59 ± 0.59 | 3.31 ± 0.77 | 60.09 ± 1.19 |
| $PECVD-II_{4.56}$ | 4.56 ± 0.32 | 36.81 ± 0.65 | 2.63 ± 0.50 | 60.55 ± 1.18 |

### 2.3.2. Sub-oxide variations (Si2p band)

In the figure 2.3, there can be observed variations of the peak values and shapes of the spectra for each energy region. As mentioned, these deliver information regarding the general atomic surroundings and configuration of the atoms in the material. For instance, the peak shifts in the N1s zone of the spectra may indicate if the nitrogen atoms are more likely linked to either O, Si, or other N atoms in a specific proportion, or form particular types of links. This kind of information is important to the understanding of the material and its further correlation to its behaviour, but the analysis of the energetic behaviour of the O1s and N1s spectra is matter of future work. This section focuses in the behaviour of silicon in the material, using the Si2p band as the main information source.

One manifestation of the fact that the silicon contents or excess is not sufficient parameter to define the material, is that two films with the same amount of Si, O and N can be different structurally if fabricated under disparate conditions, showing same areas under the XPS spectra curves, but different shapes.

In the framework of the intermediate model[20], it is known that the Si–$SiO_2$ interface presents a gradual transition from one material to the other rather than being abrupt[20, 56, 58], and five oxidation states corresponding to $Si^{x+}$ (or $Si-Si_{4-x}O_x$) are to be expected, with $x$ being an integer from 0 to 4[56]. The Si2p regions of the XPS spectra are then composed by these five sub bands, and changes in binding energy of the oxidation state, as well as the quantity of detected photo-electrons corresponding to each, can help to identify the differences in the materials when the fabrication parameters are not the same.

In order sketch a more accurate picture of the material, all the Si2p XPS spectra were fitted to 5 Gaussian-Lorentzian (voigt) peaks within the known binding energy ranges of the Si–Si bonds, silicon suboxides, and $SiO_2$ states using the *XPS Peak 4.1* software by Raymund W. M. Kwok. In the core-shell embedded in a dielectric matrix model (represented in the figure 1.1), the $SiO_2$ matrix of SRO is expected to originate the photoelectrons with energies matching the $Si^{4+}$ band, while the all-silicon core those in the $Si^0$ band[24]. The other three bands should arise from the sub-oxide transition shell.

The figure 2.4 presents the experimental results of the Si2p region in the XPS spectra obtained from four samples, along with the results delivered by the multi-voigt-peak fittings. The figure 2.5 shows in more detail the results within the energies between the states $Si^{3+}$ and $Si^0$. Note how there are samples that present significant contribution by the peaks centred in the latter energy region, indicating that the material does not comply with either the RBM or RMB, but rather the IM[20], as expected from a material containing core-shell structures.
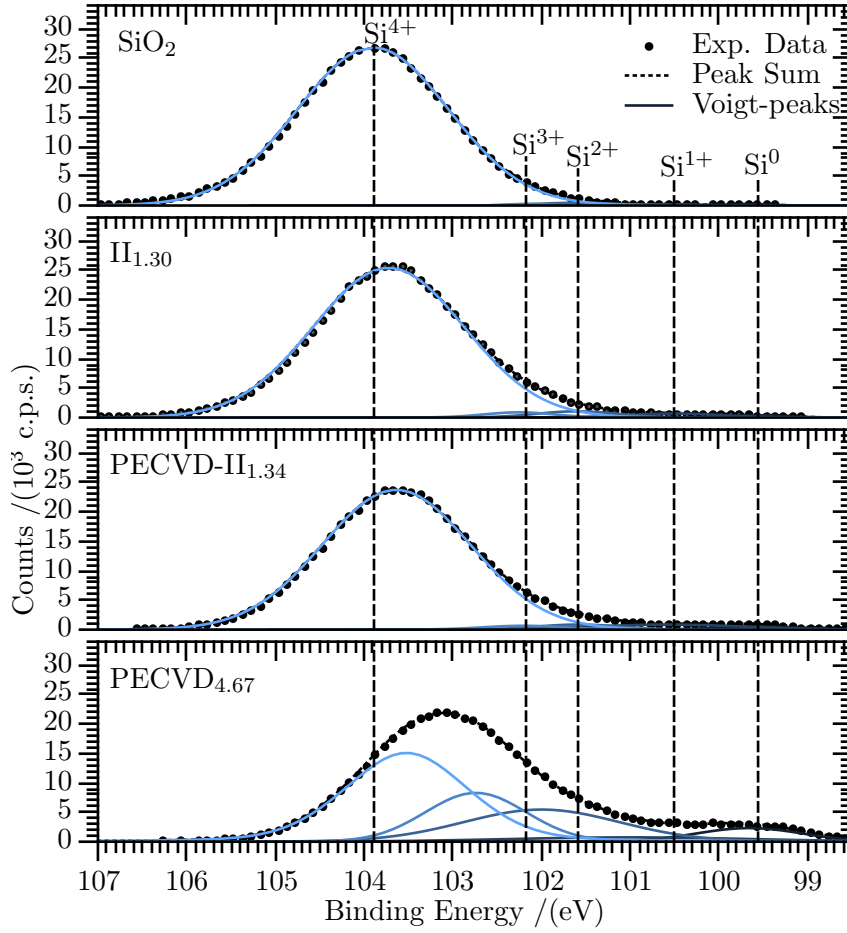
Figure 2.4: Voigt peaks obtained for the multi-peak fittings of XPS spectra in the Si2p region (continuous lines). The circles are the data points, and the dotted line is the sum of the peaks. The silicon contents of the samples is between between 34 at. % and 37 at. % (except for the $SiO_2$ film).
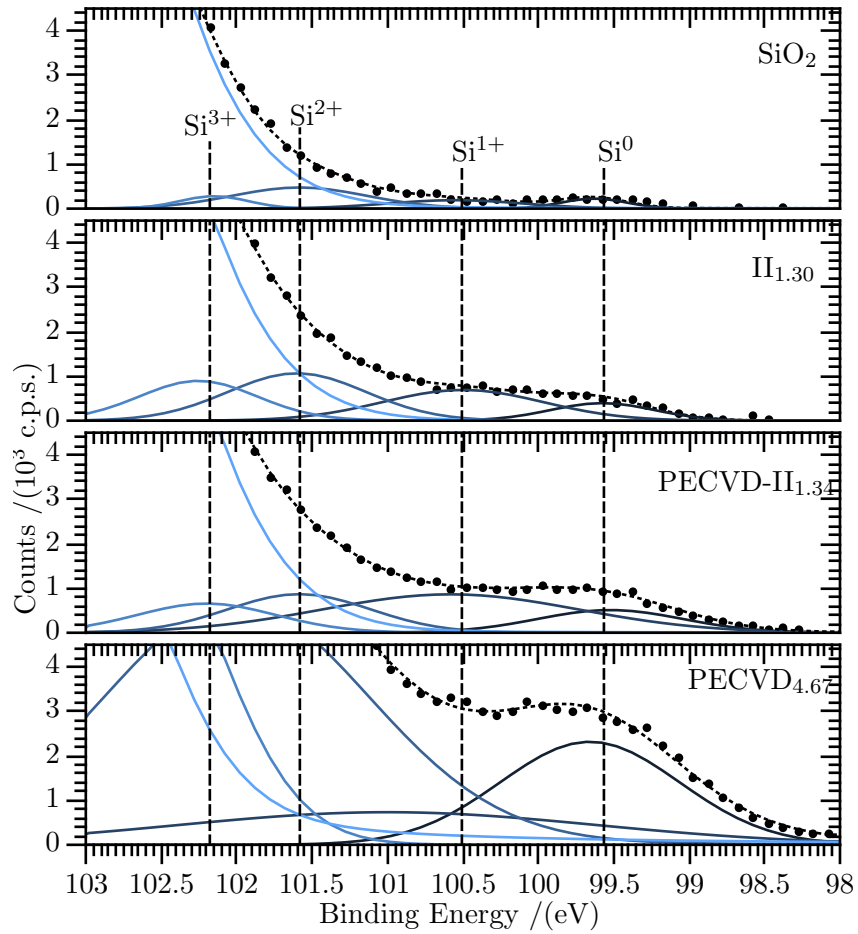
Figure 2.5: Detail of Gaussian multi-peak fittings of XPS spectra in the energy range corresponding to $Si^{3+}$, $Si^{2+}$, $Si^{1+}$ and $Si^0$ from data presented in the figure 2.4.

The figure 2.6 displays the variation of maximum energy for the peaks as related to the silicon excess, which presents the same general trends for both $XS_{Si}$ and silicon contents (remember, the first is defined by equation 2.1, and the second only the atomic percentage silicon in the material). The states $Si^0$, $Si^{1+}$ and $Si^{2+}$ show a binding energy variation below the 2 % of the average value of all samples, always trending to lower energies as the silicon excess increases. This is a small variation as compared to the energy shift of the $Si^{3+}$ and $Si^{4+}$ peaks, which according to a linear fit, present an increase at a rate of $(6.35 \pm 2.40)$ % and a decrease at a rate of $(9.25 \pm 2.60)$ %, respectively. Clark *et al.* report that the separation between the peaks of $Si^0$ and $Si^{4+}$ found in ultra thin oxides are due to the occupancy of traps and defect levels by photo-generated holes[59]. If this is also the case for the material here analysed, in the frame of the core-shell model there should be a relation between the oxide states binding energies and the PL emission due to the defects in the material if they are radiative, but it was not clearly found, neither in wavelength or in contribution to total intensity (this will be detailed in the section 2.5). This means either the defects related to PL are not the same related to the $Si^{4+}$ peak shift, or that this shift is not due to the traps and defect levels.

On the other hand, Lau and Wu attribute the shifting to the charging of the samples during the ionizing x-ray radiation[60]. In this case, a larger separation may indicate better dielectric properties of the films, which is consistent to the behavior of the samples depicted in figure 2.6, since the conductivity of the material is expected to increase with the silicon contents (as will be shown in chapter 3).

The behaviour of the contribution to total Si2p integrated spectra by that of the voigt corresponding to each oxidation state is also interesting. The changes in such proportions as the silicon excess and silicon contents are increased is presented in the figures 2.7a and 2.7b, respectively. Polynomial fittings of third order were performed to the data to allow an easier observation of the trends. The areas of bands from $Si^{1+}$, $Si^{2+}$ and $Si^{3+}$ are presented as sum for simplicity, since, as mentioned before, these three are expected to come from the transition suboxide between the $SiO_2$ matrix and the silicon nano-particles. It is worth mentioning, nevertheless, that the maximum changes in this tree bands was due to the contribution of $Si^{3+}$.

In the case of the contribution to the area, while there is no great change in the general behaviour when switching the 'x' axis parameter between silicon excess (figure 2.7a) or contents (figure 2.7b), the trend seems less clear if using the later. In particular, the sample $PECVD_{2.96}$ (silicon contents of $\sim$36.66 at. %), deviates from the polynomial fitting noticeably more. This is likely to be related to the significantly higher contents of nitrogen in the PECVD samples, and remarks the importance
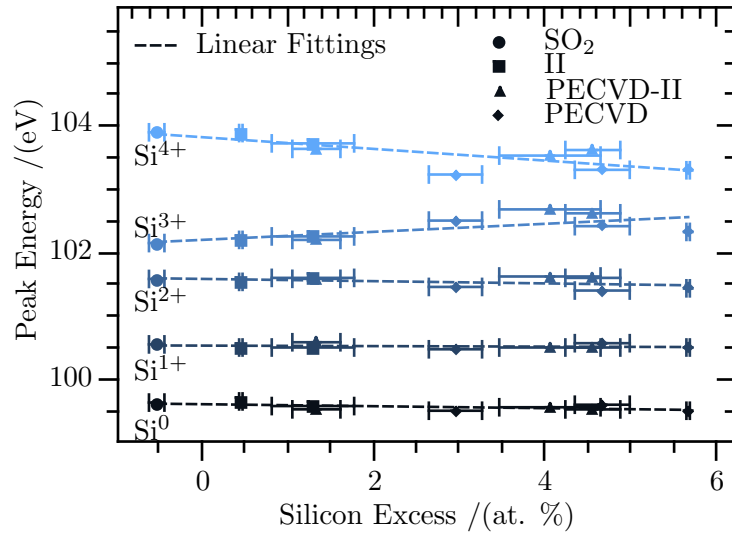
Figure 2.6: Variation of the binding energy for the components of the Si2p region of XPS spectra with silicon excess. The discontinuous lines are linear fittings of the experimental points.
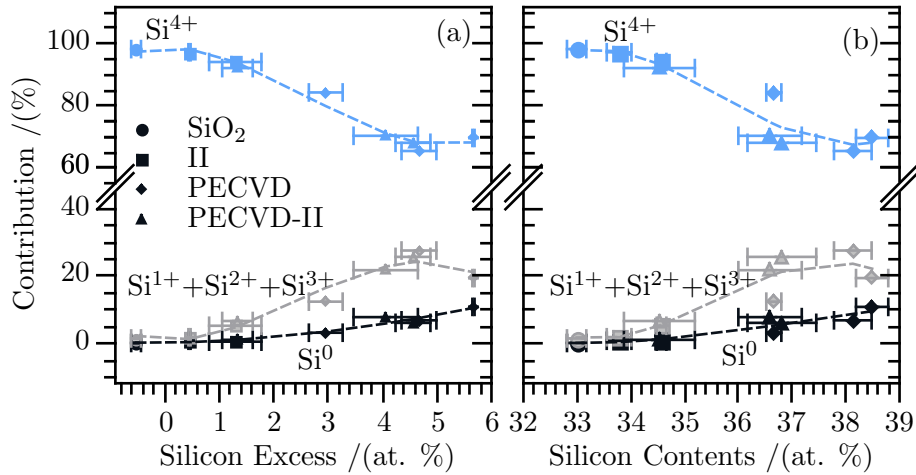


Figure 2.7: Contribution to the integrated Si2p spectra by the integrated voigt peaks corresponding to $Si^{0+}$, $Si^{4+}$ and the sum $Si^{1+}+Si^{2+}+Si^{3+}$ compared by (a) silicon excess and (b) silicon contents. The discontinuous lines are fittings to third order polynomial equations only to be used as guides for the eye, and are not based in any physical model.

of considering this factor when interpreting the material and the usefulness of the $XS_{Si}$ parameter. The figure 2.8 allows a closer inspection of the trend using this quantity as comparison calibre. There is an apparent exponential increment in the contribution by Si-Si bonds as the silicon excess augments, which means more and/or larger nanoparticles are formed. The shell-related peaks also presents an exponential growth at least until the $XS_{Si} \approx 4.7$ at. %, at which value there is a change in the trend. In particular, $Si^{3+}$ bonds seem to diminish in favour of $SiO_2$ formation from this point on. Unfortunately, there is only one datum for above this silicon excess, making impossible to assure if the trend is stabilizing, diminishing or simply a bad point.

## 2.4. Photoluminescence in SRO

Since the main objective of the present work is the use of the luminescent capabilities of the material, it is desired to obtain the most precise knowledge of the real causes for this phenomenon in order to take as much advantage as possible from it. Photoluminescence studies can deliver information on this regard in a relatively easy way, since they do not require more processes than the material obtaining, as opposite to EL which requires the fabrication of a more complex device, apart from a generally more elaborated stimulation-measure set-up.

Many PL studies have already been performed to materials similar to those here analysed[15, 13, 23, 27, 28, 61, 62]. Using that information as a base, this study was focused in the final procurement of a better EL device, thus the experiments were principally aimed to the clear identification of the mechanisms in order to later establish the compromises between all the variables involved in the EL process, which is more complex because it includes transport, electric field, efficiency, among other things that must be considered during the design.

On the other hand, it is important to remember that the output EL of devices built with a particular material may not be the same as the PL of it[15, 27, 29]. This may be due to one of two reasons: optical phenomena defined by the design of the device and electrode materials[27, 29, 43], or differences in the mechanisms of light emission under distinct stimuli[15]. The study of these differences and their causes, in the case of the particular devices and materials reported in this work, is addressed in the chapter 3, as well as in two peer reviewed publications[43, 63], one of which is a very good mainly theoretical work by Juvert *et al.*[63].

The samples presented PL only if thermally annealed (non annealed pilots were also tested), and their emission spectra is always in the range between 900 nm and 690 nm (1.4 eV and 1.8 eV), as expected[15, 29, 27]. As already mentioned, the general consensus advances towards the theory
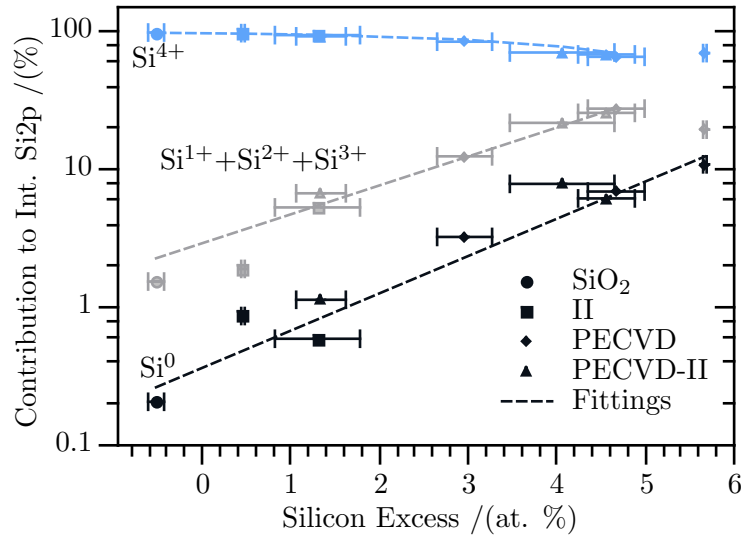
Figure 2.8: Silicon excess versus contribution to the integrated Si2p spectra by the integrated voigt peaks corresponding to $Si^0$, $Si^{4+}$ and the sum $Si^{1+}+Si^{2+}+Si^{3+}$ in logarithmic scale. The discontinuous lines are fittings to the exponential equation $y = exp(A \times x + y_0)$, except for $Si^{4+}$, for which is $y = 1 - exp(A_0 \times x + y_0) + exp(A_1 \times x + y_1)$. Note that the last point escapes the projection of the fittings for the upper bands, indicating a change of trend.

that in SRO and similar materials, luminescence comes from a combination of radiative deffect-related centres and quantum confinement[23, 27, 28, 29]. With this in mind, all PL spectra were fitted to Gaussian multi-peak equations in an effort to isolate the different contributions. Previous experiments showed that in the studied range, PL is composed by two bands[19, 28]. Then, the experimental data was fitted to the equation:

$$I = I_0 + \sqrt{2/\pi} \times \frac{A_1}{w_1} \times exp(\frac{-2(\lambda - PL_1)^2}{w_1^2}) + \sqrt{2/\pi} \times \frac{A_2}{w_2} \times exp(\frac{-2(\lambda - PL_2)^2}{w_2^2})$$
(2.2)

Where $I$ is the emission intensity; $\lambda$ the emission wavelength; $I_0$ an offset intensity value; and $A_1$ and $A_2$, $w_1$ and $w_2$; $PL_1$ and $PL_2$ the areas, widths and peak value of the bands $PL_1$ and $PL_2$, respectively.

This model delivered good fittings to the experimental data obtained (an average $R^2$ higher than 0.99). The figure 2.9 shows the experimentally obtained spectra of samples $II_{1.30}$, $PECVD$-$II_{1.34}$ and $PECVD_{4.67}$; the multi-peak fittings to them; and their respective Gaussian peaks. All the samples characterized and listed in table 2.1, except for the $SiO_2$, presented PL with different spectra, and all were possible to fit to the two-Gaussain peak equation 2.2, although after analysis, sample $II_{0.46}$ was found to be best modelled if fitted to a null contribution of one of them. The two Gaussian components used ranged from 752 nm to 785 nm (called $PL_1$), and from 803 nm to 894 nm (called $PL_2$), respectively.

The changes in the peak emission wavelength, as well as the centre of the two composing Gaussian peaks, is presented in the figure 2.10. Wang *et al.* found two very similar components in PL from PECVD-SRO[28]. In their study, the spectra were measured at different temperatures, finding a dependence on this parameter by $PL_1$, which varied from 740 nm to 780 nm. The $PL_2$ band, on the other hand, did not change. They state that this behaviour means that QC is the reason for $PL_1$, and Si–SiO$_x$ responsible for $PL_2$. Our data seems to contradict this theory, since there is a clear general trend towards $PL_2$ presenting longer wavelengths as the $XS_{Si}$ contents is increased, which is consistent to the general QC model. Regarding $PL_1$, no clear trend can be identified representing the data this way. However, as it is mentioned in section 2.3.1, the $XS_{Si}$ may not be the proper parameter to describe the material in all cases, and closer analysis to the relation between PL and the structural characteristics of the material should be performed to obtain more solid conclusion. This will be presented in the section 2.5.

The figure 2.11 presents the relative contribution of each Gaussian peak to the total area of PL. It can be observed that the band $PL_2$ in general becomes more important as the silicon contents increases in most of the cases, but there is not a smooth trend, indicating the need of a more detailed study taking into account the structural characteristics beyond the $XS_{Si}$
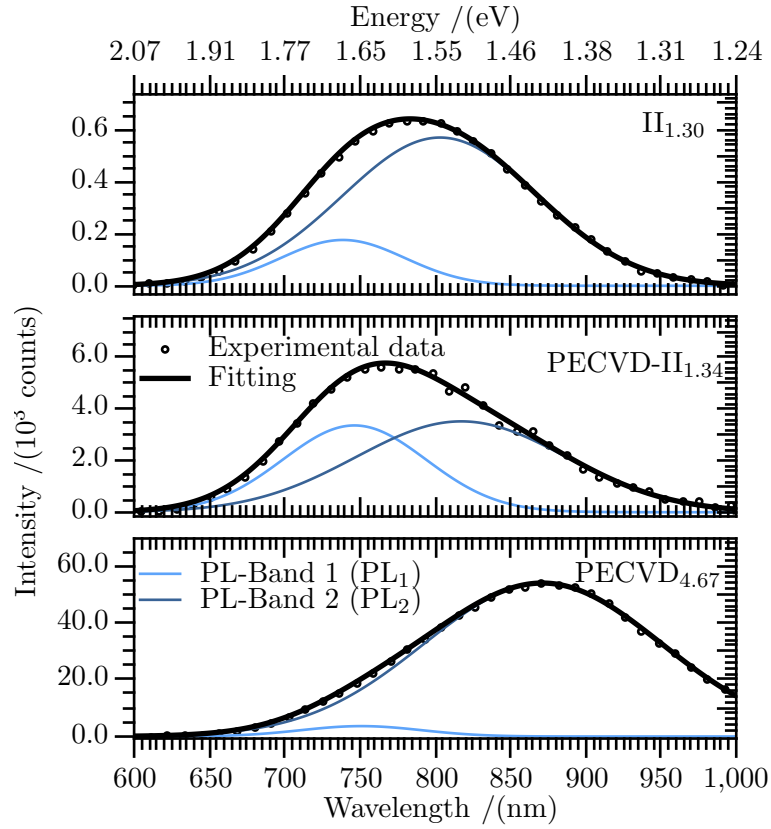
Figure 2.9: PL Spectra of SRO specimens (symbols), fitting to the experimental data using the equation 2.2 (thick line), and the two Gaussian components of such equation (thin lines) .

31
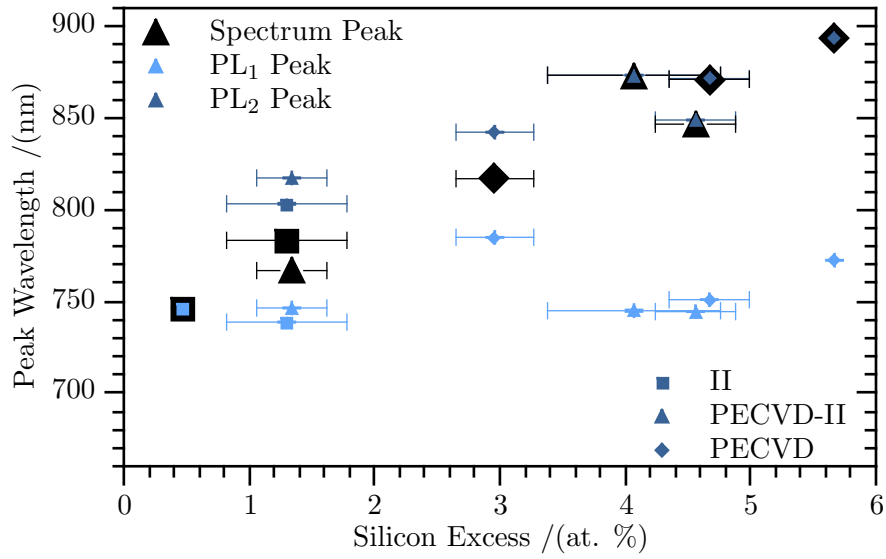
Figure 2.10: Shift of maximum values of PL spectra and their Gaussian components. The solid symbols represent the maximum of the overall peak, and the hollow symbols the centre of the gaussian corresponding to $PL_1$ and $PL_2$. II samples are represented with squares, PECVD-II with triangles, and PECVD with diamonds.
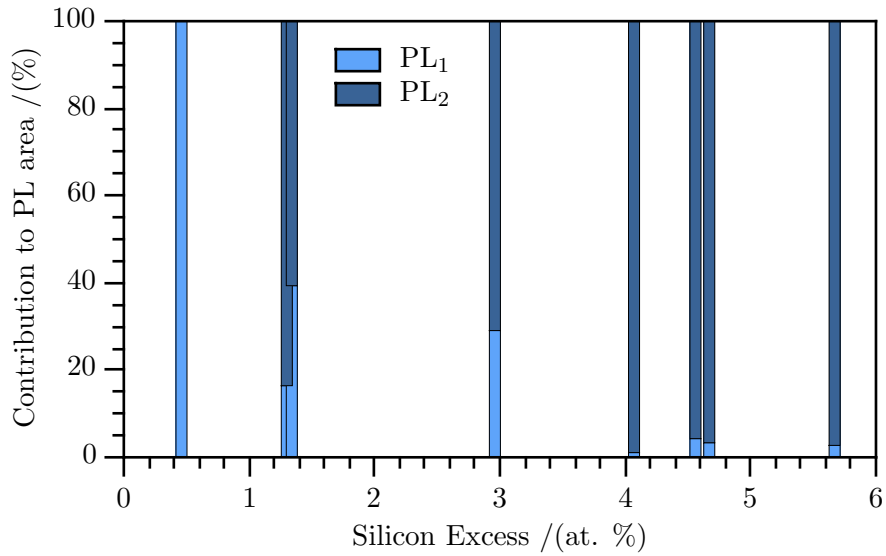


Figure 2.11: Contributions to PL spectra area by their Gauss comp.

also in this matter. Again, this will be presented in the section 2.5.

## 2.5. Composition-Luminescence relation in SRO

The results of the structural analysis of the material established a relation between the contribution to XPS spectra by the $Si^0$ peaks to the presence of nano-particles; the $Si^{1+}$, $Si^{2+}$ and $Si^{3+}$ peaks to the sub-oxyde transitional states; and the $Si^{4+}$ peaks to the silicon dioxide matrix. On the other hand PL analyses delivered data regarding its relation to QC and defect-originated emission mechanisms. Both analyses are based in the assumption that the material can be described by the core-shell model (which would even describe material without agglomerates, as the contribution by $Si^0$ bands in XPS would simply be mathematically represented as 0). This section focuses in the necessary link between XPS and PL analyses as both use the same material model.

The QC emission is based in the presence of nano-particles and the recombination of excitons within them, while the presence of radiative defects is expected to be localized in the surface of such particles and/or in the transitional sub-oxide shell. Hence, a relation should exist between the $Si^0$ bands from XPS, and the $PL_2$ band, if as suggested, it is caused by QC. Similarly, if $PL_1$ is indeed caused by defects as in the shell as the results seem to indicate, it should be related to the $Si^{1+}$, $Si^{2+}$ and $Si^{3+}$ peaks from XPS.

It can be not ignored that emission in wavelengths longer than 700 nm is usually attributed only to QC[4], but no further analysis is generally performed regarding the decomposition of the spectrum in this region. Recent studies show that the exclusive attribution of PL to QC in this range is not even consistent to the models proposed by the same authors, concluding that the PL process of the band between 1.7 eV and 1.75 eV can not be connected to the transition between the band edges related to quantum confinement[10], supporting the theory stating that the PL in this region is also related to defects to some extent.

The figure 2.12 shows the relation between the contribution by $Si^0$ states to the total area of the Si2p region from the XPS spectra, and the peak wavelength of the components of the PL spectra. Lets focus first in the $PL_2$ band, which shows a clear trend lower energy emission as the contribution by $Si^0$ increases, consistently to an increase of the particles size, suggesting that the increment in the quantity of Si–Si links is indeed related to size increment rather than to a higher density of nano-particles. To further evaluate the theory relating the contribution by $Si^0$ and QC photo-luminescence energy, it was used the simplified model based on the
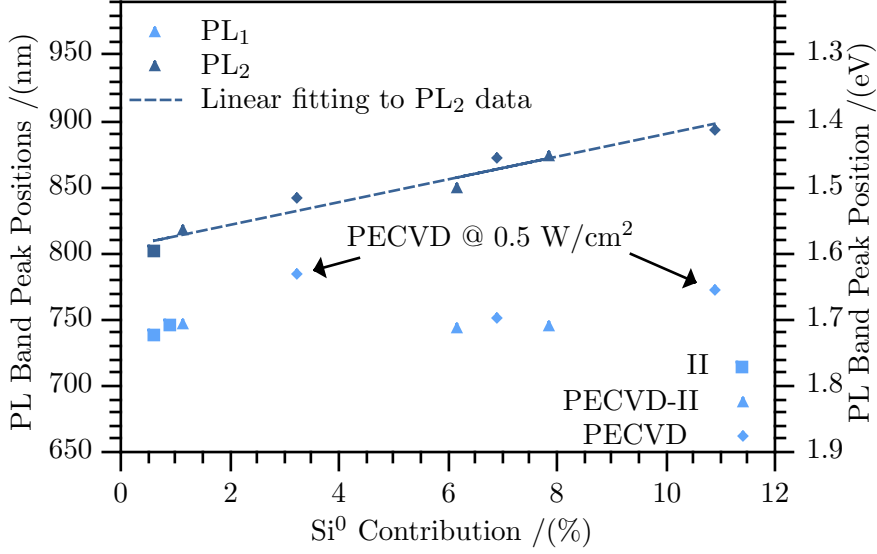
Figure 2.12: Peaks of PL components versus contribution of $Si^0$ bonds to XPS spectra areas. A linear fitting is performed to experimental data of $PL_2$. The data for $PL_1$ shows no dependency on $Si^0$ contribution.

effective mass approximation[31, 32]:

$$E_{nps} = Eg + \frac{C}{d_{nps}^2} \tag{2.3}$$

Where $E_{nps}$ is the resulting emission energy, $Eg$ is the band gap of silicon in bulk, $C$ is a confinement parameter related to the structural characteristics of the particle, and $d_{nps}$ its diameter.

The $Si^0$ from XPS is related to the Si–Si links, and hence, to the Si particles; and the depth of the measurement includes material between 0.5 nm and 5 nm from the surface down.

The quantity $[Si^0]$ can be defined as the contribution by the band $Si^0$ to the total area of the Si2p spectra. Assuming that the whole volume of the nano-particles is covered during the XPS spectra obtaining, and that their density is constant, then $[Si^0]$ can be related to the average volume of the nano particles $V_{nps}$ trough a constant $\alpha$ by the expression:

$$V_{nps} = \alpha[Si^0] \tag{2.4}$$

On its turn, the average volume and average diameter of the spheres formed by the Si–Si links $d_{nps}$, are related through the expression:

$$V_{nps} = \frac{1}{6}\pi(d_{nps})^3 \tag{2.5}$$

Combining the equations 2.3, 2.4 and 2.5; the relation between the QC emission energy and $Si^0$ contribution can be written as:

$$E = Eg + \frac{C}{\beta[Si^0]^{2/3}} \qquad (2.6)$$

Where $\beta = (6\pi\alpha)^{2/3}$. This relation is only valid for nano-particles with diameter below 5 nm, since that is the maximum depth covered by the XPS equipment. Larger particles would not keep the same relation between diameter and $[Si^0]$. According to the calculi by Trwoga *et al.*[12], their emission would be at energies higher than 1.45 eV.

The figure 2.13 shows the fitting of the equation 2.6 to the experimental data for the energy values of the PL related to QC ($PL_2$ peaks). The results of the fittings deliver consistent values for the parameters involved in equation 2.6 up to $[Si^0]$=6.5 %, with a confinement constant of $C = 4.25$ and an energy $Eg = 1.44$ eV, which are inside the range of strong confinement reported by other authors[27, 31, 32]. This suggest that the nano-particles in the material are amorphous[32], and that the increase of $[Si^0]$ is more likely related to the increment of the nano-particles diameter, and not to an increase on their quantity.

The points with $[Si^0]$ higher than 6.5 % are expected to be outside of the probing range of the XPS equipment, and clearly not matching the model. In addition, it is possible that the size increment does not dominates the contribution by $[Si^0]$ any more, but an increment on the nano-particles density is now important, (although the decrease in emission energy suggest that there is still some increment in size). This is likely to happen, since the results of the fitting predict emission peaks corresponding to $[Si^0] > 6.4$ % at unreasonable $[Si^0]$ values according to the experimental data. Hence, not only $\beta$, but also $C$ and even $Eg$ should be different for these samples. The variations in these parameters are known to be caused by the change of confinement regime[12, 32], which is affected by the size of the particles as well as by the crystallinity and stress in the material[9, 32].

Regarding the other component of the PL spectra, $PL_1$ peaks are confined in a much narrower range of wavelengths (between 725 nm and 785 nm), and do not show an identifiable trend, which would be consistent to luminescence due to radiative defects. It is remarkable that two points, corresponding to the PECVD samples fabricated using a plasma power density of 0.5 W/cm$^2$ ($PECVD_{2.96}$ and $PECVD_{5.67}$), present a noticeable higher $PL_1$ emission wavelength than the average of the rest of the samples, namely 778.67 nm $\pm$ 6.25 nm (1.59 eV $\pm$ 0.01 eV), as compared to the 741.74 nm $\pm$ 12.79 nm (1.67 eV $\pm$ 0.03 eV) of the rest. This does not conflict with the theory of $PL_1$ being caused by defects, since these are expected to be different in the samples fabricated with lower plasma powers, because this changes the generation of active species. However, the reasons
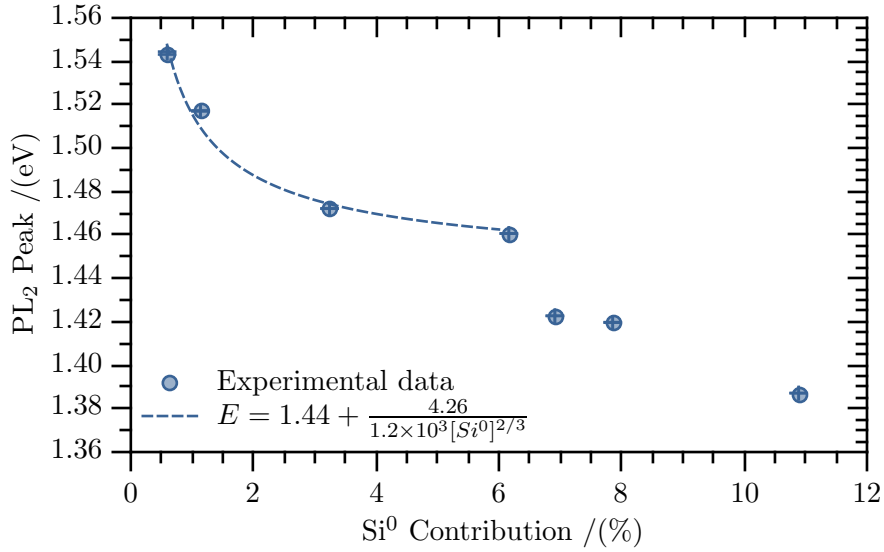
Figure 2.13: Fitting of the equation 2.6 to experimental data with emission under 1.45 eV (diameters below 5 nm).

for the change in the defect emission of these two particular samples was not possible to identify in the analysis of the XPS results, which are limited to Silicon, Nitrogen and Oxygen incorporation. A possible explanation is related to the incorporation of hydrogen into the material, which is known to influence the grain formation in nano-crystalline silicon[10]. Nevertheless, this matter is one to be studied closely in the future.

The relative contribution to the total PL intensity by each band, as related to the proportion of Si-Si links in the material, was also studied. The results are illustrated in figure 2.14. Note that in this case, a clear trend is identifiable for $Si^0$ contribution values greater than 0.6 %, which is another example of the possible misleads raised by the use of $XS_{Si}$ if this is compared to the figure 2.11, which uses this parameter as the 'x' axis. As already suggested, the increment of the contribution of $Si^0$ could be related either to bigger Si nanoparticles, or to a higher density of them. But the clear dominance of $PL_2$ with it suggests the first as a more likely explanation. Additional support to this theory is that the model of equation 2.6 used to fit the wavelength shift data with the good results presented in figure 2.13 relies in such assumption.

However, it cannot be ignored the evident disruption in the trend caused by the datum for the lowest $[Si^0]$ in figure 2.14. This could be a consequence if the presence of very small nanoparticles in which the surrounding shell is not developed enough in order to dominate the emission. Clearly more
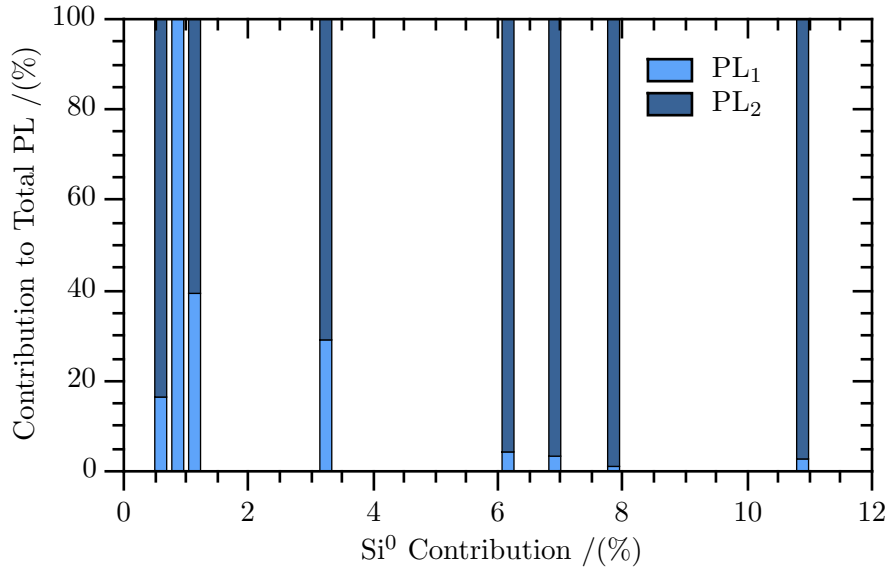
Figure 2.14: Proportion of each PL band to total emission as related to contribution of Si$^0$.

data is needed to explain this phenomenon, and the particular behaviour for this small contributions by [Si$^0$] are to be further studied in the future.

## 2.6. Si$_3$N$_4$-SRO Bi-layers

As mentioned, studies suggest that the inclusion of a silicon nitride layer can improve the results when fabricating luminescent devices[36, 38, 44]. It has been proposed that the presence of a film of this material reduces the current leakage in a MOS-like device[44], as well as the electric field in the oxide layer, which results in a general improvement of efficiency and lifetime[36, 38].

The experiments performed for the development of this work show indeed that some benefit can be obtained when adding (or not removing) a nitride film to obtain bi-layer devices in electroluminescence, as will be seen in chapter 3. However, it was also observed a significant variation on the light emission spectra, in concordance to previous studies[53].

This section discusses the results of the characterization of Si$_3$N$_4$–SRO bi-layer systems as those represented in the figure 2.15, and which fabrication is summarized in the section 2.1.2 and detailed in the appendix C.1. Such results are compared to those from the monolayers, in order to explain the reasons for the found differences and the zone of the systems in

LPCVD Si$_3$N$_4$ → ∼ 30 nm

Si$^+$ Implanted → ∼ 30 nm
zone

LPCVD Si$_3$N$_4$ → ∼ 30 nm

Implanted
SiO$_2$ or → ∼ 30 nm
PECVD-SRO

SiO$_2$ or
PECVD-SRO → ∼ 270 nm

p-Si Substrate →

(a)

p-Si Substrate →

(b)
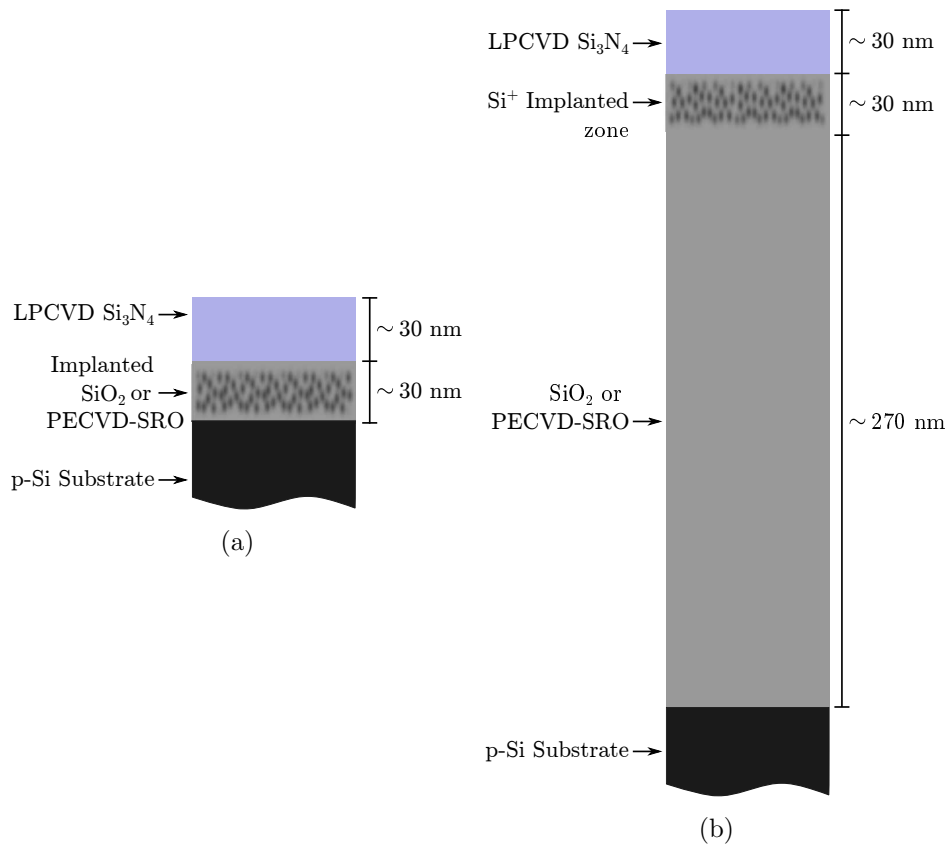
Figure 2.15: Schematic of layer structures of nitride-SRO samples with SRO nominal thicknes of 30 nm (a), and 300 nm (b). The reference sample Bi-SiO$_x$ presents the same scheme as (a) except for the SRO layer, which is a silicon oxide with no silicon excess.

which the luminescence is originated. The influence of the thickness and fabrication technique of the SRO film in the multi-layered structure is also studied and discussed.

### 2.6.1. Structural studies of Bi-layers with 30 nm-thick SRO

The table 2.4 summarizes the results of the XPS studies for the $\sim$30 nm-thick SRO films of the bi-layer structures depicted in figure 2.15a. Note that the atomic concentrations for the sample Bi-SiO$_x$ deliver a negative value of $XS_{Si}$ which absolute is higher than that of the SiO$_2$ reference sample (see table 2.3). This is because of the higher atomic percentage of nitrogen and oxygen, which results in a deficit of Si atoms according to the model represented in equation 2.1.

Nevertheless, the Si2p spectra show indeed that the proportions of the Si oxidation states typical of Si$^{4+}$ and Si$^0$ are around 98.25 % and 0.21 %, respectively; and these values are precisely the same obtained for the SiO$_2$ reference sample, meaning that the oxide layer in sample Bi-SiO$_x$ cannot be considered SRO, and is much closer to SiO$_2$ but with a higher concentration of suboxides. This is consistent to the PL results as will be shown later.

Regarding the contents of Si in the silicon nitride films, the results are presented in table 2.5. For this element, all the samples present essentially the same characteristics in the first 25 nm from the surface, despite receiving different Si-implantation doses. There are, however, changes in the proportion of N and O.

The figure 2.16, which shows the element contents depth profiles, helps to understand this and illustrates what happens in the rest of the film. The depth values were calculated measuring the etching rates of the Ar$^+$ sputter gun (described in section 2.2.1) in very well controlled thickness-wise Si$_3$N$_4$ and SiO$_2$ samples; then, the former was used to calculate the depth values in the nitride layers, wile the later those in the SRO films. The etching rate for the transition layers were assumed to be the average of both as a

Table 2.4: Silicon excess and elemental atomic percentages in the SRO layers of bi-layer samples. The studies of the single layer peers are presented in the table 2.3 of section 2.3.

| Sample | $XS_{Si}$ in SRO /(at. %) | Element Contents in SRO/(at. %) | | |
|---|---|---|---|---|
| | | Si | N | O |
| Bi-SiO$_x$ | -1.37 $\pm$ 0.30 | 32.70 $\pm$ 0.20 | 1.65 $\pm$ 0.12 | 65.65 $\pm$ 0.18 |
| Bi-II$_{0.46}$ | 0.46 $\pm$ 0.02 | 33.78 $\pm$ 0.23 | 0.84 $\pm$ 0.19 | 65.39 $\pm$ 0.21 |
| Bi-II$_{1.30}$ | 1.30 $\pm$ 0.48 | 34.57 $\pm$ 0.09 | 2.25 $\pm$ 0.47 | 63.18 $\pm$ 0.44 |
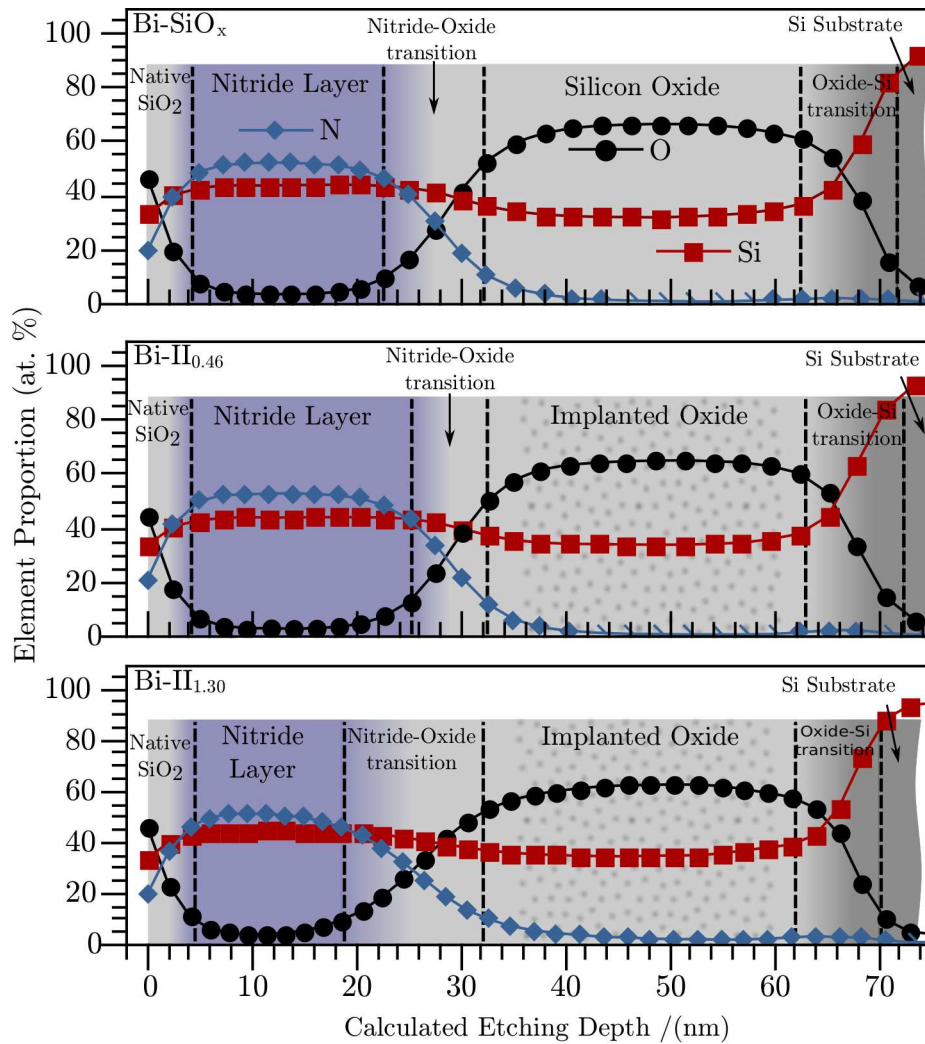
Figure 2.16: Element contents depth profiles as extracted from XPS results for the bi-layered samples of table 2.4, and a schematic representation of the multi-layer structure.

Table 2.5: Elemental atomic percentages in the nitride layers of bi-layer samples. The values were averaged for the first 25 nm of the nitride layer. The results of a pilot Si$_3$N$_4$ film deposited by the same technique are presented as reference values.

| Sample | Element Contents in Nitride Layer/(at. %) | | |
|---|---|---|---|
|  | Si | N | O |
| Nominal Si$_3$N$_4$ | 43.41 ± 0.35 | 52.89 ± 0.40 | 3.70 ± 0.75 |
| Bi-SiO$_x$ | 43.78 ± 0.19 | 51.77 ± 0.60 | 4.45 ± 0.42 |
| Bi-II$_{0.46}$ | 43.93 ± 0.43 | 52.31 ± 0.19 | 3.76 ± 0.63 |
| Bi-II$_{1.30}$ | 43.37 ± 0.02 | 49.12 ± 2.80 | 6.51 ± 2.78 |

first approximation.

In the profiles of the figure 2.16, a Nitride-Oxide transition zone can be defined as that in which there is, simultaneously, a contents of N and O higher than 10 at. % for each element. The variations on the proportions of N and O are due to the different widths of the transition zones between the nitride buffer and the silicon oxide film, which affect the average values of these two elements.

As it can be seen, the sample Bi-II$_{1.30}$ presents a Nitride-Oxide transition zone significantly greater than the sample Bi-II$_{0.46}$, at least 42 % wider. Note that the silicon oxide region does not change significantly, and an increment in the width of the transition region results in a decrement of the nitride layer width.

In any case, the contents of Si in the nitride for all the samples is clearly comparable to the Si$_3$N$_4$ pilot sample, as it can be observed in the table 2.5, since in the worst case scenario, the difference is 0.4 at. %, which is lower than the error for the contents of this element found in the sample Bi-II$_{0.46}$ (±0.43 at. %). This allows to establish that there is no significant excess of this element in the nitride layer.

Summarizing the results from the material analysis of the multi-layer samples, four main facts should be highlighted before discussing the PL results, namely: the equivalence of SRO in bi-layer samples to that of their single-layer counterparts, the equivalence of the mid-layer of sample Bi-SiO$_x$ to silicon dioxide for the purposes of this analysis, the absence of significant Si atoms from the implantation in the nitride layers, and a noteworthy transition region between nitride and oxide in all the samples.

### 2.6.2. Photoluminescence in Bi-layers with 30 nm-thick SRO

The PL experiments to the bi-layers were conducted in the same session and way as that for the single-layer counterpart of each sample, described in section 2.4. The resulting spectra are presented in figure 2.17, in which a clear shape and wavelengths match between the emission above 700 nm of both types of samples can be observed. Note that in the sample Bi-SiO$_x$, with no Si excess in the dioxide layer, only PL below 700 nm was found; while the sample with the single oxide film (that to which the nitride was removed) did not present detectable PL. Hence, the emission of wavelengths shorter than 700 nm is clearly caused by the presence of the nitride film.

The Spectra for the bi-layers was possible to fit to the sum of six Gaussian peaks, four of them centred around wavelength values of reported radiative centres found in silicon nitrides and oxinitrides[37, 64, 65, 66], and the other two matching the known components of the SRO previously characterized (section 2.4).

The values of the centre of each Gaussian are listed in the table 2.6, and the fittings are presented in the figure 2.18. The table also includes the results for the fittings to the PL from their single SRO layer counterparts II$_{0.46}$ and II$_{1.30}$, which presented the bands PL$_1$ and/or PL$_2$ . These two bands were found practically unaltered in their positions in the bi-layer samples that include the same SRO, confirming once more this zone of the spectra is originated in the silicon oxide layer of the structures.

The rest of the bands of the spectra, assumed to be nitride-related, and hereafter referred to as PL$_A$, PL$_B$, PL$_C$ and PL$_D$, are respectively centred at average values of 411.6 nm $\pm$ 0.6 nm ($\sim$3 eV), 458 nm $\pm$ 4.2 nm ($\sim$2.7 eV), 508.9 nm $\pm$ 0.1 nm ($\sim$2.4 eV), and 588.8 nm $\pm$ 1.8 nm ($\sim$2.1 eV). As can be seen, the deviation in centre value is lower than 1 % at most, indicating that it can be considered that the differences on the whole emission spectra of the samples, arise only from the changes in the contribution of each of these peaks to total PL.

As mentioned, the nitride-related four peaks are centred in the emission wavelengths of well known and reported radiative centres found in silicon nitrides and oxinitrides. Emission matching PL$_A$ has been reported as caused by nitrogen dangling bonds in SiN$_x$O$_y$ films[65]. This is the only significant contribution to luminescence in sample Bi-SiO$_x$. The band PL$_B$ could be due to two possible causes, since similar emission has been related to a N–Si–O defect induced by the presence of oxygen in SiN$_x$ films, which allows the transition $\equiv$Si$^0$ $\longrightarrow$$\equiv$N$-$Si$-$O.[66]; but it has also been attributed a state in the band gap due to nitrogen dangling bonds[64]. The peak PL$_C$ most likely arises from transitions between the silicon nitride conduction band and defect levels of the type $\equiv$Si$^0$[37]. Finally, PL$_D$ has been either related to $\equiv$Si$^-$ [65], or $\equiv$Si$^0$[66] defect levels.

The clear distinction between PL caused by SRO and nitride has been
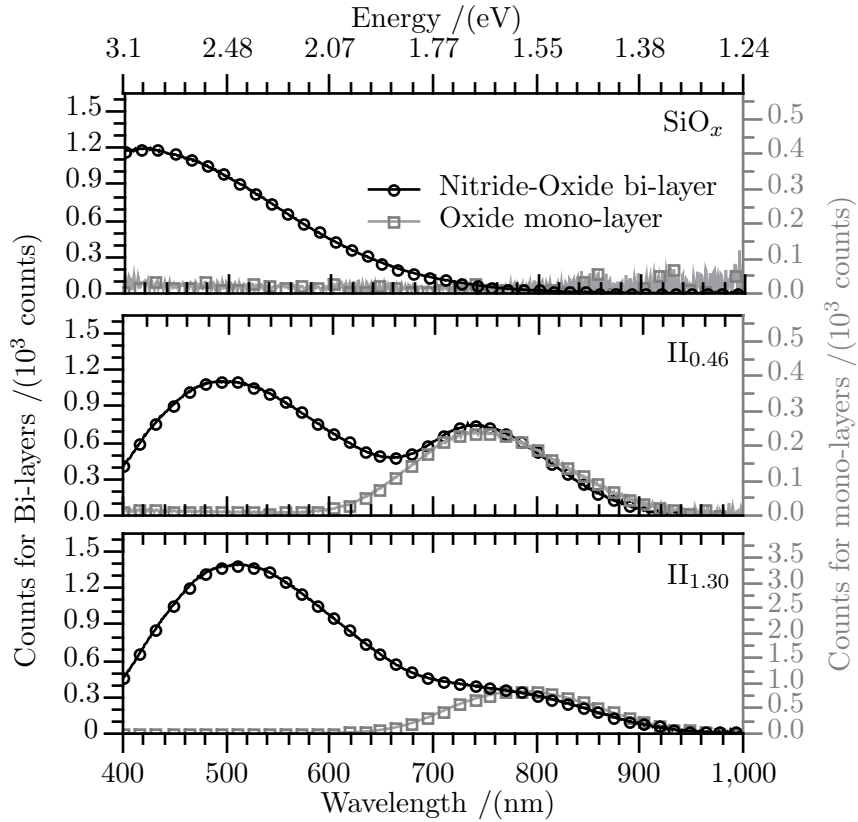
Figure 2.17: PL spectra of the Silicon Nitride-Silicon oxide samples presented in table 2.4 (circles) and their "twin" single-layer samples (squares, also analysed in section 2.4). The left 'x' axis presents the scale for the results of the bi-layers, and the right one that of the mono-layers.
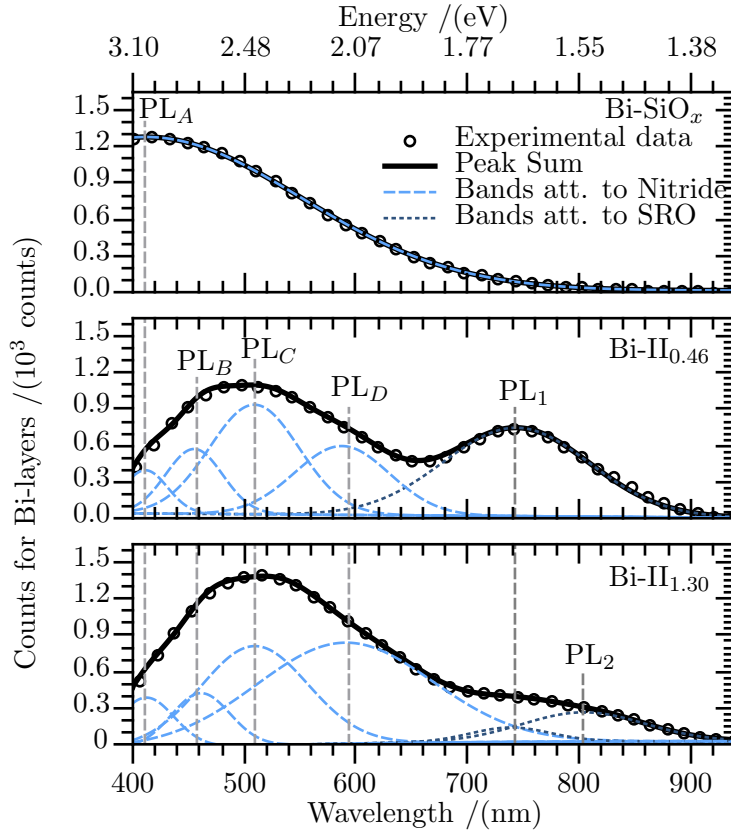
Figure 2.18: Multi-peak fittings of PL spectra from the bi-layer samples listed in table 2.4. The circles represent the experimental data; the solid black lines are the results of the fitting, while the Gaussian components are represented with a dashed line for those attributed to the nitride presence, and a dotted line for those originated in SRO. Guidelines are placed at the wavelengths corresponding to the emission by different radiative centres responsible for the luminescence, which are labelled according to their description in the text.

Table 2.6: Peak wavelengths of the bands composing PL of II-SRO mono and bi-layers from multi-Gaussian peak fittings of PL spectra. The results of II-SRO mono layers confirm the activity of the same radiative centres in bi-layers.

| Sample | Centre of bands composing PL, related to | | | | | |
| | Silicon Nitride /(nm) | | | | SRO /(nm) | |
| | PL$_A$ | PL$_B$ | PL$_C$ | PL$_D$ | PL$_1$ | PL$_2$ |
|---|---|---|---|---|---|---|
| Bi-II$_{0.46}$ | 411.2 | 455.0 | 509.0 | 587.5 | 744.0 | – |
| Bi-II$_{1.30}$ | 412.0 | 460.9 | 508.9 | 590.0 | 738.5 | 803.4 |
| II$_{0.46}$ | – | – | – | – | 746.5 | – |
| II$_{1.30}$ | – | – | – | – | 738.6 | 803.7 |

observed previously in the work of Barreto and Perálvarez[53], and they attribute this to an excess of Si in the nitride. Additionally, studies to single SiN$_x$ films have shown that the abundance of Si in the nitride is the cause for strong PL in them[66]. Contrarily, in the case of the samples here presented, there is no Si excess in the nitride layer according to the XPS profiles, but there is a proportional abundance of Si in the nitride-oxide transition zone, as can be observed when analysing the figure 2.16. This suggests that is in this area where the emission due to the presence of nitrogen is originated. Such hypothesis is consistent to the behaviour of the intensities of the bands, which increase with the transition zone widths, as it can be observed if relating the figure 2.16 to the figure 2.17.

It is worth to note that the intensities of the SRO-related bands are not the same of the single-layer ones. In particular, the Bi-II$_{0.46}$ presents much higher emission for the SRO-related band than the single-layer sample, since the area of the PL spectrum of the first is around 4.3 times higher, despite having a narrower nitride-oxide transition zone than II$_{1.30}$. On the other hand, in the samples II$_{1.30}$ and Bi-II$_{1.30}$ this does not stand, since the area of the PL spectrum of the single layer sample is 2.8 times greater than the SRO-related emission of the bi-layer. The finding of the reasons for this is not a trivial problem, and further studies should be conducted.

### 2.6.3. The influence of SRO thickness in Bi-layers

Apart from the "twin" samples described and analysed previously, other set was fabricated to investigate the results if the thickness of SRO and Si$_3$N$_4$ were asymmetrical, and to verify the influence of a larger volume in the implanted oxide matrix for SRO obtained by ionic implantation.

This section presents the analysis of results from studies to bi-layer

samples as the depicted in the figure , *i. e.*, systems with 30 nm of LPCVD silicon nitride on top of 30 nm and 300 nm-thick SRO films. The SRO layers were obtained by ion implantation of Si in both SiO$_2$ and PECVD-SRO films, the later already enriched in Si with $XS_{Si} \simeq 4$ at. %. The same implantation doses, energies, and thermal annealing, were used for all thicknesses and materials.

The fabrication process of these samples is summarized in the section , and detailed step-by-step fabrication run in the appendix C.4.

**Atomic composition**

The figures 2.19 and 2.20 show the element contents depth profiles as obtained from the XPS studies. Note that in the case of the samples presented in this section, the nomenclature uses the thickness to define the labels, since it is the comparison parameter in which the analysis will focus. For these samples, the resolution of the XPS depth profiles was lower than that of the section 2.6.1, and the experimental points depicted by symbols, while the lines are eye guides built with Akima interpolation operations.

The inspection of the figure 2.20 allows to conclude that the SRO in the sample Bi-PECVD-II$_{300nm}$ ended being around 40 nm shorter than the thermally grown SRO. This was attributed to higher compaction due to H desorption after annealing due to the known fact that PECVD-SRO presents more hydrogen contents[47]. This must be taken into account when performing the luminescence analysis, as will be emphasized in the section 2.6.3.

The table 2.7 shows the values for the average silicon excess in the implanted zone of all samples, obtained averaging the results from the experimental points in the zones indicated as implanted in figures 2.19 and 2.20. It also presents the average values of the points in the zone after implantation for the thicker samples Bi-SiO$_2$-II$_{300nm}$ and Bi-PECVD-II$_{300nm}$, respectively marked as thermal SiO$_2$ and PECVD-SRO in figure 2.20.

Unlike in the case of the symmetrical Si$_3$N$_4$ samples previously discussed, no single-layer pilots were fabricated for the asymmetrical samples. For this reason, the detailed analysis of the Si2p region of XPS spectra was performed directly on the bi-layers in specific depth points. The results of the contribution by Si$^0$ states to total Silicon bonds at the specific depth studied are summarized in the table 2.8.

As expected due to its pre-implantation silicon contents, the sample Bi-PECVD-II$_{30nm}$ presents higher silicon excess than Bi-SiO$_2$-II$_{30nm}$ in the SRO ($\sim$1.62 at. % as compared to $\sim$1.03 at. %). However, the contribution by Si$^0$ to total Si is slightly higher for the second (0.16 % and 0.56 % in the point around 42 nm deep for Bi-PECVD-II$_{30nm}$ and Bi-SiO$_2$-II$_{30nm}$, respectively). It can be observed that in samples with 300 nm-thick SRO
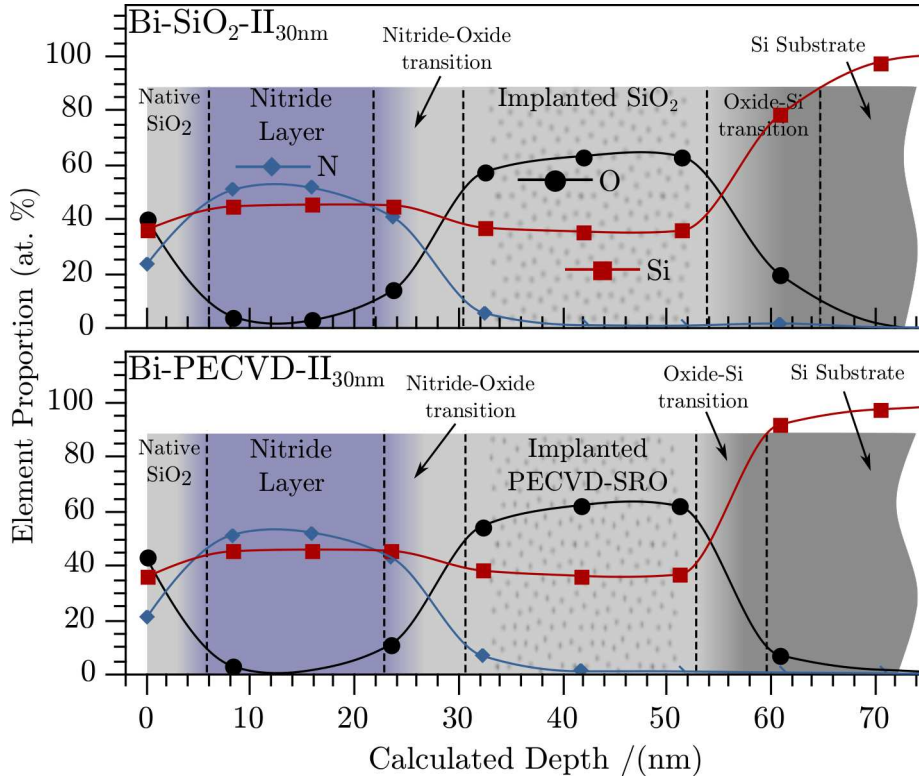
Figure 2.19: Element contents depth profiles as extracted from XPS results for the 30 nm-thick SRO bi-layered samples included in table 2.7, and a schematic representation of the multi-layer structure.

Table 2.7: Silicon excess, average elemental atomic percentages, and nominal thickness in the SRO of bi-layer samples. The $XS_{Si}$ values in the implanted zone are the average of the first 30 nm. The $XS_{Si}$ values in the oxide matrix are the averages from 30 nm to 300 nm inside the SRO or SiO$_2$.

| Sample | Nominal matrix Thickness /(nm) | $XS_{Si}$ in Implanted zone /(at. %) | $XS_{Si}$ in Oxide matrix /(at. %) |
|---|---|---|---|
| Bi-SiO$_2$-II$_{30nm}$ | 30 | $1.03 \pm 0.15$ | – |
| Bi-SiO$_2$-II$_{300nm}$ | 300 | $0.83 \pm 0.06$ | $0.29 \pm 0.03$ |
| Bi-PECVD-II$_{30nm}$ | 30 | $1.62 \pm 0.24$ | – |
| Bi-PECVD-II$_{300nm}$ | 300 | $1.22 \pm 0.20$ | $4.14 \pm 1.01$ |
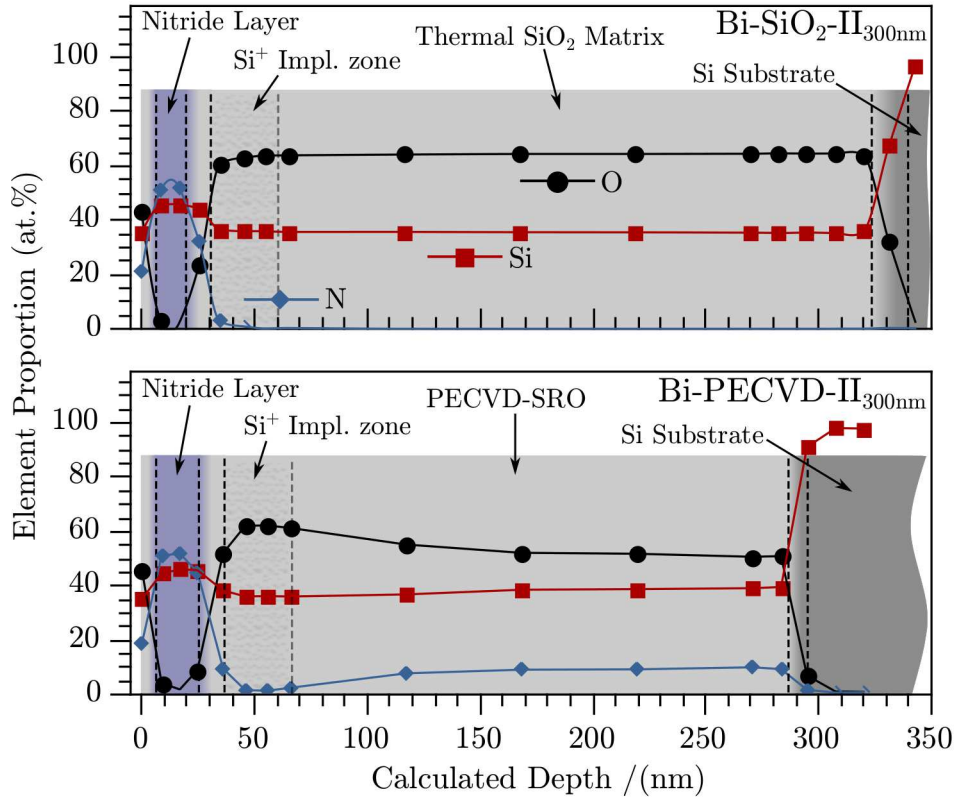
Figure 2.20: Element contents depth profiles as extracted from XPS results for the 300 nm-thick SRO bi-layered samples included in table 2.7, and a schematic representation of the multi-layer structure.

Table 2.8: Contribution by Si$^0$ band to total area of Si2p spectra at specific depth points in the SRO layers. The calculus method is the same described in section 2.3.

| Sample | Si$^0$ Contr. at $(42 \pm 2)$ nm depth /(at. %) | Si$^0$ Contr. at $(218 \pm 2)$ nm depth /(at. %) |
|---|---|---|
| Bi-SiO$_2$-II$_{30nm}$ | $0.56 \pm 0.06$ | – |
| Bi-SiO$_2$-II$_{300nm}$ | $0.98 \pm 0.10$ | $0.00 \pm 0.01$ |
| Bi-PECVD-II$_{30nm}$ | $0.16 \pm 0.02$ | – |
| Bi-PECVD-II$_{300nm}$ | $0.64 \pm 0.06$ | $3.66 \pm 0.37$ |

the implanted zone present significant differences in $XS_{Si}$ values, meaning that the distribution of the implanted silicon ions is not uniform despite the thermal annealing. As can be corroborated in table 2.7, the sample Bi-SiO$_2$-II$_{300nm}$ presents $XS_{Si}$ ~0.83 at. % in the implanted zone, and a clear diminution to $XS_{Si}$ ~0.29 at. % in the rest of the matrix, consistent to the expected behaviour for the implanted Si is to diffuse from higher to lower concentration zones. Note, however, that no nucleation of Si is obtained in the non-implanted zone, as 0 % of $Si^0$ contribution was found, as table 2.8 shows.

On the other hand, the behaviour of sample Bi-PECVD-II$_{300nm}$ is opposite, rather contra-intuitively. In this case, the implanted zone presents $XS_{Si}$ ~1.22 at. %, while the rest of the PECVD-SRO matrix presents $XS_{Si}$ ~4.14 at. %. The explanation for this can be found observing the contents of oxygen variation presented in the figure 2.20: note how the proportion of oxygen in the implanted zone is much higher as compared to that in the rest of the SRO matrix: (63.34±5.26) at. % and (54.47±1.91) at. %, respectively. This translates in an increment of the $XS_{Si}$ value. The variation of the N contents plays a smaller role in this situation since it is already relatively low.

This oxygen change also accounts for the significant differences in the contribution to total Si bonds by $Si^0$ type, which goes from ~0.64 % in the implanted zone, to ~3.66 % in the rest of the PECVD-SRO. This means that the implantation of ions contribute to the introduction of oxygen in the material, hence hindering the generation of Si agglomerates if an excess of this element is already present, despite introducing more atoms. This is consistent to the results from the analysis of the bands composing the XPS spectra, in which the PECVD samples present the highest $Si^0$ contribution, as seen in the figures 2.7 and 2.8.

**Photoluminescence**

With the general knowledge of the material composition of the samples, lets analyse their PL behaviour. The Figure 2.21 presents the PL spectra for all the samples listed in table 2.7.

The first notable feature is that samples Bi-SiO$_2$-II$_{30nm}$ Bi-PECVD-II$_{30nm}$ and Bi-SiO$_2$-II$_{300nm}$ present similar peak intensities (between 200 and 250 counts), but sample Bi-PECVD-II$_{300nm}$ has a maximum value two orders of magnitude higher. It appears that the latter does not present emission in the range previously identified as originated by the presence of nitride ($\lambda$ <700 nm), while the other clearly show it, although in the case of Bi-SiO$_2$-II$_{300nm}$ is smaller and with a shape that is different to the previously observed. In a closer inspection, it can be seen that Bi-PECVD-II$_{300nm}$ not only presents this emission indeed, but that it is remarkably similar in shape to that of Bi-SiO$_2$-II$_{300nm}$, and that the very high emission
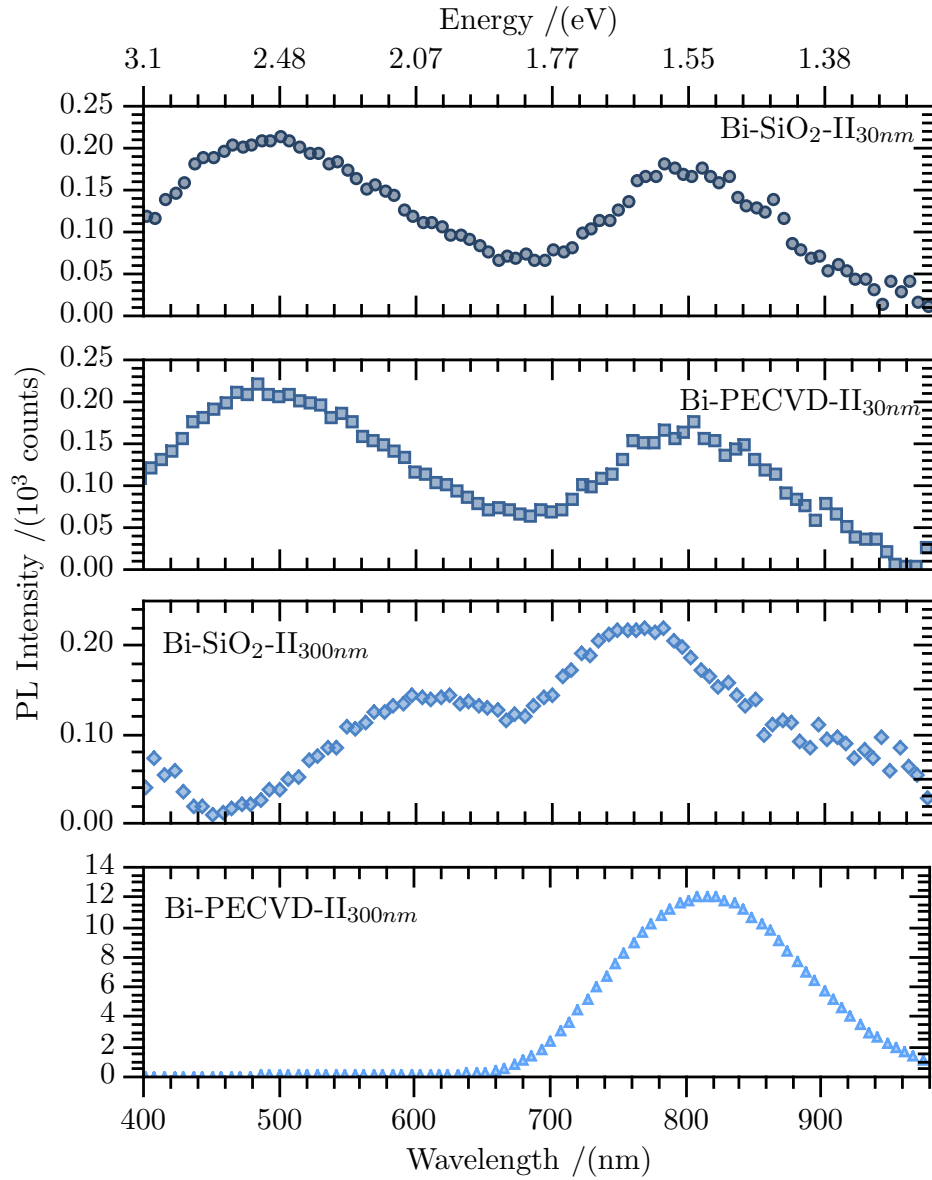
Figure 2.21: Photoluminescence spectra of bi-layered samples listed in table 2.7.

related to SRO screens its detection if not properly scaled. The figure 2.22 shows this region of the spectra in a more appropriate scale.

As mentioned before, the shapes of the two spectra for wavelengths below 650 nm of samples with 300 nm-thick SRO are noticeably similar, but seem to be shifted around 50 nm. Their difference to the respective emission detected from 30 nm-thick SRO samples is undoubtedly due to optical reflection and interference phenomena, which is important for this wavelength range in the samples 300 nm-thick, as previously mentioned. These phenomena also accounts for the shift between the 300 nm-thick samples visible in the figure 2.22, as there is a thickness difference $\sim$ 50 nm (see figure 2.20). All this indicates that the emission with wavelengths shorter than 650 nm can be considered to have the same origin in all systems, namely, the centres related to the presence of nitride listed in the section 2.6.2.

On the other hand, Bi-SiO$_2$-II$_{30nm}$ Bi-PECVD-II$_{30nm}$ present the same spectra almost exactly as can be observed in figure 2.23. The XPS results already indicate that the materials are remarkably similar despite of the fabrication differences, and the PL results are very well consistent to this, confirming the dominance of the Si implanted in the final characteristics of the material regardless of the pre-implanted oxide matrix, at least if the implant is tuned to be even along it all. Optical phenomena is expected to have no influence in 30 nm-thick SRO samples, unlike in the 300 nm-tick samples.

In the Bi-SiO$_2$-II$_{300nm}$, the PL is expected to be originated in the implanted zone, and not in the rest of the SiO$_2$ matrix, in which marginal XS$_{Si}$ and no Si$^0$ bonds were found (see tables 2.7 and 2.8;) otherwise, a much higher intensity would be expected, as it is the case of Bi-PECVD-II$_{300nm}$, in which the whole PECVD-SRO matrix clearly dominates the emission as indicated by the fact that the two orders of magnitude thicker SRO layer matches the two orders of magnitude higher intensity, although the current information does not allow to establish a reliable conclusion regarding the intensity-SRO thickness relation.

Regarding the emission coming from the PECVD-SRO matrix of sample Bi-PECVD-II$_{300nm}$, the obtained material characteristics expectedly match the PL behaviour. The figure 2.24 shows the two-band PL decomposition for the SRO emission region. The first band PL$_1$ is centred around 773 nm (1.6 eV), which is the value that all PECVD samples with deposition power of 0.5 W/cm$^2$ presented for defect-related luminescence; and the second band PL$_2$ matches the QC model described by the equation 2.6 proposed in section 2.5, since the XPS results delivered a proportion of Si$^0$ in the middle of the PECVD-SRO layer of around 3.65 %, and the model predicts a PL band centred around 1.47 eV for this value under the conditions indicated in figure 2.13, as compared to the 1.48 eV (835 nm),
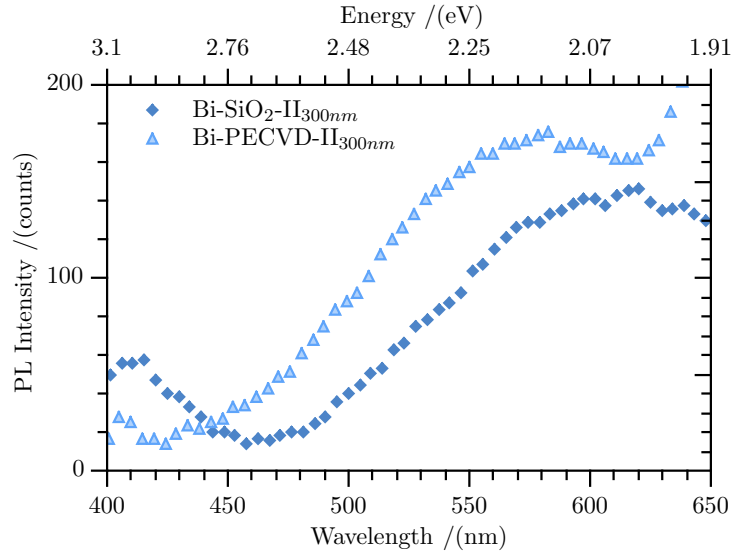
Figure 2.22: Nitride-related PL region for the samples listed in 2.7 with 300 nm-thick SRO.
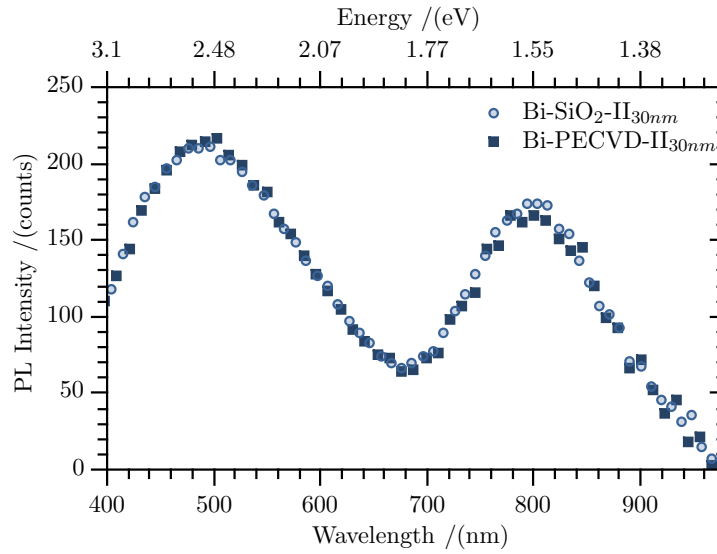


Figure 2.23: Comparison of PL from bi-layer samples with 30 nm-thick II-SRO. The spectra are remarkably similar despite the original oxide matrix being PECVD-SRO in one case (squares) and thermal SiO$_2$ in the other (circles).
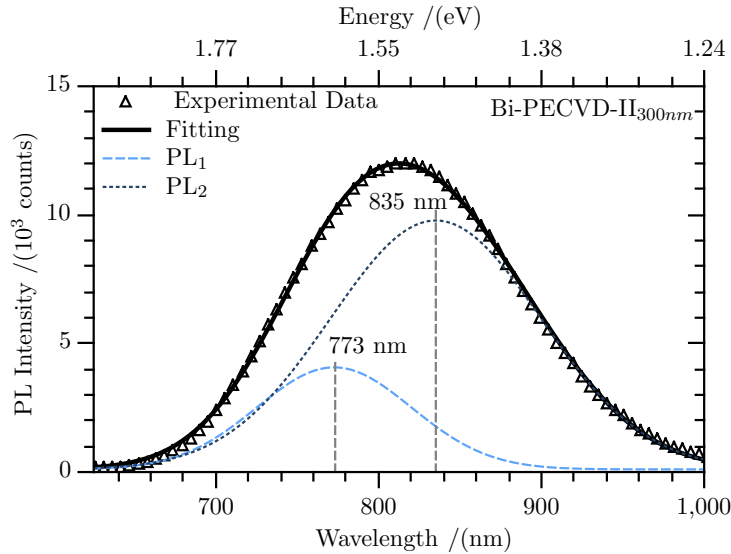
Figure 2.24: Multi-peak fitting of the SRO-related PL region of sample Bi-PECVD-II$_{300nm}$. The results match the defect-QC combined PL model proposed in section 2.5.

in which the fitted PL$_2$ is centred.

## 2.7.    Conclusions

The evidence gathered allows to conclude that luminescence in SRO is due to a combination of quantum confinement and energetic states introduced by defects related to oxygen vacancies in the material. The relative combination of these two mechanisms defines the final and usable spectrum. It is known that size and distribution of nanoparticles, in which the quantum confinement takes place, can be controlled by the parameters of the different fabrication techniques, but the defect-related contribution presents less flexibility and controllability.

The results from the structural analysis were possible to explain using the core-shell model (based on the Intermediate Model) for the used range of fabrication techniques and parameters.

It was shown that the silicon excess is a good enough variable for some simple comparisons between materials, but not sufficient to define it, particularly when analysing its emissive characteristics. A better alternative, based on the proportion of the oxidation states of the silicon atom is proposed, which uses XPS as main tool.

It was found that as more indication of silicon agglomerates is in the

material, the quantum confinement contribution to PL becomes clearly the dominant factor, to a point in which it is reasonable to assume that all the emission is controlled by the nanoparticles and the defects are not important. This, however, must be validated by the QC model, which in this case was limited by the XPS depth of analysis. Hence, this can be only affirmed for nanoparticles with diameters below 5 nm due to the limited resources available to the development of the present study.

It was observed that the presence of a silicon nitride film on top of the SRO results in the modification of the overall emission characteristics, due to the apparition of an additional PL band. With this, the spectra of the light originated in the SRO remained unchanged in its general shape, but its intensity can be noticeably altered. The overall intensity, however, is clearly improved.

The nitride-related additional band was found to be originated in the oxynitride that exist in the transition zone between the SRO and the $Si_3N_4$, and by a variety of radiative defects related to nitrogen dangling bonds and oxygen vacancies. The wavelength range in which this band emits (below 700 nm), makes it necessary to take additional cautions when into account optical phenomena that may alter the output spectra.

It was found that the implantation of ions does not contribute to the generation of Si agglomerates if an excess of this element is already present in PECVD-SRO, but the opposite. This was linked to an observed diminution of the N proportion, and an increase of the O atomic percentage in the implanted zone.

The results concluded that it would be worth the effort to further study the control of the nitride-related emission based on the fabrication characteristics of the double layer system, as well as its combination to the control of the emission by SRO, since even better results could be achieved if there were optimized the width of the transition zone or the proportion of its components.

# Chapter 3

# The Light Emitting Device

As mentioned in the section 1, the interest in luminescent materials based on Si and obtainable by standard IC fabrication processes is greatly related to their promising capabilities of integration to circuits. Therefore, the achievement and study of an electroluminescent device is one of the main objectives of the project.

Several previous studies were performed to light emitting devices based on SRO as initial approximations[2, 15, 47, 67, 68, 69, 70]. The first step towards an improvement in the EL characteristics so far achieved, was an extensive study of such devices already fabricated at our disposal. This labour resulted in two peer reviewed articles[2, 71] (included in the appendixes B.1 and B.2), and helped to start exploring the electro-optical behaviour of the material. But the precise knowledge on its composition, and the true influence of the overall device architecture on the output were not accessible (if even existing), impeding the generation of a full picture to allow the understanding of the mechanisms in this particular type of luminescence.

Once the photo luminescent behaviour of the materials was analysed, this chapter presents the results from electrical and electro-optical studies conducted to electroluminescent light emitting capacitors (LECs) fabricated with the same active materials and in the same runs as the samples studied in the previous chapter 2. It this, it was intended to gather information regarding the transport mechanisms, as well as finding the differences in the reasons for PL and EL.

Since information of the structural and PL characteristics from the exact same materials is available, a confident correspondence between all the results is possible. As mentioned, extensive previous studies on devices fabricated along the past years have already been performed and important results were extracted from them, but since no full records of the PL and structural characteristics of the active layers were available, this work mainly focuses on samples for which the fabrication process and stud-

ies were specifically designed to keep such records and allow the relevant correlations. Nevertheless, the previous analyses were an important part of the research, and since their direct incorporation would complicate the manuscript beyond what is necessary, they are included as the appendixes B.1 and B.2, and references are made to them when needed.

One of the conclusions extracted from the mentioned studies was that the fabrication technique is of extreme relevance in the final results of devices with similar silicon contents in the SRO. The step forward in the study of the material was then to focus on devices fabricated using ion implantation, due to the better balance obtained when using this technique between control in silicon contents during fabrication, onset voltages, and efficiencies.

## 3.1. Device fabrication

The architectures of the LECs are depicted in figure 3.1. They were obtained with the addition of a polycrystalline silicon gate on top of the active SRO and $Si_3N_4$-SRO layers, and an aluminium contact to the reverse of the substrates, which were crystalline Si wafers with (100) orientation and resistivity between 0.1 $\Omega\times$cm and 1.4 $\Omega\times$cm.

The fabrication runs were the same summarized in sections 2.1.1 and 2.1.2 (and detailed in the appendix C.1,) for the respective samples groups [$II_{0.46}$ and $II_{1.30}$] (listed in table 2.1), and [Bi-$II_{0.46}$, Bi-$II_{1.30}$ and Bi-$SiO_x$] (listed in table 2.5), removing the wafers not intended to become devices from the extra contact depositions and related steps. This way, the characteristics of the material to which PL and XPS experiments were conducted are assured to have the same characteristics as those forming part of the electro-luminescent devices. For the devices, only nominal thicknesses of 30 nm for the active layers were used, because the needed voltage to operate 300 nm-thick SRO devices would be beyond acceptable values.

Then, in addition to all the processes to which the active layers or bi-layers were submitted described in sections 2.1.1 and 2.1.2, the samples DEV-$II_{0.46}$, DEV-$II_{1.30}$, DEV-Bi-$II_{0.46}$, DEV-Bi-$II_{1.30}$ and DEV-Bi-$SiO_x$, received a deposition and doping with $POCl_3$ of 350 nm of polycrystalline Si (poly) to be used as the CMOS-compatible material for semi-transparent gates. The phosphosilicate formed during doping was wet etched, and the gates were defined using standard lithography and selective wet etching of the poly.

The set of masks was designed specifically for this work, and every chip included gates with six different areas: $2.5\times10^{-3}$ $cm^2$, $1\times10^{-2}$ $cm^2$, $2.25\times10^{-2}$ $cm^2$, $4\times10^{-2}$ $cm^2$, $6.25\times10^{-2}$ $cm^2$ and $9\times10^{-2}$ $cm^2$. For each area, circle-shaped and square-shaped gates were fabricated in order to verify if significant modifications in behaviour existed, which were not gen-
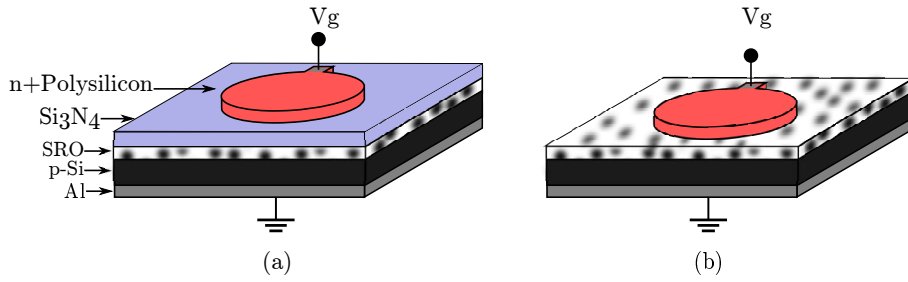
Figure 3.1: Schematic of the LEC stack structures for (a) bi-layered and (b) single-layer devices. The active layers ($Si_3N_4$-SRO and SRO) present the same characteristics as the "Bi-II" and "II" samples reported in the chapter 2.

erally observed.

A film of aluminium with a thickness of 1 $\mu$m was deposited in the back of the wafers, and in order to obtain an ohmic contact, all of them (including those that were not intended to be devices and reported in previous sections) received a boron ion implantation in the reverse, and a further 300 ℃ annealing for 30 min to activate the impurities. Finally, the aluminium for the contacts in the gates was deposited, and their areas defined by photo lithography and metal etching.

The structure and characteristics of the devices is summarized in the table 3.1.

Table 3.1: Labels and stack-structure from gate to substrate of the samples containing the electroluminescent devices studied in this section.

| Sample | $XS_{Si}$ in SRO /(at. %) | Stack Structure |
|---|---|---|
| DEV-$SiO_x$ | -1.37 $\pm$ 0.30 | Poly-$SiO_x$-Si |
| DEV-II$_{0.46}$ | 0.46 $\pm$ 0.02 | Poly-SRO-Si |
| DEV-II$_{1.30}$ | 1.30 $\pm$ 0.48 | |
| DEV-Bi-$SiO_x$ | -1.37 $\pm$ 0.30 | Poly-$Si_3N_4$-$SiO_x$-Si |
| DEV-Bi-II$_{0.46}$ | 0.46 $\pm$ 0.02 | Poly-$Si_3N_4$-SRO-Si |
| DEV-Bi-II$_{1.30}$ | 1.30 $\pm$ 0.48 | |

## 3.2. Experimental details

This section presents the details on the experimental procedures, set-ups, and equipment used to characterize the electro-optical behaviour of the fabricated devices.

### 3.2.1. Electroluminescence Spectra and Current/Voltage data

Electroluminescence (EL) is, as well as PL, the emission of light as result of energy conservation when electrons relax from higher to lower energy states. In this case, the initial stimuli for the electron to reach such higher energy state is mediated by the application of a voltage to the material.

It has been shown that electroluminescent devices fabricated with materials similar to the here studied can change their electro-optical behaviour suddenly while operation[69]. This means that if current-voltage ($I - V$) measurements are not gathered simultaneously with EL results, a further correlation could be misleading or lacking information. Because of this, for the present work the experiments were designed to register simultaneous readings of voltage, current, and electroluminescent response.

The figure 3.2 shows the experimental set-up assembled to obtain the data for the electroluminescent behaviour of the devices.

An optical fibre was used to transmit the emitted light to the spectrometer Ocean Optics QE6500 (the same used for PL as described in the section 2.2.2). A software was programmed in LabVIEW to allow the simultaneous stimulus-reading of current and voltage trough GPIB communication with the source-meter Keithley 2430, and registering of EL spectra trough USB communication with the Ocean Optics QE6500 spectrometer. As in the PL measurements, all spectra were corrected to the responsivity of the instrument.

A PCO Pixelfly VGA camera adapted to a microscope was used to monitor the devices and capture images.

### 3.2.2. Current-Voltage relation

As mentioned, a register of the voltage value for each applied current was performed during the characterization of the luminescent spectra previously described. This information was used to obtain $I - V$ relations while knowing the emission characteristics of the devices.

To complement these, and in order to analyse the carrier transport in the devices at lower current values, as well as when controlling the voltage and not only the current, a Semiconductors Parameters Analyser (SPA) HP 4155B was used to sweep the applied voltage to the devices from 0 V and using steps of 10 mV while measuring the current.
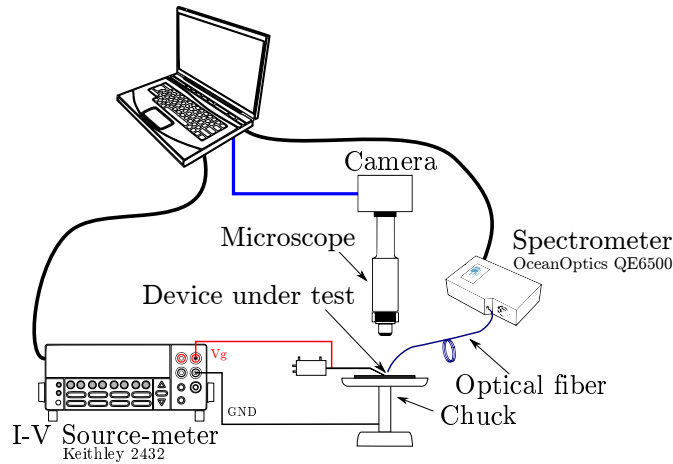
Figure 3.2: Schematic of the experimental set-up used to obtain EL spectra, I-V information, and images.

These experiments were performed in dark conditions, using a similar set-up as the depicted in the figure 3.2, but without any optical-characterization equipment and replacing the source-meter with the SPA. In this work, the units in which the current-voltage measurements are presented are current density and electric field, as calculated using the areas of the gates and thicknesses of the active layers of the respectively characterized devices.

### 3.2.3. Power and efficiency

To characterize efficiency and the general relation between radiation power and electrical stimuli, the set-up presented in the figure 3.2 was modified substituting the microscope and camera by a power meter Newport 1931-C with a sensor Newport 918D-UV-OD3 as illustrated in the figure 3.3.

The spectra-measurement part of the system was also removed to approach the detector as much as possible to the wafer. To calculate the value of emission power of the devices, the responsivity spectrum of the sensor and the particular EL spectra previously obtained for each sample were considered.

In order to approximate as much as possible to the real characteristics of the emitted light, and to be able to compare results from different gate areas, an estimation of the total emission was made based on the assumption that it is all evenly distributed along the gate area, an that it follows the cosine law of Lambert. Details on the mathematical treatment of the data are presented in the appendix B.2 (reference [71]).

The software programmed was also able to simultaneously control the

Figure 3.3: Schematic of the experimental set-up used to obtain EL power simultaneously with I-V data.

source-meter and the power meter. It is worth mentioning that the same software was used to control a motorized chuck, in order to perform various measurements to several devices along the wafer, to gather statistical information and verifying the behavioural uniformity.

## 3.3. Electroluminescence behaviour

### 3.3.1. EL type and Spectra

It is known that EL can manifest in SRO based LEC-type devices in at least two different ways, namely bright dots (D-EL) and full gate area illumination (FA-EL)[69]. The mechanisms for each can be different, and the $I-V$ relation is in general strongly related to the EL type. Since the emission is expected to be related to the carriers transiting the material, the stimuli to the devices was done controlling the applied current (and not voltage), guaranteeing control over the carrier flow regardless of material resistivity or conduction mechanism.

All the bi-layer samples presented FA-EL in reverse polarization (positive voltage in the gate), while from the single SRO layer devices, only DEV-II$_{0.46}$ presented this type of EL, but exclusively for voltages below 33 V (electric field of $1.18\times10^{-7}$ V/cm). An image of this is presented in figure 3.4. For higher fields, luminescent dots start to randomly appear, and resistivity dramatically variates as they do. If the current is further increased, or kept constant for some time, eventually all the EL becomes D-EL, but FA-EL and D-EL can coexist under given conditions. The figures 3.5a and 3.5b show this case. In the figure 3.5a, the voltage in which only FA-EL

$$J = 12 \times 10^{-2} \text{ A/cm}^2$$
$$V = (34 \pm 1) \text{ V}$$

Figure 3.4: Device from sample DEV-II$_{0.46}$ with square gate and area of $2.5 \times 10^{-3}$ cm$^2$ (500 $\mu$m $\times$ 500 $\mu$m) under full area EL operation. If the voltage is further increased, bright luminescent dots start appearing.
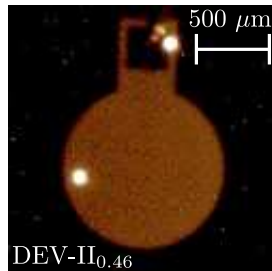


(a)
$$J = 1 \text{ A/cm}^2$$
$$V = (43 \pm 1) \text{ V}$$
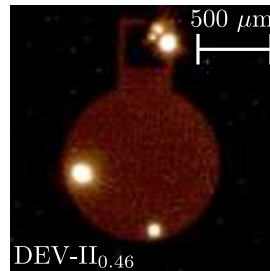
(b)
$$J = 4 \text{ A/cm}^2$$
$$V = (43 \pm 1) \text{ V}$$

Figure 3.5: Device from sample DEV-II$_{0.46}$ with round gate and area of $2.5 \times 10^{-3}$ cm$^2$ under operation with coexistence of D-EL and FA-EL. It can be observed that for the same voltage, an increase of four times the current density occurs with the apparition of a bright dot in the bottom of the gate.

61

is observed has been overcome and both types of EL are present, and the equivalent resistance has decreased. If the applied current is increased after such change, more bright dots start to appear, accompanied by a clear diminution of the FA-EL intensity (figure 3.5b), since more carriers pass trough the preferential conductive paths[69, 72] and simply do not reach the radiative centres responsible for FA-EL, as will be discussed later.

Regarding the other single layer samples (DEV-II$_{1.30}$ and DEV-SiO$_x$), no FA-EL was possible to unambiguously identify, and when operation currents achieved, D-EL was the only luminescence manifestation present at high-current regime values regardless of stimuli polarization.

The figure 3.6 shows the spectra for the D-EL of the three mono-layer samples. Care was taken to assure that D-EL was clearly dominant in sample DEV-II$_{0.46}$. Unlike in PL from the same active layers, the three spectra are remarkably similar. It is worth recalling that wile D-EL is found in DEV-SiO$_x$, no PL was found in its only active material sample counterpart, nor any SRO-related luminescence in the bi-layer samples based on SiO$_x$ (see figure 2.17).

The remarkable similitude in the D-EL spectra suggests that the mechanisms are the same among all the single-layer samples, but differentiated from those of PL, which spectra were clearly different in the three materials. This D-EL radiative centres seem not to be influenced at all by the variation of SRO characteristics within this range.

Electroluminescence with these characteristics was also observed by Di-Maria in similar materials, and attributed to the silicon dioxide rather than agglomerates[73]. More recently, it has been demonstrated that the emission can be changed from D-EL to FA-EL applying a voltage strong enough to override the conductive paths that cause the localized stimulus of specific radiative centres[46, 69]. In this case, this was not possible to achieve, and physical destruction of the pads was reached before annulment of the emission centres. The EL in this case is most likely due to carriers transitioning from the conduction band of the oxide to that of the substrate, a mechanism that is triggered by applying an electric field and not optically, which explains why this band is not present in PL. (The energetic band structure will be presented in the section 3.5 and presented in the figure 3.14).

In general, the results show that devices with single SRO films present poor characteristics regarding their reliability in terms of needed stimuli and electroluminescence, since D-EL is random in its positional origin and power consumption. This implies a serious disadvantage regarding the prospective applications, since there is very low control on the emitted light for its further use.

On the other hand, the bi-layer devices DEV-Bi-SiO$_x$, DEV-Bi-II$_{0.46}$ and DEV-Bi-II$_{1.30}$, present an evenly distributed FA-EL. The figure 3.7
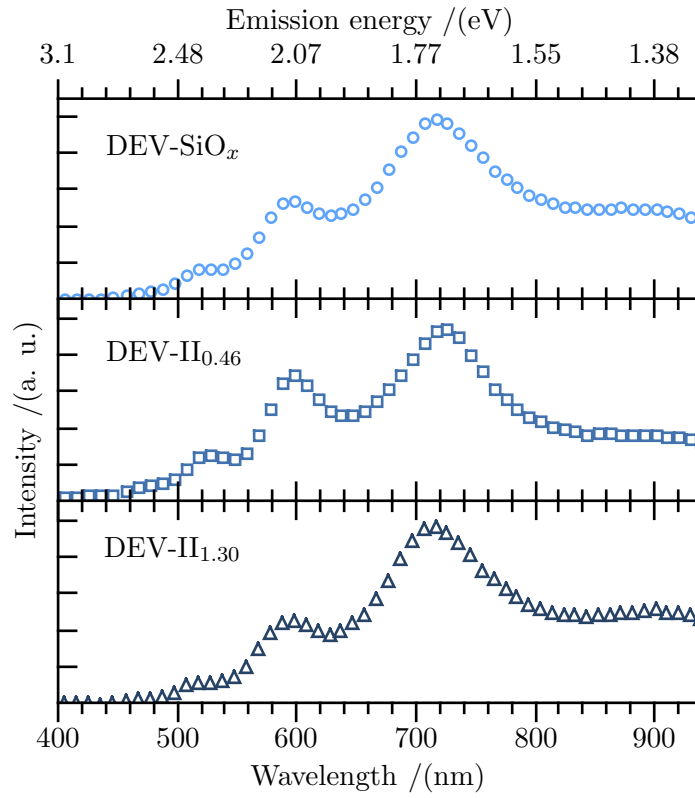
Figure 3.6: Normalized luminescence spectra of mono-layer devices at applied voltage values in which only D-EL is obtained.

shows the normalized FA-EL spectra for each, and images of the operating devices are shown in the figure 3.8.

The naked-eye visible color difference is well reflected in the graphs. The shapes of the EL spectra are noticeable different from those of PL (compare the figures 2.18 and 3.7), as the latter present periodic-like peaks typical of interference phenomena in the multi-layer system. A very good modelling work published by Juvert *et al.*[63] confirmed indeed that this is the case.

With a simple visual comparison of the figures 3.5b and 3.8b, it is clear that the presence of the nitride layer significantly improves the behaviour of the devices in the homogeneity of the distribution of the light. It is also present in all three fabricated samples, which emit with different colour each, clearly depending on the fabrication parameters, as opposite to the emission by bright dots.

There is a noticeable improvement in the efficiency of the devices as well, which will be addressed in detail later in section 3.4, but just from comparing the images 3.5 and 3.8, it can be seen that for the same voltage order, a current density around three orders of magnitude lower is necessary to obtain a clear picture of the emission for the bi-layered devices.

### 3.3.2. Influence of the transmittance

It is possible to use an experimental approach to verify if PL and FA-EL are originated by the same radiative centres despite they being excited in different ways[43], and if the differences observed in the spectra arise from the influence of the transmittance of the system, defined as the ratio between the EL and the PL spectra.

Assuming that the radiative centres that participate in EL and PL are the same, a transmittance spectrum can be defined trough the expression:

$$I_{EL(\lambda)} = I_{PL(\lambda)} \times T_{(\lambda)} \tag{3.1}$$

Where $I_{EL(\lambda)}$ is the intensity of the detected EL emission of a device for a given wavelength $\lambda$, (which would be modified by the transmittance;) $I_{PL(\lambda)}$ is the intensity of PL from the correspondent active layers at the same wavelength, (which should be the intrinsic emission;) and $T_{(\lambda)}$ is the modifying transmittance spectrum, defined by the characteristics of the structure and material.

Considering that all the spectra of PL and EL are different, and ruling out the variations in refractive index of SRO with different $XS_{Si}$ (which are lower than 3.3 % as measured by ellipsometry tests, and have no significant influence according to optical models[63]), if the same radiative centres are responsible both EL and PL indeed, then $T_{(\lambda)}$ should be the same for all the devices despite presenting different spectra for a same stimulus method, since they all present the same stack structure configuration.
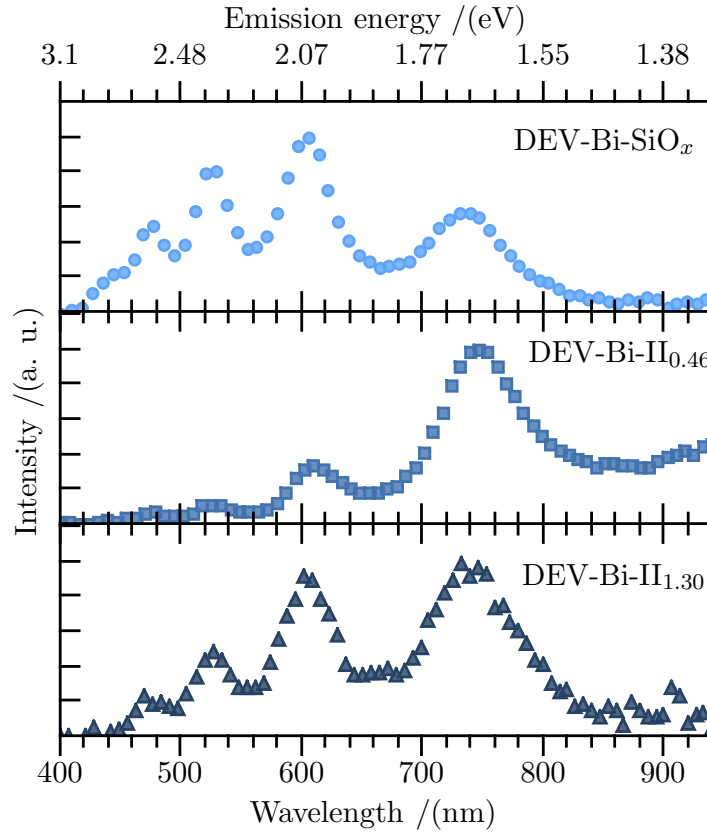
Figure 3.7: Normalized FA-EL spectra of bi-layer devices. The shapes did not show significant change as the intensity increases with applied current. The shape or area of the gate neither sowed influence.



(a)
$J = 2 \times 10^{-2}$ A/cm$^2$
$V = (52 \pm 1)$ V

(b)
$J = 2 \times 10^{-2}$ A/cm$^2$
$V = (54 \pm 1)$ V

(c)
$J = 2 \times 10^{-2}$ A/cm$^2$
$V = (47 \pm 1)$ V
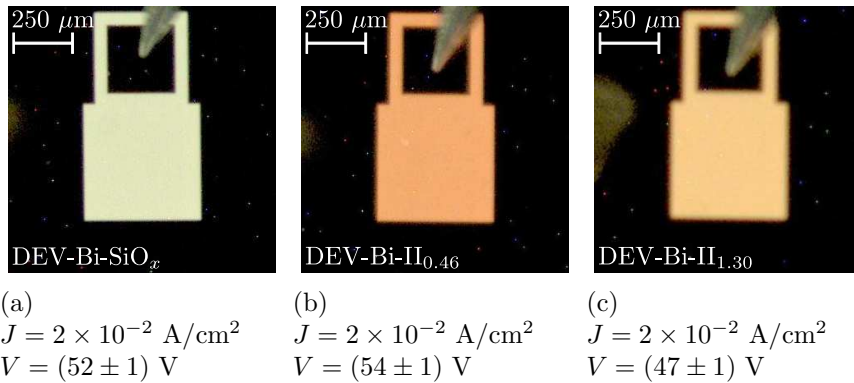
Figure 3.8: Bi-layered luminescent devices with area of $2.5 \times 10^{-3}$ cm$^2$ (500 $\mu$m $\times$ 500 $\mu$m) under operation. The probe used to apply the current of $20 \times 10^{-3}$ A/cm$^2$ can be observed on the pad on top of the image.

Notice that $T_{(\lambda)}$ would also account for possible differences in the contribution to the total light emitted by centres when stimulated electrically or optically, that is, it would consider not only the same optical phenomena, but also that the possible differences between EL and PL in recombination rates due to particular radiative centres, would be the same in all samples regardless of material differences.

Considering all this, $T_{(\lambda)}$ can be calculated for each couple of samples (device and active layer) using the expression:

$$T_{(\lambda)} = I_{EL(\lambda)}/I_{PL(\lambda)} \tag{3.2}$$

If the $T_{(\lambda)}$ is equal for all the samples, then it can be considered that the radiative centres for EL and PL are the same.

The result of the average of the three calculated transmittances (for $SiO_x$, $II_{0.46}$ and $II_{1.30}$) is represented with solid symbols in the figure 3.9. The calculi were performed using the non corrected spectra for both PL and EL, since the factors are the same in both cases, and the correction would only introduce error. Then, the error bars are produced by the differences in the average values. The deviation is always below 10 % for the plotted range of wavelengths (from 400 nm to 770 nm). This, along with the simulations reported in [63], suggest that within these boundaries, the observed differences in EL and PL are likely to be caused by optical phenomena, and not the stimulation of different radiative centres.

Some important considerations must be stated regarding the definition of the range in which the resultant transmittance spectra are valid. The intensity of EL observed for wavelengths shorter than 400 nm is too small as to be able to consider reliable the calculi below that point. On the other extreme of the plotted spectra, as PL intensity decays, the $I_{EL(\lambda)}/I_{PL(\lambda)}$ ratio increases. This means that the error of the obtained transmittance also increases as PL diminishes, and this limits the reliability of the calculation for the higher $\lambda$. Hence, the upper limit for the reliable spectra can be considered to be 770 nm, since above this value the average error between three calculated transmittance curves surpasses 10 %.

A polisilicon layer was deposited on a quartz wafer by the exact same process as that of the gate described in section 3.1, in order to verify the transmittance of a single layer of the gate material. This was obtained using a deuterium tungsten white light source (Ocean Optics DH-2000) and the spectrometer. The spectrum of the light obtained when passing trough the poly on quartz was divided by that obtained when passing trough a reference quartz wafer.

The results are presented as the dashed line in figure 3.9, and as can be observed, are significantly different from the $T_{(\lambda)}$ calculated, confirming that the effects caused by the multi-layer structure are of great importance to the final observed and/or used light, and that an inappropriate consid-
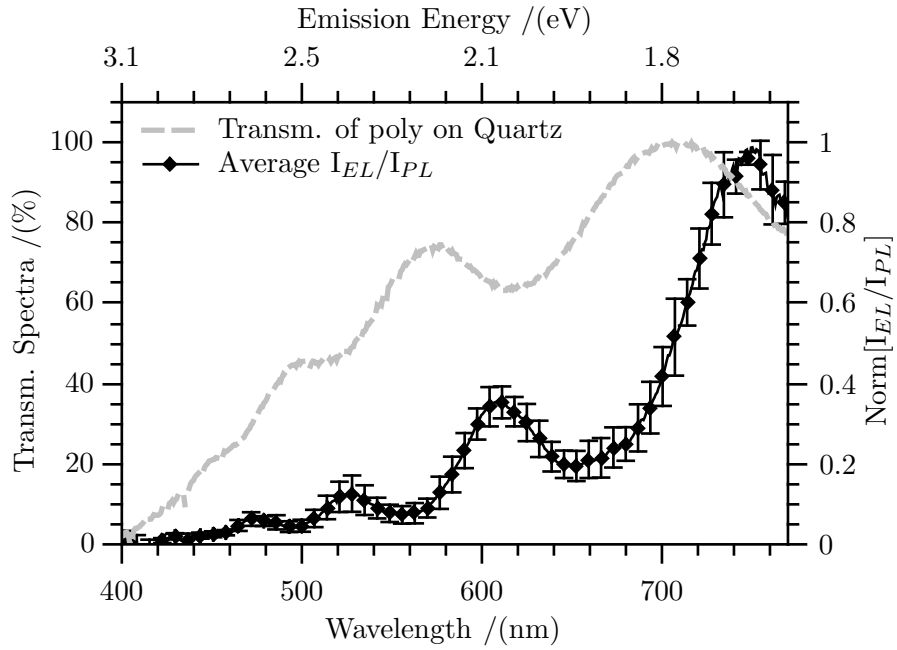
Figure 3.9: Transmittance for a 350 nm-thick poly layer fabricated under the same conditions as that used for the devices gates is also presented (dashed line) and transmittance of the multi-layer systems obtained calculating the average of the ratios of PL and EL for each bi-layer sample accordingly to equation 3.2 (symbols). The error bars are the deviation values from the average of the three samples.

eration of them, as it is only to consider the transmittance of the single-standing gate material, can deliver wrong information regarding the true nature of the luminescence extracted from EL measurements. It is worth noting that no changes were observed in the normalized FA-EL spectra when varying the applied current from 0.1 to 30 mA/cm$^2$, meaning that the transmittance of the poly does not show variation with current changes in such range.

Summarizing, Bi-layer samples present FA-EL while single layer only for the lowest $XS_{Si}$ and for a very constrained voltage operation range. The D-EL presented very similar emission spectra in all single layer samples, while those of FA-EL match the changes found in PL, concluding that the electroluminescence spectra between 400 nm and 720 nm can be constructed trough the application of one common function to the different PL spectra, regardless of the silicon excess of the material, indicating it depends on the architecture and suggesting that both types of luminescence are due to the stimulus of the same radiative centres despite the excitation techniques being different. The possibility of this being true for a wider range of wavelengths cannot be ruled out, but evidence to assure it is beyond the reach of the available instruments.

It was found that in general, bi-layer devices not only present better results, but their architecture was the only among those studied that delivered usable results without further processing or excessively narrow voltage and/or current operation ranges.

## 3.4. Radiant Power and Efficiency

### 3.4.1. Current - Radative Power relation

The figures 3.10 and 3.11 show the average relation between the radiant power $\Phi_e$ and the applied current for the devices measured along each wafer. Note that the currents to achieve similar radiant powers are three orders of magnitude lower for bi-layer samples. The error bars in these graphs arise from the variations within the results from different devices of a single wafer, since for each, generally five LECs were characterized.

As it can be observed in the figure 3.11, the bi-layer samples present a much lower error, confirming their higher result repeatability as compared to the mono-layer devices presented in the figure 3.10, the behaviour of which vary significantly more from device to device, mainly due to the random nature of the bright dots manifestation; in particular, devices from sample DEV-II$_{0.46}$ presented the highest variation.

This lack of repeatability in the mono-layer devices, caused by the mere nature of D-EL, provokes that the errors are too big to identify any conclusion from the plots. However, in the case of the bi-layer samples, an

Figure 3.10: Average Optical Power vs. Current Density plots for samples DEV-SiO$_x$, DEV-II$_{0.46}$ and DEV-II$_{1.30}$ under D-EL operation. The error bars arise from the variations within different measured LECs for the same wafer.
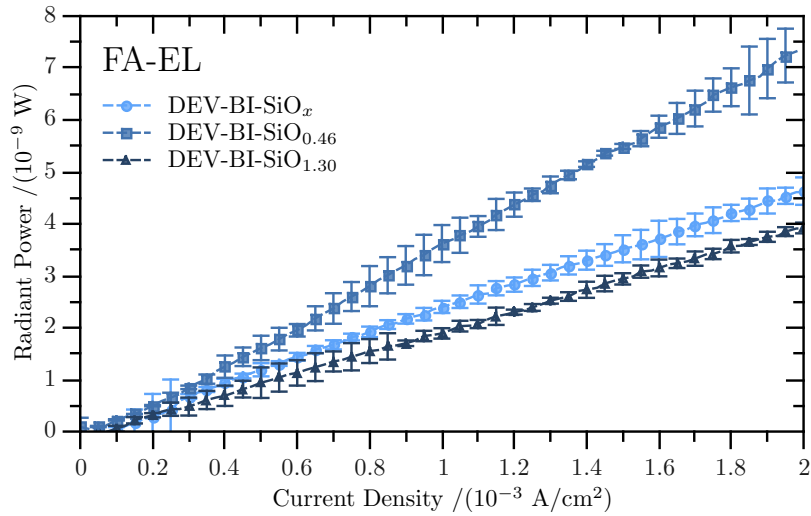


Figure 3.11: Average Optical Power vs. Current Density plots for samples DEV-Bi-SiO$_x$, DEV-Bi-II$_{0.46}$ and DEV-Bi-II$_{1.30}$ under FA-EL operation. The error bars arise from the variations within different measured LECs for the same wafer.

important result from the $\Phi_e$ vs. $J$ plots its that the relation is linear, which indicates that the EL is dominated by recombination of electron-hole pairs, rather than related to impact ionization[37]. This is consistent to the EL spectra results analysed in the previous section, which as mentioned, did not show any variation in the shape with increasing applied voltage, corroborating that the EL is controlled by current. The influence of the electric field is then limited to its impact on the carrier transport.

### 3.4.2. Efficiency

The conversion efficiency of the devices $\eta$ is defined as:

$$\eta = \frac{P}{\Phi_e} \tag{3.3}$$

Where $P$ is the applied electric power. The figures 3.12 and 3.13 present the relations between the applied current density and the conversion efficiency of the mono-layered and bi-layered devices, respectively.

As it can be observed, and as it is expected after examining the radiation power characteristics, the efficiency results for mono-layer devices (with D-EL) were very erratic as well, showing increments and decrements due to the appearing and disappearing of the bright dots, which change from device to device of a same wafer. Note the unacceptably large error bars in the figure 3.12, which reflect the great differences among the five devices measured for each sample.

On the other hand, and consistently to the observed results so far, bi-layered samples did present repeatable behaviour for all the devices studied of a same sample, as can be noted from the error bars in the figure 3.13. The erratic behaviour of the mono-layered samples does not allow to identify any trend, and it is only possible to stablish a range of values in which the efficiencies can be found. The better behaving bi-layered samples present efficiencies that, in general, show a very fast increment as the current starts to rise, then reach a maximum and begin a decreasing trend to further stabilize until failure of the device. These maximum values, found at currents lower than $1 \times 10^{-3}$ A/cm$^2$ in all cases, are obtained because some EL is detected for very low applied electrical powers. However, this ideal maximum efficiency operation point may not be the best option depending on the application, since the emission may be too low to be used. For instance, to observe EL with the naked eye, the device must work at significantly higher currents and lower efficiencies; the images presented in figure 3.8 were obtained applying a current density $J = 2 \times 10^{-2}$ A/cm$^2$, one order of magnitude higher than the value of maximum efficiency. Nevertheless, there are still applications in which not such a high intensity may be needed, for instance, inter chip light-based communications, in which very short distances between emitter and receiver, as well as external light

70
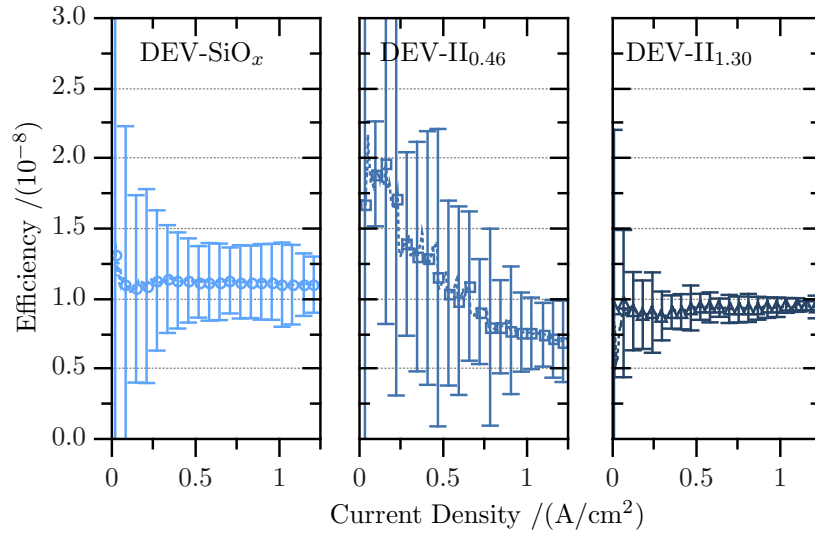
Figure 3.12: Average Efficiency vs. Current Density plots for the devices that presented the highest efficiency values of samples DEV-SiO$_x$, DEV-II$_{0.46}$ and DEV-II$_{1.30}$. This devices presented D-EL, and the averaged values were those before breaking of de device.
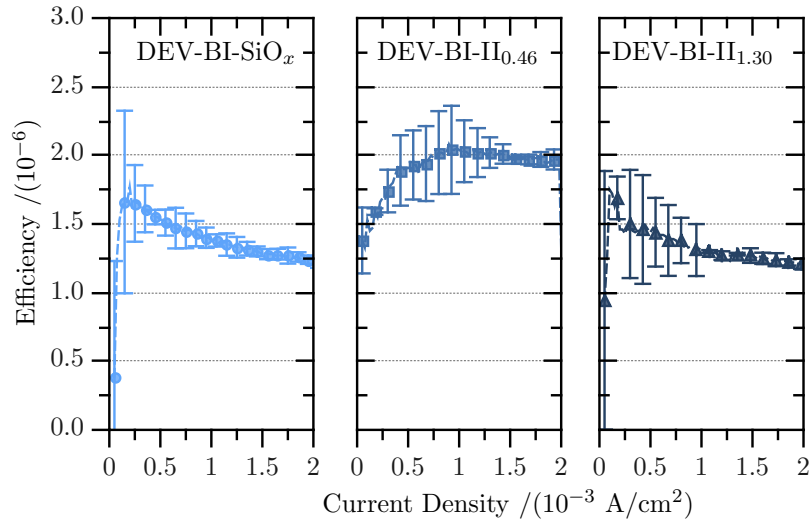


Figure 3.13: Average Efficiency vs. Current Density plots for samples DEV-Bi-SiO$_x$, DEV-Bi-II$_{0.46}$ and DEV-Bi-II$_{1.30}$ under FA-EL operation. Symbols are experimental data, the discontinuous lines are to guide the eye.

isolation, could theoretically need radiation powers matching those in the range of the maximum efficiency.

The table 3.2 displays the average values for the maximum efficiencies $\bar{\eta}_{max}$ of all samples, as well as the maximum radiant powers and current densities at such operation point ($\Phi_{e_{\bar{\eta}_{max}}}$ and $J_{\bar{\eta}_{max}}$, respectively). The radiant power at the maximum efficiency points is in the same order of magnitude for all samples, but the efficiency of bi-layers is at least two orders of magnitude higher, and the highest is presented by the sample DEV-II$_{0.46}$, for which the structural analysis revealed the highest contribution by Si$^0$ states (or Si agglomerates) of the three compared in this section (see the figure 2.8 of the section 2.3).

Despite the already proven presence of different radiative centres introduced by the presence of the silicon nitride film, the improvement in efficiency in dual layers is clearly dominated by a reduction of the needed power to reach a given EL intensity, ruled by the injection of carriers. The transport of carriers in the devices will be discussed in detail in section 3.5.

The voltage values at the $J_{\bar{\eta}_{max}}$ are of the same order of magnitude as will be shown in the section 3.5, but note in table 3.2 how such current is nearly two orders of magnitude lower for bi-layered devices. The dominance of the injection improvement on the better efficiency results was also observed when analysing mono-layer devices fabricated previously, with such results reported in [71], included in appendix B.2. No trend is objectively possible to stablish for silicon contents (or [Si$^0$]) among the studied values, as all are in the same range and within the error margins. However, the results seem consistent to the projection of the trend described in the figure 4 of the appendix B.2[71], in which mono-layer devices with $XS_{Si}$ values below 6 at. % should present efficiencies lower than $2\times10^{-7}$. Then, the introduction of the nitride layer really results in an improvement of at least two orders of magnitude for this silicon contents ranges.

The comparison between the efficiency of the here reported devices to that of other similar is not a simple task. In general, very few details are given regarding the experimental procedure and corrections considered to obtain the values in the literature, and the type of EL (whether D or FA) is rarely mentioned, hence the reported quantities are not as reliable as one would like[71, 74]. In recent works, devices with multiple layers of SiN$_x$ and SiO$_x$ intercalated, and Indium Tin Oxide (ITO) gates, reportedly presented conversion efficiencies of around $10^{-6}$[37]. Such result is of the same order of the here reported, even when the ITO generally has better transmittance for the emission wavelengths of the material[75] (not to mention that is not a standard CMOS material); additionally, the operation voltages were between 200 V and 300 V, while the here studied devices always operate under 60 V, and at voltages from 39.3 V to 46.3 V for the $J_{\bar{\eta}_{max}}$. Other authors report operation voltages as low as 1.7 V, and efficiencies of the order of

Table 3.2: Average maximum efficiency values and EL type for the Electroluminescent devices and the respective radiative powers and current densities. $\bar{\eta}_{max}$ is the average maximum efficiency, $\Phi_{e_{\bar{\eta}max}}$ the average radiant power at average maximum efficiency, and $J_{\bar{\eta}max}$ the average current density at maximum efficiency.

| Sample | $\bar{\eta}_{max}$ | $\Phi_{e_{\bar{\eta}max}}$ /$(10^{-9}$ W) | $J_{\bar{\eta}max}$ /$(10^{-3}$ A/cm$^2$) | EL Type |
|---|---|---|---|---|
| DEV-SiO$_x$ | $(1.40\pm0.45)\times10^{-8}$ | $0.14 \pm 0.06$ | 22.5 | |
| DEV-II$_{0.46}$ | $(2.17\pm0.16)\times10^{-8}$ | $1.33 \pm 0.29$ | 50.0 | D-EL |
| DEV-II$_{1.30}$ | $(0.98\pm0.59)\times10^{-8}$ | $0.78 \pm 0.56$ | 67.5 | |
| DEV-Bi-SiO$_x$ | $(1.77\pm0.45)\times10^{-6}$ | $0.41 \pm 0.59$ | 0.2 | |
| DEV-Bi-II$_{0.46}$ | $(2.08\pm0.37)\times10^{-6}$ | $3.20 \pm 0.37$ | 0.9 | FA-EL |
| DEV-Bi-II$_{1.30}$ | $(1.75\pm0.79)\times10^{-6}$ | $0.22 \pm 0.06$ | 1.0 | |

$10^{-5}$ in devices fabricated with alternating SiO$_2$ and SRO layers[76]. This is the highest reported efficiency found in literature during the elaboration of this work, but the calculation method is not clearly explained, and in another publication referring the exact same structures, the authors report an efficiency of $10^{-6}$[77], which is illustrative of the difficulties that the lack of a detailed description when performing the treatment of the experimental data implies for the possibilities of comparing results. In any case, the efficiency of the devices studied in this work is clearly inside the ranges of most previous reports, including those of formerly fabricated by our group and reported in [71]. However, it can be concluded that the efficiency is possible to improve, likely trading off other characteristics such as emission spectra and intensity.

## 3.5. Carrier transport

In the previous extensive electrical studies included in appendix B.1[2], performed to devices based on ∼60 nm-thick mono layers of PECVD-SRO and II-SRO, which according to the available information, presented $XS_{Si}$ values from 6 at. % to 16 at. %, the transport of carriers in the material was found to be complex in II-SRO. With the obtained data, it was not possible to ascribe the conduction mechanism to a single model of the tested, namely Fowler-Nordheim tunnelling (FN), Trap-assisted tunnelling (TAT) and Poole-Frenkel emission (PF). The first two were the most likely, while PF was discarded from the unreasonable physical parameters extracted from the fittings of the data.

The figures 3.14 and 3.15 present a rough estimation of the band structure of the devices studied in this section, respectively for mono and bi-layers. These were built considering the characteristics of the ideal materials, using the electrochemical potentials as obtained from literature for $SiO_2$ and $Si_3N_4$[40], and the calculated from the donor an acceptor concentrations for the substrate and polysilicon gate.

The schemes can help in the understanding of how the carriers are transported trough the systems. The present section discusses the results of the studies related to carrier transport performed to the electroluminescent devices.

### 3.5.1. Current *vs.* Voltage Relation

When compared to the devices studied in the past (reported in the appendix B.1[2]), the mono-layer devices (DEV-II$_{1.30}$, DEV-II$_{0.46}$ and DEV-SiO$_x$) presented much higher instability, and as previously mentioned, did not allow the modification of their *I-V* characteristics with "current-jumps" to low conduction states[46, 69].

Lets first focus in the devices with a single-layer active area. The $J$ *vs.* $E_f$ behaviour of these are presented in the figure 3.16, which displays with lines the results obtained when applying voltage and measuring current with the SPA, and with symbols the data from the EL measurements gathered with the Source-Meter (presented in section 3.3). The units used are current density and electric field, and were calculated considering the gate areas and active-layer thicknesses of the measured devices.

If the devices are stimulated controlling voltage, the $J - E_f$ curve shows the characteristic discontinuity of dielectric breakdown at values around $5.2 \times 10^3$ V/cm, $4.9 \times 10^3$ V/cm and $1.8 \times 10^3$ V/cm for the samples DEV-II$_{1.30}$, DEV-II$_{0.46}$ and DEV-SiO$_x$, respectively. The difference in this behaviour as compared to that of the single layer devices studied in the past is most likely due to the fact that these presented thinner active layers with lower silicon contents reported, since the failure at such comparatively low fields can be ascribed to a higher charge build up on defects in the SRO[78]. This consistent to the trends of trapped charge variation with silicon excess reduction found in the previous devices (see figure 4 of appendix B.1[2]), because the charge in those here studied is expected to be high as compared to the former.

When analysing the *J-E* results obtained while monitoring the D-EL (symbols in figure 3.16), it is observed that in all the cases, the currents are in ranges corresponding to dielectric breakdown values, even the lowest ones. This is why in the plots for DEV-SiO$_x$ and DEV-II$_{1.30}$, when controlling the applied current, the value of $J$ for the lowest electric field (first symbol in the plot of figure 3.16 ), is higher than that measured at the same field when controlling voltage (line of the same figure), since for

(a) SiO$_2$ active layer

(b) SRO active layer
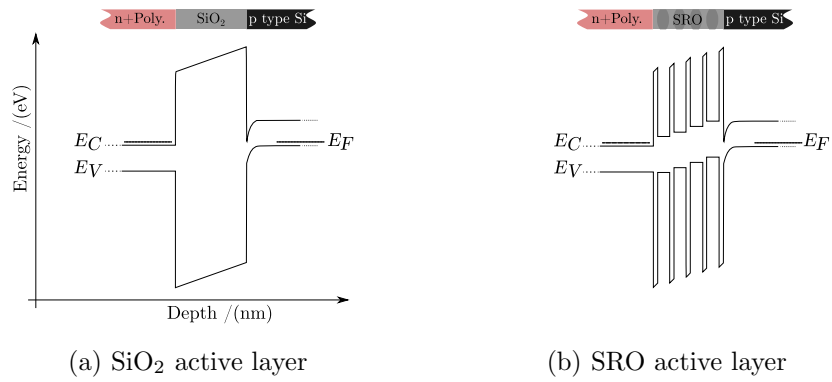
Figure 3.14: Ideal energetic band structure for mono-layered devices in thermal equilibrium.



(a) Si$_3$N$_4$-SiO$_2$ active material

(b) Si$_3$N$_4$-SRO active material
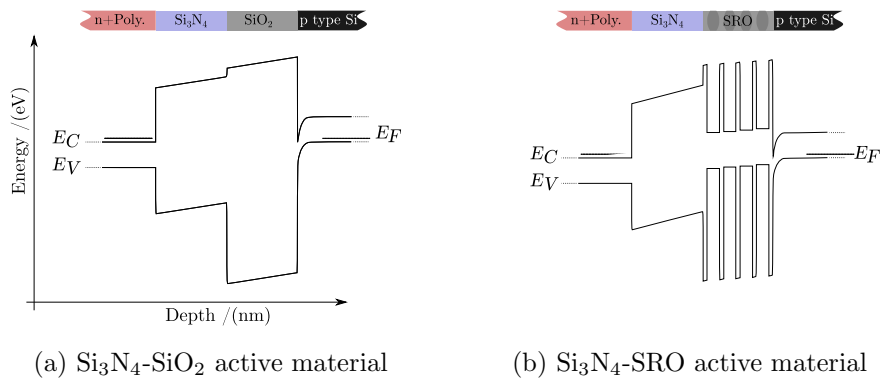
Figure 3.15: Ideal energetic band structure for bi-layered devices in thermal equilibrium.

75
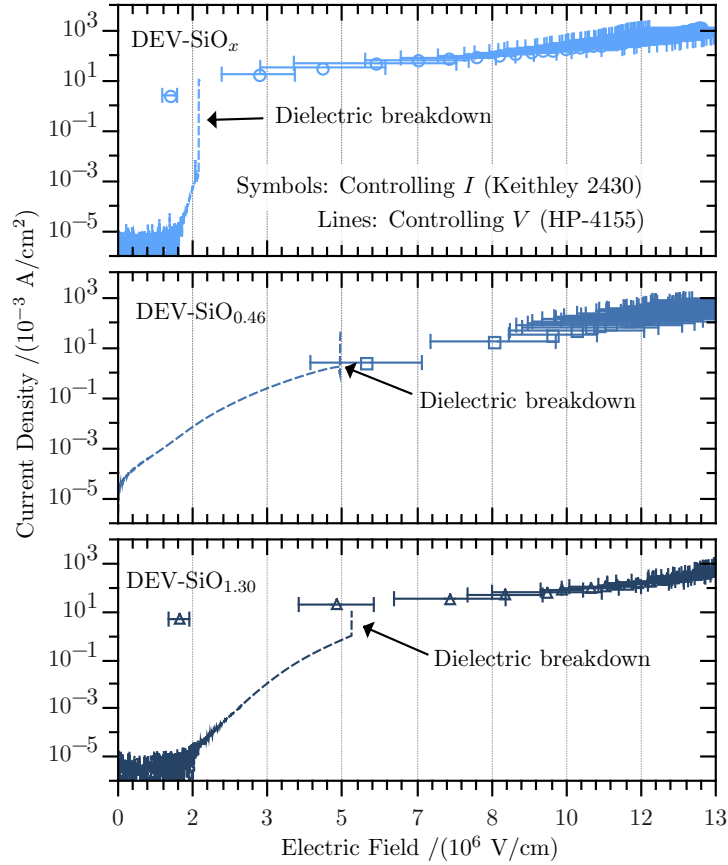
Figure 3.16: $J - E_f$ Characteristics of mono-layer devices. Discontinuous lines are obtained with the SPA applying voltage and measuring current. Symbols are obtained during the $I$-EL characterization with the source-meter, applying current and measuring voltage. The error bars arise from the error of the average of the results from 5 devices along the wafer.

the first value of applied current in the former case, the device is already in the high conduction state characteristic of breakdown.

The $J$-$E$ behaviour, as well as the built band structures, must be closely correlated to the EL of the devices. Note that the emitted wavelengths reported in the section 3.3 for D-EL found in mono-layer devices (shown in the figure 3.6) are compatible with the energetic difference between the oxide and the substrate conduction bands (schemed in the figure 3.14), suggesting that the EL may be due to the energy relaxation of carriers generated by impact ionization from the oxide conduction band to the substrate conduction band. The initial failure is probably triggered by the presence of defects, but D-EL begins to appear in ranges consistent to impact ionization, which is localized due to the generation of the specific breakdown paths known to exist in this phenomena in silicon dioxides[42].

Only the sample DEV-II$_{0.46}$ seems to present a smoother behaviour from the beginning, consistently to the simultaneous presence of both EL types reported in the section 3.3. However it does present breakdown around $5 \times 10^6$ V/cm, which would be the value after which only D-EL is observed. From the XPS studies, it is known that the SRO in devices DEV-II$_{0.46}$ present higher contribution by Si-Si links than DEV-II$_{1.30}$, which actually presented a significantly higher concentration of sub-oxides corresponding to Si$^{1+}$, Si$^{2+}$ and Si$^{3+}$ states, as can be seen in the figure 2.8 of the section 2.3. This can explain the higher similitude in the electrical behaviour between devices from samples DEV-II$_{1.30}$ and DEV-SiO$_x$.

Lets now focus in the devices with bi-layer active area. These present stable and repeatable characteristics electrically-wise, consistently to the rest of the different studies already performed. The Figure 3.17 shows the $J - E_f$ plots for such devices. In this case, there is consistency between the results when applying current and voltage (symbols and lines in figure 3.17, respectively). In bi-layered devices, the $I$-$V$ curve could be repeated in successive sweeps for fields as high as $7 \times 10^6$ V/cm, finding no material breakdown or other changes in the characteristics. In fact, noticeable destruction of the pads were obtained before clear breakdown of the active material. Remember that internal EL was proof to be the same as PL spectrum-wise, and that for bi layer samples there is a clear and distinguishable contribution by nitride and SRO, separately. Then, the inclusion of the nitride layer seems to allow the electrical excitation of the radiative centres both in the oxinitride and oxide avoiding the material breakdown.

It is clear that the presence of the nitride film helps avoiding the generation of the preferential conductive path that lead to poor behavioural consistency and D-EL. Some authors attribute the benefits from the nitride layer in carrier to the reduction of the effective field in the SRO[36], but if it was the case for the here studied devices, similar behaviour for low fields in the single-layer and the corresponding higher fields in the bi-layer

77
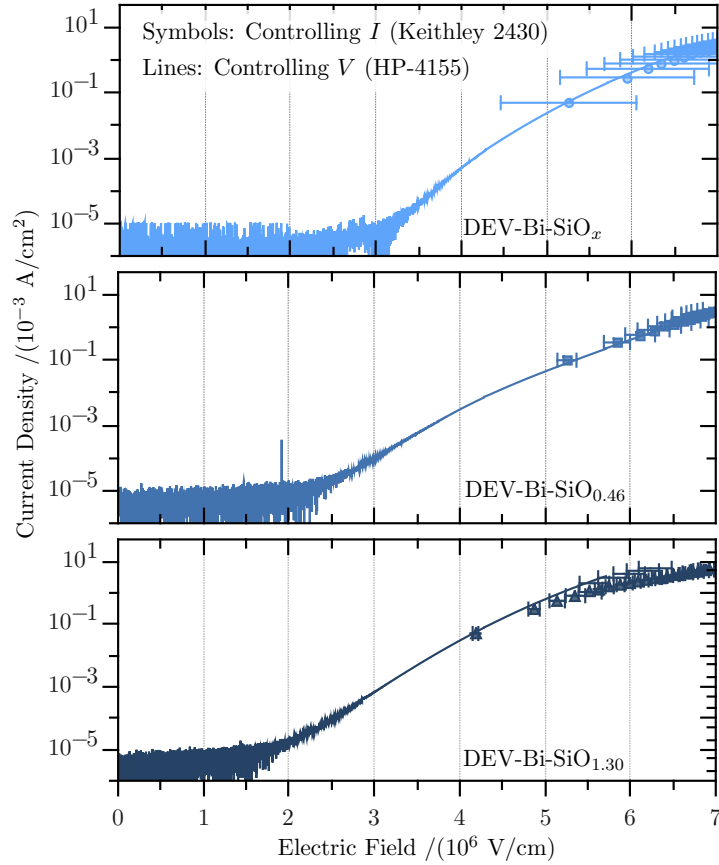
Figure 3.17: $J - E_f$ Characteristics of bi-layer devices. Continuous lines are obtained with the SPA applying voltage and measuring current. Symbols are obtained during the $I$-EL characterization with the source-meter, applying current and measuring voltage. The error bars arise from the error of the average of the results from 5 devices.

samples would be obtained, which was not observed. In this case, it is more likely related to the findings by DiMaria *et al.*, whom by performing studies on breakdown of silicon dioxide films, found that oxide degradation is related to charge generation caused by impact ionization trough the presence of interfacial defects and traps[78], concluding that nitridation of the dioxide can help preventing the material failure by reducing the hole trapping vacancies near interfaces and other trap-creation defects. This would explain the great differences found in mono and bi-layer devices, both in electrical and electroluminescent response. Indeed, benefits regarding the quality of oxides by intentional nitridation have been reported[39, 79], as well as benefits obtained by the inclusion of a nitride layer regarding transport reliability in bi-layer samples[36], which in turn translate in better EL controllability and higher efficiencies.

### 3.5.2. Carrier transport models

In order to explore the conduction mechanisms in the bi-layer devices, models of FN and TAT where used to fit the data, accordingly to the nature and thickness of the materials and structure[35, 36, 37, 38, 39], as well as taking into account the results from the studies to previous devices reported in B.1[2].

The conduction mechanisms may vary depending on the excitation field values[35]. In this case, the range of interest is that in which EL was observed. The results here reported will be restricted to this range of excitation fields.

The model for the FN mechanisms explained in the section 1.2.2 and represented with the equation 1.3, can be expressed as:

$$\ln\left(\frac{J}{E_f^2}\right) = \ln(A_{FN}) + C_{FN}\frac{1}{E_f} \tag{3.4}$$

In which $A_{FN}$ and $C_{FN}$ are defined as:

$$A_{FN} \equiv \frac{q^2 m}{8\pi h m^* \phi_B} \quad C_{FN} \equiv -\frac{8\pi\sqrt{2qm}}{3h}\left(\frac{m^* \phi_B^3}{m}\right)^{\frac{1}{2}} \tag{3.5}$$

Then, the plot of $\ln(J/E_f^2)$ *vs.* $1/E_f$, called an FN plot, should deliver a straight line if this is the conduction mechanism, and its slope would be equivalent to $C_{FN}$, from which the relation between the relative electron mass $m_r$, and the barrier height $\phi_B$, can be extracted.

If an effective barrier height $\phi_{B_{eff}}$ is defined for the bi-layer system, its value can be calculated provided the effective mass of the electron is known. The obtained value must be one within a reasonable range defined by the boundaries in which such mass can be found to consider plausible

the conduction trough the mechanism. The figure 3.18 presents the FN plot for the experimental data of the bi-layer devices (symbols) and the linear fittings applied to them (discontinuous lines).

According to the conclusions reached trough the PL results, it is expected to have a significant amount of traps in the material. These, apart from playing a role in the luminescence, are likely to influence the current transport. As mentioned, similar materials both including silicon oxide and nitride, have shown a behaviour compatible with TAT[35], which is also explained in section 1.2.2 and modelled by the equation 1.5, which can also be expressed as:

$$J \propto C_{TAT} \frac{1}{E_f} \tag{3.6}$$

Where $C_{TAT}$ is defined as:

$$C_{TAT} \equiv -\frac{8\pi\sqrt{2qm}}{3h} \left(\frac{m^* \phi_t^3}{m}\right)^{\frac{1}{2}} \tag{3.7}$$

Then again, for this mechanism a plot of $\ln(J)$ *vs.* $1/E_f$ should deliver a straight line from which slope either the electron effective mass $m^*$, or the trap state energy level $\phi_t$ can be extracted, provided one is known. The figure 3.19 presents the TAT plot for the experimental data of the bi-layer devices (symbols) and the linear fittings applied to them (discontinuous lines). Again, values extracted from the regressions should have physical coherence in order to consider them valid.

Both models (which have a very close relation) seem plausible from the first inspections. In order to validate them, the values for the relative mass of the electrons $m_r \equiv m^*/m$ were selected from results of measurements reported in the literature when studying silicon dioxides, nitrides and oxynitrides. The lowest reasonable value was considered $m_{r_{min}} = 0.4$ [38, 35] (in silicon nitride,) while the highest $m_{r_{max}} = 0.98$[40] (longitudinal relative effective mass in silicon.) As already mentioned, this is a rough approximation in which the whole bi-layer system will be modelled as an "effective material", which will yield an effective barrier height $\phi_{B_{eff}, t_{eff}}$ and to which an effective relative mass $m_{r_{eff}}$ to the electron will be assigned. The results of the values extracted from the fittings are presented in table 3.3.

While the values are not unreasonable for both models, the TAT mechanism seems more likely if the schemes depicted in figure 3.15 are taken into account, since the barrier created by the $Si_3N_4$ is not expected at first instance to be lower than 3 eV. In addition, the values from the regression of the TAT are well within result obtained trough computer simulations of similar materials[35]. This is supported by studies regarding leakage in silicon oxinitrides by computational models, which suggested that defect-like levels in the forbidden band introduced by the substitution of O atoms by
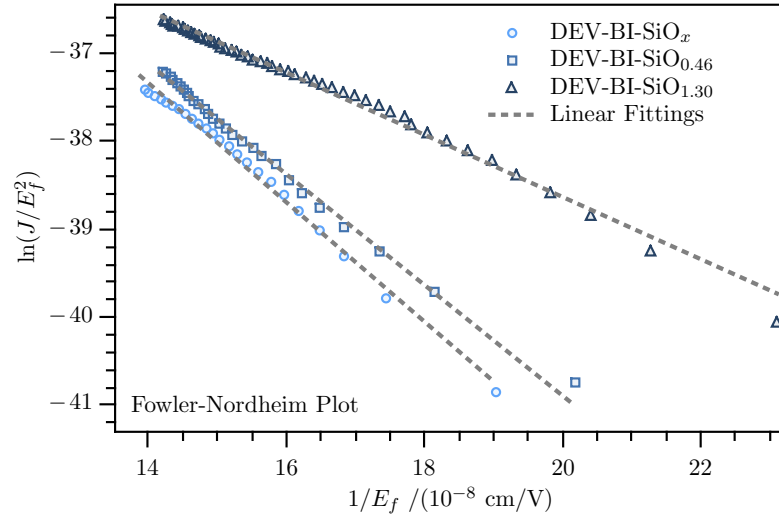
Figure 3.18: Fowler-Nordheim plot for bi-layer devices in the field region in which EL is observed. Symbols are experimental data obtained during $I$-EL measurements, applying current and measuring voltage.
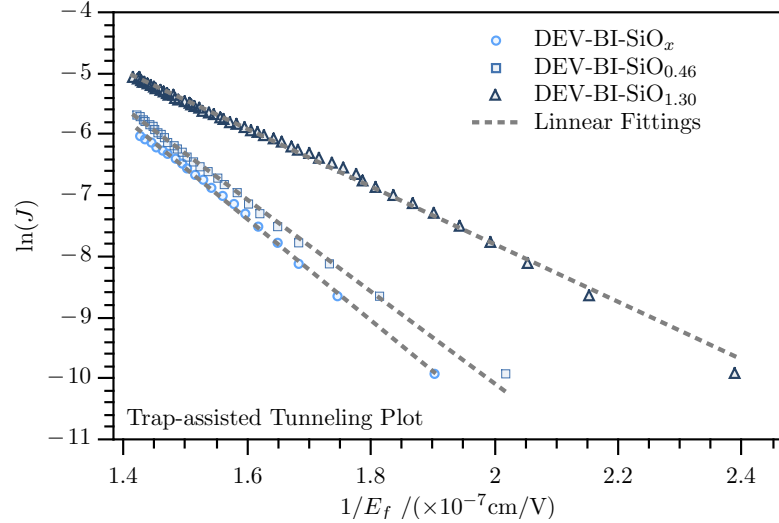


Figure 3.19: Trap-assisted Tunnelling plot for bi-layer devices in the field region in which EL is observed. Symbols are experimental data obtained during $I$-EL measurements, applying current and measuring voltage.

Table 3.3: Results of the barrier heights as extracted from the FN ($\phi_{B_{eff}}$) and TAT ($\phi_{t_{eff}}$) models considering the electron relative effective mass between $m_{r_{min}} = 0.4$ and $m_{r_{max}} = 0.98$

| Sample | $\phi_{B_{eff}}$/(eV) | $\phi_{t_{eff}}$/(eV) |
|---|---|---|
| DEV-Bi-SiO$_x$ | 1.18±0.17 | 1.35 ± 0.20 |
| DEV-Bi-II$_{0.46}$ | 1.12±0.17 | 1.26 ± 0.19 |
| DEV-Bi-II$_{1.30}$ | 0.76±0.11 | 0.92 ± 0.14 |

N atoms would make a large contribution to current leakage as compared to FN mechanisms[39].

## 3.6.   Conclusions

The results from EL characterization to the devices showed the presence of the known two types of EL, namely D-EL and FA-EL. Single layer samples present D-EL, in random localization of the bright spots and in which the emission spectra was the same regardless of silicon contents, differently from the PL results. This was found to be due to electrical failure of the SRO, in which the emission is compatible to radiative energetic transitions of electrons in the conduction band of the failed SRO to the substrate.

The efficiency of the mono-layer devices was two orders of magnitude lower as compared to the one found in bi-layer devices, which where the only architecture among the studied that delivered usable results without further processing or excessively narrow operation ranges, since these did present reliable and repeatable FA-EL.

The results from the comparison of FA-EL with PL concluded that the emission centres in the bi-layered devices are the same for wavelengths within 420 and 770 nm, at least, meaning that the additional processes to which the active layers were submitted in order to build the LECs (e. g. poly deposition and doping) do not significantly affect their light emission. However, the gate layer introduces important modifications in the output spectra, not only due to its transmittance, but also due to internal reflection and interference phenomena, meaning that these must be considered in the identification of radiative centres in further studies. All such optical phenomena can be accounted for by the application of an effective transmittance function, common to all devices with a same architecture.

In the case of the bi-layer samples, the Radiant Power vs. Current Density graphs confirm that EL is dominated by electron-hole recombination, since the linear relation rules out impact ionization process taking place

in the luminescence. The results clearly indicate that the influence of the nitride layer does not only affects the EL spectrum, but has a great importance in electrical stability of the device and current injection. The most likely reason for this improvements in transport is that the nitride inclusion causes a diminution of traps and defects in the interfaces that lead to SRO failure, high current leakage, and localized carrier injection.

It was fond that the conduction mechanism in bi-layered samples are best adjusted to the TAT model. Questions regarding how do the transport and emission mechanisms compete, as well as how do the defects participate in emission and/or in transport, remain relevant, and finding their answers is a very important part of the future work. Also, the problem of modelling the complex transport in the system, while very exciting and interesting, is not solved yet, and it certainly is of capital relevance for the improvement of the efficiency of the devices, therefore very worthy of pursuing its solution, as efficiency improvements were found to be dominated by the reduction of the necessary current to obtain a given EL intensity, rather than to the increment of the latter.

# Chapter 4

# The Integrated Optical System (IOS): Transceiver

As mentioned in the beginning of this thesis, one of the main reasons driving the research in devices similar to those here analysed is the perspective of their use to obtain a monolithic Integrated Optical System (IOS) compatible to standard CMOS fabrication techniques. The basic system of this type would be an integrated light transmitter–receiver (transciever), which consists on the controlled emission of light in a zone of the chip, its transmission to another zone, and its detection for the reading of the signal. The basic symbolic schematic of a transceiver is illustrated in the figure 4.1.

Three basic elements are necessary to integrate in the transciever system, namely the light emitter, the light waveguide, and the light sensor. In order to take advantage of the mentioned benefits that the use of silicon has, the fabrication of all of them must be strictly compatible to Complementary Metal-Oxide-Semiconductor techniques.

Photon sensors based on Si are a common and already extensively used in CMOS technology; waveguides based on silicon, have already proposed and developed[80, 81]; and a viable light emitter has been proposed, studied, and discussed in this work. Then, the attainment of the IOS is possible
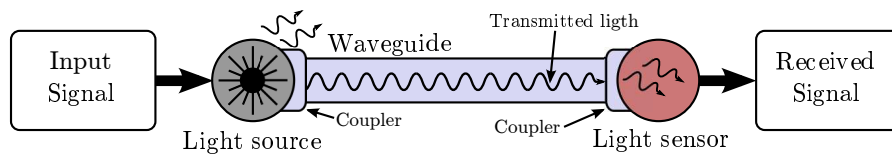


Figure 4.1: Schematic of the general configuration of an electro-optical transciever.

84

if the fabrication of one of the elements does not interferes with any of the other.

This chapter proposes the design of a transceiver architecture in an fully CMOS compatible IOS, enabled by the information presented in the previous chapters. Next, the results from the characterization of a fabricated prototype, are discussed and analysed.

## 4.1. General concept

In order to keep the system compatible to standard CMOS processes, it must be conceived as fabricated by planar technology, avoiding the use of non-standard materials and techniques. The the figure 4.2 presents architecture proposed in this work for the prototype of the Integrated Optical System, and the details of the stack structure and the materials are presented in the figure 4.3.

In this scheme, the left part of the system consist of a LEC with the same architecture of those studied in the chapter 3 directly embedded in a rectangular cross-section silicon nitride waveguide, which transmits the emitted light to the detector. The material for the latter can be obtained during the same step of the nitride layer deposition for the bi-layer devices described in section 3.1, using an appropriate lithography mask to define the geometry. To confine the light, a cladding with lower refractive index than that of the $Si_3N_4$ must be used. Silicon dioxide is appropriate for this task; however, the bottom of the guide can not be directly deposited on the Si substrate, as this has a higher refractive index. The thickness of the cladding must be enough to prevent the electric field of the light reaching the substrate. A thick $SiO_2$ film can not be simply deposited on the substrate, since it would isolate the bottom contact of the LEC if deposited in the whole wafer, or impede the aligning of the $SRO$-$Si_3N_4$ interface with the centre of the guide cross section, in which a great part of the light is generated. The proposed solution is to bury a $SiO_2$ well exactly below the waveguide, which can be obtained by silicon etching and Local Oxidation of Silicon[40, 82], a widely used technique in the fabrication of integrated circuits which will be described later.

The waveguide will transmit the light from the LEC to the sensor, which is a $p$-$n$ junction photodiode placed below its end. The higher refractive index of the silicon substrate will allow the light to be absorbed by it, generating electron-hole pairs (e–h) that will be detected as photocurrent in the terminals of the photodiode.

To electrically isolate the emitter from the sensor, it is proposed to fabricate two wells with degenerated carrier concentration of opposite type as that of the wafer. One will serve to electrically access the bottom part of the LEC, and the other as the anode of the photodiode, while the back
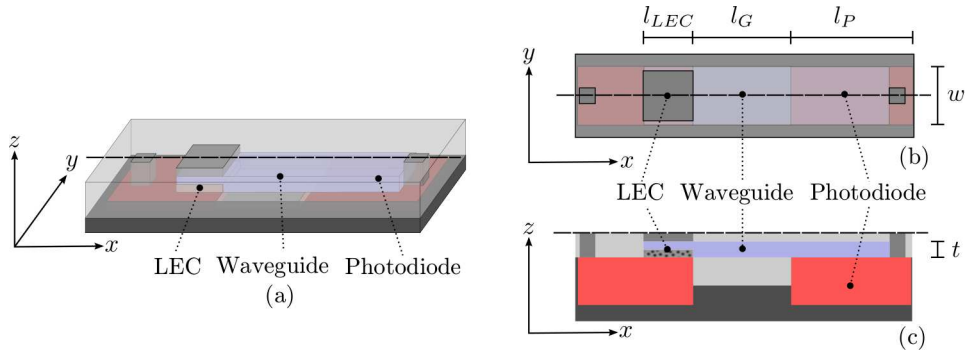
Figure 4.2: Scheme of the proposed architecture for the transceiver prototype (not on scale). (a) 3D view. (b) Top view. (c) Transversal cut view.
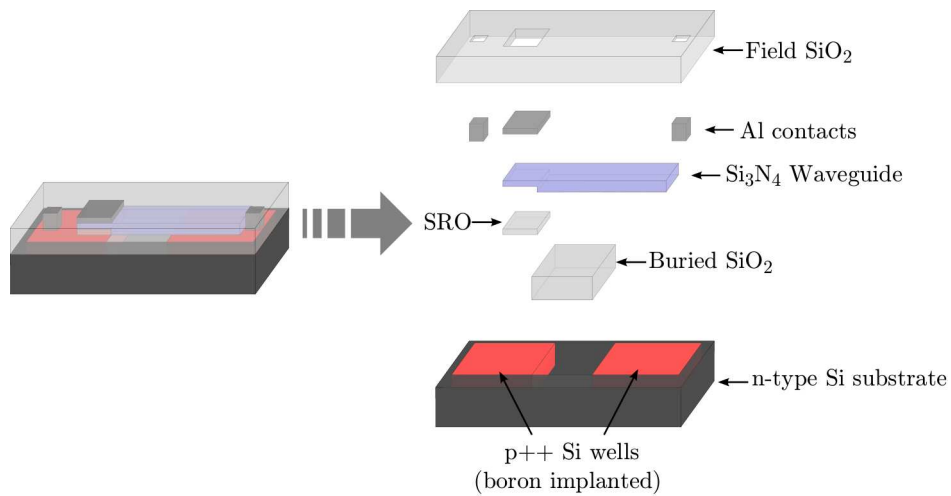


Figure 4.3: Materials used and planar configuration of the transceiver prototype (not on scale).

of the wafer will be its cathode (or the other way around, depending of the substrate type). Then, the voltage of the signal to transmit $V_{LEC}$ will be applied to the emitting device from the top of the wafer, while the transmitted information will be read trough the current in the $p$–$n$ junction $I_{pn}$ using terminals in the top and the back of the wafer, as the electric schematic in figure 4.4 depicts. A voltage $V_{pn}$ will be applied to the photodiode in order to modify its sensitivity, as will be detailed later.

## 4.2. Design and fabrication concept

The detailed step-by-step description of the system fabricated during the development of this work is included in the appendix C.5. This section focuses on indicating the general idea of how the concept can be achieved, considering the information obtained trough the previously presented research, the technological problems that arise during the integration of the elements, and the fabrication restrictions imposed by the available equipment, and the CMOS constrains. For this, the analysis is divided in two subsections, the first covering the part in charge of the emission and transmission of the light, and the last that sensing such light.

### 4.2.1. The emitter-waveguide

The proposal for the light emitting device is to use one with the same characteristics as the one that showed the highest efficiency, namely those from the sample DEV-Bi-SiO$_{0.46}$ reported in the previous chapter. Therefore, the fabrication parameters of the IOS are ruled by those for the fabrication of the former. As mentioned, the emitter will be embedded in the waveguide; this way, assuming that the emission from the active material is isotropic, most of the part in the positive $\hat{x}$ direction as defined in the
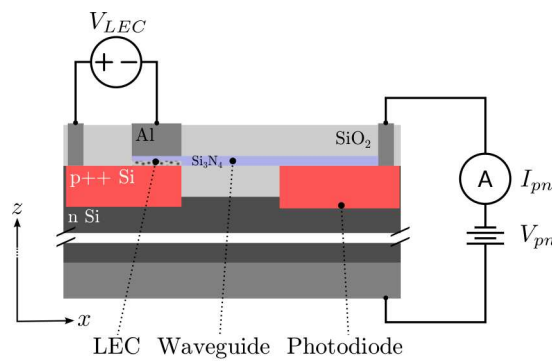


Figure 4.4: Schematic of the electrical connections for the transciever.

figure 4.2 can be transmitted, and the emission in the rest of the directions within an angle inside the critic can also contribute.

The lower cladding of the waveguide formed by the buried silicon dioxide presents a technological issue, since it is needed to be levelled to the wafer surface in order to allow the waveguide to rest on top of the photodiode (see figure 4.2c). The solution proposed was the use of a Local Oxidation of Silicon (LOCOS) process, which roughly consists on the local growth of thermal silicon dioxide in a previously etched trench[40].

To achieve this, the rest of the wafer is masked with a layer or silicon nitride (on top of which the silicon dioxide does not grow). After the oxide has been grown, the masking nitride is selectively removed and the result is a localized well of $SiO_2$. This technique presents a technological problem known as the bird's beak phenomenon[82], which introduces a perturbation in the transition from the dioxide well to the Si wafer. This can be observed in the figure 4.5a, which presents the result of the LOCOS in one test sample as observed with Scanning Electron Microscope (SEM) on a transversal cut obtained with a Focused Ion Beam (FIB). Such perturbation is important in the case of the design here presented, since it may reduce significantly the light transmission efficiency. To minimize this, it was performed a process consisting on the deposition of successive films of tetraethyl orthosilicate film (TEOS) and borophosphorous tetraethyl orthosilicate (BPTEOS), a thermal fluidification annealing to homogenize the surface, and a further dry etching of the silicate films to level it all to the original silicon substrate. Images for these two later steps are presented in the figures 4.5b and 4.5c. As it can be observed, the final result is a smooth surface in which the $SiO_2$ well, which will be the lower cladding of the waveguide, is levelled with the surface of the Si wafer.

It was already mentioned that the fabrication parameters for the light emitter to integrate should be imported from the process that presented



(a) LOCOS stage     (b) Fluidification stage     (c) Final stage
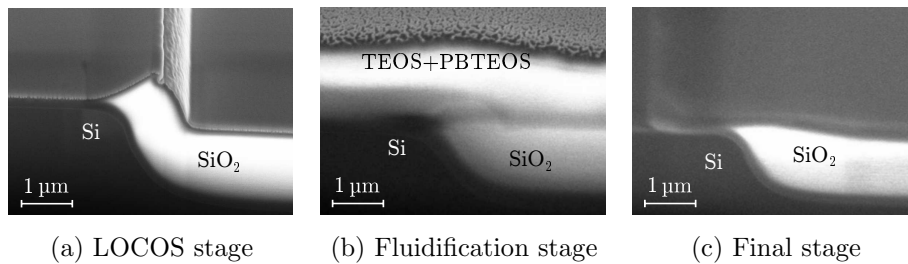
Figure 4.5: Images of a transversal cut of the wafers in the lower cladding region obtained by FIB and TEM. Three steps are shown: the result after LOCOS (a), after the deposition and fluidification of the TEOS+BPTEOS film (b), and after the dry etching of the former to obtain a cladding levelled to the Si substrate surface (c).

the highest control and efficiency in the resultant light emitters, namely that for the DEV-Bi-SiO$_{0.46}$. However, while such LECs were made of Si implanted in thermal SiO$_2$, it is simpler to use PECVD deposited dioxide, as no modification of the substrate is required for it. Otherwise, the dopant implantation to obtain the lower contact of the LEC would greatly complicate, as well as the obtaining of the buried oxide cladding. The use of PECVD instead of thermal growth for the dioxide matrix does not change the device behaviour, as concluded in the section 2.6.3, and corroborated by the fabrication of a test run containing stand-alone LECs.

Considering all the previously discussed factors, the fabrication of the emitter-waveguide was designed as illustrated in summary in the figure 4.6 (as repeatedly mentioned, the complete process is included in the appendix C.5). After the lower cladding was obtained with the process previously described, and the contact and photodiode $p++$ type Si wells were implanted, the fabrication continued with the deposition and geometric definition of a 30 nm-thick silicon nitride film on top of the buried-dioxide cladding; then followed the deposition of the matrix PECVD SiO$_2$ to form one layer of the LEC, and the successive deposit of the other 30 nm of silicon nitride, for both the nitride layer of the LEC, and the rest of the waveguide. Finally, the Si implantation in the bi-layer region and the further thermal treatments are to be performed.
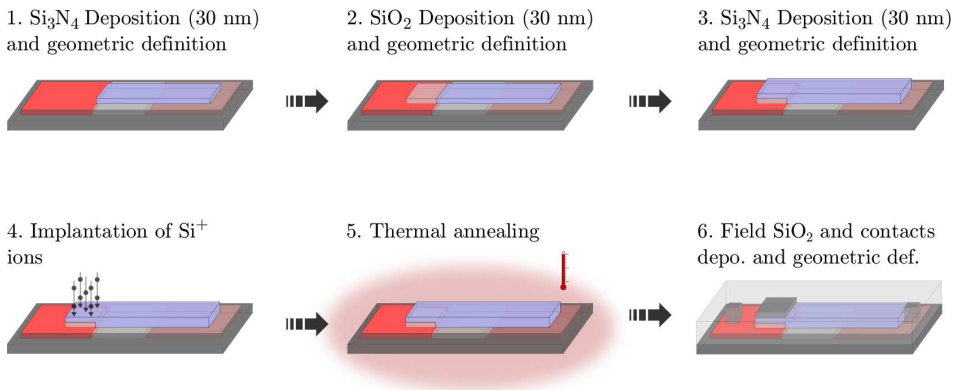


Figure 4.6: Summarised fabrication process of the LEC-Waveguide part of the IOS. The geometric definition of the structures is always done by lithography and etching of the respective materials, except in the ionic implantation, in which there is not etching, but only masking of the regions not to be implanted.

The previously described process is to obtain a waveguide with the same thickness as that of the LEC, which is the simplest solution for the system. However, such thickness value is in the same order as that of the emission wavelengths, which can introduce issues regarding the field that can be injected, confined, and/or transmitted. To reduce this problem, a different waveguide thickness can be proposed. This must be done carefully and within limits, as significant tensile forces arise in the silicon-nitride interface during thermal treatments due to the different thermal expansion coefficients, an issue that becomes more important as the thickness increases. The overall fabrication process also complicates, since the zone of the guide corresponding to the LEC must be etched in order to reach the appropriate nitride layer thickness (and keep the operation voltage in its value).

A proposal to fabricate a waveguide thicker than the LEC is presented in figure 4.7. A $SiO_2$ mask is included in the process to protect the nitride

1. $Si_3N_4$ Deposition (30 nm) and geometric definition

2. $SiO_2$ Deposition (30 nm) and geometric definition

3. $Si_3N_4$ Deposition (30 nm) and geometric definition

4. Implantation of $Si^+$ ions

5. Deposition and definition of $SiO_2$ to mask bottom nitride

6. Deposition of thick $Si_3N_4$ layer

7. Defined etch of $Si_3N_4$ and wet etch of $SiO_2$ mask

8. Thermal annealing (for SRO)

9. Field $SiO_2$ and contacts depo. and geometric def.

Figure 4.7: Summarised fabrication process of the LEC-Waveguide part of the IOS for a waveguide with a thickness different than that of the LEC. The geometric definition of the structures is always done by lithography and etching of the respective materials, except in the ionic implantation, in which there is not etching, but only masking of the regions not to be implanted.

of the LEC during the geometric definition of the guide (step 5 of figure 4.7), preserving the configuration of the bi-layers. The dioxide mask is later removed by wet etching, which can present high selectivity between $Si_3N_4$ and $SiO_2$.

**Light insertion simulations**

In order to test the ability of the waveguides to transmit the light, simulations of the propagation modes were performed using the software FIMMWAVE. The wavelengths used were 509 nm and 740 nm, which are the two principal emission wavelengths for the samples Bi-II$_{0.46}$ (see figure 2.18). The light energy density $U$ was evaluated for the first 20 allowed modes found at the beginning of the waveguide, and at 500 µm in the $\hat{x}$ direction, assuming direct injection and defining a window with the same dimensions of the LEC transversal cut, aligned to the bottom of the waveguide. In all the cases, the same uniform intensity profile of cylindrical phase front, and circular polarization was used for the simulations.

The figure 4.8 presents the results for the optical energy density propagated at the length $x = 500$ µm for the two main emission wavelengths in waveguides with both $t =60$ nm and $t =500$ nm. No significant differences in the values at $x = 0$ µm were found. Then, it can be considered that the initial injected power is the same at $x = 0$ µm and $x = 500$ µm.

The Simulations confirmed that only modes purely $E_y$ polarized propagate. This is due to the low or similar values for $t$ (the dimension in $\hat{z}$) as compared to the light wavelength. Nevertheless, light can still be transmitted in the emission wavelengths, which are well suited for the detection by the Si photodiode, since the quantum efficiency for these are good enough for wavelengths around 550 nm (above 70 %)[40].

Note that the energy density values for the 500 nm-thick waveguide are one order of magnitude lower than that of its 60 nm-thick counterpart, but since the units are in volumetric energy density, and the height $t$ is one order of magnitude higher for the first, the total energy along the area of the transversal cut must be calculated to make a proper comparison. This is presented in the table 4.1.

While in the images presented in the figure 4.8 it appears to be a greater amount of optical energy outside the waveguide in the thinner one as compared to that of the thicker, the integration values reveal otherwise. The integrated energy density inside the 500 nm-thick waveguide is always lower than that of the 60 nm-thick, and in the case of 509 nm light, one order of magnitude lower. This is expected to impact in the readable signal from the detector of the IOS. It should also be noted that in the 60 nm-thick waveguide, the energy density confinement is higher for the $\lambda =509$ nm, while conversely, the 500 nm-thick presents better results for the $\lambda =740$ nm light.
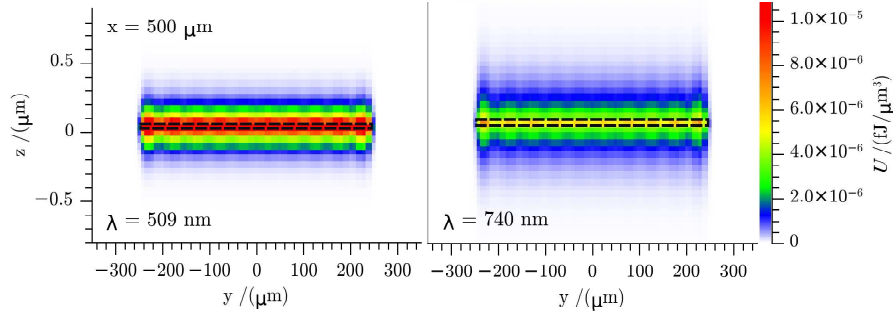
(a) $t = 60\,\text{nm}$
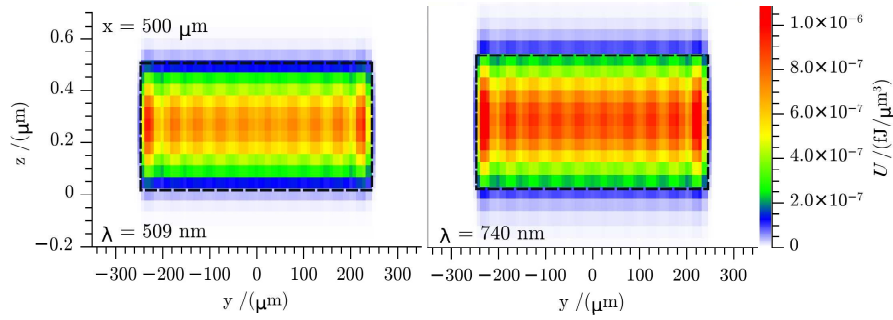


(b) $t = 500\,\text{nm}$

Figure 4.8: Energy density of the propagated light for the first 20 modes of an specific wavelength in a transversal cut of the waveguide at $x = 500\,\mu\text{m}$. Results for the two proposed thickness are shown when injecting light with wavelengths $\lambda = 509\,\text{nm}$ and $\lambda = 740\,\text{nm}$. The rectangle with discontinuous lines represents the interface between the $Si_3N_4$ waveguide, and the $SiO_2$ cladding.

Table 4.1: Integrated optical energy density $U$ inside the transversal cut of the waveguide evaluated at $x = 500\,\mu\text{m}$ for the two studied wavelengths and thickness. The injected light simulated intensity and profile was the same in all cases.

| Value $Si_3N_4$ waveguide thickness $t$ | Transmitted Wavelength | Integrated $U$ at $x = 500\,\mu\text{m}$ /(fJ/$\mu\text{m}^3$) |
|---|---|---|
| 60 nm | 509 nm | $1.57 \times 10^{-3}$ |
| | 740 nm | $6.04 \times 10^{-4}$ |
| 500 nm | 509 nm | $2.37 \times 10^{-4}$ |
| | 740 nm | $3.17 \times 10^{-4}$ |

The SiO$_2$ around the nitride guide (cladding) was designed to be 1.5 µm thick at its minimum. The electric field simulations for the $E_y$ components evaluation at $x = 500$ µm for the two studied thickness are presented in figure 4.9. Again, no important differences were observed when evaluating at $x = 0$ µm.

The results show that 1.5 µm-thick buried cladding is sufficient for preventing the field reaching the Si substrate for $\lambda = 509$ nm. But in the case of $\lambda = 740$ nm and thickness of 60 nm, while the electric field value is rather low, it is not null, meaning that longer wavelengths clearly need a higher margin for cladding thickness. On the other hand, the 500 nm-thick waveguide behaves much better in this respect, showing a significantly lower field presence outside the nitride. For instance, note how at $z = 1$ µm the graph 4.9b shows clearly no value above $2.5 \times 10^{-4}$ V/µm, while in 4.9a a shade corresponding to a value between $2 \times 10^{-3}$ V/µm and $4 \times 10^{-3}$ V/µm can still be identified.

### 4.2.2. The light sensor

The electronic devices forming the system need to be clearly isolated to avoid interference with each other. Then, the back of the wafer can only be used as terminal for either the emitters, or the detectors. As previously shown, the latter is the case of the here proposed design, and the solution to provide the other device with its second terminal is to form an opposite dopant type well that could be accessed from the top of the wafer. The naturally formed depletion region between this and the substrate isolates them.

The same type of well used to access the emitter bottom contact can be used to form the *p-n* diode that will serve as the photo detector. This is a simple, well known, and compatible device, and the reported quantum efficiency peak for Si photodiodes is between 600 nm and 1000 nm[40], which is in the range of the intrinsic emission of the materials here analysed.

The sensor can be obtained simply by inverting the carrier type of the substrate in the desired region by the implantation of dopant elements, *i.e.* Boron if the substrate is *n*-type, or Phosphorous if it is *p*-type. In this case, since the thermal treatment is not the standard used to activation of the dopant, but restricted to that necessary for the LEC fabrication, the insertion and activation of the dopants must be as controllable as possible. Then, it was decided to use an *n*-type substrate for the fabrication of the systems, since Boron is a better controlled element regarding its diffusion and reaction with Si than Phosphorous[83].

In order to have a better light detection, it is desired to achieve the wider possible depletion region in the photodiode, meaning that a low carrier concentration is better. However, to simplify the fabrication process, the access to the bottom contact of the LEC is obtained during the same
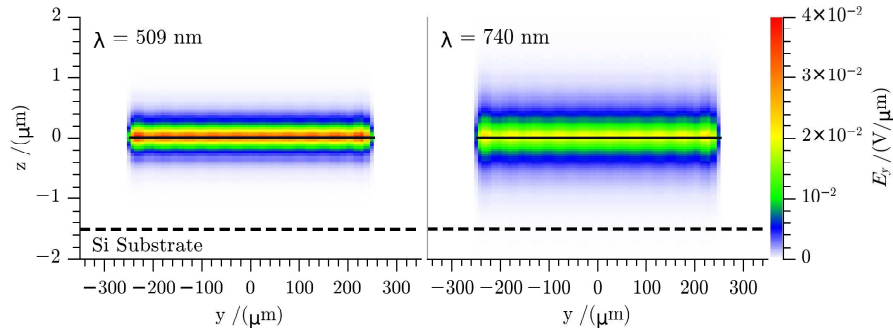
(a) $t = 60\,\text{nm}$
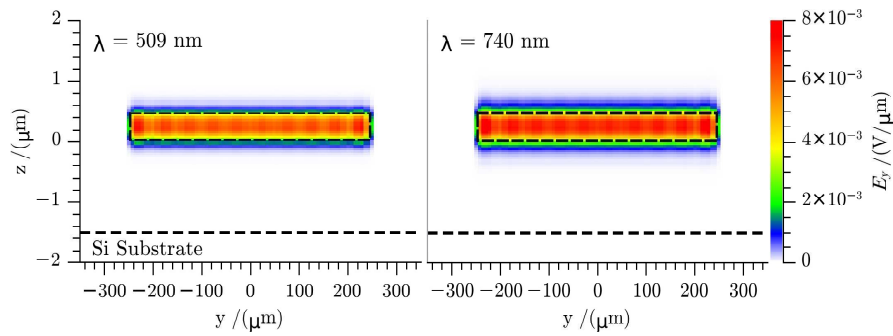


(b) $t = 500\,\text{nm}$

Figure 4.9: Electric field component $E_y$ for $\lambda = 509$ nm and $\lambda = 740$ nm at the length $x = 500\,\mu$m. The rectangle with discontinuous lines represents the interface between the $\text{Si}_3\text{N}_4$ waveguide, and the $\text{SiO}_2$ cladding. The discontinuous line at $z = -1.5\,\mu$m represents the interface between the buried $\text{SiO}_2$ cladding and the Si substrate. Note that due to the necessity of including the substrate level in the plot, the geometry of the 60 nm-thick waveguide appears a line rather than a rectangle, but this is only an effect of the scaling in the '$z$' axis.

implantation used for the $p$-part of the diode, and the former needs to be degenerately doped. Then, is the substrate (the $n$ part of the diode) the zone which should have low carrier concentration, hence sustaining most of the depletion zone.

Summarizing, the electric access to the anode of the diode will be trough a contact in the top of the wafer, while that to the cathode using the back, as depicted in the electrical scheme of the system presented in the figure 4.10. The reverse of the wafer will receive a $n++$ implantation, Al deposition, and the standard treatments to form an ohmic contact. The figure 4.11 shows an abbreviated scheme of the processes involved in the fabrication of the photo-diode (again, the full fabrication process can be found in the appendix C.5).

Simulations with SRIM and ICECREM[84] were used to verify the results of dopant distributions for the necessary thermal treatments after implantation of B in the available substrates, using standardized parameters for the fabrication of CMOS transistors in the *Centro Nacional de Microelectrónica-Instituto de Microelectrónica de Barcelona* (CNM-IMB). The figure 4.12 presents the results when implanting the substrate using a boron ions dose of $1\times10^{15}$ cm$^{-2}$ with an energy of 50 keV. The $n$-type silicon wafers available present a nominal resistivity between 1 $\Omega\times$cm and 12 $\Omega\times$cm, and the profiles were evaluated for these two extremes. The lines in the plot represent the average of the results, while the error bars accounts for the variations on the resistivity. The value $z = 0$ indicates the surface of the Si substrate, moving towards negative numbers as the depth is increased.

The junction is an abrupt one, and as mentioned, the depletion layer width $W_d$ will mostly rely on the substrate. Its value can be calculated using the expression[40]:

$$W_d = \sqrt{\frac{2\varepsilon_s(V_{bi} - V)}{qN_B}} \tag{4.1}$$

In which $\varepsilon_s$ is the silicon dielectric permittivity, $N_B$ the doping concentration of the bulk Si, $V$ the applied potential to the diode, and $V_{bi}$ the built-in potential; which on its turn can be calculated with the equation:

$$V_{bi} = \frac{kT}{q} \ln\left(\frac{N_A N_B}{n_i^2}\right) \tag{4.2}$$

Where $kT/q$ is the thermal voltage, $N_A$ the acceptor concentration in the $p$ region of the diode, and $n_i$ the intrinsic carrier concentration of the Si.

According to the fabrication process and simulation results, the $p$–$n$ junction in the transceiver should present a $W_d$ between 0.5 μm and 1.5 μm at zero bias, for the lowest and highest possible resistivity of the substrate,
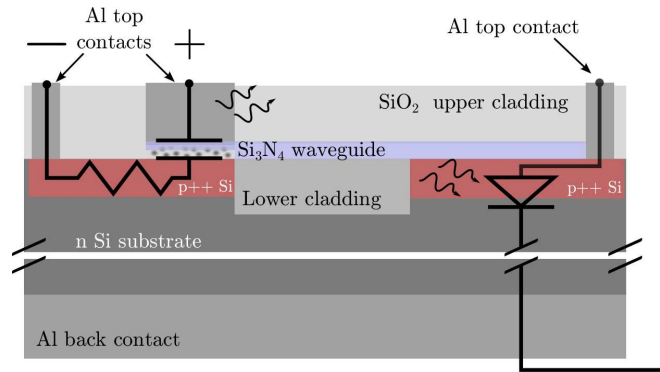
Figure 4.10: Symbolic schematic of the devices embedded in the transversal cut of the transciever as represented in figure 4.2 (c).
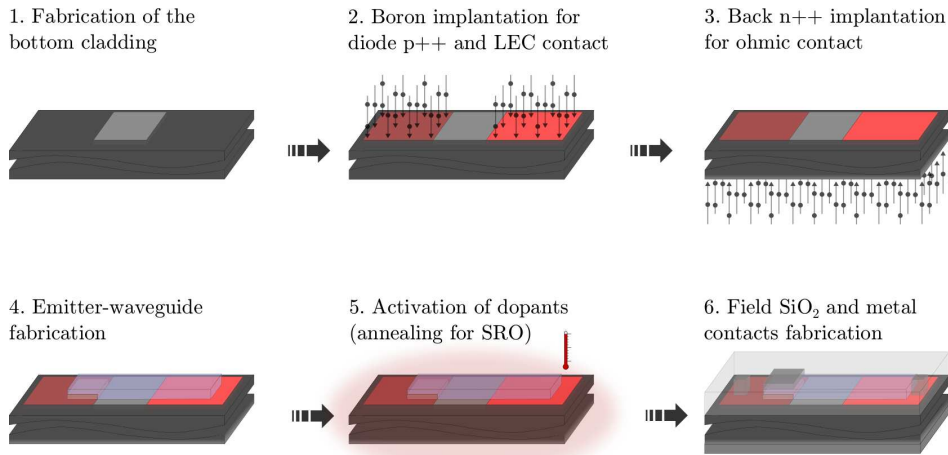


Figure 4.11: Summarised fabrication process of the sensor diode of the transciever. The geometric definition of the structures is always done by lithography and etching of the respective materials. All the steps for the fabrication process of the IOS can be consulted in the appendix C.5.
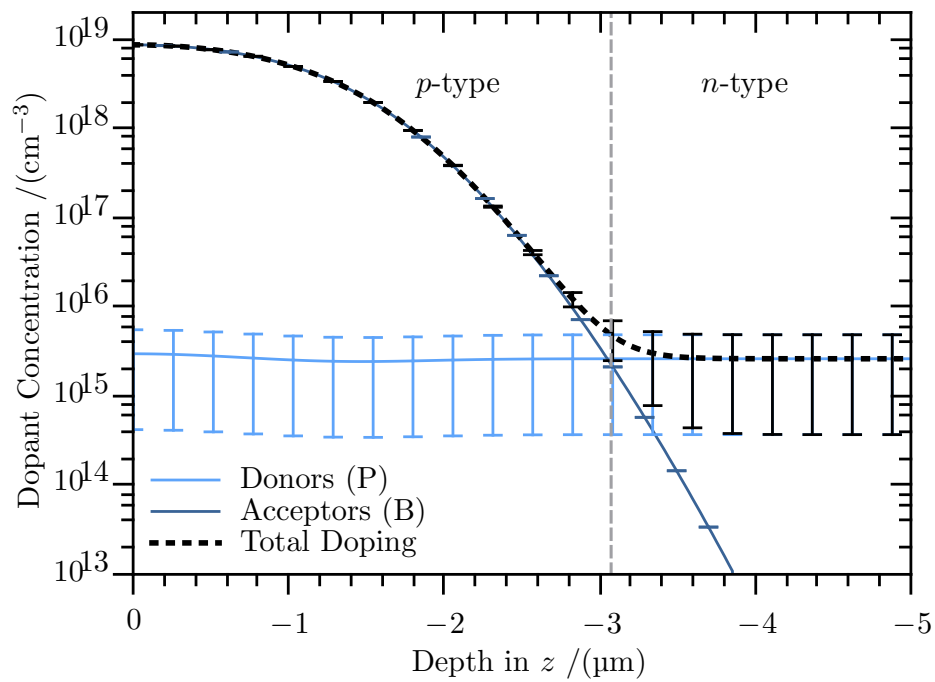
Figure 4.12: Average dopant concentration profile of boron implanted Wells. The error bars arise from the variations of the wafer resistivity, the grey discontinuous line marks the transition from $p$-type to $n$-type Si. The depth $z = 0$ is located in the surface of the Si substrate.

respectively. The effective position of the depletion region, which depends on the depth of the junction and the value of $W_d$ (both variable with the resistivity of the substrate), must be found between in the interval $z = [-2.9, -3.4]$ µm for the $\rho = 1$ $\Omega \times$cm substrate, and $z = [-3.4, -4.9]$ µm for the $\rho = 12$ $\Omega \times$cm substrate. The figure 4.13 illustrates the position of the depletion layer with no bias inside the structure for these two extreme cases.

The knowledge of the depletion layer position is important, since if the light-induced e-h are generated outside this zone, they are likely to recombine again without contributing to the current, whereas if they are generated inside it, the electric field will separate the electron and the hole, and there will be a contribution to the current.

This process is illustrated in the figure 4.14, which also presents the average depletion layer behaviour for different applied voltages $V_{pn}$, as calculated using the data obtained from the simulations. As the figure depicts, when a photon absorbed before the depletion region generates an e-h pair (1a), these two perceive a force towards each other (2a), and then recombine (3a). But if the carrier is generated within the depletion region (1b), since there is a greater electric field $E_f$ inside it, the electron is drifted away from the hole (2b), reaching the substrate and being able to contribute to the current (3b). Note that if the absorption depth surpasses the depletion region, the effect would be the same as in the case of not reaching it (1a, 2a and 3a), with no contribution to current either.

According to the work by Green[85], the wavelengths shorter than 630 nm will be absorbed before reaching the depletion layer, even in the best-case scenario, in which it starts at $z = -2.9$ µm.

The main emission bands for the nitride and SRO related luminescence were found to be respectively centred 509 nm and 744 nm for the material selected for the fabrication of the IOS (the same as in sample Bi-SiO$_{0.46}$). Assuming this is properly replicated, only carriers generated by the SRO-related luminescence will be significantly contributing to the current. This is unfortunate, since the waveguide is better suited to transmit this part of the spectrum.

On the other hand, the absorption depth for the light with wavelength of 744 nm is 7 µm[85], which means that part of this will likely surpass the depletion layer when absorbed. However, while the initial point of this region is fixed by the depth of the junction in the case of an abrupt one like the one used, $W_d$, and hence its final depth, can be modified by the application of a voltage to the junction, as illustrated in the figure 4.14. In particular, a voltage of $V_{pn} = -35$ V would result in a depletion layer edge placed at an average maximum depth of $-9.7$ µm, (considering the values between which the resistivity of the wafer can be found), which is enough to capture the carriers generated by the longer wavelengths.
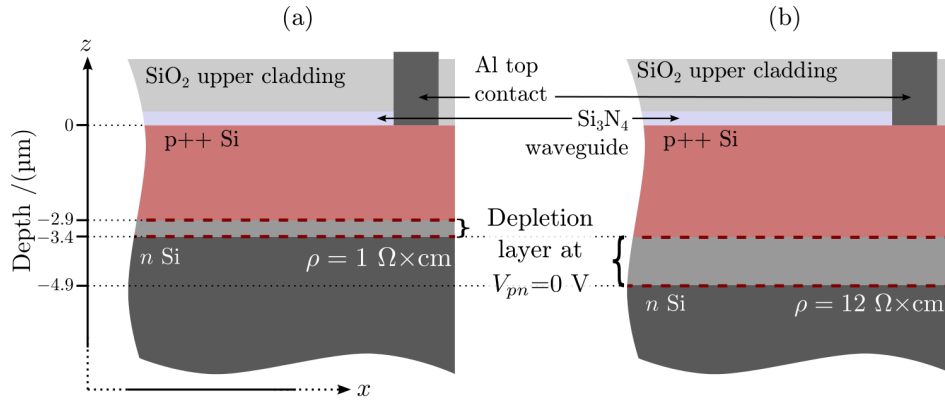
Figure 4.13: Depletion regions of the photodiode at $V_{pn} = 0$ V for the respective cases of substrate with resistivity $\rho = 1$ $\Omega\times$cm (a) and $\rho = 12$ $\Omega\times$cm (b).
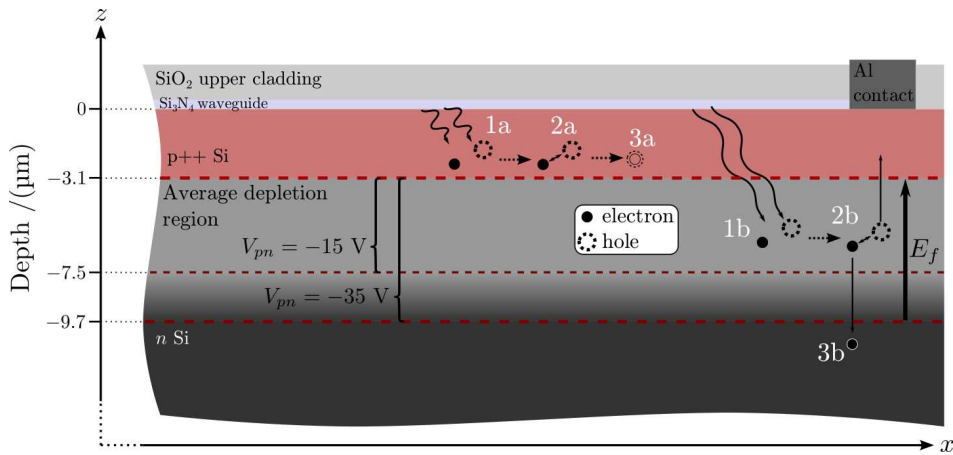


Figure 4.14: Average depletion regions of the photodiode at $V_{pn} = -15$ V and $V_{pn} = -35$ V, and depiction of photogeneration of e-h pairs that will recombine and not contribute to photocurrent (1a, 2a, and 3a), and conversely, will be separated and contribute to photocurrent (1b, 2b, and 3b).

To verify the proportion of the emitted light that could be detected by the photodiode, lets consider the PL spectra of the sample Bi-II$_{0.46}$ (presented in the figure 2.18) as the emission inserted in the wave guide. Of the total of the value resulting from the integration of the spectrum, the region below the 630 nm (with absorption depths shorter than the beginning of the depletion region) represents the 61.5 % of the emitted light, meaning that the fabricated configuration can only take advantage of the 38.5 % of the emission, at most, if applying voltage of $V = -35$ V. If the applied voltage is $V = -15$ V, the edge of the depletion region is placed at an average depth of $-7.5\,\mu$m, which would nominally be enough to separate the photo-generated pairs. However, this is an average, and in the worst case scenario, the edge of the depletion zone is placed at $z = -4.9\,\mu$m, expecting much lower photo current.

Depending on the application and the noise conditions, the value of $V$ can be varied in order to meet, for instance, power limitations (although these are likely to be dictated by the LEC). The modulation on $W_d$, could also be used to sense a specific wavelengths range, taking advantage of the dependence of the absorption depth on it. This is particularly interesting in chemical sensing applications, for instance, in which it is often analysed the behaviour of a particular wavelength. Nevertheless, note that this is significantly influenced by the uncertainty of the carrier concentration in the wafer, which is a problem that must be solved if this electric modulation of the responsivity is to be implemented.

## 4.3. Results from fabricated prototypes

To the date of the writing of this work, it was completed the fabrication of the IOS with waveguides with the same thickness as that of the emitting device, like the one depicted in the figure 4.6.

Two pilot wafers were fabricated in addition to that containing the regular IOS: one intended to allow the verification of the characteristics of the active layers without field oxide, waveguide material, or contacts (labelled IOS$_{ActMat}$), and other to study the characteristics of the EL from the emitters (labelled IOS$_{PolyGate}$), using the doped polysylicon used for the fabrication of the LECs as top contacts instead of aluminium. As mentioned before, the fully detailed processes for all the wafers are included in the appendix C.5.

In order to obtain accurate theoretical information on the characteristics of the photodiode, the resistivity of a number of wafers was measured, selecting those which presented the lowest variation, since many characteristics of such device highly depend on this parameter. The average resistivity value of the used wafers was $\rho = (1.98 \pm 0.02)\ \Omega \times$cm.

The layouts for the IOS were designed to have chips with devices with

different values of $l_{LEC}$, $l_G$, and $l_P$ to verify the influence of these parameters in the behaviour of the system. The present work particularly analyses the influence of $l_{LEC}$, comparing results from devices with $l_{LEC} = 2$ mm, $l_{LEC} = 1$ mm, and $l_{LEC} = 0.5$ mm. How the rest of the geometric parameters affect results is matter of future work.

### 4.3.1. Experimental details

The details on the experimental procedures, set-ups, and equipment used to characterize the different elements of the IOS fabricated, as well as its function as a complete system, are as follows.

**Photodiode response characterization**

The layout of the chip containing the system included test photodiodes which were subjected to the same fabrication steps as those included in the IOS, but to which the nitride on top was removed during the etching that defined the geometry of the waveguides. The figure 4.15 schemes the set-up used to measure the response of these.

A standard intensity regulated microscope lamp was used to change the illumination conditions and measure the sensor response. Using the spectrometer Ocean Optics QE65000, the spectra for each intensity point was captured and integrated, in order to verify spectrum changes, and to obtain the total counts received by the instrument. The dark spectrum was subtracted in all cases.

Simultaneously, the source-meter Keithley 2430 was used to perform a voltage sweep to the photodiodes for each light intensity, hence obtaining information on the electrical behaviour of the devices under different optical stimulation conditions.
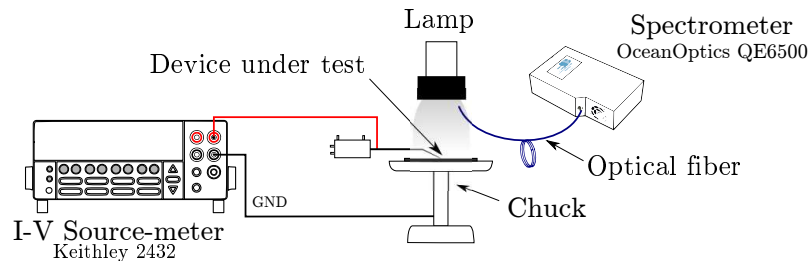


Figure 4.15: Schematic of the experimental set-up used to obtain the *I-V* response of the test photodiodes under different illumination conditions.

**Photoluminescence of the active material**

Photoluminescence tests where performed to a wafer with only active material on it (pilot wafer labelled $IOS_{ActMat}$ in the appendix C.5). The spectra were obtained using the same set-up described in the section 2.2.2 and depicted in the figure 2.2, namely the He+Cd laser at a wavelength $\lambda = 325$ nm incident at an angle of 45°, with the corresponding optical arrangement both in the stimulation and measuring sections of the set-up, using the Ocean Optics QE65Pro to capture the PL spectra in this case.

Since now the objective of the measurements was the comparison between the material in which the IOS was based, and the actual result after the fabrication processes, the original sample of the model material (Bi-$II_{0.46}$) was measured again to assure the same conditions when obtaining the compared data. In order to reduce errors, no correction to the responsivity of the instruments was performed, since no analyses on the components of the spectra were intended in this case.

**Electroluminescence Spectra**

Tests of EL were performed to pilot devices on a wafer in which the gates were fabricated with polycrystalline silicon instead of aluminium. This wafer is labelled $IOS_{PolyGate}$ in the more detailed fabrication process included in the appendix C.5.

The set-up was the same depicted in the figure 3.2 reported in the section 3.3, which was used to obtain the EL spectra and images of the stand-alone emitting devices. The only modifications to the arrangement were the use of the spectrometer Ocean Optics QE65Pro instead of the QE65000, and the necessary use of two probes to stimulate the device as described in the figure 4.4.

**$I$-$V$ of the LEC, and IOS function**

The figure 4.16 depicts the experimental arrangement used to verify the function of the emission-detection system.

The stimuli to the emitting devices was the same used to study the stand-alone LECs and the EL spectra in the $IOS_{PolyGate}$ wafer, using the Keithley 2430 source meter. Equivalently, the readings of the sensing device were registered with a set-up similar to the one arranged to study the test photodiodes. In this case, however, the source-meter used to measure the current passing trough the photodiode was a Keithley 2636, since it can measure currents in the order of $10^{-12}$ A, three orders of magnitude lower than the Keithley 2430.

The measurement-stimulation instruments were controlled and synchronized using the software LabTracer 2.7, which allowed the programming of
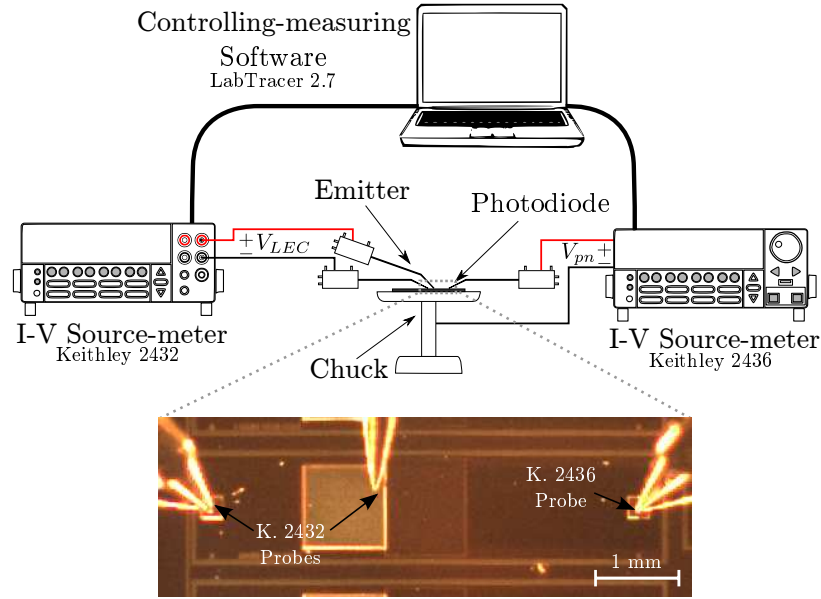
Figure 4.16: Schematic of the experimental set-up used to apply/measure simultaneously $V_{LEC}$ and $I_{LEC}$ in the emitter, and $V_{pn}$ and $I_{pn}$ in the sensor.

the stimulus, and measurement of the data from the instrument connected to the emitter and the sensor, while taking timestamps of all data, assuring the correlation of emitter action–sensor reaction (*i. e.*, the relation between $I_{LEC}$-$V_{LEC}$, and $I_{pn}$-$V_{pn}$).

This configuration allowed two types of measurements: applying and reading of $V_{LEC}$ and/or $I_{LEC}$ with the 2430, while applying a constant polarization voltage $V_{pn}$ and reading of $I_{pn}$ with the 2436; and applying constant $V_{LEC}$ and reading of $I_{LEC}$ with the 2430 while performing $I_{pn}$-$V_{pn}$ sweeps with the 2436.

Unless indicated otherwise, the tests were performed in dark conditions in order to avoid optical noise as much as possible, always assuring that the readings in the ammeter connected to the photodiode were below 10 pA prior to the beginning of all the measurement routines.

## 4.3.2. Photodiode response results

As mentioned, test photodiodes were fabricated in order to verify the characteristics of the sensors. These are exact the same as those that form part of the IOS, but without the $Si_3N_4$ of the waveguide on top. The field oxide (upper cladding of the waveguide) on the other hand, is present on top of them, but known to be transparent to the visible spectrum.

During the tests to these devices, the photodiodes presented clear photo-

current readings as soon as the probe was placed on the pad, with noticeable variations in accordance to the modification of the light reaching it, without the need of biasing the junction. The figure 4.17 presents the *I-V* response of the diode for different illumination intensities $\Phi_e$. Note that the values in the axis are negative to make easier the observation of current increments. Hereafter, this will be the convention for the present work. The curve for $\Phi_{e_0}$ is the expected curve for a typical diode with no optical stimulation.

There is noticeable noise because for these simple measurements, no special care was taken to perform the tests in dark conditions. Despite this, the signal is clearly higher than the noise, and the shift in the reverse current values with higher illumination intensity is easily observable, confirming the appropriate functioning of the devices.

Instead of using the data directly measured in the photodiode, the photocurrent $I_{photo}$ can be defined in order to eliminate the component of the leakage current, and only account for the flow of carriers generated by the incidence of light. The value of this quantity when the diode es biased with $V_{pn}$ Volts, and the emitting device is stimulated with $V_{LEC}$ Volts, is delivered by the equation:

$$I_{photo(V_{pn},V_{LEC})} = I_{pn(V_{pn},V_{LEC})} - I_{pn(V_{pn},0)} \qquad (4.3)$$

Where $I_{pn(V_{pn},V_{LEC})}$ is the current flowing trough the photodiode when it is biased using $V_{pn}$ Volts, and the emitting device is stimulated with $V_{LEC}$ Volts; and $I_{pn(V_{pn},0)}$ is the current flowing trough the photodiode when it is biased using the same $V_{pn}$ Volts, and the emitting device is not polarized, *i. e.*, the leakage current in dark conditions for the particular diode polarization voltage.

The figure 4.18 presents the relation between the photocurrent and the total counts registered by the instrument used to obtain spectra of the illumination lamp. Results for bias voltages of $V_{pn} = 0$ V, $V_{pn} = -15$ V, and $V_{pn} = -30$ V are presented.

At least two linear-like behaviour zones can be identified, with a diminution of the slope noticeable after $1 \times 10^6$ counts per second with the available data.

Such change is explained by a modification in the spectrum of the incident light as the power of the lamp is increased. This is presented in the figure 4.19, which shows spectra for intensities divided in three levels, namely low (integrated counts per second below $1 \times 10^{-7}$ c. p. s.), medium (integrated counts per second above $1 \times 10^{-7}$ c. p. s. and below $2 \times 10^{-6}$ c. p. s.), and high (integrated counts per second above $2 \times 10^{-6}$ c. p. s.).

As the intensity increases, there is an increment in the proportional contribution by wavelengths shorter than 630 nm. It has been already mentioned that this part of the spectra is expected to be absorbed before reaching the depletion layer. Therefore, despite the value of the integrated lamp
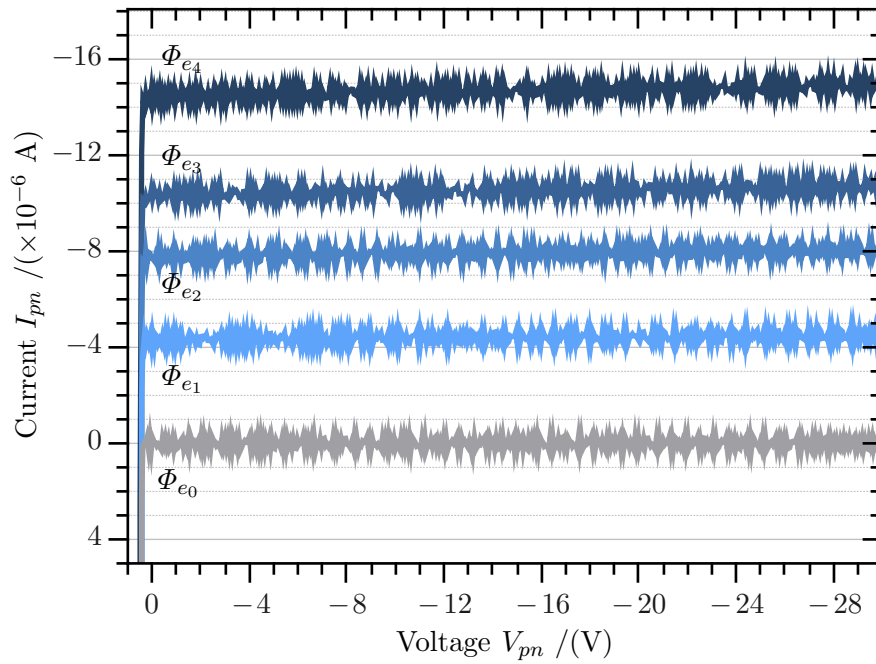
Figure 4.17: *I-V* response of the test photodiode when illuminating with the external lamp using incremental radiant powers $\Phi_e$, with $\Phi_{e_0}$ being no illumination and $\Phi_{e_4}$ the maximum intensity. Note that the values in both axis are negative.
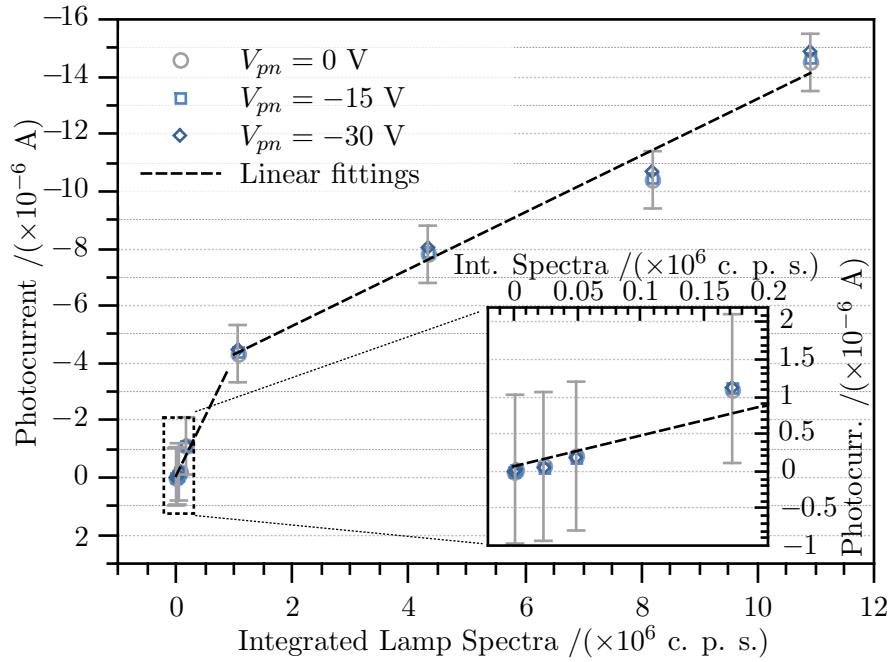
Figure 4.18: Photocurrent-Illumination relation of the photodiode when applying $V_{pn} = 0$ V, $V_{pn} = -15$ V, and $V_{pn} = -30$ V. The $I_{pn}$ under non-illumination conditions were subtracted to calculate each value of photocurrent. The inset presents the lowest intensities applied using a different scale for a better observation.
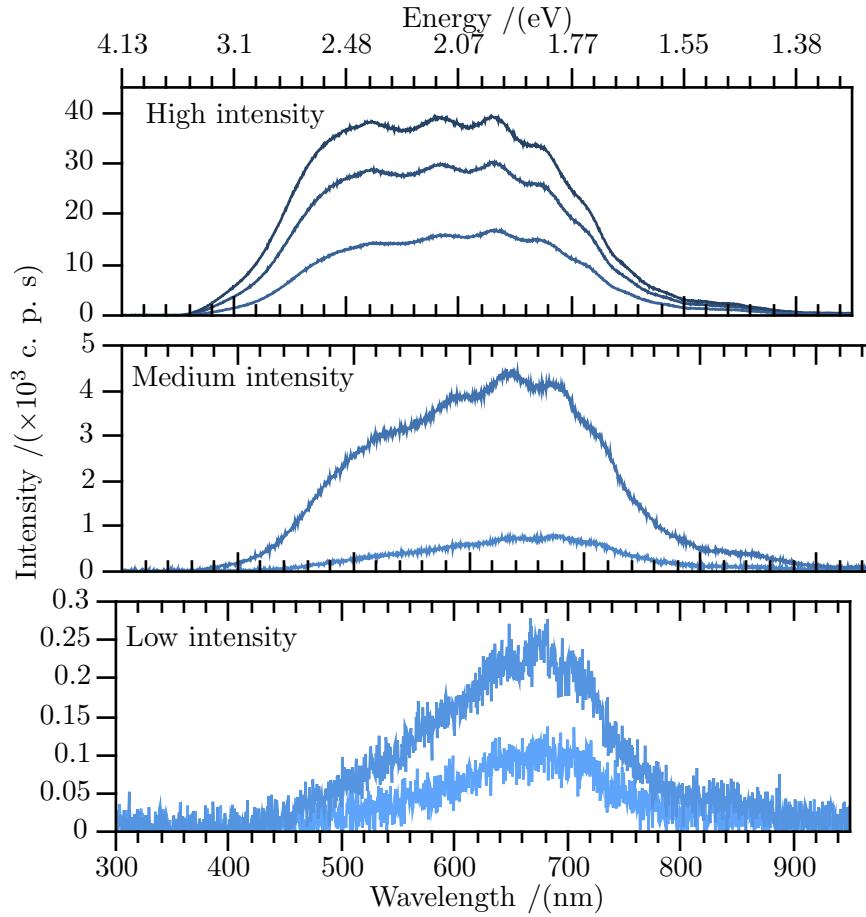
Figure 4.19: Spectra of the light used to stimulate the test photodiodes for low, medium, and high intensities (integrated counts per second below $1\times10^{-7}$ c.p.s., between $1\times10^{-7}$ c.p.s. and $2\times10^{-6}$ c.p.s., and higher than $2\times10^{-6}$ c.p.s., respectively).

spectra increases by the counting of this light, the photocurrent increases at a lower rate, since most of the e–h pairs generated by such photons do not contribute to it, resulting in the lower slope in the second region of the figure 4.18. This is in accordance to the theoretical calculations explained in the section 4.2.2.

An important conclusion from analysing the figure 4.18 is that the changes in photocurrent readings always respond to the modifications in the incident light, with a negligible influence by the applied bias to the diode, since the values for the three symbols do not significantly variate. This is in accordance to the results presented in the figure 4.17, in which the changes as the bias voltage is increased are insignificant as compared to the shift when changing $\Phi_e$.

This confirms the possibility of using the depletion region modulation to select the wavelength range of detected light, as it was explained in the section 4.2.2. It also indicates that the detector will not be significantly sensitive to possible variations of the real $V_{pn}$, which could occur when stimulating the emitter of the IOS.

In summary, the results of the photodiode characterization show its adequate operation, with appropriate linearity characteristics and stability in the current leakage when applying a polarization bias to increment the depletion layer width, allowing its modulation.

### 4.3.3. Integrated light emitter results

**Photoluminescence of the active material**

As stated earlier, in order to corroborate the congruence between the characteristics of the luminescent material used in the DEV-Bi-SiO$_{0.46}$ and the one used in the IOS, a pilot wafer to analyse the active bi-layers was included in the fabrication run.

This was subjected to the same oxide deposition, nitride deposition, ion implantation, and the rest of the thermal processes (including those for activation of impurities during the creation of $n + +$ wells and back contact). Such wafer is labelled IOS$_{ActMat}$, and as in the case of rest of the wafers for the IOS, more details on the fabrication process are included in the appendix C.5.

The PL spectrum of the active material in the sample IOS$_{ActMat}$ is presented in the figure 4.20. The plot also includes the results from the sample Bi-SiO$_{0.46}$, which was model for the fabrication parameters.

As it can be observed, both spectra present the same features. The differences in the total intensity and relative contribution by the two main bands are likely due to inequality of the thicknesses of the films in the compared samples. Nevertheless, the relevant data in this comparison is that the peaks match as expected, corroborating that the PL characteristics
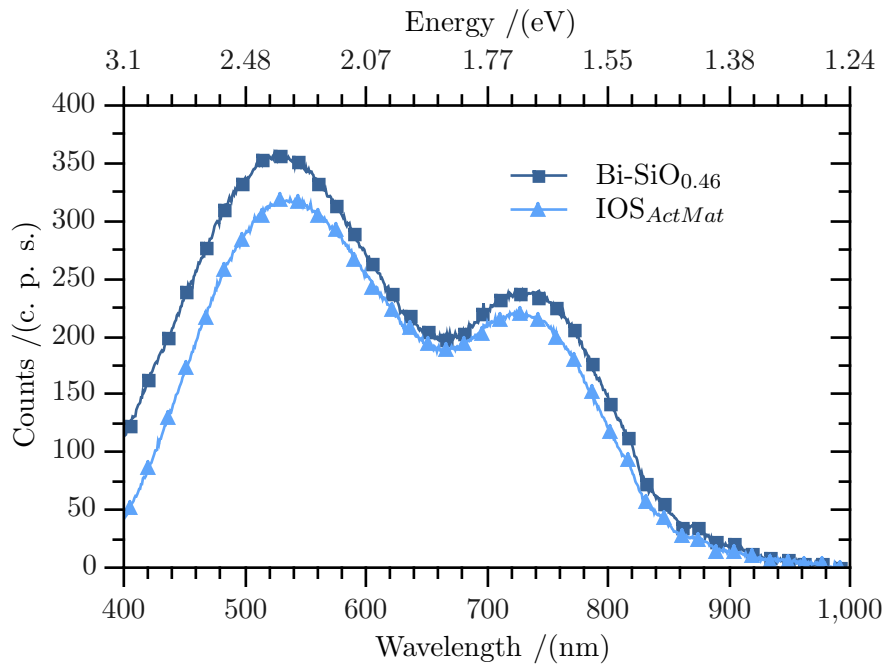
Figure 4.20: Spectrum of PL obtained from the active layers of the LEC used for the IOS (triangles) as compared to that of the Bi-SiO$_{0.46}$ films (squares).

of the active material in the finished IOS are not importantly altered by the additional processes needed to obtain the complete system.

**Behaviour of the embedded LEC**

It has already been mentioned that the fabrication parameters chosen for the obtaining of the light emitter embedded in the IOS were the same used during for the fabrication of the stand-alone emitting devices of the DEV-Bi-SiO$_{0.46}$ sample, except for the SRO matrix dioxide, which was PECVD-fabricated instead of thermal SiO$_2$, and the use Al for gate material instead of polysilicon (although poly-gated pilots were also obtained).

When analysing the *I-V* behaviour of the devices, it was clear from the beginning that the values observed were not consistent to those typical of full area electroluminescence. Instead, there were found the so-called high conduction states[69, 72] right from the initial stimulations, if applying voltage and measuring current. Very careful *V-I* sweeps controlling current were then performed, in order to avoid the reaching of breakdown voltages as much as possible. The figure 4.21 presents the *J–V* curves for devices with gate area of 1 mm$^2$, both controlling voltage and current. The characteristics presented in this figure are the generally observed behaviour in the LECs forming part of the IOS along the whole wafer, and not an anomaly. The devices always presented the switch from low-conduction states to high-conduction states before reaching the $10\times^6$ V/cm if controlling current very carefully. After this, as well as every time that voltage was the controlled variable, the devices presented the high conduction states related to emission not uniformly distributed along the area, described and analysed in the section 3.3.1. The conduction also presents a remarkably linear behaviour, which maintains at least until reaching 30 V, indicating it is likely ohmic within this range.

These results are unexpected, since the stand alone devices used as models did presented stable FA-EL, and the corresponding *J–V* behaviour.

The pilot wafer IOS$_{PolyGate}$, with polysilicon gates instead Al, was used to verify the presence of EL in the devices and observe its characteristics. Contrary to the expected by the design, and in accordance to the electronic transport behaviour, the electroluminescence observed was not FA-EL, but edge luminescence, which is due to mechanisms much similar to dot EL[63]. The figures 4.22 and 4.23 present images of this luminescence, and its normalized spectrum, respectively. The figure 4.23 also includes the spectra of the D-EL found in the samples DEV-Bi-SiO$_x$ and FA-EL in DEV-Bi-SiO$_{0.46}$, to compare with the results from the devices of the IOS. Note that the external FA-EL is the emission observed trough the poly gates, not the intrinsic one expected to be transmitted.

As expected, the emission clearly presents more similitude to D-EL than to the FA-EL observed in the single-standing LEC. Remember that
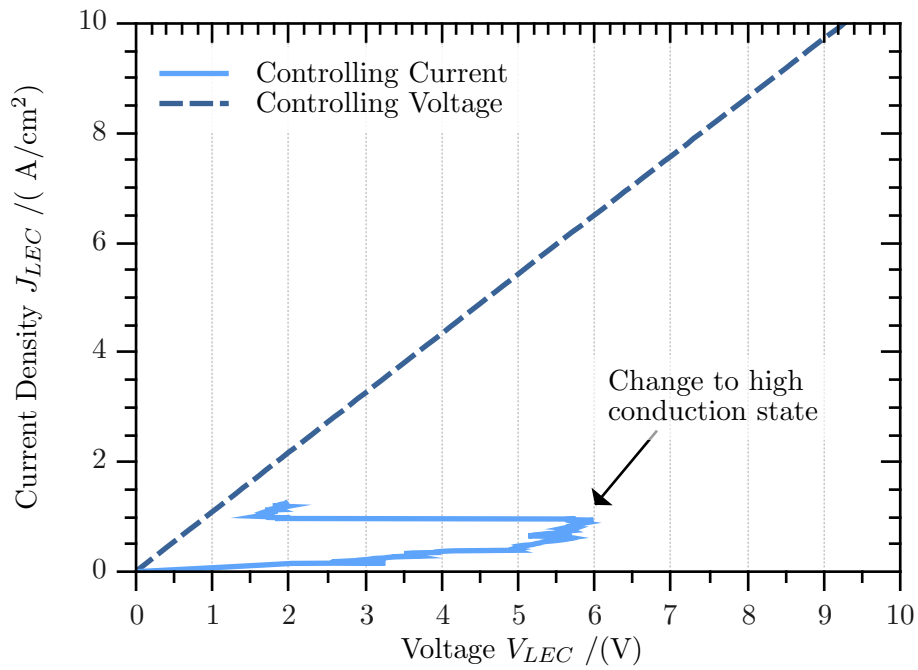
Figure 4.21: $J$–$V$ Behaviour of LEC embedded in the IOS. The continuous line presents the curve when controlling applied current, and the discontinuous when applying voltage.
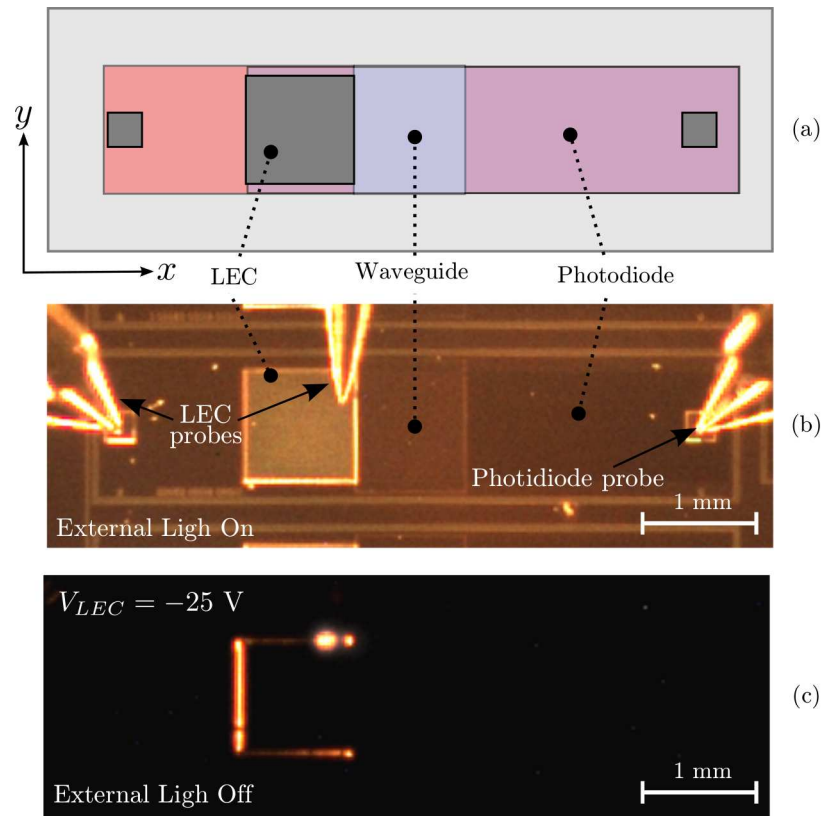
Figure 4.22: (a) Scheme of the top view of an IOS as defined in the figure 4.2. (b) Micro-photographs of the device in the set-up to analyse EL from the LEC with polysilicon gate and the external light on. (c) Micro-photograph of the same device under operation at $V_{LEC} = -25$ V with the external light off and EL in the edges of the gate.
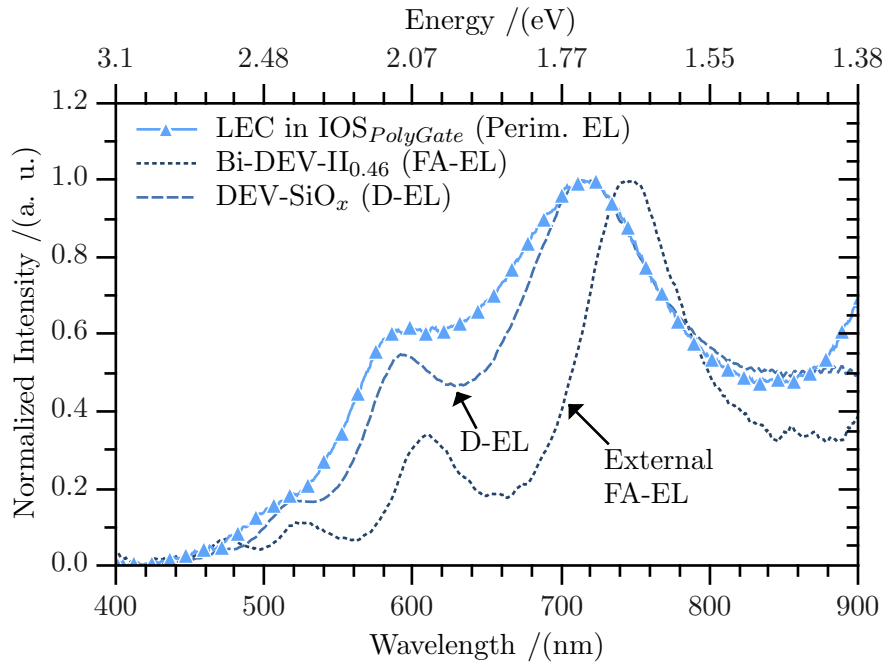
Figure 4.23: Spectrum of the perimeter EL from the LECs embedded in the IOS at $V_{LEC} = -25$ V as compared to the typical spectra of D-EL and the external FA-EL from the device Bi-DEV-II$_{0.46}$. Note that the external FA-EL is the one observed trough the poly gates, and not the intrinsic expected to be transmitted.

this type of EL does not depend on the silicon contents, and it is due to preferential conduction trough localized paths, instead of an uniform carrier flow distribution.

Note that in the case of the LEC of the IOS there is an increasing contribution after the 850 nm by light consistent to Si-Si transitions (1.1 eV emission). This is not expected to happen in devices with Al gate, and only in those from $IOS_{PolyGate}$, as this facilitates the silicon inter-band transition.

A plausible explanation for the presence of luminescence in the perimeter as opposite to FA-EL, is that the edges of the devices present lower resistance for the electrons in the interface between the field top oxide and the edges of the multi-layer structure of the LECs, possibly due to a higher concentration of defects. Then this would not happen in the single-standing LECs because the active layer structure is not in contact with the field oxide that promotes the presence of such defects.

This theory is supported by the fact that the current does not flow uniformly along the top area of the LEC as it happens in FA-EL, which manifests trough the differences in the current–voltage relations found when comparing devices with different gate length $I_l$ (which is defined in the figure 4.2). This is presented in the figure 4.24, which shows, for each of the three side lengths of the LEC gates $l_{LEC}$ fabricated, the relations between applied voltage $V_{LEC}$ and the flowing current $I_{LEC}$, the current per unit of area of the LEC $J_{LEC}$, and the current per unit of length of one side of the gate $I_{l-LEC}$.

As expected, the current $I_{LEC}$ flowing at a given applied voltage $V_{LEC}$ increases with longer gate edges, and hence greater areas. However, it can be seen that $J_{LEC}$ is not the same for all the $l_{LEC}$ values, as it should be for uniform carrier flow along the area, as it is typical for FA-EL.

On the other hand, if is assumed that the current flows exclusively trough a two dimensional sheet along the edges of the LEC, and defining the current per unit of length $I_{l-LEC}$ as the division of the flowing current $I_{LEC}$ by the length of the side of the gate $l_{LEC}$, then it would be expected that the $I_{l-LEC}$–$V_{LEC}$ relations would maintain the same regardless of the value of $l_{LEC}$, since all gates have the same square shape.

However, as the figure 4.24 shows, there are still noticeable discrepancies in these values, despite of finding significantly lower variations from length to length in the $I_{l-LEC}$–$V_{LEC}$ plots as compared to the results of current density from the $J_{LEC}$–$V_{LEC}$ relations.

Summarizing, the carrier transport and EL type in the devices embedded in the IOS are significantly different from those of the single-standing prototype LECs, but there still is EL in a wide spectra from wavelengths at least between the 450 nm and the 850 nm. These new effects are probably related to the field oxide, which is not present in the previously studied

114
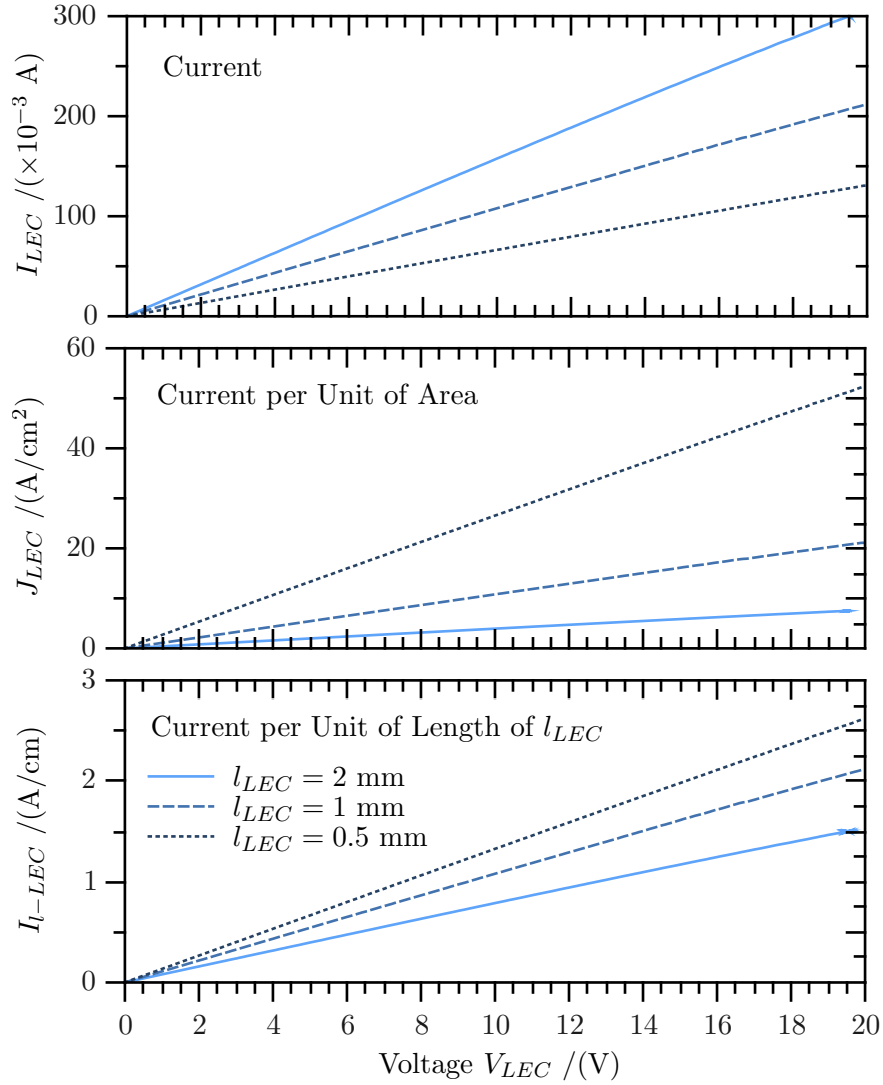
Figure 4.24: Relations between applied voltage $V_{LEC}$ and flowing current $I_{LEC}$, current per unit of area of the LEC $J_{LEC}$, the current per unit of length of one side of the gate $I_{l-LEC}$. Results are shown for LECs embedded in the IOS with side lengths $l_{LEC} = 2$ mm (continuous lines), $l_{LEC} = 1$ mm (discontinuous lines), and $l_{LEC} = 0.5$ mm (doted lines).

electroluminescent devices, as well as the main modification to the original architecture. However, still many future studies must be performed to gain understanding of these newly observed phenomena and their implications.

### 4.3.4. IOS Stimulating-Sensing results

The figure 4.25 shows, for the three studied gate sizes, the response of the photocurrent detected in the photodiode $I_{photo}$ as the voltage applied to the emitting device $V_{LEC}$ is incremented. Results for three different photodiode polarization voltages are presented, namely $V_{pn}$=0 V, $V_{pn}$=-15 V, and $V_{pn}$=-35 V.

There is a clear response by the photocurrent to the stimulus of the LEC in all the cases when the photodiode is reverse-biased. However, special attention must be paid to the possible responsibility of electronic cross talk in the readings, as the signal could be significantly influenced by this, and not only by actual light emission-transmission-detection processes.

If so, there are two possible ways in which this can occur: the leakage of current flowing to the back contact caused by the stimulus of the emitting device, and/or a modification in the effective voltage in the $p$–$n$ junction.

In the first case, the leaked carriers would contribute to the detected current in the diode, causing increments or decrements in the value of $I_{pn}$. However, this should be independent of the polarization of the photodiode, meaning that the measurements when $V_{pn}$=0 V would also be affected, which is not the case, as can be observed in the top plot of the figure 4.25.

In general, the lack of variation in the readings when applying $V_{pn}$=0 V regardless of the voltage and current in the emitter, is a very strong indication that the response in the photodiode does not come from electrical cross talk. On the contrary, it is consistent to the expected behaviour for the light detection, since when no polarization bias is applied to the diode, the depletion width is not wide enough to capture the e–h pairs generated by the transmitted light.

Regarding the modification of the voltage relying on the junction by influence of $V_{LEC}$, the experimental set-up characteristics makes it very unlikely (independently from the discussion on how influential could be this in the actual modulation of the depletion width), since the source used was programmed to maintain the voltage at a certain value, and the readings of this quantity are clearly registered without detectable change, as can be observed in the figure 4.26, which presents the values along time of all the registered parameters: $I_{pn}$, $V_{pn}$, $I_{LEC}$, and $V_{LEC}$.

This plot is from a particular case in which breakdown of the emitter was reached after applying a constant voltage $V_{LEC} = 30$ V for 130 seconds (the particular device had already been tested in several ways, and the response shown in this figure is not representative of its lifetime or that of the systems in general). As it can be observed, the value $V_{pn}$ remains constant at all

116
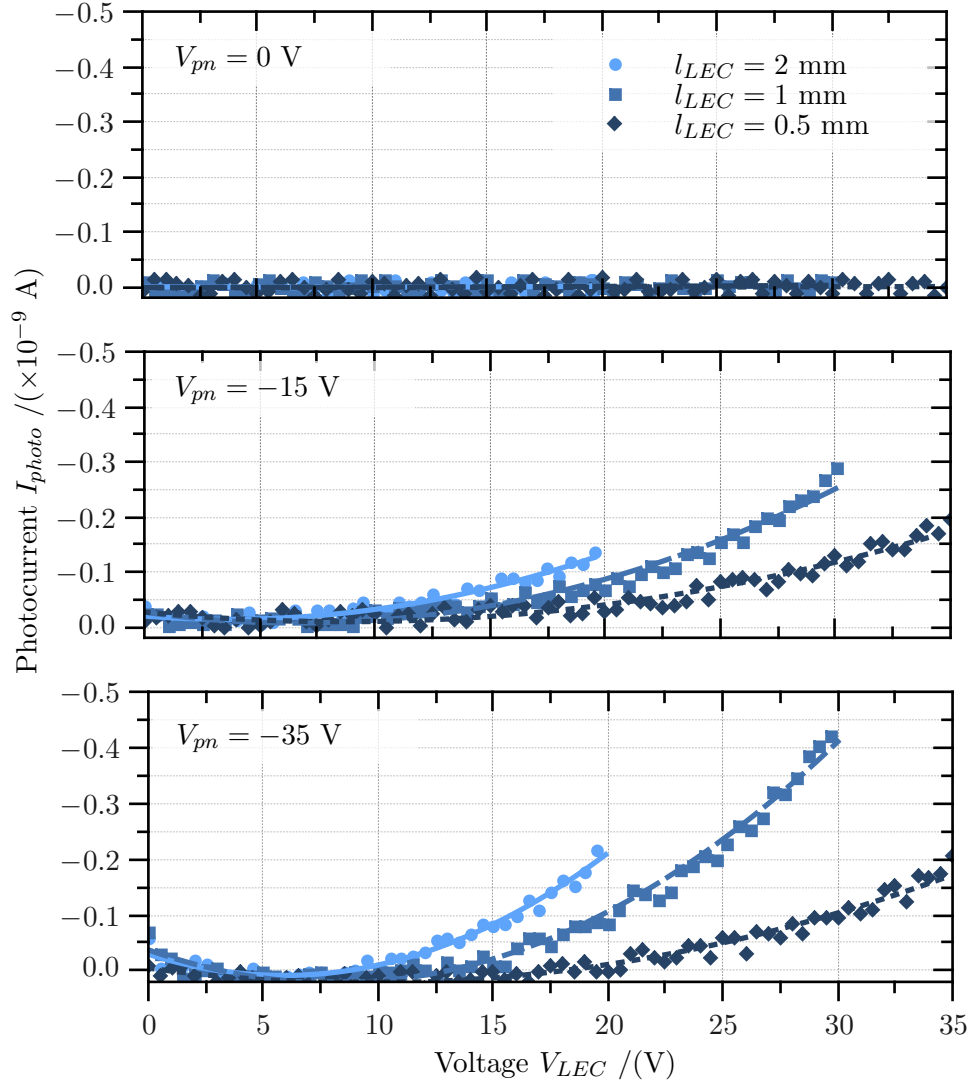
Figure 4.25: Photocurrent detected in the photodiode $I_{photo}$ versus voltage applied to the light emitting device $V_{LEC}$ for devices with side length $l_{LEC} = 2$ mm, $l_{LEC} = 1$ mm, and $l_{LEC} = 0.5$ mm. Data is presented for polarization voltages of $V_{pn}$=0 V, $V_{pn}$=-15 V, and $V_{pn}$=-35 V.
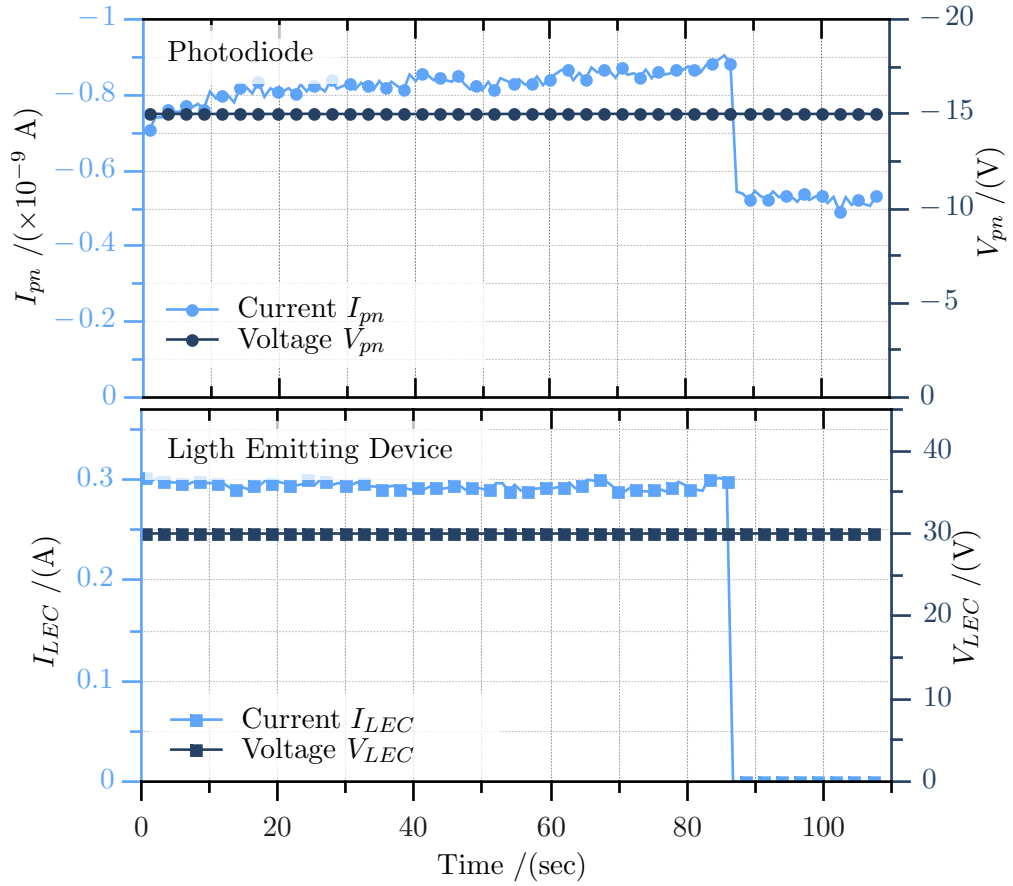
Figure 4.26: Voltage and current in photodiode, $V_{pn}$ and $I_{pn}$, respectively; and voltage and current applied to the emitting device, $V_{LEC}$ and $I_{LEC}$, respectively; versus time of stimulation. The left axis corresponds to the values for the current data, and the right axis to the values for the voltage data.

times regardless of the variations on the rest of the parameters, due to the action of the polarization source. It can also be observed how when the current stops flowing trough the LEC, the current registered along the diode drops to the dark condition value, because the LEC stops emitting light, hence no more carriers are photo-generated.

The figure 4.27, presents the $I_{pn}$ vs. $V_{pn}$ relation for reverse bias and different voltages applied to the emitter. Three regions can be identified for its analysis: the first with $V_{pn}$ between 0 V and $-1.5$ V, the second from $-1.5$ V to around $-26$ V, and the third with absolute voltage values above this.

In the first zone of the plot ($V_{pn}$ between 0 V and $-1.5$ V), the depletion region is between 3.1 µm and 4.2 µm-deep from the surface of the substrate, which is not wide enough as to capture a significant amount of carriers generated by the arriving photons, as it can be corroborated if examining the spectra of the emitted light depicted in the figure 4.23, since wavelengths at 705 nm, are absorbed beyond the 5.7 µm and wavelengths below 630 nm before reaching the $p$–$n$ junction at around 3.07 µm[85].

As the diode bias voltage is increased, the depletion layer expands and more carriers can be captured to contribute to the current. When reaching the second region of the plot ($V_{pn}$ between $-1.5$ V and $-26$ V), the wavelengths between 630 nm and 705 nm generate carriers well within the depletion layer, and as its width is constantly increased by the increment of $-V_{pn}$, the value of $-I_{pn}$ increases linearly, until around $V_{pn} = -26$ V are reached.

Around this point, a third region begins, in which the depletion layer is wide enough as to capture carriers generated by light with wavelengths longer than 705 nm[85]. Again, if examining the EL spectrum presented in the figure 4.23, it can be observed that there is a peak around the 720 nm. The possibility of capturing the carriers generated by this emission band translates in a change of the rate at which the current increases in the $I_{pn}$–$V_{pn}$ relation. This manifests as the separation between the linear projections and the experimental points after this voltage value that can be observed in the figure 4.27.

The concordance between the known characteristics of the emitted light and the modification of the $I_{pn}$ response by the changes in the applied bias voltage, corroborates the possibility of modulating the detected light controlling $V_{pn}$ as suggested in the section 4.2.2.

Note that the previously described behaviour is common for all the cases in which $V_{LEC} > 0$ V. Then, as long as the device is emitting light with a constant intensity, regardless of the voltage applied to it, there is a clear change of slope in the linear trend after reaching the point in which the depletion region can capture carriers generated by another luminescence band, indicating one more time that the response by the diode is due to

119
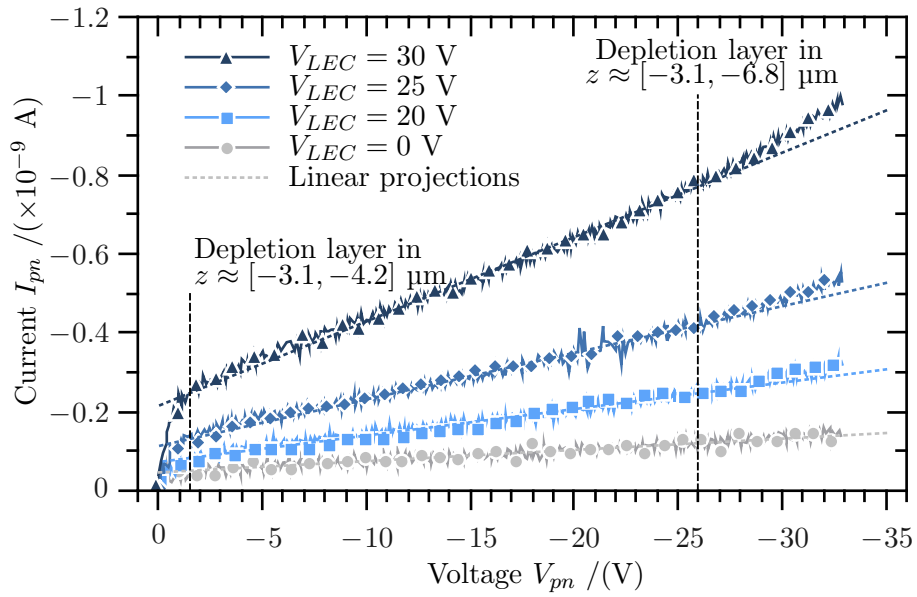
Figure 4.27: $I_{pn}$–$V_{pn}$ Relation when applying voltages to the light emitting capacitor of $V_{LEC} = 0$ V, $V_{LEC} = 20$ V, $V_{LEC} = 25$ V, and $V_{LEC} = 30$ V. The discontinuous lines are linear projections of the data according to its values between $V_{pn} = -1.5$ V and $V_{pn} = -36$ V.

optical and not electrical stimuli. The lack of changes in the trend for the curve when $V_{LEC} = 0$ V confirms this, and also rules out the possibility of the variations in the slope arising from a transport regime change in the leakage current of the diode.

Summarising, while this work only presents the initial analysis to the IOS, and many tests are required to know specific characteristics of it, the operation of the system based on the concept was proven to work as intended. There is an evident relation between the stimuli to the emitter, and the readings of the sensors, finding that the response is clearly due to optical stimulation in the photodiode, ruling out the electron-related crosstalk. This is supported by the theoretical projections on the response by the sensor according to the emitted light spectra, the known absorption depths of its bands, and the $p$–$n$ junction characteristics and behaviour. Based on such information, the possibility of modulating the width of the detected spectra trough the control of the bias voltage applied to the sensor was corroborated.

## 4.4. Conclusions

Based on the information gathered along the extensive studies presented in this work, an integrated optical system was proposed, consisting of a light emitter, a waveguide, and a photodiode, fabricated using only compatible CMOS processes and materials.

Two waveguide thickness were proposed, namely 60 nm and 500 nm, respectively restricted by the emitter architecture, and the limits on the thickness of the nitride given the destructive tensile forces faced during the necessary thermal treatments.

Computer simulations of the performance of the waveguide indicated that, although there are many possibilities for the optimization of the design, it was possible to use this simple one to transmit light with the characteristics of that emitted by the active material; in particular, modes of the $E_y$ components of the field.

The simulations indicated that the 60 nm-thick waveguide presents a higher total optical power for the injected and transmitted light, but also lower electric field confinement, increasing the risk of it reaching the substrate, as well as the possibility of having optical cross-talk, as significant part of the light may be transmitted trough the field oxide to reach detectors not intended to be stimulated. This problem is greater for wavelengths in the red zone of the spectrum. It was found that, in general, the shorter the wavelength, the lower the power lost outside the waveguide, indicating that the blue-shifted emission seems the best option regarding light transmission efficiency.

A prototype of the IOS was fabricated using the 60 nm-thick waveg-

uide configuration, and the parameters of the LEC with highest efficiency reported in the previous studies. The response of the test photodiodes was as expected from the theoretical projections, but the emission from the integrated LEC was not the same as the full area electroluminescence observed in the stand-alone device used as model, despite observing the same PL characteristics in the active layers. Instead, the luminescence was originated along edges of the devices, presenting spectra similar to those from localized bright dots observed in single-layer devices, which nevertheless, still is within the characteristics necessary for its transmission trough the fabricated waveguides. The carrier transport in the light emitting devices also presented similitude to that registered when this type of localized luminescence is observed. Such behaviour is most likely due to effects introduced by the interface between the active layers and the field oxide.

The viability of light transmission was confirmed by the finding of an unequivocal relation between an applied signal to the emitter, and a detected signal by the receiver, which delivered the positive outcome of the proof of the concept proposed, although still wide room for testing and improvements is to be explored and matter of future work.

Trough tests performed reverse-biasing the photodiode using different voltage values, it was possible to identify the stimulating-sensing relation as due to optical transmission, finding unlikely the existence of significant electronic cross-talk between emitter and sensor, although characterization of optical cross-talk between different IOS in the same chip, rather likely according to the simulations of the light confinement in the waveguide, is still to be performed. These experiments also indicated the possibility to modulate the width of the spectra to detect from the arriving light trough the control of the bias voltage applied to the photodiode.

# Chapter 5

# General Conclusion and Perspectives

The development of the present work started and evolved from extensive studies for the comprehension of the luminescent process taking place in the SRO and bi-layers of SRO-$Si_3N_4$, the approach for which was strongly based on the deep knowledge of the structure and characteristics of the materials. Then, such knowledge was used to move forward and use these materials to obtain an electroluminescent device, which was also studied to understand the processes taking place in it, in order to have a picture of its characteristics as accurate as possible. Next, this information was used to take another step forward, and design an integrated optical system theoretically functional, which was finally fabricated and experimentally tested, with positive results. All of this, using exclusively CMOS compatible techniques and materials. Thus, the work was divided in three main themes, namely the active materials, the discrete light emitting devices, and the integrated optical system.

Regarding the **active materials**, several SRO films with different silicon concentrations were fabricated and studied, observing photoluminescence with wide spectra in wavelengths between 650 nm and 1000 nm. This emission was found to be the result of the relative contribution by two main radiative mechanisms, namely quantum confinement-enabled recombination, and defect-related luminescence. In all the cases, the PL behaviour was in accordance to the results from structural characterization of the films, focusing in the final characteristics of the material, regardless if its fabrication technique, allowing the generalization of the conclusions. It was found that the silicon excess itself, does not dictate the emission characteristics of the SRO, and that a better parameter to define the material for this applications is the percentage of Si-Si links in it. This also indicated that the model that best fits the results is the core-shell one,

based on the so called Intermediate Model.

The deposition of a $Si_3N_4$ film on top of the SRO resulted in a modification of the known single-standing SRO film photoluminescent spectra. The main changes manifested as the addition of a band centred between the 400 nm and 590 nm, and a notorious improvement of the overall intensity. Such additional nitride-related luminescence was most likely originated in the oxynitride formed in the transition from one film to another, and consistent to defects caused by nitrogen dangling bonds and oxygen vacancies.

To obtain the **light emitting devices** based on the previously studied materials, capacitor-like structures were manufactured using doped poly-crystalline silicon as semi-transparet gate. Devices were fabricated with both SRO layer and SRO-$Si_3N_4$ bi-layer configurations, with a variety of material characteristics.

Two types of EL were identified, described as Dots-EL or D-EL, and Full Area-EL or FA-EL. The first was generally observed in single-layered devices, and consists of randomly-located bright spots, always presenting the same shape of EL spectrum, regardless of the atomic composition of the active materials, in contrast to the PL results. In addition, the current values for the operation (light emitting state) of the devices, variate according to the number of bright dots, which was also random.

On the other hand, the SRO-$Si_3N_4$ bi-layer devices presented Full Area-EL, which is characterized by an uniform illumination along the whole gate area. The spectra does variate according to material composition, and the radiative centres were found to be the same as those for PL from the active materials at least between 420 nm and 770 nm, despite the observed output light being significantly modified, as it is highly influenced by optical phenomena in the multi-layered system. The current-voltage relations on the devices were consistent and repeatable, as opposite to those for D-EL, and their conversion efficiencies are two orders of magnitude higher than those of the mono-layered devices. Such improvement was observed to be due to a significant reduction of the needed current to obtain EL, rather than a higher luminescence intensity.

Transceivers in **integrated optical systems** were designed using the bi-layered devices that presented the highest efficiency and reliability as models, embedding these in a silicon nitride waveguide, and adding a photodiode to detect the emitted and transmitted light.

Simulations of the light insertion in two proposed waveguide architectures were performed using the known intrinsic electroluminescence spectra. Some potential issues were identified, but it was corroborated the viability of light transmission and partial confinement.

There were simulated and studied the effects on the sensing photodiode by the needed thermal processes to obtain the emitter. There were also performed projections of its capability for detecting light with the charac-

teristics of that expected to be emitted, as well as the electrical conditions necessary for it.

After the theoretical verification of the plausibility of the successive emission, transmission, and detection of light in the system, and testing and resolving the technological issue of obtaining a proper bottom cladding for the waveguide, one of the integrated optical system designs was fabricated and characterized.

The emitter and sensor were first independently probed to test their individual performance. The photodiode behaved as expected according to its nominal characteristics. On the other hand, the emitting capacitor did not present the behaviour observed in the single-standing device from which it was replicated, as instead of obtaining the characteristics of FA-EL, the emission was localized along the edges of the gate, and the electric and optical characteristics presented higher similitude to those found in D-EL. Nevertheless, the light emission was still within the limits for its transmission trough the fabricated waveguide, as well as for its detection by the photodiode.

The operation of the system was confirmed by a clear identification of a stimulating–sensing relation in the emitter–photodiode characterization, which was clearly identified as due to optical reasons.

**Chalenges and perspectives**

It is clear that the efficiency values for the single-standing light emitting devices here reported are unacceptable for applications intended to compete with state of the art non-CMOS compatible light sources. To improve the performance in this regard, it would be necessary either to significantly increment in the luminescence intensity, or to reduce the necessary power to obtain it.

The augmentation of intensity would need an increment of the number of radiative centres, and/or a more efficient stimulation of them with the injected carriers. With the information gathered so far, none of these possibilities are likely to be achieved trough simply modifying the Si contents in the active material, which is the main controllable parameter during fabrication.

On the other hand, the reduction of applied power necessary to observe EL would need the lowering of the total electric field trough the diminution of the film thickness, in order to operate in the conduction regimes compatible with luminescence, and keep the emission spectra unmodified. This thinning is limited both technologically and intrinsically. The technological limit is already very close, at least with the techniques here proposed; and the intrinsic is limit is initially dictated by the size of the nano-agglomerates in the SRO, as these must be isolated from gate and substrate.

If the burden of the light emission is changed from being on the nano-

particles to being on the defects, the latter obstacle can be avoided, and thinner defect-based luminescent films could be theoretical achieved. For instance, the emission due to nitride in the bi-layers was comparatively higher than that due to SRO, and the transition layer, found to be the origin of luminescence, presents around half the thickness of the SRO film. Then, it seems promising to perform extensive analyses on the seldom studied SRO-$Si_3N_4$ transition zone of the system, since it can help to obtain more efficient devices in the future. Nonetheless, this approach has an important setback: the eventual need of dealing with the control of defects, which is generally complicated, and limits the influence of the design on the control over emitted spectra.

However, the advantages of the devices and materials here presented do not lie in the efficiency or intensity of light, but in the CMOS fabrication and integrability. This is why the results obtained with the functional Integrated Optical System prototype are very exciting, as they are the first tangible indication that the advantages of the CMOS compatible fabrication can really be exploited for useful potential applications of the SRO-based light emitting devices.

Of course, there still are many things to probe and improve, as it is expected from an initial test. One of the most relevant, is the identification of the reasons why the integrated devices, while not behaving in a completely unknown way, did not present the expected characteristics. In this regard, the great amount of information gathered during the studies to the stand-alone devices is expected to pay off, since the characteristics of its emission and electric behaviour, are well known in the D-EL devices.

While my suggestion is to keep pushing the applications of the already working system with the here presented results, I also think that the solution to this problem, as well as to improve the efficiency of the emitters, should be pursued in parallel.

Another issue, partially derived from the red shift in the obtained emission as compared to the expected, is the poor confinement of the light. The correction of the spectra from the devices, and the consequent emission of shorter wavelengths, would help the better confinement, but since an important portion of red light in the known spectra remains, cross talk issues are still to be expected.

To resolve this, the design of the photodiode could be modified to optimize the detection of the blue light while ignoring the rest of the spectra, and another approach would be to isolate each waveguide from each other in a chip with multiple IOS, for instance, using a regular guard ring. Of course, a better design of the waveguide would also be desirable in any case, as it could additionally increase the overall efficiency of the system.

The sensing photodiode, while proofing being a good solution to the detection, still can be improved and specialized. The previously mentioned

adjusting of its fabrication to optimize it for the detection of a particular portion of the light, is just one of many examples of the advantages that this tuning feature represents, in this case applied to the reduction of optical cross-talk. But these adjusting capabilities introduce great flexibility in the systems, which combined with the possibility of fabricating several in one chip enabled by the CMOS process, makes the IOS interesting for a variety of applications that can take advantage of the availability of transmitting and detecting several different wavelengths, such as chemical sensing.

Of course, the study, problem solution, and optimization of the IOS, still have a long way to go, but the results here presented open the door for the beginning of the use in practical applications, of the vast information and knowledge gathered during a long lasting work.

# Bibliography

[1] L. T. Canham. Silicon quantum wire array fabrication by electro-chemical and chemical dissolution of wafers. *Applied Physics Letters*, 57(10):1046, 1990.

[2] A. A. González-Fernández, J. Juvert, Alfredo. Morales-Sánchez, Jorge Barreto, M. Aceves-Mijares, and C. Domínguez. Comparison of electrical and electro-optical characteristics of light-emitting capacitors based on silicon-rich Si-oxide fabricated by plasma-enhanced chemical vapor deposition and ion implantation. *Journal of Applied Physics*, 111(5):053109–053109–9, March 2012.

[3] J. Juvert. *Development and optimization of silicon based light sources for integration into a sensor platform*. Ph. d. thesis, Universitat de Barcelona, 2013.

[4] Gong-Ru Lin, Chun-Jung Chi-Kuan Lin, Li-Jen Chou, and Yu-Lun Chueh. Oxygen defect and Si nanocrystal dependent white-light and near-infrared electroluminescence of Si-implanted and plasma-enhanced chemical-vapor deposition-grown Si-rich SiO[sub 2]. *Journal of Applied Physics*, 97(9):94306, 2005.

[5] Emmanouil Lioudakis, Andreas Othonos, G. C. Hadjisavvas, P. C. Kelires, and A. G. Nassiopoulou. Quantum confinement and interface structure of Si nanocrystals of sizes 3–5nm embedded in a-SiO2. *Physica E: Low-dimensional Systems and Nanostructures*, 38(1-2):128–134, April 2007.

[6] Y. Berencén, J. M. Ramírez, O. Jambois, C. Domínguez, J. A. RodríGuez, and B. Garrido. Correlation between charge transport and electroluminescence properties of Si-rich oxide/nitride/oxide-based light emitting capacitors. *Journal of Applied Physics*, 112(3):33114, 2012.

[7] M. Aceves-Mijares, N. D. Espinosa-Torres, F. Flores-Gracia, A. A. González-Fernández, R. López-Estopier, S. Román-López, G. Pedraza,

C. Domínguez, A. Morales, and C. Falcony. Composition and emission characterization and computational simulation of silicon rich oxide films obtained by LPCVD. *Surface and Interface Analysis*, 46(4):216–223, April 2014.

[8] M. Perálvarez, C. García, López M., B. Garrido, J. Barreto, C. Domínguez, and J. A. Rodríguez. Field effect luminescence from Si nanocrystals obtained by plasma-enhanced chemical vapor deposition. *Applied Physics Letters*, 89(5):51112, 2006.

[9] M. R. Esmaeili-Rad, A. Sazonov, A. G. Kazanskii, A. A. Khomich, and A. Nathan. Optical properties of nanocrystalline silicon deposited by PECVD. *Journal of Materials Science: Materials in Electronics*, 18(S1):405–409, March 2007.

[10] Atif Mossad Ali. Optical properties of nanocrystalline silicon films deposited by plasma-enhanced chemical vapor deposition. *Optical Materials*, 30(2):238–243, October 2007.

[11] B. M. Monroy, Aduljay Remolina Millán, M. F. García-Sánchez, A. Ponce, M. Picquart, and G. Santana. Structure and Optical Properties of Silicon Nanocrystals Embedded in Amorphous Silicon Thin Films Obtained by PECVD. *Journal of Nanomaterials*, 2011(i):1–9, 2011.

[12] P. F. Trwoga, A. J. Kenyon, and C. W. Pitt. Modeling the contribution of quantum confinement to luminescence from silicon nanoclusters. *Journal of Applied Physics*, 83(7):3789, 1998.

[13] Gong-Ru Lin, Chun-Jung Lin, and Kuo-Chen Yu. Time-resolved photoluminescence and capacitance–voltage analysis of the neutral vacancy defect in silicon implanted SiO[sub 2] on silicon substrate. *Journal of Applied Physics*, 96(5):3025, 2004.

[14] Liang Ding, T. P. Chen, Ming Yang, Jen It Wong, Zhanhong Cen, Yang Liu, Furong Zhu, and Ampere A. Tseng. Relationship Between Current Transport and Electroluminescence in $Si^+$-Implanted $SiO_2$ Thin Films. *IEEE Transactions on Electron Devices*, 56(11):2785–2791, November 2009.

[15] M. Aceves-Mijares, A. A. González-Fernández, R. López-Estopier, A. Luna-López, D. Berman-Mendoza, A. Morales, C. Falcony, C. Domínguez, and R. Murphy-Arteaga. On the Origin of Light Emission in Silicon Rich Oxide Obtained by Low-Pressure Chemical Vapor Deposition. *Journal of Nanomaterials*, 2012:1–11, 2012.

[16] B. Fazio, M. Vulpio, C. Gerardi, Y. Liao, I. Crupi, S. Lombardo, S. Trusso, and F. Neri. Residual Crystalline Silicon Phase in Silicon-Rich-Oxide Films Subjected to High Temperature Annealing. *Journal of The Electrochemical Society*, 149(7):G376, 2002.

[17] N. Daldosso, G. Das, S. Larcheri, G. Mariotto, G. Dalba, L. Pavesi, A. Irrera, F. Priolo, F. Iacona, and F. Rocca. Silicon nanocrystal formation in annealed silicon-rich silicon oxide films prepared by plasma enhanced chemical vapor deposition. *Journal of Applied Physics*, 101(11):113510, 2007.

[18] Eric G. Barbagiovanni, David J. Lockwood, Peter J. Simpson, and Lyudmila V. Goncharova. Quantum confinement in Si and Ge nanostructures: Theory and experiment. *Applied Physics Reviews*, 1(1):011302, March 2014.

[19] A. A. González-Fernández, J. Juvert, M. Aceves-Mijares, A. Llobera, and C. Dominguez. Influence of Silicon Binding Energy on Photoluminescence of Si-Implanted Silicon Dioxide. *ECS Transactions*, 49(1):307–314, October 2012.

[20] Yu. N. Novikov and V. a. Gritsenko. Short-range order in amorphous SiOx by x ray photoelectron spectroscopy. *Journal of Applied Physics*, 110(1):014107, 2011.

[21] F. Bell and L. Ley. Photoemission study of $SiO_x$ ($0 \leq x \leq 2$) alloys. *Physical Review B*, 37(14):8383–8393, May 1988.

[22] K. Hübner. Chemical bond and related properties of $SiO_2$. VII. Structure and electronic properties of the $SiO_x$ region of Si–$SiO_2$ interfaces. *Physica Status Solidi (a)*, 61(2):665–673, October 1980.

[23] Mallar Ray, T. S. Tuhin Shuvra Basu, Arpita Jana, Nil Ratan Bandyopadhyay, Syed Minhaz Hossain, Ashit Kumar Pramanick, and Robert F. Klie. Luminescent core-shell nanostructures of silicon and silicon oxide: Nanodots and nanorods. *Journal of Applied*, 107:64311, 2010.

[24] Sung Kim, Min Choul Kim, Suk-Ho Choi, Kyung Joong Kim, Han Na Hwang, and Chan Cook Hwang. Size dependence of Si 2p core-level shift at Si nanocrystal/$SiO_2$ interfaces. *Applied Physics Letters*, 91(10):103113, 2007.

[25] A. Irrera, F. Iacona, G. Franzò, S. Boninelli, D. Pacifici, M. Miritello, C. Spinella, D. Sanfilippo, G. Di Stefano, P.G. G Fallica, and F. Priolo. Correlation between electroluminescence and structural properties of Si nanoclusters. *Optical Materials*, 27(5):1031–1040, February 2005.

[26] Roushdey Salh. Defect Related Luminescence in Silicon Dioxide Network: A Review. In Sukumar Basu, editor, *Silicon Nanocluster in Silicon Dioxide: Cathodoluminescence, Energy Dispersive X-Ray Analysis, Infrared Spectroscopy Studies, Crystalline Silicon - Properties and Uses,*, chapter 8. InTech, 2011.

[27] Nae-Man Park, Tae-Soo Kim, and Seong-Ju Park. Band gap engineering of amorphous silicon quantum dots for light-emitting diodes. *Applied Physics Letters*, 78(17):2575, 2001.

[28] X. Wang, J. Zhang, L. Ding, B. Cheng, W. Ge, J. Yu, and Q. Wang. Origin and evolution of photoluminescence from Si nanocrystals embedded in a $SiO_2$ matrix. *Physical Review B*, 72(19), 2005.

[29] B. Garrido, M. Lopez, A. Perezrodriguez, C. Garcia, P. Pellegrino, R. Ferre, J. Moreno, J. Morante, C. Bonafos, and M. Carrada. Optical and electrical properties of Si-nanocrystals ion beam synthesized in $SiO_2$. *Nuclear Instruments and Methods in Physics Research Section B: Beam Interactions with Materials and Atoms*, 216:213–221, February 2004.

[30] A. D. Yoffe. Low-dimensional systems: Quantum size effects and electronic properties of semiconductor microcrystallites (zero-dimensional systems) and some quasi-two-dimensional systems. *Advances in Physics*, 51(2):799–890, March 2002.

[31] Tae-Wook Kim, Chang-Hee Cho, Baek-Hyun Kim, and Seong-Ju Park. Quantum confinement effect in crystalline silicon quantum dots in silicon nitride grown using $SiH_4$ and $NH_3$. *Applied Physics Letters*, 88(12):123102, 2006.

[32] E. G. Barbagiovanni, D. J. Lockwood, P. J. Simpson, and L. V. Goncharova. Quantum confinement in Si and Ge nanostructures. *Journal of Applied Physics*, 111(3):34307, 2012.

[33] Linards Skuja. Optically active oxygen-deficiency-related centers in amorphous silicon dioxide. *Journal of Non-Crystalline Solids*, 239(1-3):16–48, October 1998.

[34] I. Balberg. Electrical transport mechanisms in three dimensional ensembles of silicon quantum dots. *Journal of Applied Physics*, 110(6):061301, 2011.

[35] Rohana Perera, Akihiro Ikeda, Reiji Hattori, and Yukinori Kuroki. Trap assisted leakage current conduction in thin silicon oxynitride films grown by rapid thermal oxidation combined microwave excited plasma nitridation. *Microelectronic Engineering*, 65(4):357–370, May 2003.

131

[36] M. Perálvarez, J. Carreras, J. Barreto, A. Morales, C. Domínguez, and B. Garrido. Efficiency and reliability enhancement of silicon nanocrystal field-effect luminescence from nitride-oxide gate stacks. *Applied Physics Letters*, 92(24):241104, 2008.

[37] Hung-Yu Tai, Yung-Hsiang Lin, and Gong-Ru Lin. Wavelength-Shifted Yellow Electroluminescence of Si Quantum-Dot Embedded 20-Pair SiNx/SiOx Superlattice by Ostwald Ripening Effect. *IEEE Photonics Journal*, 5(1):6600110–6600110, February 2013.

[38] Xiang Wang, Rui Huang, Chao Song, Yanqing Guo, and Jie Song. Effect of barrier layers on electroluminescence from Si/SiOxNy multi-layer structures. *Applied Physics Letters*, 102(8):081114, 2013.

[39] L. F. Mao, Z. O. Wang, J. Y. Wang, and G. Y. Yang. The effective mass issues in light nitride silicon oxide. *Semiconductor Science and Technology*, 20(10):1078–1082, October 2005.

[40] S. M. Sze. *Semiconductor Devices: Physics and Technology*. Wiley, 2002.

[41] T. Hori. *Gate dielectrics and MOS ULSIs: principles, technologies, and applications*. Springer series in electronics and photonics. Springer, 1997.

[42] M. L. Green, E. P. Gusev, R. Degraeve, and E. L. Garfunkel. Ultrathin (<4 nm) $SiO_2$ and Si–O–N gate dielectric layers for silicon microelectronics: Understanding the processing, structure, and physical and electrical limits. *Journal of Applied Physics*, 90(5):2057, 2001.

[43] A. A. González-Fernández, J. Juvert, M. Aceves-Mijares, A. Llobera, and C. Dominguez. Influence by Layer Structure on the Output EL of CMOS Compatible Silicon-Based Light Emitters. *IEEE Transactions on Electron Devices*, 60(6):1971–1974, June 2013.

[44] C. G. Parker, G. Lucovsky, and J.R. Hauser. Ultrathin oxide-nitride gate dielectric MOSFET's. *IEEE Electron Device Letters*, 19(4):106–108, April 1998.

[45] A Morales, M. Aceves-Mijares, A. A. González-Fernández, K. Monfil-Leyva, J. Juvert, and C. Domínguez-Horna. Blue and red electroluminescence of silicon-rich oxide light emitting capacitors. In *Proceedings of SPIE*, volume 7719, page 77190N, Brussels, Belgium, 2010.

[46] A. Morales-Sanchez, K. Monfil-Leyva, A. A. González-Fernández, M. Aceves-Mijares, J. Carrillo, J. A. Luna-Lopez, C. Dominguez,

J. Barreto, and F. J. Flores-Gracia. Strong blue and red luminescence in silicon nanoparticles based light emitting capacitors. *Applied Physics Letters*, 99(17):171102, 2011.

[47] M. Perálvarez, J. Barreto, J. Carreras, A. Morales, D. Navarro-Urrios, Y. Lebour, C. Domínguez, and B. Garrido. Si-nanocrystal-based LEDs fabricated by ion implantation and plasma-enhanced chemical vapour deposition. *Nanotechnology*, 20(40):405201, October 2009.

[48] James F. Ziegler. SRIM-2003. *Nuclear Instruments and Methods in Physics Research Section B: Beam Interactions with Materials and Atoms*, 219-220:1027–1036, June 2004.

[49] I. H. Malitson. Interspecimen Comparison of the Refractive Index of Fused Silica. *Journal of the Optical Society of America*, 55(10):1205, October 1965.

[50] Dieter K. Schroder. *Semiconductor Material and Device Characterization*. John Wiley & Sons, Inc., Hoboken, NJ, USA, third edition, 2006.

[51] Alain C. Diebold, David Venables, Yves Chabal, David Muller, Marcus Weldon, and Eric Garfunkel. Characterization and production metrology of thin transistor gate oxide films. *Materials Science in Semiconductor Processing*, 2(2):103–147, July 1999.

[52] Fabio Iacona, Giorgia Franzò, and Corrado Spinella. Correlation between luminescence and structural properties of Si nanocrystals. *Journal of Applied Physics*, 87:1295, 2000.

[53] Jorge Barreto, Alfredo Morales, Mariano Perálvarez, Blas Garrido, and Carlos Domínguez. Stoichiometry of silicon-rich dielectrics for silicon nanocluster formation. *Physica Status Solidi (c)*, 8(3):804–807, March 2011.

[54] A. Morales, J. Barreto, C. Dominguez, M. Riera, M. Aceves, and J. Carrillo. Comparative study between silicon-rich oxide films obtained by LPCVD and PECVD. *Physica E: Low-dimensional Systems and Nanostructures*, 38(1-2):54–58, 2007.

[55] Jason H. Rouse and Gregory S. Ferguson. Preparation of thin silica films with controlled thickness and tunable refractive index. *Journal of the American Chemical Society*, 125(50):15529–15536, December 2003.

[56] G. Hollinger and F. J. Himpsel. Probing the transition layer at the $SiO_2$-Si interface using core level photoemission. *Applied Physics Letters*, 44(1):93, 1984.

[57] Andrew Proctor and Peter M. a. Sherwood. Data analysis techniques in x-ray photoelectron spectroscopy. *Analytical Chemistry*, 54(1):13–19, January 1982.

[58] D.-Q. Yang, Jean-Numa Gillet, M. Meunier, and E. Sacher. Room temperature oxidation kinetics of Si nanoparticles in air, determined by x-ray photoelectron spectroscopy. *Journal of Applied Physics*, 97(2):24303, 2005.

[59] K. B. Clark, J. A. Bardwell, and J. M. Baribeau. Physical characterization of ultrathin anodic silicon oxide films. *Journal of Applied Physics*, 76(5):3114, 1994.

[60] W. M. Lau and X. W. Wu. Measurements of interface state density by X-ray photoelectron spectroscopy. *Surface Science*, 245(3):345–352, April 1991.

[61] R. Ferre, B. Garrido, P. Pellegrino, M. Perálvarez, C. García, J. A. Moreno, J. Carreras, and J. R. Morante. Optical-geometrical effects on the photoluminescence spectra of Si nanocrystals embedded in $SiO_2$. *Journal of Applied Physics*, 98(8):84319, 2005.

[62] J. Barreto, J. Rodriguez, M. Peralvarez, A. Morales, B. Garrido, and C. Dominguez. Photoluminescence characterization of silicon nanostructures embedded in silicon oxide. *Superlattices and Microstructures*, 43(5-6):588–593, 2008.

[63] Joan Juvert, A. A. González-Fernández, Andreu Llobera, and C. Dominguez. The effect of absorption and coherent interference in the photoluminescence and electroluminescence spectra of SRO/SRN MIS capacitors. *Optics Express*, 21(8):1513–1516, 2013.

[64] Chi-mei Mo, Lide Zhang, Cunyi Xie, and Tao Wang. Luminescence of nanometer-sized amorphous silicon nitride solids. *Journal of Applied Physics*, 73(10):5185, 1993.

[65] G. Sombrio, P. L. Franzen, R. L. Maltez, L. G. Matos, M. B. Pereira, and H. Boudinov. Photoluminescence from $SiN_xO_y$ films deposited by reactive sputtering. *Journal of Physics D: Applied Physics*, 46(23):235106, June 2013.

[66] Yuzhen Liu, Yuqin Zhou, Wanquan Shi, Lingli Zhao, Baoyin Sun, and Tianchun Ye. Study of photoluminescence spectra of Si-rich SiNx films. *Materials Letters*, 58(19):2397–2400, July 2004.

134

[67] Y. Berencén, Josep Carreras, O. Jambois, J. M. Ramírez, J. A. Rodríguez, C. Domínguez, Charles E. Hunt, and B. Garrido. Metal-nitride-oxide-semiconductor light-emitting devices for general lighting. 19(May):1048–1052, 2011.

[68] A. Morales-Sánchez, J. Barreto, C. Domínguez, M. Aceves-Mijares, M. Perálvarez, B. Garrido, and J. A. Luna-López. DC and AC electroluminescence in silicon nanoparticles embedded in silicon-rich oxide films. *Nanotechnology*, 21(8):085710, 2010.

[69] A. A. González-Fernández, M. Aceves-Mijares, A. Morales-Sánchez, and K. Leyva. Intense whole area electroluminescence from low pressure chemical vapor deposition-silicon-rich oxide based light emitting capacitors. *Journal of Applied Physics*, 108(4):43105, 2010.

[70] J. Barreto, M. Peralvarez, J. Antoniorodriguez, A. Morales, M. Riera, M. Lopez, B. Garrido, L. Lechuga, and C. Dominguez. Pulsed electroluminescence in silicon nanocrystals-based devices fabricated by PECVD. *Physica E: Low-dimensional Systems and Nanostructures*, 38(1-2):193–196, 2007.

[71] J. Juvert, A. A. González-Fernández, A. Morales-Sanchez, J. Barreto, M. Aceves, A. Llobera, and C. Dominguez. DC Electroluminescence Efficiency of Silicon Rich Silicon Oxide Light Emitting Capacitors. *Journal of Lightwave Technology*, 31(17):2913–2918, September 2013.

[72] A. Morales, J. Barreto, C. Domínguez-Horna, M. Aceves-Mijares, J. A. Luna-López, A. Morales-Sánchez, C. Domínguez, and M. Aceves. The mechanism of electrical annihilation of conductive paths and charge trapping in silicon-rich oxides. *Nanotechnology*, 20(4):045201, January 2009.

[73] D. J. DiMaria, J. R. Kirtley, E. J. Pakulis, D. W. Dong, T. S. Kuan, F. L. Pesavento, T. N. Theis, J. a. Cutro, and S. D. Brorson. Electroluminescence studies in silicon dioxide films containing tiny silicon islands. *Journal of Applied Physics*, 56(2):401, 1984.

[74] A. Marconi, A. Anopchenko, G. Pucker, and L. Pavesi. Power efficiency estimation of silicon nanocrystals based light emitting devices in alternating current regime. *Applied Physics Letters*, 98(May):1–3, 2011.

[75] H. Kim, J. S. Horwitz, G. Kushto, A. Piqué, Z. H. Kafafi, C. M. Gilmore, and D. B. Chrisey. Effect of film thickness on the properties of indium tin oxide thin films. *Journal of Applied Physics*, 88(10):6021, 2000.

[76] A. Marconi, A. Anopchenko, M. Wang, G. Pucker, P. Bellutti, and L. Pavesi. High power efficiency in Si-nc/SiO$_2$ multilayer light emitting devices by bipolar direct tunneling. *Applied Physics Letters*, 94(22):221110, 2009.

[77] M. Wang, A. Anopchenko, A. Marconi, E. Moser, S. Prezioso, L. Pavesi, G. Pucker, P. Bellutti, and L. Vanzetti. Light emitting devices based on nanocrystalline-silicon multilayer structure. *Physica E: Low-dimensional Systems and Nanostructures*, 41(6):912–915, May 2009.

[78] D. J. DiMaria, E. Cartier, and D. Arnold. Impact ionization, trap creation, degradation, and breakdown in silicon dioxide films on silicon. *Journal of Applied Physics*, 73(7):3367, 1993.

[79] Philippe Jamet, Sima Dimitrijev, and Philip Tanner. Effects of nitridation in gate oxides grown on 4H-SiC. *Journal of Applied Physics*, 90(10):5058, 2001.

[80] V. J. Cadarso, A. Llobera, I. Salinas, D. Izquierdo, I. Garcés, and C. Domínguez. Silicon-based rectangular hollow integrated waveguides. *Optics Communications*, 281(6):1568–1575, March 2008.

[81] D. Izquierdo. *Guías Ópticas Fertemente Mmultimodales: Aplicación a Sensores Ópticos e Iintegración.* Ph. d. thesis, Universidad de Zaragoza, Spain, 2011.

[82] B. El-Kareh. *Fundamentals of Semiconductor Processing Technology.* Kluwer Academic Publishers, cop., Boston, 1995.

[83] W R Runyan. *Silicon semiconductor technology.* Texas Instruments electronics series. McGraw-Hill, New York: USA, 1st edition, 1965.

[84] P. Pichler. ICECREM, 1996.

[85] Martin A. Green. Self-consistent optical parameters of intrinsic silicon at 300K including temperature coefficients. *Solar Energy Materials and Solar Cells*, 92(11):1305–1310, November 2008.

# Appendices

# Appendix A

# List of Publications

Following, it is presented a list in chronological order of the works published during the period of development of the thesis.

1. Aceves-Mijares, M., Espinosa-Torres, N. D., Flores-Gracia, F., **González-Fernández, A. A.**, López-Estopier, R., Román-López, S., Falcony, C. Composition and emission characterization and computational simulation of silicon rich oxide films obtained by LPCVD. *Surface and Interface Analysis*, 46(4), 216–223, 2014. doi:10.1002/sia.5212

2. **González-Fernández, A. A.**, Juvert, J., Aceves-Mijares, M., Llobera, A., & Dominguez, C. Influence by Layer Structure on the Output EL of CMOS Compatible Silicon-Based Light Emitters. *IEEE Transactions on Electron Devices*, 60(6), 1971–1974, 2013. doi:10.1109/TED.2013.2258158

3. **González-Fernández, A. A.**, Juvert, J., Jimenez-Jorquera, C., Aceves-Mijares, M., & Dominguez, C. On the role of material parameters in the luminescence of Si-nanostructures embedded in SiO2. *Proceedings of 2013 EMN Fall Meeting*, 24, 2013.

4. **González-Fernández, A. A.**, Juvert, J., Llobera, A., Jimenez-Jorquera, C., Aceves, M., & Dominguez, C. Luminescence from SRO-Si3N4 interface in nano-structured bi-layers. *Proceedings of CETC2013 Conference on Electronics, Telecommunications and Computers*, 29, 2013.

5. Juvert, J., **Gonzalez Fernandez, A. A.**, Morales-Sanchez, A., Barreto, J., Aceves, M., Llobera, A., & Dominguez, C. DC Electroluminescence Efficiency of Silicon Rich Silicon Oxide Light Emitting Capacitors. *Journal of Lightwave Technology*, 31(17), 2913–2918, 2013. doi:10.1109/JLT.2013.2276435

6. Juvert, J., **González-Fernández, A. A.**, Llobera, A., & Dominguez, C. The effect of absorption and coherent interference in the photoluminescence and electroluminescence spectra of SRO/SRN MIS capacitors. *Optics Express*, 21(8), 1513–1516, 2013. doi:10.1364/OE.21.010111

7. Llorens, J., Postigo, P., Juvert, J., **González-Fernández, A. A.**, & Domínguez, C. Enhancement of light extraction in silicon-rich oxide light-emitting diodes by one-dimensional photonic crystal gratings. In G. S. Subramania & S. Foteinopoulou (Eds.), *Proceedings of SPIE*, 8808, 88080D, 2013. doi:10.1117/12.2023946

8. **González-Fernández, A. A.**, Juvert, J., Morales-Sánchez, A., Barreto, J., Aceves-Mijares, M., & Domínguez, C. Comparison of electrical and electro-optical characteristics of light-emitting capacitors based on silicon-rich Si-oxide fabricated by plasma-enhanced chemical vapor deposition and ion implantation. *Journal of Applied Physics*, 111(5), 053109–053109–9, 2012. doi:10.1063/1.3692082

9. **González-Fernández, A. A.**, Juvert, J., Aceves-Mijares, M., Llobera, A., & Dominguez, C. Influence of Silicon Binding Energy on Photoluminescence of Si-Implanted Silicon Dioxide. *ECS Transactions*, 49(1), 307–314, 2012. doi:10.1149/04901.0307ecst

10. Aceves-Mijares, M., **González-Fernández, A. A.**, López-Estopier, R., Luna-López, A., Berman-Mendoza, D., Morales, A., Murphy-Arteaga, R. On the Origin of Light Emission in Silicon Rich Oxide Obtained by Low-Pressure Chemical Vapor Deposition. *Journal of Nanomaterials*, 2012, 1–11, 2012. doi:10.1155/2012/890701

11. Juvert, J., **González-Fernández, A. A.**, Morales-sánchez, A., Barreto, J., Aceves-mijares, M., & Domínguez, C Analysis of the electrical behavior of silicon rich silicon oxides Análisis del comportamiento eléctrico de óxidos de silicio enriquecidos en silicio. *Óptica Pura Y Aplicada*, 45(2), 155–161, 2012. doi:10.7149/OPA.45.2.155

12. Morales-Sanchez, A., Monfil-Leyva, K., **González-Fernández, A. A.**, Aceves-Mijares, M., Carrillo, J., Luna-Lopez, J. a., Flores-Gracia, F. J. Strong blue and red luminescence in silicon nanoparticles based light emitting capacitors. *Applied Physics Letters*, 99(17), 171102, 2011. doi:10.1063/1.3655997

# Appendix B

# Relevant Published Papers

## B.1.  Journal of Applied Physics, 111(5), (2012)

This work was performed jointly with J. Juvert, and equal contributions to its development and results interpretation are to be credited to both of us.

# Comparison of electrical and electro-optical characteristics of light-emitting capacitors based on silicon-rich Si-oxide fabricated by plasma-enhanced chemical vapor deposition and ion implantation

A. A. González-Fernández,[1,a)] J. Juvert,[1] Alfredo Morales-Sánchez,[2] Jorge Barreto,[3] M. Aceves-Mijares,[4] and C. Domínguez[1]

[1]*Institut de Microelectrònica de Barcelona, CNM-CSIC, Campus UAB, Bellaterra 08193, Spain*
[2]*Centro de Investigación en Materiales Avanzados S. C., Unidad Monterrey-PIIT, Apodaca, Nuevo León 66600, Mexico*
[3]*NPRL, School of Physics and Astronomy, University of Birmingham, Birmingham B15 2TT, United Kingdom*
[4]*INAOE, Dpt. of Electronics, P.O. Box 51, Puebla, Pue. 72000, Mexico*

This work presents electrical and electro-optical studies performed on light-emitting capacitors with silicon-rich silicon oxide fabricated by plasma-enhanced chemical vapor deposition and by the implantation of Si ions in thermally grown $SiO_2$. The influence of the fabrication technique and silicon content on electrical, electro-optical, and emission spectra characteristics has been studied. Results on the electrical behavior show a significant dependence on both the fabrication technique and Si content that translates in variations on electroluminescence with fabrication technique and silicon excess. © *2012 American Institute of Physics*. [http://dx.doi.org/10.1063/1.3692082]

## I. INTRODUCTION

For almost two decades, there has been an important study and improvement in the knowledge and optimization of luminescence in silicon-based materials. Ever since the discovery of photoluminescence in porous silicon,[1] new materials have been tested to obtain improved chemical stability and fabrication compatibility with the integrated circuit fabrication standards. Silicon-rich silicon oxide (SRO) is a promising material, as it is highly stable and can be fabricated by a variety of methods, many of which are fully compatible with complementary metal-oxide-semiconductor (CMOS) technology, such as low pressure chemical vapor deposition (LPCVD),[2–4] plasma-enhanced chemical vapor deposition (PECVD),[5–7] and the implantation of silicon ions on silicon dioxide.[8–11]

Despite the exciting early results, the difficulties in understanding the mechanisms taking place in this complex material have kept back the optimization of the electroluminescence widely observed in it. The luminescence has been mainly attributed to quantum confinement or to defects in the material and a combination of both.[7,12,13] The conduction has been explained by Fowler-Nordheim injection,[14] trap-assisted-tunneling,[15] and direct tunneling,[6] among others. However, no consensus has been reached on either luminescence or current transport. Although recent studies reveal that the electrical and optical characteristics of devices based in those materials depend significantly on technological parameters,[3,5,8] a clear relation with the fabrication technique is still missing.

In this work, electrical and electro-optical studies, under direct current (DC), of capacitive devices based on SRO with several different content of silicon excesses ranging from 6% to 16% and fabricated by both PECVD (PECVD-SRO) and silicon ion implantation into thermally grown $SiO_2$ (II-SRO) are presented. The objective of the study is to get a step forward in the elucidation of the mechanism responsible for the electro-optical properties of the materials containing silicon nanoparticles.

## II. EXPERIMENTAL

Silicon-rich silicon oxide films were fabricated by plasma-enhanced chemical vapor deposition (PECVD-SRO samples) and silicon ion implantation of thermally grown $SiO_2$ (II-SRO samples). A set of samples was obtained for each fabrication technique, and the fabrication parameters were selected based on the best luminescence results obtained in previous studies.[13–17] In all the cases, the SRO layers were deposited on 4" p-type Si wafers with (100) crystalline orientation and resistivity between 0.1 and 1.4 $\Omega \times$ cm. The PEVCD-SRO layers were deposited using undiluted $SiH_4$ and $N_2O$ as precursor gases. The silicon excess of the layers $(XS_{Si})$[18] was controlled by modulating the ratio of the partial pressures produced by the precursor gases in the chamber $(P[N_2O]/P[SiH_4])$. The deposition times were selected to obtain films with a thickness close to 45 nm. During deposition, the substrate temperature and radio frequency power density were $300\,^\circ$C and $0.07$ W/cm$^2$, respectively. After deposition, all the PECVD samples were annealed in $N_2$ atmosphere at $1250\,^\circ$C for 60 min to induce $Si$ nucleation and the formation of silicon nano-particles (Si-nps). The characteristics of the fabricated films are summarized in Table I. A more detailed description of the PECVD fabrication process can be found elsewhere.[16]

The fabrication of the II-SRO films started with a dry thermal growth of a 60-nm-thick $SiO_2$ layer at $1000\,^\circ$C. Then, a 30-nm-thick silicon nitride ($Si_3N_4$) film was deposited by LPCVD at $800\,^\circ$C using $SiH_2Cl_2$ and $NH_3$ as precursor gases.

a)Electronic mail: alfredo.gonzalez@imb-cnm.csic.es.

**111**, 053109-1

142

TABLE I. PECVD-SRO characteristics and fabrication parameters. Thickness was obtained before thermal annealing.

| Sample | $\dfrac{P[N_2O]}{P[SiH_4]}$ | Silicon excess (at. %) | Thickness (nm) |
|---|---|---|---|
| PECVD-1 | 13 | $6.0 \pm 0.2$ | $53 \pm 5$ |
| PECVD-2 | 10 | $8.0 \pm 0.6$ | $55 \pm 6$ |
| PECVD-3 | 7 | $12.0 \pm 0.2$ | $60 \pm 9$ |
| PECVD-4 | 5 | $16.0 \pm 0.6$ | $59 \pm 7$ |

Two consecutive $Si$ ions implantations were performed on the bi-layer structure in order to obtain a uniform $Si$ distribution within the $SiO_2$ accordingly to stopping and range of ions in matter (SRIM) simulations.[19] The implantation doses and the final $Si$ excesses are shown in Table II.

In this case, samples were annealed at $1100\,°C$ for $4\,h$ in a $N_2$ atmosphere to induce $Si$ agglomeration,[10] and the nitride layer was removed by wet etching. Details on Si-implanted SRO fabrication technique can be found elsewhere.[14,16]

After the PECVD-SRO and II-SRO fabrication, the following steps were carried out for both sample sets: A 350-nm-thick n+ polycrystalline silicon layer (poly) highly doped with $POCl_3$ was deposited by LPCVD. A photolithographic process was used to define the poly pattern to be etched and fabricate squares with areas of $9.604 \times 10^{-3}$ $cm^2$ and $2.304 \times 10^{-3}$ $cm^2$ on top of the SRO. Finally, a $1.0$-$\mu$m-thick $Al$ layer was deposited by sputtering on the back of every wafer, and the structures were all sintered in forming gas at $350\,°C$. The resulting device is the light-emitting capacitor (LEC) schematically represented in Fig. 1.

In order to take into account the influence of the gate on the observed emission spectra, a poly layer was deposited on a quartz substrate under the same conditions as those used for the devices; its transmittance was then obtained using an Ocean Optics HL-2000-CAL as a light source and an Ocean Optics QE65000 spectrometer.

Electrical measurements were performed at room temperature on 5 devices from each wafer in a Karl Süss probe station with Süss Microtech PH120 probe heads and $7\,\mu$m tungsten probes. Current-voltage (I-V) characteristics were obtained with a Keithley 2430 source meter, and capacitance-voltage (C-V) characteristics were measured with an HP 4192 A LF impedance analyzer.

The electrical measurements protocol has been the same in all samples: firstly, the capacitance-voltage curves were obtained on as-fabricated devices (those that have never been electrically stressed previously in any way) from inversion to accumulation and back to inversion with a voltage ramp of 0.1 V/s and a 30 mV coupled AC signal at 100 KHz.

In order to induce carrier generation, devices were exposed to white illumination from a $10\,W$ halogen light bulb for 5 seconds prior to the C-V characterization. After obtaining the C-V curves, current-voltage characteristics were measured applying a voltage sweep from 0 to $-9$ MV/cm (considering the thickness of each sample); this is referred to as electrical stress. Finally, the capacitance-voltage curves were acquired again under the same conditions to verify possible changes in their characteristics.

The electroluminescence spectra have been acquired with an Ocean Optics QE65000 spectrometer. All spectra have been corrected for the responsivity of the instrument. Electroluminescence-voltage and electroluminescence-current measurements were performed with a custom-made software that controlled the stimulus applied by the Keithley 2430 source meter as it gathered the photocurrent results obtained by a Newport MPC35 power meter using a Newport 918 D-UV-OD3 photodetector placed directly on top of the devices. The results were also corrected, taking into account the emission spectra and the responsivity of the photodetector.

At least five different devices have been measured for each wafer (from Tables I and II). However, for the sake of clarity, only the most relevant curves are shown in the figures.

## III. RESULTS AND DISCUSSION

### A. Electrical

#### 1. Capacitance-voltage

The electrical characteristics obtained from the C-V measurements are summarized in Table III. Figure 2 shows the typical behavior of the hysteresis C-V curves obtained before and after the voltage sweep. The scale in the ordinate axis represents the ratio of the maximum measured capacitance value ($C_{SRO}$) to that of an equivalent stoichiometric $SiO_2$ capacitor ($C_0$). This is to make possible the comparison of the results by ruling out the effects introduced by the thickness of the material, while keeping the effect of its relative permittivity ($\varepsilon_r$). Figure 3 shows the behavior of the maximum capacitance/relative permittivity as the $Si$ content varies for each fabrication technique; $\varepsilon_r$ values were extracted from C-V results (assuming the SRO to be a linearly homogeneous material and neglecting edge effects in the electric field), except for the value for $SiO_2$, which is taken from Ref. 20. The error values are dominated by the uncertainty from the thickness of the layers rather than by the observed variations in capacitance values, which were marginal. These relatively high error values do not allow us to identify differences related to the fabrication techniques in

TABLE II. Ion implantation-SRO characteristics and fabrication parameters. Thickness was obtained before thermal annealing.

| Sample | 1st dose ($\times 10^{16}\,cm^{-2}$) | 2nd dose ($\times 10^{16}\,cm^{-2}$) | Silicon exc. (at. %) | Thickness (nm) |
|---|---|---|---|---|
| II-1 | 1.2 | 5.0 | $12.0 \pm 0.3$ | $45 \pm 5$ |
| II-2 | 1.4 | 6.0 | $13.0 \pm 0.4$ | $48 \pm 4$ |
| II-3 | 1.8 | 7.2 | $14.0 \pm 0.2$ | $49 \pm 9$ |
| II-4 | 2.0 | 8.3 | $15.0 \pm 0.5$ | $57 \pm 1$ |

FIG. 1. (Color online) Schematic of the general structure of LECs (the thickness of the layers is not on scale).

the $\varepsilon_r$ and $XS_{Si}$ relation. However, an evident increase in permittivity with the silicon content can be observed, regardless of the technique, as expected.

The charge-trapping characteristics showed a clear dependence on the silicon excess and notorious differences between PECVD and II samples. The charge trapped in the SRO ($Q_{SRO}$) for these particular stimulus conditions and measurement protocol was calculated from the obtained capacitance of the devices and the shifts in the flatband voltage during C-V hysteresis cycles ($\Delta V_{fb}$). It was assumed that the charge from mobile ions trapped in the SRO-Si interface is much lower than $Q_{SRO}$, and the C-V characteristics show the possibility of $V_{fb}$ variations being caused by charge traps in the SRO-Si interface to be negligible; hence, $Q_{SRO}$ was calculated from the equation

$$Q_{SRO} = -\Delta V_{fb} \times C. \quad (1)$$

The results are shown in Table III and Fig. 4. Note that the $Q_{SRO}$-$XS_{Si}$ behavior is opposite in materials obtained with different techniques. This is because there is a compromise between charge trapping and conductivity: with more Si-nps, more charge-trapping centers can be found in the material, but it is also more conductive (as will be shown in the current-voltage results section), making the de-trapping of charge easier as less resistive paths to the substrate (or gate) are formed. This is why PECVD-SRO samples with higher $XS_{Si}$ trapped more charge, while II-SRO samples retain less charge as the silicon content increases.

A report on structural characterization with energy-filtered transmission electron microscopy (EFTEM) profiles of the active materials is presented in Ref. 14. In this study, it was shown that II-SRO presents higher density and smaller

size of Si-nps than PECVD-SRO with the same silicon concentration; as for $XS_{Si} \approx 12\%$, II-SRO presents values for density and size of $\sim 1.6 \times 10^{18}\,\mathrm{cm^{-3}}$ and $\sim 3.10\,\mathrm{nm}$, respectively, while for PECVD-SRO, the density and size of Si-nps are $\sim 9.0 \times 10^{17}\,\mathrm{cm^{-3}}$ and $\sim 3.60\,\mathrm{nm}$, respectively.

These differences in Si-nps size and concentration may explain the trapping of charge with different polarity in materials with the same $XS_{Si}$ (note, in Fig. 4, that the PECVD-SRO samples capture positive charge, while the II-SRO samples retain negative charge). Within the frame of quantum confinement (QC), there should be a certain asymmetry in the ability of nano-particles to trap electrons and holes, due to their different effective masses. This asymmetry is also related to the size of the Si-nps, causing the differences in the charge-trapping behavior if it is provoked by the QC.

The structural studies also showed the presence of a superficial low-quality oxide layer between the substrate and PECVD-SRO samples that is not present in II-SRO; this would contribute both to a higher charge trapping and a lower conductivity in devices with PECVD-SRO.

### 2. Current-voltage

The J-V results showed an increase in conductivity with Si content for all samples, as expected. Figure 5 shows the typical curves obtained from PECVD-4 ($XS_{Si} \approx 8\%$), PECVD-3 ($XS_{Si} \approx 12\%$), and II-1 ($XS_{Si} \approx 12\%$); the horizontal axis represents the voltage per unit of thickness (V/cm) in order to eliminate the influence of the thickness when comparing active layer characteristics. A low conduction zone was found ($J < 10^{-5}$ A/cm$^2$), followed by an abrupt increment of the current after a characteristic onset voltage, which value showed to decrease with increasing silicon content, as can be observed in Fig. 6. A similar low-conduction regime has been found in LPCVD-SRO samples, but only after an electrical anneal, and it has been related to the presence of full area EL and the annihilation of preferential conductive paths.[15,21] In the case of II-SRO and PECVD-SRO, the number of voltage sweeps (electrical annealing) makes no difference in J-V behavior and no region or stage of conduction through preferential paths was identified. As in the case of conduction-onset voltage, the breakdown voltage ($V_{br}$) of the devices is clearly related to the $XS_{Si}$ rather than fabrication technique, as shown in Fig. 7. Breakdown occurred in the devices with the lowest Si content (PECVD-1, $XS_{Si} \approx 6\%$), not due to the SRO, but to the poly gate instead.

TABLE III. Parameters extracted from C-V curves for all samples. Only results from fresh devices are shown; results after I-V showed neglectable variations.

| Sample | $XS_{Si}$ (at. %) | $\varepsilon_{SRO}$ | $C_{SRO}$ ($\times 10^{-10}$ F) | $\Delta V_{fb}$ (V) | $Q_{SRO}$ ($\times 10^{-10}$ C) |
|---|---|---|---|---|---|
| II-1 | 12 ± 0.3 | 6.6 ± 0.6 | 2.97 ± 0.03 | 2.5 ± 0.2 | −7.5 ± 0.7 |
| II-2 | 13 ± 0.4 | 7.0 ± 0.7 | 2.98 ± 0.02 | 2.3 ± 0.2 | −6.9 ± 0.6 |
| II-3 | 14 ± 0.2 | 8.1 ± 0.8 | 3.23 ± 0.02 | 1.4 ± 0.2 | −4.7 ± 0.7 |
| II-4 | 15 ± 0.5 | 9.0 ± 0.9 | 3.21 ± 0.04 | 0.5 ± 0.2 | −1.8 ± 0.7 |
| PECVD-1 | 6 ± 0.2 | 5.9 ± 1.0 | 2.27 ± 0.06 | 0.0 ± 0.2 | 0.0 ± 0.4 |
| PECVD-2 | 8 ± 0.6 | 6.5 ± 1.2 | 2.41 ± 0.06 | 0.0 ± 0.1 | 0.0 ± 0.2 |
| PECVD-3 | 12 ± 0.2 | 8.0 ± 0.7 | 2.74 ± 0.05 | −5.3 ± 0.2 | 14.3 ± 0.3 |
| PECVD-4 | 16 ± 0.6 | 8.4 ± 0.5 | 2.93 ± 0.11 | −9.7 ± 0.2 | 28.3 ± 0.5 |
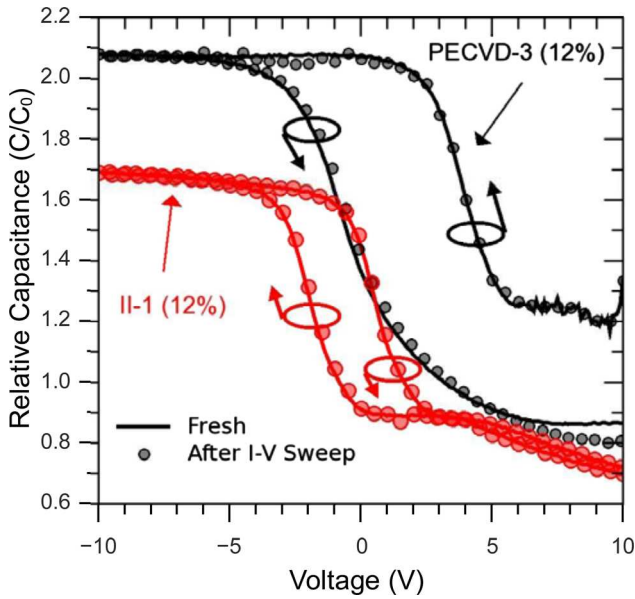
FIG. 2. (Color online) Typical C-V characteristics for devices before and after applying V sweep. Results for PECVD-3 and II-1 ($XS_{Si} \approx 12\%$) are shown.

In general, the J-V curves show that the conduction mechanism does not change with $XS_{Si}$, but with the fabrication technique. This was related to the different distribution and sizes of Si-nps in II and PECVD reported in Ref. 14, which are due to fabrication technique rather than to $XS_{Si}$ variation; these differences translate in distinct percolation distances, energies, critical nano-cluster densities, and other effects. Since the carrier injection is a determinant factor in EL, the above results prove the importance of the fabrication method in the device efficiency.

Three possible mechanisms for the carrier transport in the material were studied, namely Fowler-Nordheim tunneling (FN), trap-assisted tunneling (TAT), and Poole-Frenkel emission (PF).
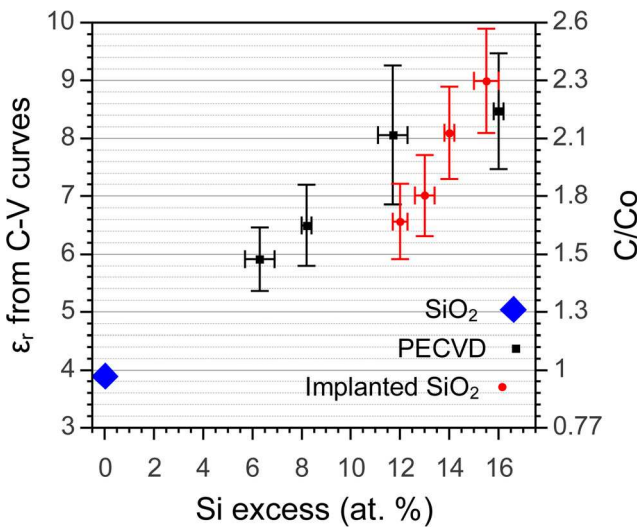


FIG. 3. (Color online) Relative permittivity and relative capacitance of samples with both II-SRO and PECVD-SRO as calculated from C-V measurements. The $\varepsilon_r$ of $SiO_2$ (Ref. 20) is indicated with a rhombus as 0% Si-excess reference.
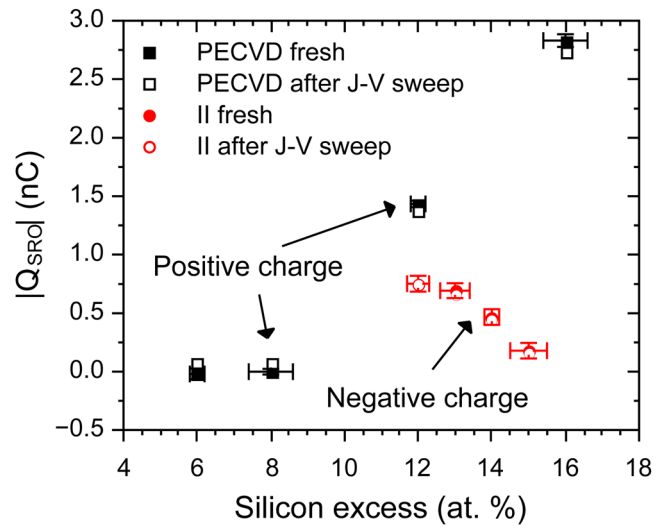


FIG. 4. (Color online) Absolute value of charge trapped for all samples as extracted from $\Delta V_{fb}$ in C-V curves; white-filled symbols represent the values obtained for the material after J-V sweep. Note that PECVD samples trapped positive charge, while II samples trapped negative charge.

Fowler-Nordheim tunneling was modeled by the following equation

$$J = \frac{q^2 m E_i^2}{8\pi h \phi_B m^*} \times \exp\left(-\frac{8\pi\sqrt{2qm^*}\phi_B^{\frac{3}{2}}}{3hE_i}\right), \quad (2)$$

where $q$ is the charge of an electron, $h$ is Planck's constant, $m$ and $m^*$ are, respectively, the mass and effective mass of an electron, $\phi_B$ is the barrier height, and $E_i$ is the electric field across the insulator. A plot of $\ln\left(J/E_i^2\right)$ against $1/E_i$ delivers a straight line that can be fitted with a first degree polynomial (Fig. 8). Values of $\phi_B$ or $m_r \equiv m^*/m$ can be extracted from the slope of the fit. Notice that one of the
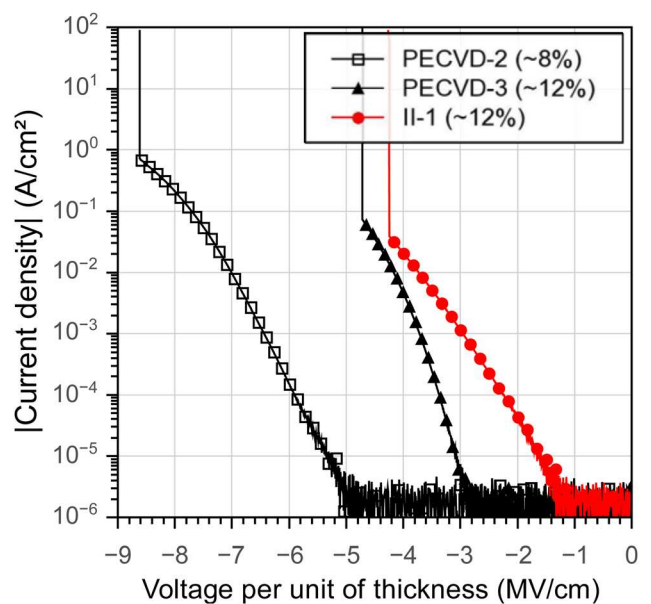


FIG. 5. (Color online) Typical J-V behavior for devices of PECVD-2 ($XS_{Si} \approx 8\%$), PECVD-3 ($XS_{Si} \approx 12\%$), and II-1 ($XS_{Si} \approx 12\%$). The voltage has been normalized to the thickness of each active layer.
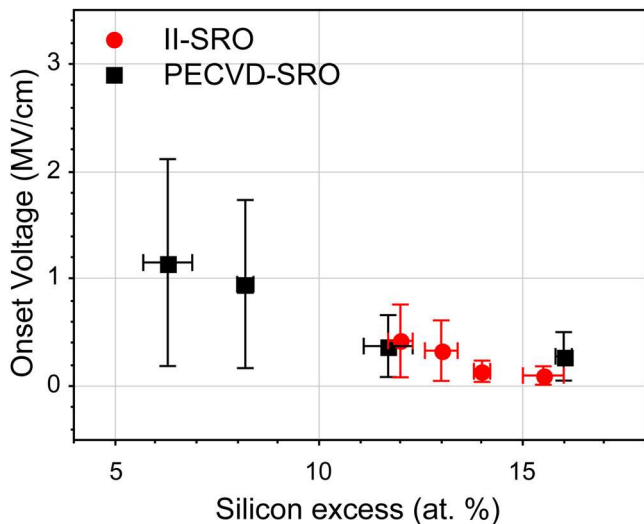
FIG. 6. (Color online) Volts per unit of thickness at which the devices presented current values higher than $10^{-5}$ A/cm$^2$.

parameters must be known in order to determine the other, since the fit only yields $C = \phi_B^3 \times m_r$.

Trap-assisted tunneling was modeled with the equation

$$J \propto \exp\left(-\frac{8\pi\sqrt{2qm^*}\,\phi_B^{\frac{3}{2}}}{3hE_i}\right). \tag{3}$$

A plot of $\ln J$ versus $1/E_i$ gives a straight line that was fitted with a first degree polynomial, as shown in Fig. 9. As with the Fowler-Nordheim plot, $m_r$ or $\phi_B$ can be extracted from the slope of the fit, provided one of them is known.

Poole-Frenkel emission is described by the equation

$$J \propto E_i \times \exp\left(\frac{-q(\phi_B - \sqrt{qE_i/\pi\varepsilon_i})}{kT}\right), \tag{4}$$

where $k$ is Boltzmann's constant, $\varepsilon_r$ is the relative permittivity of the insulator, and $T$ is the temperature. A plot of $\ln(J/E_i)$
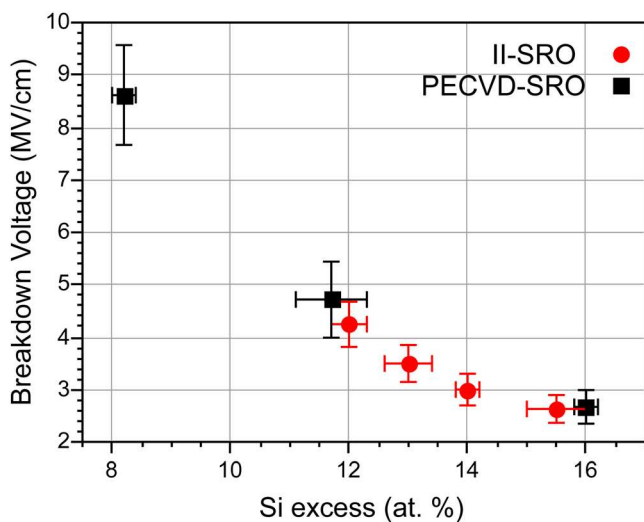


FIG. 7. (Color online) Volts per unit of thickness at which the devices presented average breakdown.
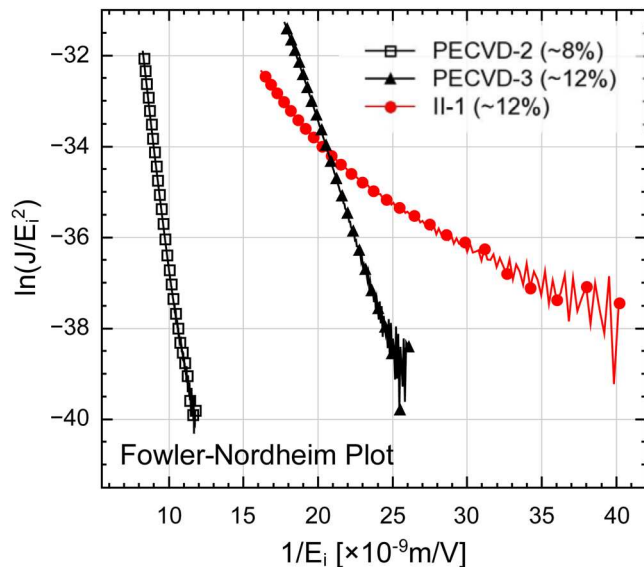


FIG. 8. (Color online) Fowler-Nordheim plots of devices from samples PECVD-3 ($XS_{Si} \approx 12\%$), PECVD-2 ($XS_{Si} \approx 8\%$), and II-1 ($XS_{Si} \approx 12\%$). Results for all samples can be observed in Table IV.

versus $\sqrt{E_i}$ delivers a straight line that was fitted to a first degree polynomial as for the FN and TAT approaches (see Fig. 10). From the slope of the fit, $\varepsilon_r$ can be obtained.

Although Figs. 8 and 9 only show typical results for three samples, it is worth remarking here that the studies were performed in five devices of each sample included in Tables I and II.

In the case of PECVD, all the samples presented a rather linear behavior in FN and TAT plots, suggesting a transport dominated by one of these mechanisms. For each sample, the value of $C = \phi_B^3 \times m_r$ was extracted from FN and TAT plots. Therefore, any pair ($\phi_B^3 \times m_r$) that satisfies the previous equation fits the experimental data. In order to limit the possible values of $\phi_B$, the masses for an electron in silicon[22]
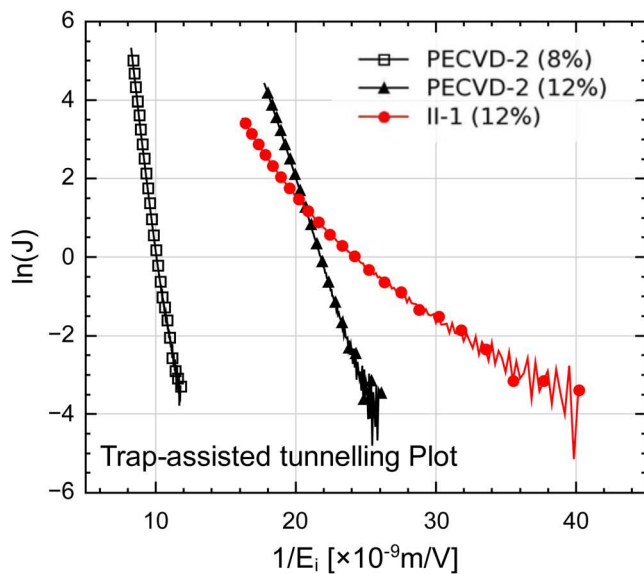


FIG. 9. (Color online) Trap-assisted tunneling plots of devices from samples PECVD-3 ($XS_{Si} \approx 12\%$), PECVD- 2 ($XS_{Si} \approx 8\%$), and II-1 ($XS_{Si} \approx 12\%$). Results for all samples can be observed in Table IV.
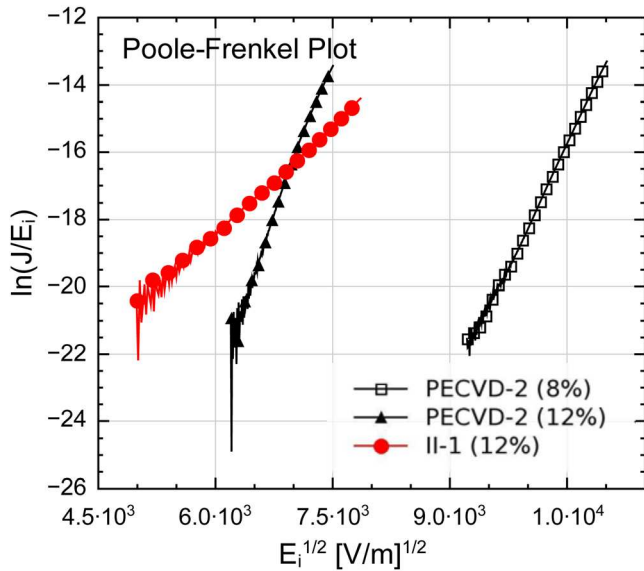
FIG. 10. (Color online) Poole-Frenkel plots of devices from samples PECVD-3 ($XS_{Si} \approx 12\%$), PECVD-2 ($XS_{Si} \approx 8\%$), and II-1 ($XS_{Si} \approx 12\%$). Results for all samples can be observed in Table IV.

were assumed to be $m_r = 0.98$ (longitudinal relative effective mass) and $m_r = 0.19$ (transverse relative effective mass), and for an electron in thermal $SiO_2$, $m_r = 0.42$.[23] Regarding holes in silicon, there were considered $m_r = 0.16$ (light holes) and $m_r = 0.49$ (heavy holes),[22] while in $SiO_2$, $m_r = 0.58$.[24] Since the studied material is composed by silicon nanoclusters embedded in $SiO_2$, it seems reasonable only to accept values of $m_r$ between 0.98 and 0.16. This range of accepted values of $m_r$ translates to a range of $\phi_B$ through the equation $C = \phi_B^3 \times m_r$. The results are quoted in Table IV. Notice that the difference between the values obtained from FN and TAT fits are very small due to the close relation between the two models.

Considering that $\phi_B = 2.8$ eV in thermal $SiO_2$,[25] the values quoted in Table IV for the effective barrier height of the PECVD samples are acceptable. Moreover, if a value for $m_r$ is fixed, the values of $\phi_B$ decrease when the $XS_{Si}$ of the PECVD samples increases, which is an expected trend. The PECVD samples also behave linearly in a PF plot (Fig. 10). However, the values of the relative permittivity extracted from the fits (see Fig. 11) are one order of magnitude lower than the values extracted from the C-V measurements (see Fig. 3) and even below the minimum expected, which should be that for $SiO_2$. Moreover, the value of $\varepsilon_r$ extracted from the

TABLE IV. Range of possible values of the effective barrier height $\phi_B$ for the PECVD and ion-implanted samples extracted from FN and TAT models after limiting the range of $m_r$ to [0.16, 0.98]. Samples II-1 and II-2 did not adjust to the model.

| Sample | $XS_{Si}$ (at. %) | $\phi_B^{FN}$ (eV) | $\phi_B^{TAT}$ (eV) |
|---|---|---|---|
| II-3 | $14 \pm 0.2$ | [0.03, 0.11] | [0.04, 0.15] |
| II-4 | $15 \pm 0.5$ | [0.02, 0.09] | [0.04, 0.11] |
| PECVD-1 | $6 \pm 0.2$ | [0.53, 1.22] | [0.56, 1.22] |
| PECVD-2 | $8 \pm 0.6$ | [0.45, 1.13] | [0.48, 1.19] |
| PECVD-3 | $12 \pm 0.2$ | [0.23, 0.55] | [0.25, 0.58] |
| PECVD-4 | $16 \pm 0.6$ | [0.14, 0.34] | [0.15, 0.37] |
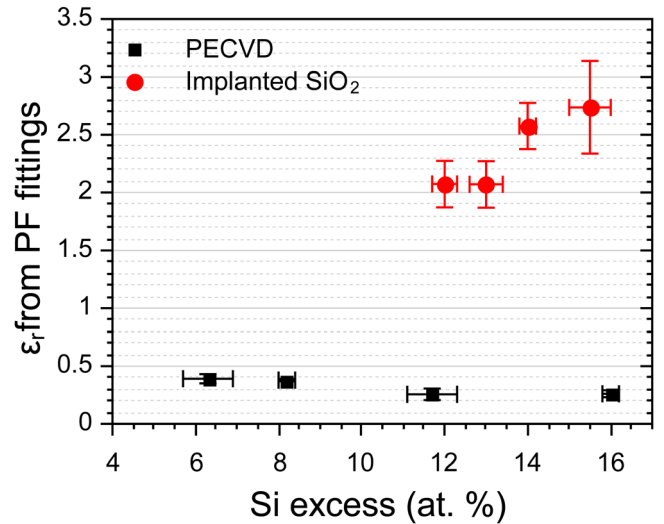


FIG. 11. (Color online) Values of $\varepsilon_r$ extracted from the Poole-Frenkel fittings.

PF fits decreases slightly as the $XS_{Si}$ increases, which is in clear contradiction to the expected trend and the one observed in Fig. 3. Given these results, FN and TAT seem to fit reasonably well the J-V characteristics of the PECVD samples in the measured range of current densities. Although it is difficult to decide which of these two mechanisms dominates, the TAT seems a better candidate, given the nature of the SRO.

The ion-implanted samples present a different behavior than the PECVD samples. In FN and TAT plots, a linear region was identified at low electric fields in samples with 14% and 15% $XS_{Si}$. This region is not observed in the samples with 12% and 13% $XS_{Si}$, at least, not within our measurement range. After fitting FN and TAT in the linear regions of the samples with 14% and 15% $XS_{Si}$ and applying the same considerations applied to the PECVD samples, the range of values of the energy barrier was found. The results are also quoted in Table IV. Although the values of $\phi_B$ obtained from the two highest $XS_{Si}$ ion-implanted samples follow the expected trend, they are one order of magnitude smaller than those obtained from the PECVD samples.

The nonlinear regions of the ion-implanted samples in the FN and TAT plots turned out to be linear in a PF plot. The fitting of PF model in those regions (the whole curve in the case of the samples with 12% and 13% $XS_{Si}$) delivered the values of relative permittivity plotted in Fig. 11. These values present the same trend (increasing $\varepsilon_r$ with increasing $XS_{Si}$) and are of the same order of magnitude as those calculated from the C-V measurements (Fig. 3), but are still below the value for $SiO_2$. Therefore, even when there seems to be a contribution of PF to the transport in ion-implanted samples for electric fields above $\sim 0.2$ MV/cm, no clear conclusion can be extracted.

## B. Electro-luminescence

### 1. Spectra

Electro-luminescence was observed and characterized in the whole area of all devices, except for sample PECVD-4

($XS_{Si} \sim 16\%$), damaged at relatively low current values ($< 10^3$ A/cm$^2$) and before achieving EL. The normalized electroluminescence spectra of the samples PECVD-2 ($XS_{Si} \sim 8\%$), PECVD-3 ($XS_{Si} \sim 12\%$), and II-1 ($XS_{Si} \sim 12\%$) when applying the maximum voltage possible (before breakdown) are shown in Fig. 12. The transmittance of the poly gate has been plotted along with the spectra. It seems clear that the poly gate has a strong influence on the spectra. It is likely that interference also play an important role, particularly due to the reflection effects from the silicon substrate.[26,27]

Figure 13 shows the spectra from the same samples as in Fig. 12 after removing the effect of the polysilicon gate. The results, however, are affected by a slight mismatch between the peaks of transmittance and emission spectra, most likely due to small changes in the respective experiment conditions. Nevertheless, at least two different main emission bands were identified: a broad band from 410 nm to 800 nm, present in the PECVD-1 (not shown) and PECVD-2 samples ($XS_{Si}$ of $\sim 6\%$ and $\sim 8\%$), and a broad band centered around 820 nm, present in the PECVD sample with 12% as well as in all the ion-implanted samples (all with $XS_{Si} \geq 12\%$).

It appears that the emission spectrum is not dependent on the fabrication technique, but only on the $XS_{Si}$; this is clear from Figs. 12 and 13, in which samples with $XS_{Si} \approx 12\%$ present remarkably similar spectra, despite the fact that they present significant electrical differences, as already discussed. This along with the structural characteristics reported in Ref. 14 suggest that quantum confinement does not contribute significantly to the emission effects. Furthermore, there are no changes within the same technique and different $XS_{Si}$, as would be expected for QC, and the emission bands are outside the range predicted by models for such a mechanism for the sizes of the Si-nps present in the material.[28,29]

Some authors have also suggested that, if the peak positions and shapes of EL spectra change with the applied field, emission is due to the recombination of quantum-confined electron-hole pairs generated by impact excitation within the



FIG. 13. (Color online) Normalized EL spectra of samples PECVD-3 ($XS_{Si} \approx 12\%$), PECVD-2 ($XS_{Si} \approx 8\%$), and II-1 ($XS_{Si} \approx 12\%$) after removing the effect of the poly gate.

Si-nps.[6,7] Such changes are not present in the devices here reported. As an example, the inset in Fig. 12 shows that the EL spectra of sample II-1 presents no noticeable change at different applied voltages. It seems more likely for the wide bands of the EL to be caused mainly by the transition of the injected carriers with relatively high energies to lower energy states introduced by the defects related to the Si-nps in the material. Similar EL bands have been observed in the past for LPCVD samples, also with emission only dependent on the $XS_{Si}$;[21,30] a luminescence band centered around 820 nm has been reported many times in the literature, always related to the emission from silicon nanoclusters in silica.[6,14,31,32] Photoluminescence bands within the range from 400 to 700 nm have also been reported in SRO[13] and in colloidal solutions of $Si$–$SiO_2$ core-shell nanostructures[33,34] and have been attributed to defects in the Si-oxide interface.



FIG. 12. (Color online) Normalized EL spectra of samples PECVD-3 ($XS_{Si} \approx 12\%$), PECVD-2 ($XS_{Si} \approx 8\%$), and II-1 ($XS_{Si} \approx 12\%$); the transmittance spectrum of the polysilicon gate is plotted in gray with a solid line. The inset shows the normalized EL spectra of sample II-1 for different applied voltages; no change was observed.
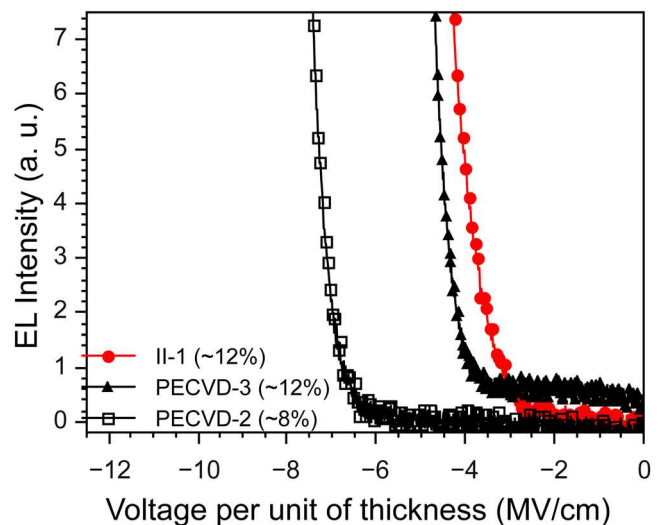


FIG. 14. (Color online) Typical electroluminescence vs applied field curves for samples PECVD-3 ($XS_{Si} \approx 12\%$), PECVD-2 ($XS_{Si} \approx 8\%$), and II-1 ($XS_{Si} \approx 12\%$).
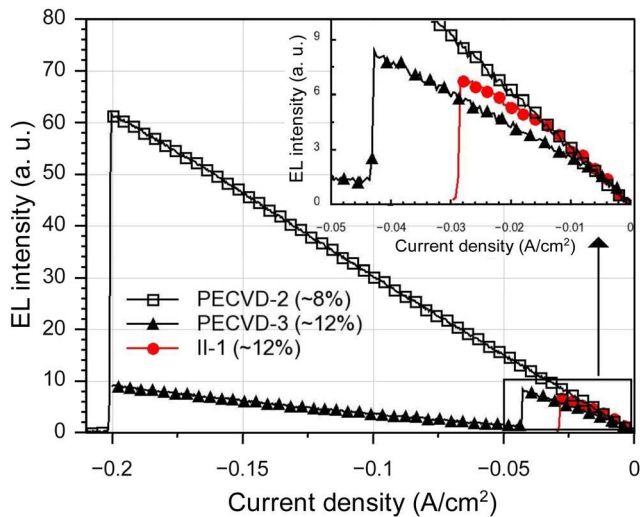
FIG. 15. (Color online) Typical electroluminescence vs current density characteristics for samples PECVD-3 ($XS_{Si} \approx 12\%$), PECVD-2 ($XS_{Si} \approx 8\%$), and II-1 ($XS_{Si} \approx 12\%$). The abrupt EL intensity drop corresponds to the current at which the devices break and stop emitting in the full gate area.

### 2. EL intensity-current and EL intensity-voltage

The relation between the electroluminescence and the applied bias for PECVD-2 ($XS_{Si} \sim 8\%$), PECVD-3 ($XS_{Si} \sim 12\%$), and II-1 ($XS_{Si} \sim 12\%$) is shown in Fig. 14. It can be seen that, the higher the silicon excess, the lower the voltage needed to produce detectable electroluminescence, and for the same $XS_{Si}$, implanted samples require lower fields to emit detectable light. The typical relations between the electroluminescence and the electrical current flowing through the active layer for these same samples are shown in Fig. 15.

It is worth it to mention that the relation between the current and the electroluminescence was not linear in general, although it appears so for PECVD-2. It is noticeable that the devices capable of withstanding the highest current densities are also those that emit most intensely. However, this can be misleading when choosing the best combination of $XS_{Si}$ and fabrication technique, as the highest breaking current value does not necessarily match the highest efficiency. In fact, in this case, it can be seen that PECVD-2 bears higher currents than the other two samples presented in Fig. 15, but it also needs higher voltages to achieve a given EL intensity, as shown in Fig. 14.

Efficiency calculations deserve a careful treatment as to take into account the several factors that may modify the real values. In that regard, a manuscript dedicated to the efficiency results from the samples presented here is being prepared for its future publication; however, preliminary calculations clearly indicate that devices from II-1 present higher efficiency than those from PECVD-2 (around one order of magnitude) and that the most efficient devices are from sample II-4 ($XS_{Si} \approx 15\%$).

### IV. CONCLUSION

Both electrical and electro-luminescent characteristics of devices with SRO as the active layer and fabricated by PECVD and implantation of Si-ions in $SiO_2$ were studied.

Consistently with previous results of similar materials, silicon excess variations influence the effective relative permittivity of the material, its conductivity, the quantity of trapped charge, and the electro-luminescence emission profiles. On the other hand, the choice of fabrication technique showed to have a significant effect in the electrical properties, in particular, on the type of trapped charge and in the conduction mechanisms.

Samples fabricated by ion implantation presented a lower emission threshold power, while PECVD-SRO required higher voltages to operate in general, but were able to conduct higher currents before breakdown, hence, reaching higher emission intensities with lower efficiency. No evidence of impact excitation of electrons was found. Emission spectra only depended on $XS_{Si}$, and the EL was attributed to a combination of mechanisms in which the dominant was the energy relaxation of carriers through centers introduced by defects in the active material.

Differences in electrical characteristics between materials with the same $XS_{Si}$, but distinct fabrication were attributed to the different Si-nps size and distribution and to the presence of parasitic $SiO_2$ layers in PECVD-SRO. The conduction mechanism in the PECVD-SRO is best adjusted to trap-assisted tunneling within a reduced range of possible values for the parameters of the model. On the other hand, the parameter values for all the tested models obtained for II-SRO delivered non-conclusive results, showing once again the high complexity for the modeling of the material, which is most likely a combination of different mechanisms.

None of the analyzed devices presented bright dots or a preferential conductive paths stage, and unlike LPCVD-SRO devices, no electrical treatment was needed to obtain full-area EL.

The performed studies showed the relevance of the choice and control of the fabrication technique and that this parameter may be as important as Si content for the optimization of an SRO-based electroluminescent device.

[1]L. T. Canham, Appl. Phys. Lett. **57**, 1046 (1990).
[2]A. Morales-Sánchez, J. Barreto, C. Domínguez, M. Aceves-Mijares, M. Perálvarez, B. Garrido, and J. A. Luna-López, Nanotechnology **21**, 085710 (2010).
[3]A. Morales, J. Barreto, C. Dominguez, M. Riera, M. Aceves, and J. Carrillo, Physica E **38**, 54 (2007).
[4]J. A. Luna-López, A. Morales-Sánchez, M. Aceves-Mijares, Z. Yu, and C. Domínguez, J. Vac. Sci. Technol. A **27**, 57 (2009).
[5]A. Irrera, F. Iacona, G. Franzò, S. Boninelli, D. Pacifici, M. Miritello, C. Spinella, D. Sanfilippo, G. Di Stefano, and P. G. Fallica, Opt. Mater. **27**, 1031 (2005).
[6]G. Franzò, A. Irrera, E. C. Moreira, M. Miritello, F. Iacona, D. Sanfilippo, G. Di Stefano, P. G. Fallica, and F. Priolo, Appl. Phys. A: Mater. Sci. Process. **74**, 1 (2002).
[7]A. Irrera, D. Pacifici, M. Miritello, G. Franzò, F. Priolo, F. Iacona, D. Sanfilippo, G. Di Stefano, and P. G. Fallica, Appl. Phys. Lett. **81**, 1866 (2002).

[8]J. Carreras, J. Arbiol, B. Garrido, C. Bonafos, and J. Montserrat, Appl. Phys. Lett. **92**, 091103 (2008).

[9]T. Shimizu-Iwayama, S. Nakao, and K. Saitoh, Appl. Phys. Lett. **65**, 1814 (1994).

[10]L. Ding, T. P. Chen, M. Yang, J. I. Wong, Z. Cen, Y. Liu, F. Zhu, and A. A. Tseng, IEEE Trans. Electron Devices **56**, 2785 (2009).

[11]J. Valenta, N. Lalic, and J. Linnros, Appl. Phys. Lett. **84**, 1459 (2004).

[12]F. Iacona, G. Franzò, and C. Spinella, J. Appl. Phys. **87**, 1295 (2000).

[13]A. Morales-Sánchez, M. Aceves-Mijares, A. González-Fernández, K. Monfil-Leyva, J. Juvert, and C. Domínguez-Horna, in *Proceedings of SPIE* (Brussels, Belgium, 2010), p. 77190N.

[14]M. Perálvarez, J. Barreto, J. Carreras, A. Morales, D. Navarro-Urrios, Y. Lebour, C. Domínguez, and B. Garrido, Nanotechnology **20**, 405201 (2009).

[15]A. Morales-Sánchez, J. Barreto, C. Domínguez, M. Aceves, and J. A. Luna-López, Nanotechnology **20**, 045201 (2009).

[16]M. Perálvarez, C. García, M. López, B. Garrido, J. Barreto, C. Domínguez, and J. A. Rodríguez, Appl. Phys. Lett. **89**, 051112 (2006).

[17]M. Perálvarez, M. López, B. Garrido, J. R. Morante, J. Barreto, V. J. Cadarso, M. Riera, K. Zinoviev, and C. Dominguez, MRS Proceedings **832**, (2004).

[18]J. Barreto, A. Morales, M. Perálvarez, B. Garrido, and C. Domínguez, Phys. Status Solidi C **8**, 804 (2011).

[19]J. Ziegler, Nucl. Instrum. Methods Phys. Res. B **219–220**, 1027 (2004).

[20]P. Gray, *Analysis and Design of Analog Integrated Circuits*, 5th ed. (Wiley, Chichester, 2008).

[21]A. A. G. Fernández, M. A. Mijares, A. M. Sánchez, and K. M. Leyva, J. Appl. Phys. **108**, 043105 (2010).

[22]S. M. Sze and K. K. Ng, in *Physics of Semiconductor Devices* (Wiley, Hoboken, NJ, 2006), p. i–x.

[23]M. Lenzlinger, J. Appl. Phys. **40**, 278 (1969).

[24]R. Kumar Chanana, J. Appl. Phys. **109**, 104508 (2011).

[25]K. J. Hebert and E. A. Irene, J. Appl. Phys. **82**, 291 (1997).

[26]O. Crawford and R. Ritchie, Phys. Rev. A **37**, 787 (1988).

[27]J. Barreto, J. Rodriguez, M. Peralvarez, A. Morales, B. Garrido, and C. Dominguez, Superlattices Microstruct. **43**, 588 (2008).

[28]P. F. Trwoga, A. J. Kenyon, and C. W. Pitt, J. Appl. Phys. **83**, 3789 (1998).

[29]N.-M. Park, T.-S. Kim, and S.-J. Park, Appl. Phys. Lett. **78**, 2575 (2001).

[30]W. K. Tan, Q. Chen, J. D. Ye, M. B. Yu, G.-Q. Lo, and D.-L. Kwong, IEEE Electron Device Lett. **29**, 344 (2008).

[31]J. Barreto, M. Peralvarez, J. Antonio Rodriguez, A. Morales, M. Riera, M. Lopez, B. Garrido, L. Lechuga, and C. Dominguez, Physica E **38**, 193 (2007).

[32]B. Garrido Fernandez, M. López, C. García, A. Pérez-Rodríguez, J. R. Morante, C. Bonafos, M. Carrada, and A. Claverie, J. Appl. Phys. **91**, 798 (2002).

[33]M. Ray, T. S. Basu, A. Jana, N. R. Bandyopadhyay, S. M. Hossain, A. K. Pramanick, and R. F. Klie, J. Appl. Phys. **107**, 064311 (2010).

[34]Z. Ding, B. Quinn, S. Haram, L. Pell, B. Korgel, and A. Bard, Science **296**, 1293 (2002).

## B.2. Journal of Lightwave Technology, 31(17), (2013)

**The principal author of this paper is Joan Juvert, and the theoretical work must be credited to him in its totality**. The experimental activities and analyses involved in the development of the manuscript were performed jointly.

# DC Electroluminescence Efficiency of Silicon Rich Silicon Oxide Light Emitting Capacitors

Joan Juvert, Alfredo Abelardo González Fernández, Alfredo Morales-Sánchez, Jorge Barreto, Mariano Aceves, *Member, IEEE*, Andreu Llobera, and Carlos Domínguez, *Member, OSA*

*Abstract*—We analyze the influence of the fabrication technique and the silicon excess on the power efficiency and evolution with time of the electroluminescence of silicon rich silicon oxide in metal—oxide—semiconductor like light emitting capacitors under direct current. The silicon rich silicon oxide layers have been fabricated using two different techniques, namely plasma enhanced chemical vapor deposition and silicon ion implantation. Six different silicon excesses have been studied, ranging from 6 at. % to 15 at. %. It is shown that both the power efficiency and external quantum efficiency increase with the silicon excess due to a decrease in the electroluminescence current threshold. The maximum value of the power efficiency has been found to be $(2.6 \pm 0.3) \times 10^{-5}$ in the ion implanted sample with 15 at. % silicon excess. Significant differences in the evolution of the electroluminescence with time are found depending on the fabrication technique.

*Index Terms*—Electroluminescence, electroluminescent devices, MIS devices, nanoparticles, nanostructured materials, semiconductor devices, silicon devices.

## I. INTRODUCTION

SILICON based light sources are an essential component for silicon photonics to achieve its full potential. In order to obtain a silicon based light source, several approaches and materials have been proposed. Complementary metal-oxide-semiconductor (CMOS) compatibility is particularly interesting in order to leverage the existing microelectronics industry and for the future integration of such a silicon based light source in a microelectronic device.

Examples of CMOS compatible materials for silicon based light sources that can be found in the literature are silicon rich silicon nitride films [1], [2] ($Si_3N_x$, $x < 4$, SRN), silicon rich silicon oxide films [2]–[4] ($SiO_x$, $x < 2$, SRO) and $Si/SiO_2$ [5], [6], $SRO/SiO_2$ [7], [8] or $Si/SRN$ [9] superlattices.

Efficiency, power and durability are all required in order to fabricate a viable, integrated silicon based photonic system. A precise knowledge of the mechanisms that influence all those variables is key in devising strategies to improve silicon based light sources.

Reported values for the power or quantum efficiency of CMOS compatible silicon based light sources vary greatly depending on the material (SRO, SRN), the structure of the device (single layer, multilayers) and the electrical stimuli (direct current (DC), pulsed), ranging from $\approx 10^{-7}$ for SRO single layers in DC [10] to $\approx 10^{-3}$ for $SRO/SiO_2$ multilayers in alternating current (AC) [8]. Unfortunately, although the accurate measurement of the efficiency is not trivial, experimental procedures, approximations or corrections taken into account are not always included when reporting efficiency values. Studies of the influence of the stimuli conditions [8] and the device structure [10], [11] on the efficiency have been already published by other authors.

The present work focuses on the influence of the fabrication technique and the silicon excess ($XS_{Si}$, see Section II) on the electroluminescence (EL) efficiency and the evolution of the EL with time of metal-SRO-semiconductor structures operated in DC with the SRO layer fabricated using silicon ion implantation and plasma enhanced chemical vapor deposition within a range of silicon excesses from 6 at. % to 15 at. %.

## II. EXPERIMENTAL

Two techniques have been used to obtain the SRO active layer of the studied devices, namely plasma enhanced chemical vapor deposition (PECVD) and silicon ion implantation of thermally grown silicon dioxide. A set of samples was fabricated using each technique. The fabrication parameters for each technique were selected according to the highest luminescence intensity obtained in previous studies [12]–[15]. All the SRO layers were deposited on $4''$ p-type Si wafers with (100) crystalline orientation and resistivity between 0.1 and 1.4 $\Omega cm$.

The PECVD layers were deposited using undiluted $SiH_4$ and $N_2O$ as precursor gasses. The temperature of the substrate was $300°C$ and the radio frequency power density was $0.07\,W/cm^2$. The $XS_{Si}$ of the layers was controlled by modulating the ratio of the partial pressures of the precursor gasses in the chamber

TABLE I
FABRICATION PARAMETERS FOR THE PECVD LAYERS. THICKNESS WAS MEASURED BY ELLIPSOMETRY BEFORE THERMAL ANNEALING

| Sample | $\frac{P[N_2O]}{P[SiH_4]}$ | $XS_{Si}$ (at %) | Thickness (nm) |
|--------|------|------|------|
| PECVD-1 | 13 | $6.0 \pm 0.2$ | $53\pm5$ |
| PECVD-2 | 10 | $8.0 \pm 0.6$ | $55\pm6$ |
| PECVD-3 | 7 | $12.0 \pm 0.2$ | $60\pm9$ |
| PECVD-4 | 5 | $16.0 \pm 0.6$ | $59\pm7$ |

TABLE II
CHARACTERISTICS AND FABRICATION PARAMETERS OF THE ION IMPLANTED SAMPLES. THICKNESS WAS OBTAINED BY ELLIPSOMETRY BEFORE THE THERMAL ANNEALING AND ION IMPLANTATION

| Sample | 1st Dose 25 keV ($\times 10^{16}$ cm$^{-2}$) | 2nd Dose 50 keV ($\times 10^{16}$ cm$^{-2}$) | $XS_{Si}$ (at %) | Thick. (nm) |
|--------|------|------|------|------|
| II-1 | 1.2 | 5.0 | $12.0 \pm 0.3$ | $45 \pm 5$ |
| II-2 | 1.4 | 6.0 | $13.0 \pm 0.4$ | $48 \pm 4$ |
| II-3 | 1.8 | 7.2 | $14.0 \pm 0.2$ | $49 \pm 9$ |
| II-4 | 2.0 | 8.3 | $15.0 \pm 0.5$ | $57 \pm 1$ |

$(P[N_2O]/P[SiH_4])$. The deposition times were selected to obtain films with a thickness close to 45 nm. After deposition, all the PECVD samples were annealed in $N_2$ atmosphere at $1250°C$ for 60 minutes to induce Si nucleation and the formation of silicon nanoparticles (Si-nps) [16]. The characteristics of the fabricated films are summarized in Table I. A more detailed description of the PECVD fabrication process can be found elsewhere [13].

The fabrication of the ion implanted films started with a dry thermal growth of 60 nm thick $SiO_2$ layers at $1000°C$, followed by the deposition of a 30 nm thick $Si_3N_4$ film by low pressure chemical vapor deposition (LPCVD) at $800°C$ using $SiH_2Cl_2$ and $NH_3$ as precursor gasses. Two consecutive Si ion implantations (25 and 50 keV, respectively) were performed on the resulting bilayer structure in order to obtain a uniform Si distribution in the $SiO_2$ as simulated in SRIM [17] (Stopping and Range of Ions in Matter). The implantation doses and the final $XS_{Si}$ are shown in Table II.

The ion implanted films were then annealed at $1100°C$ for 4 hours in a $N_2$ atmosphere to induce Si agglomeration [18]. The annealing was followed by a wet etching of the nitride layer. More details on the ion implanted-SRO fabrication technique can be found elsewhere [12], [13].

The uncertainties in the thickness quoted in Tables I and II correspond to the standard deviation over measurements in five different points on each wafer, and therefore are a measure of the uniformity of the samples.

$XS_{Si}$ is defined as the atomic concentration of silicon not bound to oxygen (forming $SiO_2$) or nitrogen (forming $Si_3N_4$), that is, free to nucleate into silicon nanoclusters.

$$XS_{Si} = [Si] - \frac{1}{2}[O] - \frac{q3}{4}[N] \qquad (1)$$

Here, [Si], [O] and [N] are the atomic concentrations of silicon, oxygen and nitrogen, respectively, as measured by X-ray photoelectron spectroscopy (XPS) measurements.



Fig. 1. Schematic view of the fabricated devices (not to scale).

After the fabrication of the SRO the same steps were carried out for all the samples regardless of the technique used to obtain the active layer. A 350 nm thick, highly $POCl_3$ doped, n+ polycrystalline silicon layer was deposited by LPCVD. Photolitography and a dry etching process were used to define a pattern of squares on the polycrystalline silicon, with area of $2.304 \times 10^{-3}$ cm$^2$. Finally, a 1.0 $\mu$m thick Al layer was deposited by sputtering on the back of all wafers and the structures were sintered in forming gas at $350°C$. The vertical layout of the devices is shown in Fig. 1.

The EL emission, which was homogeneous across the whole area of the devices, was obtained stimulating the samples with a Keithley 2430 source-meter, which can be set as either voltage or current source. The wafers are placed on an aluminum chuck and biased with a Süss Microtech PH100 probehead and a 25 $\mu$m tungsten probe. All the samples have been biased with negative gate voltages (operation in accumulation regime).

Two detectors have been used to measure the electroluminescence (EL) of the devices: a calibrated Newport 918D-UV-OD3 detector connected to a Newport 1931-C power meter and a Hamamatsu H9656-20 photomultiplier tube (PMT).

The PMT was used together with a Stanford Research SR830 lock-in amplifier to improve the signal to noise ratio. An unipolar pulsed bias was used with this setup (on time 5.00 ms, off time 5.52 ms). The trigger output of the Keithley source was fed into the reference input of the lock-in. The on time was configured to be the longest allowed by the source and the EL measurement was performed at the end of the on period in order to make sure that the system had reached the steady state and therefore the DC EL was measured. This setup was used for the measurement of the time evolution of the EL (Section III-B).

The spectra of the samples have been measured with an Ocean Optics QE65000 spectrometer.

When using the source in pulsed mode only the EL and one electrical variable (either voltage or current) can be measured simultaneously. In contrast, when measuring in pure DC mode with the calibrated Newport detector, it is possible to measure the optical power and both electrical parameters (voltage and current) simultaneously. That allows calculating the injected electrical power for each measurement of the EL and therefore calculate the efficiency (Section III-A).

All the measurements taken with the calibrated detector and the spectrometer were corrected for the responsivity of the whole detection system. In particular, given the responsivity of the Newport 918D-UV-OD3 detector $r(\lambda)$ in A/W and the spectrum of the sample $Ps_n(\lambda)$ in W/nm (where $P$ is the unknown optical power and $s_n(\lambda)$ the spectrum normalized

to area 1), the generated photocurrent in the detector can be expressed as

$$i = P \int_0^\infty r(\lambda) s_n(\lambda) \mathrm{d}\lambda \qquad (2)$$

Since the generated photocurrent $i$ is measured by the 1931-C power meter, the unknown $P$ can be calculated as $P = i \times f$, where

$$f^{-1} = \int_0^\infty r(\lambda) s_n(\lambda) \mathrm{d}\lambda \qquad (3)$$

The factor $f$ depends on the sample through $s_n(\lambda)$. Therefore, it is necessary to measure the spectrum of each sample in order to numerically calculate the respective $f$ and then convert the measured photocurrent into the optical power received by the detector.

Since the detector does not collect all the light emitted by the device, a correction has also been made to compensate for the limited solid angle subtended by the detector. The emission profile of the samples is assumed to follow Lambert's cosine law, as shown with similar samples fabricated previously [19]. The error incurred in assuming a perfectly Lambertian emission is much smaller than the other sources of error and therefore it will be ignored. With the assumption of Lambertian emission it is straightforward to show that the relation between the total power $P_T$ and the collected power $P$ is

$$P_T = \frac{2}{1 - \cos 2\alpha} P \qquad (4)$$

where $2\alpha$ stands for the plane angle corresponding to the projection of the solid angle subtended by the detector. This angle can be calculated from the size of the active area and the detector and the distance between them using simple trigonometry. In our setup, the factor between $P_T$ and $P$ is $17 \pm 2$.

All the measurements have been performed at room temperature in a dark environment on a minimum of 5 different devices per wafer.

## III. RESULTS AND DISCUSSION

### A. Power Efficiency

Fig. 2 shows typical curves of power efficiency vs. current density of PECVD and ion implanted samples (circles and squares respectively). The errors arise from the uncertainty in the measurement of the photocurrent and the uncertainty in the measurement of the solid angle subtended by the 918D-UV-OD3 detector. Notice that the error fraction that corresponds to the uncertainty in the solid angle is a systematic error that affects all points in the same measure and therefore accounts for the product of the whole curve by an uncertain factor, but not for a change in its functional form. Since the power efficiency is calculated as the ratio of the measured optical power to the injected electrical power, the error in the
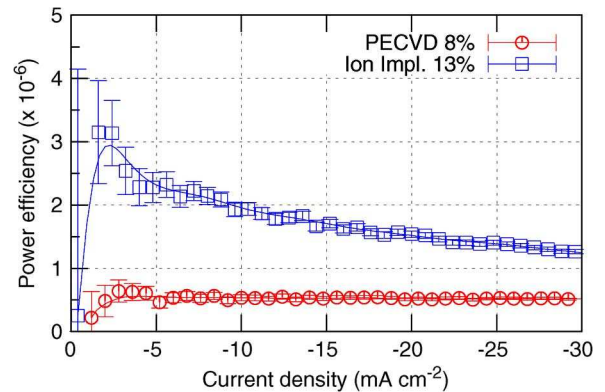


Fig. 2. Typical power efficiencies of PECVD and ion implanted samples as a function of current density (circles and squares, respectively). The lines are smoothings of the data points.
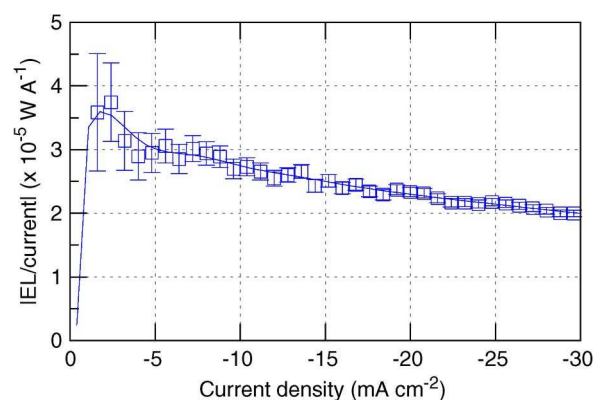


Fig. 3. Absolute value of the EL divided by the current (related to the quantum efficiency) as a function of the current density for the ion implanted sample with 13 at. % $XS_{Si}$. The line is a smoothing of the data points.

efficiency increases significantly for small values of the current density. The solid lines are Bézier smoothings of the measured data points.

A plot of EL divided by the current (which is related to the external quantum efficiency) as a function of the current density (Fig. 3) shows essentially the same features as the curves of power efficiency. That is so because the variation of the voltage in the range of studied currents is relatively small. It only accounts for about 3% of the variation of the electrical power in that range of currents. The same considerations on the errors apply to Fig. 3.

All the samples, regardless of fabrication technique or $XS_{Si}$, present a similar behavior. The efficiency increases at low currents until it reaches a maximum and then decreases slowly until breakdown. This kind of behavior has been reported for very thin $SiO_2$ and $HfO_2$ films [20]. Notice that for the PECVD sample the evolution after the initial transient is almost flat. That is consistent with the linear behavior of the EL-I curves reported in [21]. Similarly, the clear decrease in efficiency after the maximum in the ion implanted samples is consistent with the negative second derivative of the EL-I behavior reported in [21] (that is, $\sim x^a$ behavior, $0 < a < 1$). Since the efficiency is ultimately defined by a competition between radiative and nonradiative recombinations, this behavior could mean that the radiative and/or
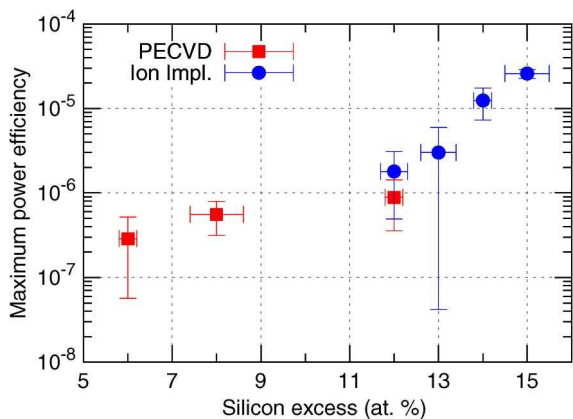
Fig. 4. Maximum power efficiency as a function of the $XS_{Si}$.
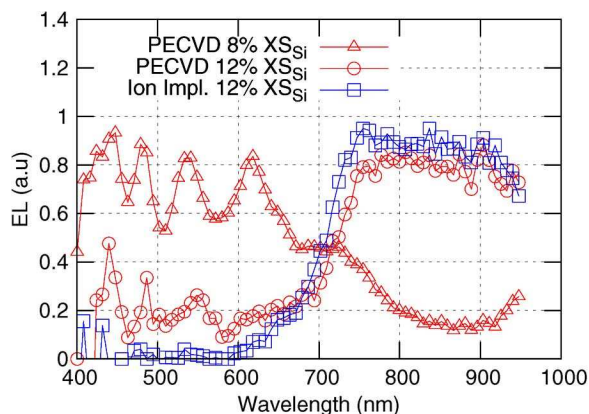


Fig. 5. The normalized spectra of the samples with $XS_{Si} < 12$ at. % show a broad band around 500 nm, while samples with $XS_{Si} \gtrsim 12$ at. % show a broad band around 850 nm regardless of the fabrication technique. For clarity, only three samples are shown. The effect of the transmittance of the polysilicon gate on the spectrum has been subtracted.



Fig. 6. Current density at which the maximum external efficiency is observed as a function of the $XS_{Si}$.

nonradiative recombination rates are affected by the field in the structure, or that the buildup of defects in the SRO during operation modifies the frequencies of the radiative and nonradiative transitions. This point will be discussed further in Section III-B.

It is worth noting that, in all cases, the maximum efficiency is observed at absolute current values below $10\ \mathrm{mA\ cm^{-2}}$, where the EL was difficult to observe with the unaided eye. Therefore, an actual use of the devices would require a compromise between the efficiency and the absolute emitted optical power.

Fig. 4 shows the maximum power efficiency as a function of the $XS_{Si}$ for all samples except sample PECVD-4. It was not possible to obtain reliable luminescence measurements for that sample because dielectric breakdown would occur before or immediately after the onset of the luminescence.

Two slightly different slopes might be identified in Fig. 4, one for PECVD and the other for ion implanted samples. However, that change could be due to the $XS_{Si}$ itself rather than the different fabrication technique. Indeed, the measured spectra (see Fig. 5) show two well differentiated groups of samples: for $XS_{Si}$ lower than 12 at. % a broad band around 500 nm is observed, whereas for $XS_{Si}$ equal or higher than 12 at. % a broad band around 850 nm is observed. Both the PECVD and ion implanted samples with 12 at. % $XS_{Si}$ present a very similar spectrum.

Due to the uncertainties in the measurements and the fact that there is only one common $XS_{Si}$ in both fabrication techniques (12 at. %), no unambiguous conclusions can be drawn from Fig. 4 as to the dependence of the efficiency on the fabrication technique. The ion implanted and PECVD samples with 12 at. % $XS_{Si}$ can be considered to have the same efficiency within the error.

Fig. 6 shows the current density at which the maximum external efficiency is observed, also as a function of the $XS_{Si}$. The errors in the maximum efficiency and the current at maximum efficiency arise from the uncertainty in the efficiency (which in turn stems from the uncertainty in the measurement of the photocurrent and the solid angle subtended by the detector as already discussed) and the dispersion of the signals measured from different devices of the same wafer.

The maximum power efficiency increases with the $XS_{Si}$, from $\approx 3 \times 10^{-7}$ in the PECVD sample with 6 at. % $XS_{Si}$ to $\approx 2 \times 10^{-5}$ in the ion implanted sample with 15 at. % $XS_{Si}$ (Fig. 4). This is not only because with higher $XS_{Si}$ higher EL intensities are achieved, but also for the notoriously lower current needed to obtain EL as the $XS_{Si}$ increases. This is confirmed in Fig. 6, in which it is clear that the absolute value of the current density at which the maximum efficiency is achieved decreases with the $XS_{Si}$, from $\approx 8\ \mathrm{mA\ cm^{-2}}$ of the PECVD sample with 6 at. % $XS_{Si}$ down to $\approx 1\ \mathrm{mA\ cm^{-2}}$ in the ion implanted sample with 15 at. % $XS_{Si}$.

There is a factor $\approx 73$ between the maximum efficiency of the PECVD sample with 6 at. % $XS_{Si}$ and the ion implanted sample with 15 at. % $XS_{Si}$. Of that 73, only a factor 2.6 arises from the increment in the emitted optical power, while a factor 26 comes from the decrease of the electrical power needed to reach the maximum efficiency.

The spectra of the samples is shown in Fig. 5 (for clarity, only three samples are plotted). The effect of the transmittance of the polysilicon gate on the spectra has been subtracted in Fig. 5, but it has been kept for the calculation of $f$ (equation (3)) since the spectrum received by the power meter includes the effect of the gate.

According to the measured spectra, the samples with $XS_{Si} \gtrsim 12$ at. % emit at lower energies than the samples with $XS_{Si} < 12$ at. % regardless of the fabrication technique. Since the emitted
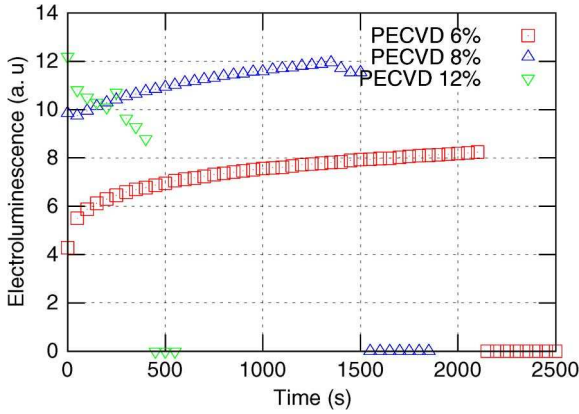
Fig. 7. Time evolution of the EL of the PECVD samples with varying $XS_{Si}$. The current density was fixed at $-6 \, \mathrm{mA/cm^{-2}}$.
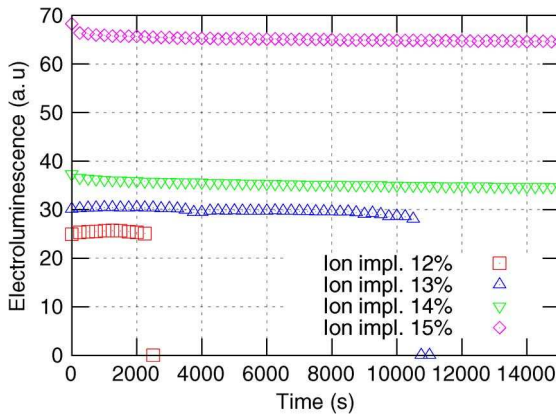


Fig. 8. Time evolution of the EL of the ion implanted samples with varying $XS_{Si}$. The current density was fixed at $-6 \, \mathrm{mA/cm^{-2}}$.

optical power is larger in the ion implanted sample with 15 at. % $XS_{Si}$ and its emission takes place at lower energies, either the recombination rate or the density of radiative centers is higher in that sample than in the PECVD sample with 6 at. % $XS_{Si}$. In either case, since the current at maximum efficiency is smaller in the ion implanted sample by a factor $\approx 8$ and there are more generated photons, the quantum efficiency must be higher. In fact, the ratio EL/current at the maximum measured power efficiency is larger in the ion implanted sample with 15 at. % $XS_{Si}$ than in the PECVD sample with 6 at. % $XS_{Si}$ by a factor $\approx 21$.

In [21] the luminescence of our devices was attributed to recombination through defects. We expect a higher density of defects in the samples with higher silicon excess. That would explain the lower energy required for the conduction into the active layer, thus increasing the power efficiency, and the higher recombination rates that would result in an improved quantum efficiency.

### B. Time Evolution of the Electroluminescence

Figs. 7 and 8 show the time evolution of the EL for PECVD and ion implanted samples, respectively, at a fixed current density of $-6 \, \mathrm{mA \, cm^{-2}}$. The voltage needed to keep the current at this level depends on the sample, from about $-40 \, V$ for the

PECVD sample with 6 at. % $XS_{Si}$ to about $-5 \, V$ for the ion implanted sample with 15 at. % $XS_{Si}$.

The EL of the PECVD devices with 6 at. % $XS_{Si}$ increases by a factor 2 before falling to zero after about 35 minutes of operation. When the EL falls to zero the voltage needed to keep the current at the specified level also drops dramatically to less than 1 V, which indicates that dielectric breakdown has occurred. When that happens, the current ceases to flow uniformly and starts to flow through a limited number of conductive paths and the luminescence disappears [22]. The PECVD sample with 8 at. % $XS_{Si}$ shows a similar behavior, although the relative change in the EL is smaller and the lifetime is shorter. Also, a small decrease in the EL is observed during the first seconds of operation before increasing. PECVD devices with 12 at. % $XS_{Si}$ behave differently. The EL decreases rapidly and the lifetime is even shorter. As already noted, the sample with 16 at. % breaks down before any luminescence can be reliably detected. In some of the devices the measurements become unstable near the end of their life (see samples with 8 at. % and 12 at. % $XS_{Si}$ in Fig. 7). This is probably related to a blinking of the EL [5] at frequencies above the driving frequency. Since the output signal is filtered by a lock-in amplifier, a change of the frequency spectrum of the optical signal between measurements will affect the output of the lock-in in a rather unpredictable way. Therefore, in this circumstances the measurements become unreliable.

The ion implanted samples with 12 at. % and 13 at. % $XS_{Si}$ show a slight increase of the EL during the first minutes of operation. Afterwards, the EL tends to decrease slowly. The EL of the devices with 14 at. % and 15 at. % $XS_{Si}$ decreases from the beginning of the operation, although at a very slow pace.

The typical lifetime of the ion implanted samples increases with the $XS_{Si}$, contrary to the trend exhibited by their PECVD counterparts. The ion implanted samples with 14 at. % and 15 at. % $XS_{Si}$ were still emitting after 27 hours of continuous operation. It is worth noting here that, under the pulsed operation described in Section II, the devices are in the on state only half the total time of operation.

It is not completely clear why PECVD and ion implanted samples exhibit an opposite dependence of the lifetime as a function of silicon excess. However, it is worth noting that PECVD samples store positive charge, with an increasing amount with silicon excess, whereas ion implanted samples store negative charge with a decreasing amount with silicon excess, as extracted from capacitance-voltage measurements [21].

Since the current density is kept constant during the experiment, a constant EL intensity would be expected. However, the electrical properties of the devices do not remain constant. Fig. 9 shows a typical evolution of the voltage with time when the current is fixed at $-6 \, \mathrm{mA \, cm^{-2}}$. The high voltages needed in the PECVD samples probably induce the injection of hot electrons in the SRO layer, which would explain its rapid degradation. Charge trapping [21] and the degradation induced by the buildup of defects in the bulk of the SRO or the SRO/Si interface [23] due to hot electrons are most likely responsible for this change in the voltage (and electric field) and could account for a modification of the radiative and/or nonradiative recombination rates, therefore modifying the EL intensity.
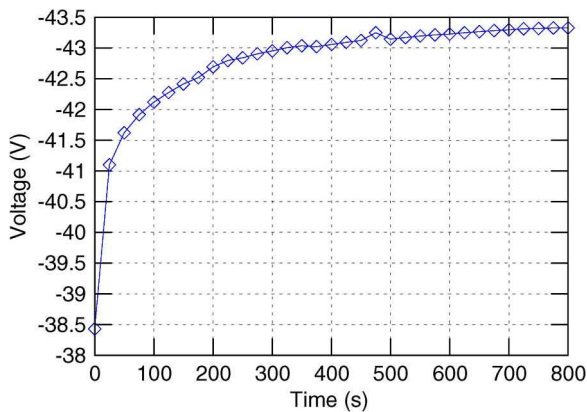
Fig. 9. Typical time evolution of the voltage. The curve corresponds to the PECVD sample with 6 at. % $XS_{Si}$ and the current density was fixed at $-6 \text{ mA/cm}^{-2}$.

## IV. CONCLUSIONS

The electroluminescence power efficiency in DC has been measured as a function of the current density in SRO layers fabricated by PECVD and silicon ion implantation with different $XS_{Si}$. The maximum efficiency increases with the $XS_{Si}$, while the current density at which the maximum is observed decreases with the $XS_{Si}$. The sample that presents the highest value of both power and quantum efficiency among those measured was fabricated by ion implantation with 15 at. % $XS_{Si}$. The maximum power efficiency is $(2.6 \pm 0.3) \times 10^{-5}$. The enhancement of the maximum efficiency arises primarily from the decrease in the electrical power drawn at maximum efficiency rather than the increased electroluminescence intensity.

The evolution of the EL intensity with time when a constant electrical current is applied indicates that the quantum efficiency varies during operation. This behavior has been related to the change in the voltage needed to keep the current at the specified level due to the buildup of defects and charge trapping in the active layer, which can effectively modify the ratio between the probabilities of radiative and nonradiative recombinations.

Endurance tests show that the ion implanted samples are more stable and have a longer lifetime than their PECVD counterparts.

## REFERENCES

[1] L. Dal Negro, J. H. Yi, J. Michel, L. C. Kimerling, T.-W. F. Chang, V. Sukhovatkin, and E. H. Sargent, "Light emission efficiency and dynamics in silicon-rich silicon nitride films," *Appl. Phys. Lett.*, vol. 88, p. 233109, 2006.

[2] G.-R. Lin, Y.-H. Pai, C.-T. Lin, and C.-C. Chen, "Comparison on the electroluminescence of Si-rich SiNx and SiOx based light-emitting diodes," *Appl. Phys. Lett.*, vol. 96, p. 263514, 2010.

[3] A. Anopchenko, S. Prezioso, Z. Gaburro, L. Ferraioli, G. Pucker, P. Bellutti, and L. Pavesi, "Charge transport and electroluminescence in PECVD grown silicon-nanocrystals-based LEDs," in *Proc. IEEE Group IV Photonics*, 2007, pp. 70–72.

[4] X. Wang, J. Zhang, L. Ding, B. Cheng, W. Ge, J. Yu, and Q. Wang, "Origin and evolution of photoluminescence from Si nanocrystals embedded in a SiO2 matrix," *Phys. Rev. B*, vol. 72, p. 195315, 2005.

[5] M. Meretoja, R. Punkkinen, H.-P. Hedman, L. Heikkilä, M. Hirvonen, T. Suominen, and M. Heinonen, "Electroluminescence in Si/SiO2 microstructures," *Physica Scripta*, vol. T114, pp. 53–56, 2004.

[6] L. Ding, M. Yu, X. Tu, G. Lo, S. Tripathy, and T. Chen, "Laterally-current-injected light-emitting diodes based on nanocrystalline-Si/SiO 2 superlattice," *Opt. Exp.*, vol. 19, pp. 2729–2738, 2011.

[7] M. Zacharias, J. Heitmann, R. Scholz, U. Kahler, M. Schmidt, and J. Bläsing, "Size-controlled highly luminescent silicon nanocrystals: A SiO/SiO2 superlattice approach," *Appl. Phys. Lett.*, vol. 80, p. 661, 2002.

[8] A. Marconi, A. Anopchenko, G. Pucker, and L. Pavesi, "Power efficiency estimation of silicon nanocrystals based light emitting devices in alternating current regime," *Appl. Phys. Lett.*, vol. 98, p. 201103, 2011.

[9] J. Warga, R. Li, S. N. Basu, and L. Dal Negro, "Electroluminescence from silicon-rich nitride/silicon superlattice structures," *Appl. Phys. Lett.*, vol. 93, p. 151116, 2008.

[10] M. Wang, A. Anopchenko, A. Marconi, E. Moser, S. Prezioso, L. Pavesi, G. Pucker, P. Bellutti, and L. Vanzetti, "Light emitting devices based on nanocrystalline-silicon multilayer structure," *Physica E: Low-Dimensional Syst. Nanostructures*, vol. 41, pp. 912–915, 2009.

[11] A. Marconi, A. Anopchenko, M. Wang, G. Pucker, P. Bellutti, and L. Pavesi, "High power efficiency in Si-nc/SiO2 multilayer light emitting devices by bipolar direct tunneling," *Appl. Phys. Lett.*, vol. 94, p. 221110, 2009.

[12] M. Perálvarez, J. Barreto, J. Carreras, A. Morales, D. Navarro-Urrios, Y. Lebour, C. Domínguez-Horna, and B. Garrido, "Si-nanocrystal-based LEDs fabricated by ion implantation and plasma-enhanced chemical vapour deposition," *Nanotechnology*, vol. 20, p. 405201, 2009.

[13] M. Perálvarez, C. García, M. Løpez, J. Barreto, B. Garrido, C. Domínguez-Horna, and J. A. Rodríguez, "Field effect luminescence from Si nanocrystals obtained by plasma-enhanced chemical vapor deposition," *Appl. Phys. Lett.*, vol. 89, p. 051112, 2006.

[14] B. Garrido, M. López, C. García, A. Pérez-Rodríguez, J. R. Morante, C. Bonafos, M. Carrada, and A. Claverie, "Influence of average size and interface passivation on the spectral emission of Si nanocrystals embedded in SiO2," *J. Appl. Phys.*, vol. 91, pp. 798–807, 2002.

[15] J. Barreto, M. Perálvarez, A. Morales-Sánchez, B. Garrido, J. Montserrat, and C. Domínguez-Horna, "Broad range adjustable emission of stacked SiN x/SiO y layers," *J. Mater. Res.*, vol. 23, pp. 1513–1516, 2011.

[16] J. A. Luna-López, A. Morales-Sánchez, M. Aceves-Mijares, Z. Yu, and C. Domínguez, "Analysis of surface roughness and its relationship with photoluminescence properties of silicon-rich oxide films," *J. Vacuum Sci. Technol. A*, vol. 27, p. 57, 2009.

[17] J. Ziegler [Online]. Available: http://www.srim.org

[18] L. Ding, T. P. Chen, M. Yang, J. I. Wong, Z. Cen, Y. Liu, F. Zhu, and A. A. Tseng, "Relationship between current transport and electroluminescence in Si+ -implanted SiO2 thin films," *IEEE Trans. Electron Devices*, vol. 56, pp. 2785–2791, 2009.

[19] D. Izquierdo, M. C. Garralaga, Í. Salinas, J. Barreto, and C. Domínguez-Horna, "Silicon nanocrystals light emitting devices: Characterization and coupling to SU-8 waveguides," in *Proc. SPIE Photonics Eur.*, Brussels, 2010, p. 7719M.

[20] T. Arguirov, C. Wenger, M. Lukosius, T. Mchedlidze, M. Reiche, and M. Kittler, "Silicon based light emitter utilizing tunnel injection of excess carriers via MIS structure," *Phys. Stat. Sol. (C)*, vol. 8, pp. 1302–1306, 2011.

[21] A. A. González-Fernández, J. Juvert, A. Morales-Sánchez, J. Barreto, M. Aceves-Mijares, and C. Domínguez, "Comparison of electrical and electro-optical characteristics of light-emitting capacitors based on silicon-rich Si-oxide fabricated by plasma-enhanced chemical vapor deposition and ion implantation," *J. Appl. Phys.*, vol. 111, p. 053109, 2012.

[22] A. González-Fernández, M. Mijares, A. Sánchez, and K. Leyva, "Intense whole area electroluminescence from low pressure chemical vapor deposition-silicon-rich oxide based light emitting capacitors," *J. Appl. Phys.*, vol. 108, p. 043105, 2010.

[23] D. Dimaria, "Defect production, degradation, and breakdown of silicon dioxide films," *Solid-State Electron.*, vol. 41, pp. 957–965, 1997.

# Appendix C

# Fabrication Processes

## C.1.   II-SRO Films and Devices Fabrication Run

**(CNM record number: 6418-PHD)**

| | Process Step | Description | Samples[a] |
|---|---|---|---|
| 1. | Take and label wafers | P-type wafers. Resitivity of 0.1 $\Omega\times$cm – 1.4 $\Omega\times$cm. | $\cdot$(DEV-)II$_{SiO_x}$ $\cdot$(DEV-)II$_{0.46}$ $\cdot$(DEV-)II$_{1.30}$ $\cdot$(DEV-)Bi-II$_{SiO_x}$ $\cdot$(DEV-)Bi-II$_{0.46}$ $\cdot$(DEV-)Bi-II$_{1.30}$ |
| 2. | Cleaning of wafers | Elimination of organic and metallic residues. | $\cdot$(DEV-)II$_{SiO_x}$ $\cdot$(DEV-)II$_{0.46}$ $\cdot$(DEV-)II$_{1.30}$ $\cdot$(DEV-)Bi-II$_{SiO_x}$ $\cdot$(DEV-)Bi-II$_{0.46}$ $\cdot$(DEV-)Bi-II$_{1.30}$ |
| 3. | Thermal oxidation | Dry growth of 30 nm of $SiO_2$ at 1000℃. | $\cdot$(DEV-)II$_{SiO_x}$ $\cdot$(DEV-)II$_{0.46}$ $\cdot$(DEV-)II$_{1.30}$ $\cdot$(DEV-)Bi-II$_{SiO_x}$ $\cdot$(DEV-)Bi-II$_{0.46}$ $\cdot$(DEV-)Bi-II$_{1.30}$ |
| 4. | Elimination of back oxide | Protection of the front with resist, elimination of $SiO_2$ and further elimination of resits. | $\cdot$(DEV-)II$_{SiO_x}$ $\cdot$(DEV-)II$_{0.46}$ $\cdot$(DEV-)II$_{1.30}$ $\cdot$(DEV-)Bi-II$_{SiO_x}$ $\cdot$(DEV-)Bi-II$_{0.46}$ $\cdot$(DEV-)Bi-II$_{1.30}$ |
| 5. | LPCVD of a $Si_3N_4$ film | Deposition of 30 nm-thick $Si_3N_4$ at 800℃ using $NH_3$ and $SiH_2Cl_2$. | $\cdot$(DEV-)II$_{SiO_x}$ $\cdot$(DEV-)II$_{0.46}$ $\cdot$(DEV-)II$_{1.30}$ $\cdot$(DEV-)Bi-II$_{SiO_x}$ $\cdot$(DEV-)Bi-II$_{0.46}$ $\cdot$(DEV-)Bi-II$_{1.30}$ |
| 6. | Initial silicon ion implantation (lowest final dose) | Dose: $2.4\times10^{15}$ cm$^{-2}$ Energy: 25 keV | $\cdot$(DEV-)II$_{0.46}$ $\cdot$(DEV-)Bi-II$_{0.46}$ |

[a]The notation "(DEV-)II$_{XXXX}$" indicates that both II$_{XXXX}$ and DEV-II$_{XXXX}$ samples were included in the specific process step.

| | Process Step | Description | Samples[a] |
|---|---|---|---|
| 7. | Final silicon ion implantation (lowest final dose) | Dose: $9.6 \times 10^{15}$ cm$^{-2}$ <br> Energy: 50 keV | $\cdot$(DEV-)II$_{0.46}$ <br><br> $\cdot$(DEV-)Bi-II$_{0.46}$ |
| 8. | Initial silicon ion implantation (mid. final dose) | Dose: $3 \times 10^{15}$ cm$^{-2}$ <br> Energy: 25 keV | $\cdot$(DEV-)II$_{SiO_x}$ <br><br> $\cdot$(DEV-)Bi-II$_{SiO_x}$ |
| 9. | Final silicon ion implantation (mid final dose) | Dose: $12 \times 10^{15}$ cm$^{-2}$ <br> Energy: 50 keV | $\cdot$(DEV-)II$_{SiO_x}$ <br><br> $\cdot$(DEV-)Bi-II$_{SiO_x}$ |
| 10. | Initial silicon ion implantation (highest final dose) | Dose: $6 \times 10^{15}$ cm$^{-2}$. <br> Energy: 25 keV. | $\cdot$(DEV-)II$_{1.30}$ <br><br> $\cdot$(DEV-)Bi-II$_{1.30}$ |
| 11. | Final silicon ion implantation (highest final dose) | Dose: $24 \times 10^{15}$ cm$^{-2}$. <br> Energy: 50 keV. | $\cdot$(DEV-)II$_{1.30}$ <br><br> $\cdot$(DEV-)Bi-II$_{1.30}$ |
| 12. | Thermal annealing | Temperature: 1100℃. <br> Time: 240 minutes. <br> Atmosphere: N$_2$ gas. | $\cdot$(DEV-)II$_{SiO_x}$ <br> $\cdot$(DEV-)II$_{0.46}$ <br> $\cdot$(DEV-)II$_{1.30}$ <br> $\cdot$(DEV-)Bi-II$_{SiO_x}$ <br> $\cdot$(DEV-)Bi-II$_{0.46}$ <br> $\cdot$(DEV-)Bi-II$_{1.30}$ |
| 13. | Protection of the obverse with resist | Deposition of photoresist on top of the silicon nitride layer. | $\cdot$(DEV-)Bi-II$_{SiO_x}$ <br> $\cdot$(DEV-)Bi-II$_{0.46}$ <br> $\cdot$(DEV-)Bi-II$_{1.30}$ |

[a]The notation "(DEV-)II$_{XXXX}$" indicates that both II$_{XXXX}$ and DEV-II$_{XXXX}$ samples were included in the specific process step.

| Process Step | Description | Samples[a] |
|---|---|---|
| 14. Etching of $Si_3N_4$ | Elimination of the silicon nitride deposited in the back in the LPCVD. | ·(DEV-)Bi-II$_{SiO_x}$<br>·(DEV-)Bi-II$_{0.46}$<br>·(DEV-)Bi-II$_{1.30}$ |
| 15. Removing of protective resist | Elimination of the resist used to protect the obverse of the wafers. | ·(DEV-)Bi-II$_{SiO_x}$<br>·(DEV-)Bi-II$_{0.46}$<br>·(DEV-)Bi-II$_{1.30}$ |
| 16. Etching of $Si_3N_4$ | Wet etching of silicon nitride both in obverse and reverse of the wafers. | ·(DEV-)II$_{SiO_x}$<br>·(DEV-)II$_{0.46}$<br>·(DEV-)II$_{1.30}$ |
| 17. Implantation of Boron in the reverse | Implantation of B in the back the ohmic contact of devices. Dose: $5 \times 10^{14}$ cm$^{-2}$. Energy: 80 keV. | ·(DEV-)II$_{SiO_x}$<br>·(DEV-)II$_{0.46}$<br>·(DEV-)II$_{1.30}$<br>·(DEV-)Bi-II$_{SiO_x}$<br>·(DEV-)Bi-II$_{0.46}$<br>·(DEV-)Bi-II$_{1.30}$ |
| 18. Thermal annealing | Temperature: 800℃. Time: 30 minutes. | ·(DEV-)II$_{SiO_x}$<br>·(DEV-)II$_{0.46}$<br>·(DEV-)II$_{1.30}$<br>·(DEV-)Bi-II$_{SiO_x}$<br>·(DEV-)Bi-II$_{0.46}$<br>·(DEV-)Bi-II$_{1.30}$ |
| 19. End of the process for SRO films (devices continue) | Extraction of wafers for characterization of active layers. | ·II$_{SiO_x}$<br>·II$_{0.46}$<br>·II$_{1.30}$<br>·Bi-II$_{SiO_x}$<br>·Bi-II$_{0.46}$<br>·Bi-II$_{1.30}$ |
| 20. Deposition of $SiO_2$ in reverse | Deposition of 30 nm of PECVD $SiO_2$ in the back of te wafers. | ·DEV-II$_{SiO_x}$<br>·DEV-II$_{0.46}$<br>·DEV-II$_{1.30}$<br>·DEV-Bi-II$_{0.46}$<br>·DEV-Bi-II$_{1.30}$ |

[a]The notation "(DEV-)II$_{XXXX}$" indicates that both II$_{XXXX}$ and DEV-II$_{XXXX}$ samples were included in the specific process step.

162

| | Process Step | Description | Samples |
|---|---|---|---|
| 21. | Deposition of polycrystalline silicon | Deposition of 350 nm of polycrystalline Si using LPCVD with Silane at at 630℃. | ·DEV-II$_{SiO_x}$<br>·DEV-II$_{0.46}$<br>·DEV-II$_{1.30}$<br>·DEV-Bi-II$_{SiO_x}$<br>·DEV-Bi-II$_{0.46}$<br>·DEV-Bi-II$_{1.30}$ |
| 22. | Doping of the polycrystalline silicon | Doping using POCl$_3$ at 900℃. | ·DEV-II$_{SiO_x}$<br>·DEV-II$_{0.46}$<br>·DEV-II$_{1.30}$<br>·DEV-Bi-II$_{SiO_x}$<br>·DEV-Bi-II$_{0.46}$<br>·DEV-Bi-II$_{1.30}$ |
| 23. | Phosphosilicate Glass (PSG) Etching | Wet etching of PSG glass formed during the polysilicon doping. | ·DEV-II$_{SiO_x}$<br>·DEV-II$_{0.46}$<br>·DEV-II$_{1.30}$<br>·DEV-Bi-II$_{SiO_x}$<br>·DEV-Bi-II$_{0.46}$<br>·DEV-Bi-II$_{1.30}$ |
| 24. | Photolitography | Photolitography process to define the gates of the devices with photoresist (obverse of wafers). | ·DEV-II$_{SiO_x}$<br>·DEV-II$_{0.46}$<br>·DEV-II$_{1.30}$<br>·DEV-Bi-II$_{SiO_x}$<br>·DEV-Bi-II$_{0.46}$<br>·DEV-Bi-II$_{1.30}$ |
| 25. | Dry etchin of polysilicon in obverse | Reactive Ion Etching of polysilicon. Front of the wafers. | ·DEV-II$_{SiO_x}$<br>·DEV-II$_{0.46}$<br>·DEV-II$_{1.30}$<br>·DEV-Bi-II$_{SiO_x}$<br>·DEV-Bi-II$_{0.46}$<br>·DEV-Bi-II$_{1.30}$ |
| 26. | Dry etchin of polysilicon in reverse | Reactive Ion Etching of the polysilicon deposited in the reverse of the wafers. | ·DEV-II$_{SiO_x}$<br>·DEV-II$_{0.46}$<br>·DEV-II$_{1.30}$<br>·DEV-Bi-II$_{SiO_x}$<br>·DEV-Bi-II$_{0.46}$<br>·DEV-Bi-II$_{1.30}$ |
| 27. | Removing of resist | Elimination of the resist used to define the gate areas. | ·DEV-II$_{SiO_x}$<br>·DEV-II$_{0.46}$<br>·DEV-II$_{1.30}$<br>·DEV-Bi-II$_{SiO_x}$<br>·DEV-Bi-II$_{0.46}$<br>·DEV-Bi-II$_{1.30}$ |

| | Process Step | Description | Samples |
|---|---|---|---|
| 28. | Protection of the obverse with resist | Deposition of resist in the front of the wafers. | ·DEV-II$_{SiO_x}$<br>·DEV-II$_{0.46}$<br>·DEV-II$_{1.30}$<br>·DEV-Bi-II$_{SiO_x}$<br>·DEV-Bi-II$_{0.46}$<br>·DEV-Bi-II$_{1.30}$ |
| 29. | Etching of SiO$_2$ in reverse and elimination of resist | Wet etching of the SiO$_2$ deposited in step 20. Further elimination of the resist in the front. | ·DEV-II$_{SiO_x}$<br>·DEV-II$_{0.46}$<br>·DEV-II$_{1.30}$<br>·DEV-Bi-II$_{SiO_x}$<br>·DEV-Bi-II$_{0.46}$<br>·DEV-Bi-II$_{1.30}$ |
| 30. | Deposition of Al in the obverse | Elimination of native oxide and deposition of 11 µm of Al in the front of the wafers. | ·DEV-II$_{SiO_x}$<br>·DEV-II$_{0.46}$<br>·DEV-II$_{1.30}$<br>·DEV-Bi-II$_{SiO_x}$<br>·DEV-Bi-II$_{0.46}$<br>·DEV-Bi-II$_{1.30}$ |
| 31. | Photolithography and Al-etching obverse | Photolitography to define the pads of the gates, etch of the Al deposited, and elimination of resist. | ·DEV-II$_{SiO_x}$<br>·DEV-II$_{0.46}$<br>·DEV-II$_{1.30}$<br>·DEV-Bi-II$_{SiO_x}$<br>·DEV-Bi-II$_{0.46}$<br>·DEV-Bi-II$_{1.30}$ |
| 32. | Deposition of Al in the reverse | Al contacts. Deposition of 1 µm in the back of the wafer to form the back contact. | ·DEV-II$_{SiO_x}$<br>·DEV-II$_{0.46}$<br>·DEV-II$_{1.30}$<br>·DEV-Bi-II$_{SiO_x}$<br>·DEV-Bi-II$_{0.46}$<br>·DEV-Bi-II$_{1.30}$ |
| 32. | Annealing for Al contacts. | Temperature: 350℃. Time: 120 min. Ambient: N$_2$/H$_2$. | ·DEV-II$_{SiO_x}$<br>·DEV-II$_{0.46}$<br>·DEV-II$_{1.30}$<br>·DEV-Bi-II$_{SiO_x}$<br>·DEV-Bi-II$_{0.46}$<br>·DEV-Bi-II$_{1.30}$ |
| 33. | **End of the run** | Extraction of wafers. | ·DEV-II$_{SiO_x}$<br>·DEV-II$_{0.46}$<br>·DEV-II$_{1.30}$<br>·DEV-Bi-II$_{SiO_x}$<br>·DEV-Bi-II$_{0.46}$<br>·DEV-Bi-II$_{1.30}$ |

164

## C.2.  PECVD-SRO Fabrication Run

**(CNM record number: 6190)**

| | Process Step | Description | Samples |
|---|---|---|---|
| 1. | Take and label wafers | P-type wafers. Resitivity of $4\ \Omega\times$cm – $40\ \Omega\times$cm. | $\cdot$PECVD$_{2.96}$ $\cdot$PECVD$_{4.67}$ $\cdot$PECVD$_{5.67}$ |
| 2. | Cleaning of wafers | Elimination of organic and metallic residues. | $\cdot$PECVD$_{2.96}$ $\cdot$PECVD$_{4.67}$ $\cdot$PECVD$_{5.67}$ |
| 3. | PECVD of Si oxide | Temperature: 400 ℃. RF Power: 100 W. Total Flow: 1300 sccm. Flow ratio: 1185/115 (N$_2$O/SiH$_4$). Pressure: 2.8 Torr. Thickness: 300 nm | $\cdot$PECVD$_{2.96}$ |
| 4. | PECVD of Si oxide | Temperature: 400 ℃. RF Power: 300 W. Total Flow: 1300 sccm. Flow ratio: 1085/215 (N$_2$O/SiH$_4$). Pressure: 2.8 Torr. Thickness: 300 nm | $\cdot$PECVD$_{4.67}$ |
| 5. | PECVD of Si oxide | Temperature: 400 ℃. RF Power: 100 W. Total Flow: 1300 sccm. Flow ratio: 1085/215 (N$_2$O/SiH$_4$) Pressure: 2.8 Torr. Thickness: 300 nm | $\cdot$PECVD$_{5.67}$ |
| 6. | Thermal annealing | Temperature: 1240℃. Time: 60 min. Atmosphere: N$_2$ gas. | $\cdot$PECVD$_{2.96}$ $\cdot$PECVD$_{4.67}$ $\cdot$PECVD$_{5.67}$ |
| 7. | **End of the run** | Extraction of wafers. | $\cdot$PECVD$_{2.96}$ $\cdot$PECVD$_{4.67}$ $\cdot$PECVD$_{5.67}$ |

## C.3. PECVD-II-SRO Fabrication Run

**(CNM record number: 5800-PHD)**

| | Process Step | Description | Samples |
|---|---|---|---|
| 1. | Take and label wafers | P-type wafers. Resitivity of $0.1\ \Omega \times cm - 1.4\ \Omega \times cm.$ | ·PECVD-II$_{1.34}$ ·PECVD-II$_{4.06}$ ·PECVD-II$_{4.56}$ |
| 2. | Cleaning of wafers | Elimination of organic and metallic residues. | ·PECVD-II$_{1.34}$ ·PECVD-II$_{4.06}$ ·PECVD-II$_{4.56}$ |
| 3. | PECVD of SiO$_2$ | Deposition of 30 nm-thick stoichiometric SiO$_2$ according to CNM protocol (confirmed by ellipsometry). | ·PECVD-II$_{1.34}$ ·PECVD-II$_{4.06}$ ·PECVD-II$_{4.56}$ |
| 4. | LPCVD of Si$_3$N$_4$ | Deposition of 30 nm-thick sacrificial Si$_3$N$_4$ at 800℃ using NH$_3$ and SiH$_2$Cl$_2$ | ·PECVD-II$_{1.34}$ ·PECVD-II$_{4.06}$ ·PECVD-II$_{4.56}$ |
| 6. | Initial silicon ion implantation | Dose: $5\times10^{15}$ cm$^{-2}$ Energy: 25 keV | ·PECVD-II$_{1.34}$ |
| 7. | Final silicon ion implantation | Dose: $21\times10^{15}$ cm$^{-2}$ Energy: 50 keV | ·PECVD-II$_{1.34}$ |
| 8. | Initial silicon ion implantation | Dose: $15\times10^{15}$ cm$^{-2}$ Energy: 25 keV | ·PECVD-II$_{4.06}$ |

| Process Step | Description | Samples |
|---|---|---|
| 9. Final silicon ion implantation | Dose: $59 \times 10^{15}$ cm$^{-2}$<br>Energy: 50 keV | ·PECVD-II$_{4.06}$ |
| 10. Initial silicon ion implantation | Dose: $11 \times 10^{15}$ cm$^{-2}$<br>Energy: 25 keV | ·PECVD-II$_{4.56}$ |
| 11. Final silicon ion implantation | Dose: $42 \times 10^{15}$ cm$^{-2}$<br>Energy: 50 keV | ·PECVD-II$_{4.56}$ |
| 12. Thermal annealing | Temperature: 1100℃.<br>Time: 240 minutes.<br>Atmosphere: $N_2$ gas. | ·PECVD-II$_{1.34}$<br>·PECVD-II$_{4.06}$<br>·PECVD-II$_{4.56}$ |
| 13. Etching of $Si_3N_4$ | Wet etching of silicon nitride both in obverse and reverse of the wafers. | ·PECVD-II$_{1.34}$<br>·PECVD-II$_{4.06}$<br>·PECVD-II$_{4.56}$ |
| 14. Thermal annealing | Temperature: 800℃.<br>Time: 30 min.<br>Ambient: $N_2$<br>(typical for activation of B when implanting back contact). | ·PECVD-II$_{1.34}$<br>·PECVD-II$_{4.06}$<br>·PECVD-II$_{4.56}$ |
| 15. Thermal annealing | Temperature: 350℃.<br>Time: 120 min.<br>Ambient: $N_2/H_2$.<br>(typical for Al contacts). | ·PECVD-II$_{1.34}$<br>·PECVD-II$_{4.06}$<br>·PECVD-II$_{4.56}$ |
| 16. **End of the run** | Extraction of wafers. | ·PECVD-II$_{1.34}$<br>·PECVD-II$_{4.06}$<br>·PECVD-II$_{4.56}$ |

# C.4. Different SRO thickness Fabrication Run

**(CNM record number: 6753-IMM)**

| Process Step | Description | Samples |
|---|---|---|
| 1. Take and label wafers | P-type wafers.<br>Resitivity of<br>4 $\Omega \times$cm – 40 $\Omega \times$cm. | ·Bi-SiO$_x$-II$_{30nm}$<br>·Bi-SiO$_x$-II$_{300nm}$<br>·Bi-PECVD-II$_{30nm}$<br>·Bi-PECVD-II$_{300nm}$ |
| 2. Cleaning of wafers | Elimination of organic and metallic residues. | ·Bi-SiO$_x$-II$_{30nm}$<br>·Bi-SiO$_x$-II$_{300nm}$<br>·Bi-PECVD-II$_{30nm}$<br>·Bi-PECVD-II$_{300nm}$ |
| 3. Thermal oxidation | Dry growth of 30 nm of SiO$_2$ at 1000℃. | ·Bi-SiO$_x$-II$_{30nm}$ |
| 4. Thermal oxidation | Humid growth of 300 nm of SiO$_2$ at 1100℃. | ·Bi-SiO$_x$-II$_{300nm}$ |
| 5. PECVD of Si oxide | Temperature: 400 ℃.<br>RF Power: 100 W.<br>Total Flow: 1300 sccm.<br>Flow ratio: 1185/115 (N$_2$O/SiH$_4$).<br>Pressure: 2.8 Torr.<br>Thickness: 30 nm. | ·Bi-PECVD-II$_{30nm}$ |
| 6. PECVD of Si oxide | Temperature: 400 ℃.<br>RF Power: 100 W.<br>Total Flow: 1300 sccm.<br>Flow ratio: 1185/115 (N$_2$O/SiH$_4$).<br>Pressure: 2.8 Torr.<br>Thickness: 300 nm. | ·Bi-PECVD-II$_{300nm}$ |

168

| Process Step | | Description | Samples |
|---|---|---|---|
| 7. | LPCVD of $Si_3N_4$ | Deposition of 30 nm-thick $Si_3N_4$ at 800°Cusing $NH_3$ and $SiH_2Cl_2$ | ·Bi-SiO$_x$-II$_{30nm}$<br>·Bi-SiO$_x$-II$_{300nm}$<br>·Bi-PECVD-II$_{30nm}$<br>·Bi-PECVD-II$_{300nm}$ |
| 8. | Initial silicon ion implantation | Dose: $3\times10^{15}$ cm$^{-2}$<br>Energy: 25 keV | ·Bi-SiO$_x$-II$_{30nm}$<br>·Bi-SiO$_x$-II$_{300nm}$<br>·Bi-PECVD-II$_{30nm}$<br>·Bi-PECVD-II$_{300nm}$ |
| 9. | Final silicon ion implantation | Dose: $12\times10^{15}$ cm$^{-2}$<br>Energy: 50 keV | ·Bi-SiO$_x$-II$_{30nm}$<br>·Bi-SiO$_x$-II$_{300nm}$<br>·Bi-PECVD-II$_{30nm}$<br>·Bi-PECVD-II$_{300nm}$ |
| 10. | Thermal annealing | Temperature: 1240°C.<br>Time: 60 minutes.<br>Atmosphere: $N_2$ gas. | ·Bi-SiO$_x$-II$_{30nm}$<br>·Bi-SiO$_x$-II$_{300nm}$<br>·Bi-PECVD-II$_{30nm}$<br>·Bi-PECVD-II$_{300nm}$ |
| 11. | **End of the run** | Extraction of wafers. | ·Bi-SiO$_x$-II$_{30nm}$<br>·Bi-SiO$_x$-II$_{300nm}$<br>·Bi-PECVD-II$_{30nm}$<br>·Bi-PECVD-II$_{300nm}$ |

# C.5.  Integrated Optical System Fabrication Run

**(CNM record number: 7272-PIC)**

| | Process Step | Description | Samples |
|---|---|---|---|
| 1. | Take wafers and measure resistivity | N-type wafers. Nominal resitivity of 1 $\Omega \times$cm – 12 $\Omega \times$cm. | |
| 2. | Select and label wafers with lowest res. variation | Result of the selection: $\overline{\rho} = (1.98 \pm 0.02)$ $\Omega \times$cm. | $\cdot$IOS$_{ActMat}$ $\cdot$IOS$_{PolyGate}$ $\cdot$IOS$_{MetalGate}$ |
| 3. | Cleaning of wafers | Elimination of organic and metallic residues. | $\cdot$IOS$_{ActMat}$ $\cdot$IOS$_{PolyGate}$ $\cdot$IOS$_{MetalGate}$ |
| 4. | Oxidation process | Dry growth of 30 nm of SiO$_2$ at 1000℃. | $\cdot$IOS$_{ActMat}$ $\cdot$IOS$_{PolyGate}$ $\cdot$IOS$_{MetalGate}$ |
| 5. | LPCVD deposition of Si$_3$N$_4$ | Deposition of 117.5 nm of Si$_3$N$_4$ at 800℃using NH$_3$ and SiH$_2$Cl$_2$. | $\cdot$IOS$_{ActMat}$ $\cdot$IOS$_{PolyGate}$ $\cdot$IOS$_{MetalGate}$ |
| 6. | LPCVD deposition of Si$_3$N$_4$ | Deposition of 117.5 nm of Si$_3$N$_4$ at 800℃using NH$_3$ and SiH$_2$Cl$_2$. | $\cdot$IOS$_{ActMat}$ $\cdot$IOS$_{PolyGate}$ $\cdot$IOS$_{MetalGate}$ |
| 7. | Photolithography | Definition of the trench that will form the bottom SiO$_2$ cladding. | $\cdot$IOS$_{PolyGate}$ $\cdot$IOS$_{MetalGate}$ |

| Process Step | Description | Samples |
|---|---|---|
| 8. Nitride etching | Plasma etching of nitride to open the windows for the trench. | ·IOS$_{PolyGate}$<br>·IOS$_{MetalGate}$ |
| 9. Dioxide etching | Wet etching of oxide to open the windows for the trench. | ·IOS$_{PolyGate}$<br>·IOS$_{MetalGate}$ |
| 10. Etching of Si | Dry etching of the exposed Si to create the trench. | ·IOS$_{PolyGate}$<br>·IOS$_{MetalGate}$ |
| 11. Removing of resist | Elimination of the resist used to define the trench areas (step 7). | ·IOS$_{PolyGate}$<br>·IOS$_{MetalGate}$ |
| 12. Oxidation process | Wet oxidation of the exposed silicon trench. 1.6 µm at 1100℃. | ·IOS$_{ActMat}$<br>·IOS$_{PolyGate}$<br>·IOS$_{MetalGate}$ |
| 13. Dioxide etching process | Wet etching of the oxinitride formed during the previous step. | ·IOS$_{ActMat}$<br>·IOS$_{PolyGate}$<br>·IOS$_{MetalGate}$ |
| 14. Nitride film elimination | Wet etching of the Si$_3$N$_4$ film deposited in the step 6. | ·IOS$_{ActMat}$<br>·IOS$_{PolyGate}$<br>·IOS$_{MetalGate}$ |
| 15. DBPTEOS layer deposition | Deposition of 130 nm of undopped TEOS and 1.1 µm of BPTEOS. | ·IOS$_{ActMat}$<br>·IOS$_{PolyGate}$<br>·IOS$_{MetalGate}$ |

| | Process Step | Description | Samples |
|---|---|---|---|
| 16. | Fluidification process | Annealing in 5% $O_2$ ambient for 5 hours at 1000 ℃. | ·$IOS_{ActMat}$ ·$IOS_{PolyGate}$ ·$IOS_{MetalGate}$ |
| 17. | Oxide etching process | Highly controlled dry etching to level trench to Si substrate surface. | ·$IOS_{ActMat}$ ·$IOS_{PolyGate}$ ·$IOS_{MetalGate}$ |
| 18. | Protection of the obverse with resist | Deposition of resist in the front of the wafers. | ·$IOS_{ActMat}$ ·$IOS_{PolyGate}$ ·$IOS_{MetalGate}$ |
| 19. | Etching of oxide in the reverse and elimination of resist | Etching of the $SiO_2$ deposited on reverse of the wafer and removal of resist. | ·$IOS_{ActMat}$ ·$IOS_{PolyGate}$ ·$IOS_{MetalGate}$ |
| 20. | Fabrication of $SiO_2$-$Si_3N_4$ masking layer | 300 nm of variable oxide at 1000 ℃, followed by 130 nm of nitride at 800 ℃. | ·$IOS_{ActMat}$ ·$IOS_{PolyGate}$ ·$IOS_{MetalGate}$ |
| 21. | Photolithography | Definition of the $p++$ wells to be implanted. | ·$IOS_{PolyGate}$ ·$IOS_{MetalGate}$ |
| 22. | Etching of $SiO_2$ and $Si_3N_4$ | Dry etching of the $Si_3N_4$, and wet etching of $SiO_2$. | ·$IOS_{ActMat}$ ·$IOS_{PolyGate}$ ·$IOS_{MetalGate}$ |
| 23. | Removing of resist | Elimination of the resist used to define the $p++$ areas (step 21). | ·$IOS_{PolyGate}$ ·$IOS_{MetalGate}$ |

| | Process Step | Description | Samples |
|---|---|---|---|
| 24. | Implantation of boron ions in the obverse | Implantation of B to obtain the $p++$ wells: Dose: $1 \times 10^{15}$ cm$^{-2}$ Energy: 50 keV. | $\cdot$IOS$_{ActMat}$ $\cdot$IOS$_{PolyGate}$ $\cdot$IOS$_{MetalGate}$ |
| 25. | Etching of SiO$_2$ and Si$_3$N$_4$ | Dry etching of the Si$_3$N$_4$, and wet etching of SiO$_2$. | $\cdot$IOS$_{PolyGate}$ $\cdot$IOS$_{MetalGate}$ |
| 26. | Implantation of phosphorous ions in the reverse | Implantation of P for the back contanct Dose: $4.2 \times 10^{15}$ cm$^{-2}$ Energy: 100 keV. | $\cdot$IOS$_{ActMat}$ $\cdot$IOS$_{PolyGate}$ $\cdot$IOS$_{MetalGate}$ |
| 27. | LPCVD of a Si$_3$N$_4$ film | Deposition of 30 nm of Si$_3$N$_4$ at 800℃ using NH$_3$ and SiH$_2$Cl$_2$. | $\cdot$IOS$_{ActMat}$ $\cdot$IOS$_{PolyGate}$ $\cdot$IOS$_{MetalGate}$ |
| 28. | Photolithography | Definition of the waveguide geometry. | $\cdot$IOS$_{PolyGate}$ $\cdot$IOS$_{MetalGate}$ |
| 29. | Etching of Si$_3$N$_4$ | Dry etching of the unmasked Si$_3$N$_4$ deposited in step 27. | $\cdot$IOS$_{ActMat}$ $\cdot$IOS$_{PolyGate}$ $\cdot$IOS$_{MetalGate}$ |
| 30. | Removing of resist | Elimination of the resist used to define waveguide area (step 28). | $\cdot$IOS$_{PolyGate}$ $\cdot$IOS$_{MetalGate}$ |
| 31. | Photolithography | Definition of the LEC geom. to remove if from the lower part of the waveguide | $\cdot$IOS$_{PolyGate}$ $\cdot$IOS$_{MetalGate}$ |

| | Process Step | Description | Samples |
|---|---|---|---|
| 32. | Etching of $Si_3N_4$ | Dry etching of the unmasked $Si_3N_4$ of the waveguide. | ·IOS$_{PolyGate}$ <br> ·IOS$_{MetalGate}$ |
| 33. | Removing of resist | Elimination of the resist used to define the LEC area (step 31). | ·IOS$_{PolyGate}$ <br> ·IOS$_{MetalGate}$ |
| 34. | PECVD of $SiO_2$ | Based on $N_2O$ and $SiH_4$. Standard laboratory conditions to obtain 30 nm-thick dioxide with $n = 1.46$. | ·IOS$_{ActMat}$ <br> ·IOS$_{PolyGate}$ <br> ·IOS$_{MetalGate}$ |
| 35. | Photolithography | Definition of the LEC geom. to remove the rest of the $SiO_2$. <br> o | ·IOS$_{PolyGate}$ <br> ·IOS$_{MetalGate}$ |
| 36. | Etching of $SiO_2$ | Wet etching of the unmasked $SiO_2$ deposited in the step 34. | ·IOS$_{PolyGate}$ <br> ·IOS$_{MetalGate}$ |
| 37. | Removing of resist | Elimination of the resist used to define the LEC geometry (step 35). | ·IOS$_{PolyGate}$ <br> ·IOS$_{MetalGate}$ |
| 38. | LPCVD of a $Si_3N_4$ film | Deposition of 30 nm of $Si_3N_4$ at 800℃ using $NH_3$ and $SiH_2Cl_2$. | ·IOS$_{ActMat}$ <br> ·IOS$_{PolyGate}$ <br> ·IOS$_{MetalGate}$ |
| 39. | Photolithography | Definition of the waveguide geometry. | ·IOS$_{PolyGate}$ <br> ·IOS$_{MetalGate}$ |

174

| | Process Step | Description | Samples |
|---|---|---|---|
| 40. | Etching of $Si_3N_4$ | Dry etching of the unmasked $Si_3N_4$ deposited in step 27. | ·IOS$_{PolyGate}$ ·IOS$_{MetalGate}$ |
| 41. | Removing of resist | Elimination of the resist used to define the waveguide (step 39). | ·IOS$_{PolyGate}$ ·IOS$_{MetalGate}$ |
| 42. | Photolithography | Definition of the area to implant silicon ions. | ·IOS$_{PolyGate}$ ·IOS$_{MetalGate}$ |
| 43. | Annealing to photorresist | Baking of photorresist at 180℃for 30 min. | ·IOS$_{PolyGate}$ ·IOS$_{MetalGate}$ |
| 44. | Initial silicon ion implantation | Dose: $2.4 \times 10^{15}$ cm$^{-2}$ Energy: 25 keV | ·IOS$_{ActMat}$ ·IOS$_{PolyGate}$ ·IOS$_{MetalGate}$ |
| 45. | Final silicon ion implantation | Dose: $9.6 \times 10^{15}$ cm$^{-2}$ Energy: 50 keV | ·IOS$_{ActMat}$ ·IOS$_{PolyGate}$ ·IOS$_{MetalGate}$ |
| 46. | Thermal annealing | Temperature: 1100℃. Time: 240 minutes. Atmosphere: $N_2$ gas. | ·IOS$_{ActMat}$ ·IOS$_{PolyGate}$ ·IOS$_{MetalGate}$ |
| 47. | Field oxide deposition | Deposition of 1.5 µm TEOS according to the standards for field oxide of the lab. | ·IOS$_{PolyGate}$ ·IOS$_{MetalGate}$ |

| | Process Step | Description | Samples |
|---|---|---|---|
| 48. | Photolithography | Definition of the geometries of the contact pads. | $\cdot IOS_{PolyGate}$ $\cdot IOS_{MetalGate}$ |
| 49. | Annealing to photorresist | Baking of photorresist at 300℃ for 30 min. | $\cdot IOS_{PolyGate}$ $\cdot IOS_{MetalGate}$ |
| 50. | Etching of field oxide | Dry and wet etching of the unmasked field oxide deposited in step 47. | $\cdot IOS_{PolyGate}$ $\cdot IOS_{MetalGate}$ |
| 51. | Removing of resist | Elimination of the resist used to define the pads (step 48). | $\cdot IOS_{PolyGate}$ $\cdot IOS_{MetalGate}$ |
| 52. | Deposition of polycrystalline silicon | Deposition of 350 nm of polycrystalline Si using LPCVD with Silane at at 630℃. | $\cdot IOS_{PolyGate}$ |
| 53. | Doping of the polycrystalline silicon | Doping using $POCl_3$ at 900℃. | $\cdot IOS_{PolyGate}$ |
| 54. | Phosphosilicate Glass (PSG) etching | Wet etching of PSG glass formed during the polysilicon doping. | $\cdot IOS_{PolyGate}$ |
| 55. | Metalization process | Dip in HF solution and deposition of 1.5 µm of Al/Cu | $\cdot IOS_{MetalGate}$ |

| | Process Step | Description | Samples |
|---|---|---|---|
| 56. | Photolithography | Protection of the geometries of the contact pads. | $\cdot$IOS$_{PolyGate}$ $\cdot$IOS$_{MetalGate}$ |
| 57. | Al/Cu etching | Etching of the unprotected regions of the Al/Cu deposited in step 55. | $\cdot$IOS$_{MetalGate}$ |
| 58. | Etchin of polysilicon in obverse | Etching of the unprotected regions of polysilicon deposited in step 52. | $\cdot$IOS$_{PolyGate}$ |
| 59. | Removing of resist | Elimination of the resist used to protect the pads (step 56). | $\cdot$IOS$_{PolyGate}$ $\cdot$IOS$_{MetalGate}$ |
| 60. | Protection of the obverse with resist | Deposition of resist in the front of the wafers. | $\cdot$IOS$_{PolyGate}$ $\cdot$IOS$_{MetalGate}$ |
| 61. | Etching of films in reverse with resist | Dry and wet etching of unwanted material deposited in the back of the wafers. | $\cdot$IOS$_{PolyGate}$ $\cdot$IOS$_{MetalGate}$ |
| 62. | Removing of resist | Elimination of the resist used to protect the obverse (step 60). | $\cdot$IOS$_{PolyGate}$ $\cdot$IOS$_{MetalGate}$ |
| 63. | Metalization process | Deposition of 1 µm if Al in the reverse of the wafer. Surace cleaned by sputter etch. | $\cdot$IOS$_{PolyGate}$ $\cdot$IOS$_{MetalGate}$ |

| | Process Step | Description | Samples |
|---|---|---|---|
| 64. | Annealing for Al contacts | Temperature: 350℃. Time: 120 min. Ambient: $N_2/H_2$. | $\cdot IOS_{PolyGate}$ $\cdot IOS_{MetalGate}$ |
| 64. | **End of the run** | Extraction of wafers. | $\cdot IOS_{ActMat}$ $\cdot IOS_{PolyGate}$ $\cdot IOS_{MetalGate}$ |